Visualization of HIV membrane fusion and inhibition by Serinc5 at multiple length scales

Amanda Elizabeth Ward

B.S. University of Maryland, 2015
M.S. University of Virginia, 2018

A Dissertation presented to the Graduate Faculty of the University of Virginia
in Candidacy for the Degree of Doctor of Philosophy

Department of Molecular Physiology and Biological Physics

University of Virginia
February 2021

Abstract

To establish a new infection and gain entry to a cell, Human Immunodeficiency Virus (HIV) must fuse its lipid envelope with the host cell plasma membrane. This process of HIV membrane fusion is catalyzed by conformational rearrangements of the HIV surface glycoprotein, Env, and proceeds through a series of intermediate states involving rearrangements of the host and viral membranes. We sought to better understand HIV membrane fusion and the mechanism by which it can be blocked by restriction factors Serinc3 and Serinc5.

To do so required the development of new assays and tools. We demonstrated that plasma membrane blebs incorporating the viral receptor, CD4, and co-receptor CCR5, were useful model membranes for studying HIV membrane fusion by both total internal reflection fluorescence microscopy (TIRFm) and cryo electron tomography (cryoET) (Chapter 2). Additionally, we designed a modular perfusion chamber that improved reliability and throughput of the TIRF-based fusion assay (Appendix B). With these, we characterized Serinc-disrupted and unperturbed HIV membrane fusion intermediates and showed that Serinc5 incorporation into HIV particles obstructs fusion at multiple intermediate steps.

Next, to better understand the mechanism by which Serinc5 disrupts fusion, we examined the importance of the viral membrane for Serinc5-mediated inhibition of HIV membrane fusion (Chapter 3). We found that pretreatment of HIV particles with phosphatidylethanolamine (PE) selectively increased fusion of Serinc5-containing HIV particles regardless of acyl chain length or saturation, demonstrating the importance of

lipid headgroup interactions for Serinc5 restriction. Crucially, we demonstrated that Serinc5 increases the fraction of the viral membrane in an ordered lipid phase by two methods and provided the first examination of lipid phase behavior in an intact viral membrane. Based on these data, we describe a model for the mechanism of Serinc5-mediated restriction of HIV membrane fusion.

In addition to the assays and tools listed above, we developed a method to construct semi-supported lipid bilayers (SSLBs) on holey carbon supports for cryoEM and showed that SSLBs can reproduce multiple features of conventionally prepared supported lipid bilayers (Chapter 4). We then demonstrated applications of cryoEM of SSLBs for studying protein oligomerization, assembly, and interactions with membranes at spatial frequencies not accessible by light microscopy.

The present work provides a detailed view of HIV fusion and how it is disrupted by Serinc5's alteration of the viral membrane. Additionally, we describe tools for the study of membrane processes, including fusion.

Acknowledgements

This dissertation is dedicated to my husband, Devin. Thank you for supporting, and more importantly, feeding me throughout this process.

Thank you to my advisor, Dr. Lukas Tamm for your support and flexibility. Thank you for giving me the opportunity to pursue so many different projects and ideas.
To my committee members, thank you for your helpful mentorship and feedback throughout the years. Thank you to Dr. Barbie Ganser-Pornillos for your frequent encouragement and generous mentorship. To Dr. Judith White, thank you for your dedication to my growth as a virologist, even in your retirement.

Thank you for helpful discussions and camaraderie to my colleagues in the Tamm lab.

Table of Contents

Chapter 1: Introduction

1.1 Introduction to Lipid Membranes:

Lipids are a class of biomolecules defined by their hydrophobicity but diverse in their structure and function. In organisms, lipids enable many functions including energy storage, cell signaling, and compartmentalization of biological functions. This property of forming a barrier that chemically separates one set of molecules from another is so fundamental that it defines the very beginnings of life when fatty acids aggregated and sequestered other proto-biomolecules, forming the first protocells (Cornell et al., 2019; Yewdall et al., 2018). Millions of years later, we study the emergent properties of membrane formation and lipid organization as it relates to human health and disease.

The lipid species that compose biological membranes are amphipathic: one side hydrophobic and the other hydrophilic. To minimize the entropic penalty of ordered water molecules around hydrophobic molecules, amphipathic lipids spontaneously self-assemble into micelles or bilayers or other structures (Sych et al., 2018). The existence of two layers of lipids surrounding cells was first proposed by Gorter and Grendel in 1925 after they showed the surface area of lipids extracted from “chromocytes,” now called red blood cells, was twice the surface area of the cells. Ten years later, Danielli and Davson proposed proteins may be associated with the “lipoidal film” but it was not until 1972 that Singer and Nicolson theorized proteins were inserted into fluid lipid bilayers.

The exact composition of biological membranes varies by species and organelle but, in humans, the lipid portion of membranes is primarily composed of phospholipids,

sphingolipids, and cholesterol (Casares et al., 2019; Spector and Yorek, 1985). Phospholipids are defined structurally by two fatty acid "tails" linked to a glycerol-3-phosphate. The phosphate can be additionally modified with a variety of polar headgroups that impart charge or curvature. Of the phospholipids in eukaryotic membranes, approximately half have a phosphatidylcholine (PC) headgroup. Its net zero charge and lack of curvature make it a common structural lipid (Van Meer et al., 2008). Sphingolipids are derived from sphingosine which has a long alkyl chain, analogous to one fatty acid in phospholipids. An additional fatty acid is attached to sphingosine by an amide linkage to generate a ceremide. Ceremide can be further modified with various head groups to produce sphinogomyelin (choline), cerebrosides (monosaccharide), or gangliosides (oligosaccharide) (Casares et al., 2019). The alkyl chain of sphingosine is saturated and the fatty acids attached to sphingosine are generally saturated or trans-unsaturated, meaning the molecule has a flat, columnar shape that packs well with other flat lipids, generally saturated lipids and sterols (Merrill, 2008). Sphingolipids pack particularly well with cholesterol—so well that this has been dubbed the "umbrella model" where the polar headgroup of a taller sphingolipid shields the much shorter and more hydrophobic cholesterol from solvent interactions (Huang and Feigenson, 1999). Additionally, the planar four ring structure of cholesterol packs well against the straight alkyl chains of sphingolipids while allowing the hydroxyl group on cholesterol to hydrogen bond with the amide nitrogen on sphingosine (Figure 1.1) (Fantini and Barrantes, 2013).

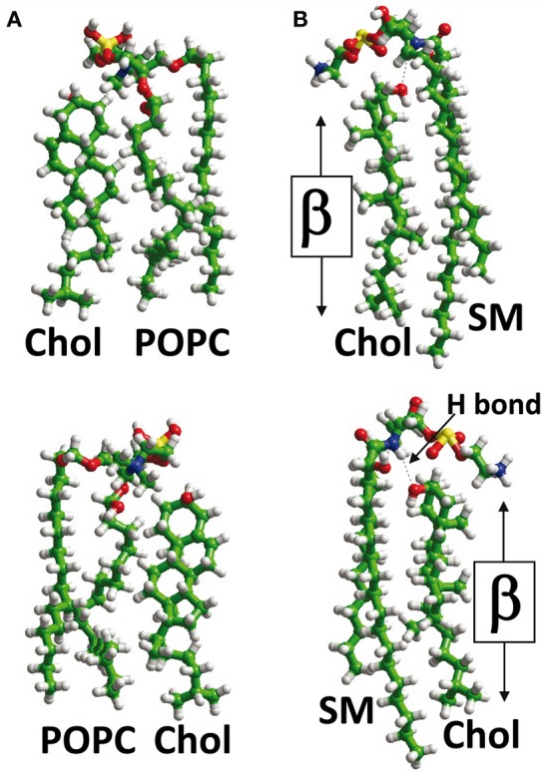

Figure 1.1 Configurations of cholesterol interactions with other membrane lipids. Ball and stick models of cholesterol interacting with the phospholipid, palmitoyloleoylphosphatidylcholine (POPC) **A**. or sphingomyelin (SM) **B.** A hydrogen bond between the cholesterol hydroxyl and SM amine orients cholesterol with its α face towards SM and its β face towards other lipids in the membrane. This configuration of cholesterol and SM is referred to as the umbrella model. Reproduced from Fantini and Barrantes, 2013.

The relative concentrations of lipid species varies based on organism, cell type and organelle (Symons et al., 2020), but in eukaryotes, the concentrations of sphingolipids and cholesterol correlate with each other. In most eukaryotic cells, there

exists a gradient of sphingolipids and cholesterol through the secretory pathway such that the endoplasmic reticulum is poor in sphingolipids and cholesterol but the plasma membrane is enriched in both (Van Meer et al., 2008). There are also compositional differences in the two leaflets of the bilayer. For example, in the plasma membrane, phosphatidylserine (PS), phosphatidylethanolamine (PE), and phosphatidylinositols (PIs) are largely confined to the inner, cytoplasmic leaflet while PC and sphingomyelin (SM) are enriched in the outer leaflet. The degree to which specific species are enriched or excluded appears to depend on the cell type studied and method used but these broad generalizations are nonetheless useful for understanding the layers of organization of lipid composition within cells (Van Meer et al., 2008).

Cholesterol is the notable exception to asymmetric composition and is found in approximately equal concentrations in both leaflets (Van Meer, 1989). Due to its small size and hydrophobicity, it is able to rapidly flip between leaflets (Müller and Herrmann, 2002; Steck et al., 2002). It is energetically unfavorable for most phospholipids to flip from one leaflet to the other as the hydrophilic headgroup would have to pass through the hydrophobic bilayer interior. Even so, this process of flipping does occur on the time scale of hours to days so cells must input energy to maintain concentration gradients of lipids via ATP-dependent flippases (Daleke, 2003; Eeman and Deleu, 2010). To justify this input of energy, lipid asymmetry must have utility to a cell and indeed, a few examples have been observed. The best known example is the externalization of PS by calcium-independent scramblases upon apoptosis as an “eat me” signal to macrophages

(Suzuki et al., 2013). To maintain the specificity of this response, leaflet asymmetry must actively be maintained.

1.2 Lipid Phases:

The lipid composition of membranes is spatially heterogeneous across cellular compartments and leaflets as discussed above. The following section summarizes lateral heterogeneity driven by phase separation within membranes. Lipid bilayers exist in one of five phases: liquid ordered (L_o), liquid disordered (L_d), gel solid-ordered (S_o), pseudocrystaline (L_c), and ripple (P_b) (Tristram-Nagle and Nagle, 2004). A lipid bilayer composed of a single phospholipid species will be in a solid-ordered phase at temperatures up to its melting temperature (T_m) and in a liquid crystalline or liquid disordered phase above Tm (Figure 1.2). The liquid disordered phase is a fluid state where individual lipid molecules pack very loosely, have numerous *gauche* conformations in their tails, and are able to diffuse laterally past each other. In contrast, the gel phase is a solid-like phase where lipids pack together tightly and individual lipids are not able to laterally diffuse. The liquid ordered phase is a hybrid of the properties of L_d and S_o phases where lipids pack together tightly and are more ordered with mostly *trans* conformation in their tails, yet individual lipid species are still able to diffuse laterally, making this a liquid phase (Veatch and Keller, 2005). This is only possible in membranes with sufficiently high sterol concentration to maintain fluidity of an otherwise gel-like membrane and to promote ordered packing of lipids above their melting temperature (Ackerman and Feigenson, 2015). Membranes composed of

cholesterol and two lipid species with different melting temperatures show coexistence of immiscible L_o and L_d phases at certain temperatures (Veatch and Keller, 2003). The shape and relative sizes of L_o and L_d domains within these phase separated membranes depends on many factors including composition (Veatch and Keller, 2005), curvature, and line tension (Baumgart et al., 2003). At very high concentrations of sterols and in the presence of saturated phospholipids, crystalline domains composed of sterols can spontaneously form within the bilayer. The concentration of sterol required to nucleate this pseudocrystaline phase depends on the identity of the sterol and the composition of the lipid bilayer (Ziblat et al., 2012). Lastly, the ripple phase is a periodic puckering of the lipid bilayer that is often formed as a gel phase is warmed or as heat is removed from an L_d bilayer (Akabori and Nagle, 2015; Sengupta et al., 2003). These last two phases do not occur in biological membranes but are included here for completeness.

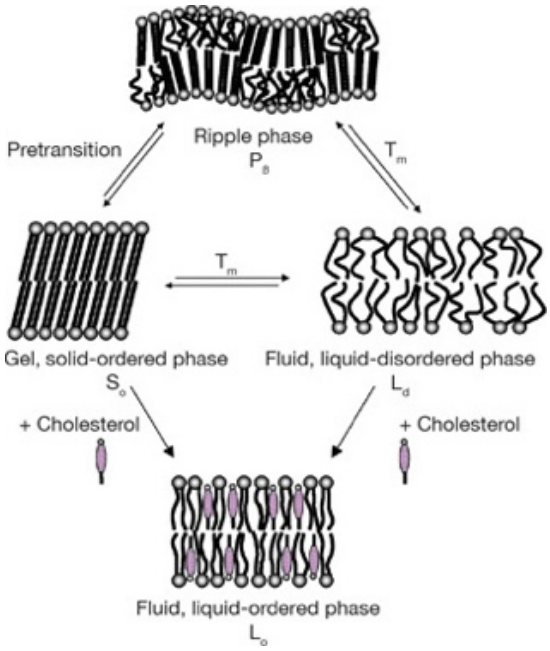

Figure 1.2: Diagram showing different lipid packing with phase transitions. A membrane in a solid-ordered phase can melt to a fluid disordered phase as temperature increases above melting temperature (Tm). Increasing cholesterol concentration in a membrane can convert both L_d and S_o phases to a liquid ordered (L_o) phase. Reproduced from Eeman & Deleu 2010

1.3 The evolution of the lipid raft model:

In their pivotal 1997 paper, Simons and Ikonen described their lipid raft model, which posited that sphingolipids and cholesterol cluster together and diffuse as a larger unit through a fluid lipid bilayer. With further study, the lipid raft hypothesis and the language used to describe it has been refined but the underlying concept of lateral heterogeneity has remained (Veatch and Keller, 2005). While all lipids interact more favorably with each other than water, some species interact slightly more favorably than others due to geometry (Fantini and Barrantes, 2013; Soloviov et al., 2020). When multiplied across the millions of lipid molecules in a membrane, this uneven mixing of lipid species gives rise to the coexistence of liquid ordered and disordered phases (Levental et al., 2020). Classically, L_o domains in biological membranes are enriched in cholesterol, sphingolipids, and saturated phospholipids (Brown and London, 2000). However, the dynamic nature of domains means all of these species are found in both L_o and L_d domains and individual lipid molecules can diffuse between them. Restating this in terms of chemical kinetics, the rate constant of L_o association is slightly higher than the rate constant of dissociation for these three types of lipids and thus they become enriched

in L_o domains. While micron-scale domains are easily observed in model membranes (Veatch and Keller, 2005), ordered domains are predicted to be nano-scale and short-lived in cellular membranes (Eggeling et al., 2009), making their observation difficult (Jacobson et al., 2007) and the biological relevance of phase separation controversial (Levental et al., 2020).

Historically, certain membrane proteins were thought to selectively concentrate into lipid rafts and were thus defined as "raft associated" by their insolubility in the detergent, Triton X-100 (Simons and Ikonen, 1997). Further study has revealed that on the whole, the concentration of proteins within L_o domains is lower than in non-domain areas and that detergent resistance is a flawed proxy for domain partitioning (Lichtenberg et al., 2005). A more modern understanding of protein-lipid domain interactions posits that lipids and certain proteins work cooperatively to nucleate and stabilize membrane heterogeneity where lipids may serve as a regularly spaced template for macromolecular assembly (Levental et al., 2020). Moreover, protein immobilization after interaction with membranes may coalesce stabilized annular lipids into larger scale domains (Lee, 2011). In addition, long filamentous proteins like cortical actin have been shown to restrict the diffusion of proteins and lipids to a small area with locally distinct properties in what has been dubbed "corralling" (Arumugam et al., 2015; Daněk et al., 2020; Goiko et al., 2016; Heinemann et al., 2013; Schütte et al., 2017; Vogel et al., 2017). As actin exclusively interacts with the inner leaflet of the plasma membrane, this raises questions about how domain formation is transmitted across the bilayer leaflets.

In model membranes, mixtures of lipids resembling the composition of the outer leaflet (PC, SM, Cholesterol) reliably phase separate in giant unilamellar vesicles (GUVs) and supported planar bilayers (Dietrich et al., 2001). However, lipid mixtures that mimic the composition of the inner leaflet of the membrane do not phase separate under most conditions (Wang and Silvius, 2001). This discrepancy gives rise to the yet unresolved question about how lipid domains arise in both leaflets of the membrane. Previous work from the Tamm lab with asymmetric supported planar bilayers showed that phase separation in one leaflet could induce phase separation in the opposite leaflet, even if the composition of that leaflet did not phase separate in symmetric bilayers. Specifically, a phase separated monolayer composed of cholesterol and two PC species with different melting temperatures induced phase separation of a mixture of PC, PE, PS, and cholesterol (Kiessling et al., 2009; Wan et al., 2008). This and other studies (Fujimoto and Parmryd, 2017) provided strong evidence that phase behavior is transmitted through the bilayer and phase separation in one leaflet can nucleate phase separation in the opposite leaflet.

1.4 Methods and Models for Studying Membranes:

A multitude of methods and model systems for studying membrane behaviors have been developed (Czogalla et al., 2014). They differ in their composition (synthetic lipids, biological lipid extracts, incorporation of proteins) and in their geometries (spherical vesicles or planar bilayers). As with all methods, each has strengths and weaknesses for answering specific questions which will briefly be discussed here for the methods relevant to this dissertation.

The simplest models for studying membranes are liposomes, also called unilamellar vesicles (Figure 1.3). These spherical bilayers can be composed of a single species or complex mixture of synthetic or extracted lipids, and can range in size from small (SUVs), to large (LUVs), to giant (GUVs), depending on how they are made. The size of the vesicle and resulting curvature of the bilayer can impart different properties. For example, as vesicle diameter decreases, lipids become more disordered, membrane line tension increases, and vesicles become more likely to undergo membrane fusion (Hernandez et al., 2014; Lin et al., 2012; Malinin and Lentz, 2004). GUV preparation is quite different from SUV or LUV preparation so the following will focus on SUVs and LUVs. There are many protocols for making unilamellar vesicles but the most common methods begin by rehydrating a dried lipid film with aqueous buffer, which causes the lipid film to swell and form multilamellar vesicles (MLVs) of varying size (Bangham and Horne, 1964). These MLVs are then fragmented by sonication (Papahadjopoulos and Watkins, 1967), or extrusion through filters of defined pore size (Olson et al., 1979) to obtain unilamellar vesicles with a smaller distribution of sizes (Lasic, 1988) or by repeated cycles of freezing and thawing to obtain more homogenous preparations of MLVs. There are exceptions to this and LUVs prepared by certain methods may also contain multilamellar vesicles (Scott et al., 2019). Alternative techniques for producing SUV and LUVs include solubilization of a lipid mixture in aqueous solution by detergent or organic solvent followed by removal of detergent/solvent (Nozaki et al., 1982; Szoka and Papahadjopoulos, 1978) or controlled injection of phospholipids in organic solvent into aqueous solution (Deamer and Bangham, 1976). Vesicles prepared these ways have a

symmetric leaflet composition although recently, techniques have been developed to prepare asymmetric vesicles as well (Doktorova et al., 2018). Additionally, membrane proteins can be reconstituted into vesicles to make proteoliposomes. This provides a more native-like environment than a detergent micelle for membrane proteins. SUVs and LUVs have the benefits of a defined composition amenable to precise control and being relatively cheap and simple to produce. They model protein-free bilayers well with the flexibility to reconstitute membrane proteins as well. Their small size can be a hindrance for fluorescence microscopy or an asset for cryo Electron Microscopy (cryoEM) or spectroscopies such as circular dichroism or fluorescence.

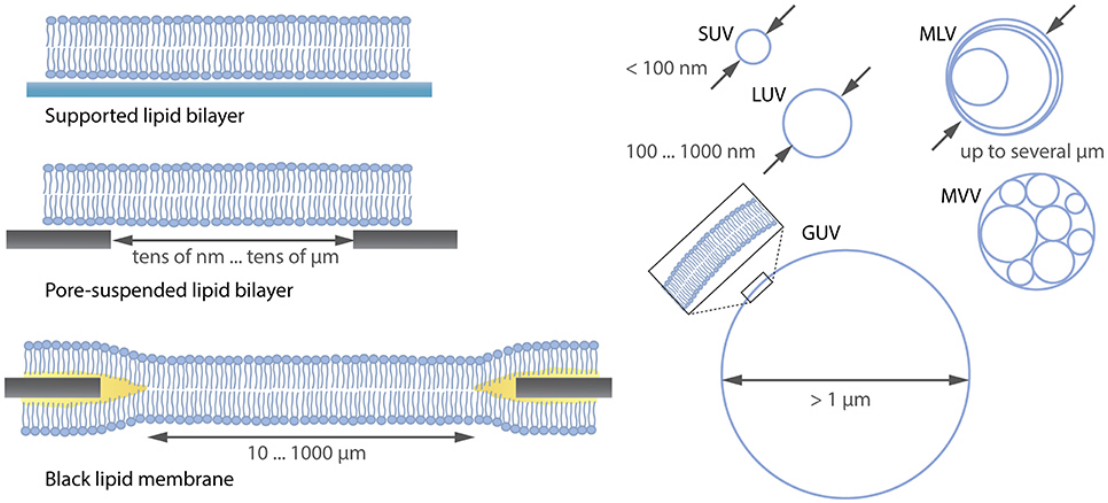

Figure 1.3 Diagram comparing common model membranes, including supported lipid bilayers (SLBs) and liposomes of varying size. Multilamellar vesicles (MLVs) can be transformed into small (SUVs) or large unilamellar vesicles (LUVs) by repeated freeze/thaw cycles, sonication, and extrusion. Adapted from Stein et al., 2017.

Microscopy of spherical model membranes requires imaging and data analysis in three spatial dimensions, which can complicate some experiments. Supported lipid bilayers (SLBs) simplify data acquisition and analysis for many experiments by reducing the number of dimensions with a planar membrane (Figure 1.3). Since they were developed about 35 years ago, many iterations and applications of supported lipid bilayers have been described (Brian and McConnell, 1984; Tamm, 1984; Tamm and Groves, 2009; Tamm and McConnell, 1985). The simplest protocol for making SLBs is via vesicle adsorption to a hydrophilic support. This produces an SLB with a symmetric composition in both leaflets (Mapar et al., 2018). One critique of SLBs is that contacts between lipid headgroups and the support constrains the motion of individual lipid molecules, altering the properties of the membrane (Collins and Keller, 2008). Since most support materials are not atomically flat, these points of contact are minimal compared to the total concentration of lipids (Kiessling et al., 2009). To further minimize interactions with the substrate, a polymer cushion can be used to increase the hydrophilic cleft between membrane and support. Polymer-supported planar membranes are more fluid and also retain leaflet asymmetry longer than non-polymer supported membranes (Kiessling et al., 2006). For all supported membrane experiments described in this dissertation, a PEGylated lipid modified with a silane was used (Wagner and Tamm, 2000). This specific polymer creates a 4 nm cleft of water between a SLB and substrate (Kiessling and Tamm, 2003). Additionally, asymmetric planar membranes can be created by sequentially depositing each leaflet on a substrate by the Langmuir-Blodgett method followed by vesicle fusion (Kalb et al., 1992) or the Langmuir-Schaefer method (Tamm

and McConnell, 1985). Furthermore, SLBs can be created from proteoliposomes to reconstitute membrane proteins and model biological processes in a defined model system (Kalb et al., 1992; Kiessling et al., 2015a).

Giant Plasma Membrane Vesicles (GPMVs or blebs) are small portions of the plasma membranes of cells (Scott, 1976). They incorporate nearly all plasma membrane proteins in their native fold, with post-translational modifications, except adhesion factors, which are largely excluded from blebs (Bauer et al., 2009). Blebs also have the same lipid composition as the plasma membrane they were prepared from (Symons et al., 2020) although leaflet asymmetry is lost during the blebbing process (Baumgart et al., 2007). Multiple methods to produce blebs have been described, ranging from hypoosmotic stress (Sarabipour et al., 2015) to laser-induced blebbing (Kelly et al., 2009). One of the most widely used involves chemical crosslinking with formaldehyde and dithiothreitol (DTT) (Gerstle et al., 2018; Sezgin et al., 2012). The exact mechanism by which this causes plasma membrane vesiculation is unknown (Levental and Levental, 2015). Blebs remain attached and contiguous with the plasma membrane unless they are mechanically disturbed. With gentle shaking, blebs can be detached and purified (Scott, 1976). These blebs can then be used in their spherical state or added to a Langmuir-Blodgett monolayer to form a supported planar plasma membrane (SPPM) (Yang et al., 2017). Blebs are one of the highest fidelity models of the plasma membrane available and are amenable to a wide range of experiments, but like every model, there are notable differences from physiological conditions that limit interpretation. Blebs are not metabolically active and are best thought of as a “dead” equilibrium state (Sezgin et al.,

2012). Also, blebs are permeable to hydrophilic solutes up to 40 kDa (Skinkle, 2019) so some cytosolic components are retained in blebs (Bauer et al., 2009) but many others leak out. A preparation of blebs will have a range of sizes, all of them smaller than the parent cell and thus blebs will always have higher curvature than the plasma membrane. This can be circumvented by transforming blebs into an SPPM. Finally, the plasma membrane is normally shaped by the cytoskeleton and while cytoskeletal proteins are found in blebs (Bauer et al., 2009), they are not likely to be polymerized and thus do not exert the same physical properties on the membrane (Schneider et al., 2017).

The selection of just these three membrane models is a focused slice through the field of membrane biology and the descriptions presented here are not exhaustive for all the variations and iterations that have been described. This reflects the diversity of processes that occur at membranes as well. We turn attention from foundational concepts in membrane biology to applications of membranes and their organization for microbiology.

1.5 Introduction to Viruses:

Viruses are particles capable of directing self-replication in cells, but by strict definitions are not considered living organisms. They are more numerous than every human who has ever lived and every star in the known universe ("Microbiology by numbers," 2011). Specifically, bacteriophages are the most abundant biological entity in the biosphere (Hatfull, 2015). With this magnitude there is vast diversity of which

science has only sampled a miniscule fraction. Statistical estimates predict roughly 320,000 undiscovered mammalian viruses (Anthony et al., 2013).

Viral diversity is classified in two major systems: the International Committee on Taxonomy of Viruses (ICTV) classifies based on conserved nucleic acid sequences (International Committee on Taxonomy of Viruses, 2012) and the Baltimore classification system classifies based on the nucleic acid that composes the viral genome and how it is replicated (Baltimore, 1971). Practically, viruses can also be classified based on their physical features such as the nucleic acid that composes the genome, the presence or absence of a lipid envelope, or the shape, size, and symmetry of the capsid (Lwoff et al., 1962). This thesis will focus on enveloped viruses and their interactions with membranes.

The replicative cycle of a virus follows the same plot as any heist; get in, take all you can, and get out without raising the alarm. In viral terms this translates to cell entry, protein translation, genome replication, and finally particle assembly and release (Ryu, 2017). The details of each step varies between viruses but many follow this general pattern. For enveloped viruses, particle assembly and release involves targeting viral components to assembly platforms on host membranes, inducing membrane curvature to initiate budding, and finally scission of host and progeny viral membranes (Perlmutter and Hagan, 2015). Conversely, cell entry of enveloped viruses includes fusion of host and viral membranes to release viral contents into the cytoplasm (Mercer et al., 2020; White and Whittaker, 2016)

1.6 Membrane Fusion:

During cell entry, the viral genome is introduced into the host cell from a viral particle via membrane fusion. Membrane fusion is the process by which two lipid bilayers become one continuous bilayer via a series of intermediate steps. Overall, the end point of the membrane fusion reaction is energetically downhill from the starting state (Cohen and Melikyan, 2004). However, fusion does not occur spontaneously on biologically meaningful timescales because lipid bilayers are very stable assemblies that require an input of energy to disrupt (Plemper and Melikyan, 2013).

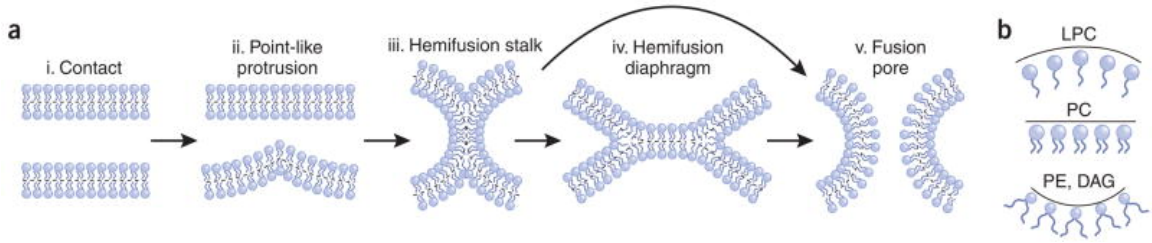

Figure 1.4 Lipidic fusion intermediates and intrinsically curved lipids. **a.** Membrane fusion begins as an area of close contact between bilayers (i.) where a point-like protrusion (ii.) interacts with the second membrane, forming a hemifusion stalk (iii.). The hemifusion stalk may either proceed directly to fusion pore opening (v.) or first convert into a hemifusion diaphragm (iv.). **b.** Lipids can have positive (lysoPC LPC), neutral (PC), or negative (PE, Diacylglycerol (DAG)) intrinsic membrane curvature. Negative intrinsic curvature of the exterior leaflet stabilizes hemifusion intermediates and positive intrinsic curvature in the interior leaflets stabilize fusion pores. Adapted from Chernomordik and Kozlov, 2008.

Before fusion can begin, membranes must overcome the repulsive hydration force. Bringing membranes within 3 nm of each other removes water molecules from their favorable interactions with phospholipid headgroups and requires an input of energy (Gawrisch et al., 1992; Leikin et al., 1993; Rand and Parsegian, 1989). Once water has been pushed aside from the cleft between membranes, dehydrated lipid headgroups of the external leaflets can interact and form a point-like area of close contact (Figure 1.4, ii) (Efrat et al., 2007). With a further input of energy to bend membrane leaflets and transiently expose lipid tails to more water, the contact area expands into a hemifusion stalk where the external leaflets of both bilayers have fused but the internal leaflets remain unfused (Figure 1.4, iii) (Chernomordik and Kozlov, 2005). The hemifusion membrane is likely free of transmembrane proteins because their hydrophilic, cytoplasmic or extracellular domains would have to transit the hydrophobic bilayer interior in order to occupy the hemifusion membrane (Nikolaus et al., 2010). Hemifusion is generally agreed upon as an on-pathway intermediate state in membrane fusion although some details remain the subject of debate. It remains undecided whether the vertically oriented, “hemifusion stalk” can proceed directly to fusion pore opening (Kuzmin et al., 2001; Siegel, 1993) or must first widen into the extended “hemifusion diaphragm” configuration (Figure 1.4, iv) (Markin et al., 1984). Many of these subtleties may depend on the properties of the membranes undergoing fusion like the composition and curvature of the membranes (Nikolaus et al., 2010). Hemifusion stalks, diaphragms, and fusion pores are highly curved membrane states. Thus, columnar lipids without intrinsic curvature, e.g. PC, must tilt or splay their acyl chains to accommodate curvature.

Tilt applied to flat lipids results in voids between acyl chains, which incurs an energetic penalty (Chernomordik and Kozlov, 2008; Siegel, 1993). Lipids with intrinsic curvature like the cone-shaped phospholipids, PE and lysoPC with negative and positive spontaneous curvature, respectively, can accommodate curvature without creating vacuums (Figure 1.4b). Accordingly, hemifusion intermediates are stabilized by negative spontaneous curvature in the exterior leaflets (Aeffner et al., 2012; Basáñez et al., 1998; Chernomordik et al., 1995, 1987; Haque and Lentz, 2004; Kasson and Pande, 2007; Kreutzberger et al., 2015; Lentz and Lee, 1999; Meers et al., 2000; Meher and Chakraborty, 2019; Yang and Huang, 2002). Additionally, small vesicles with high curvature are more fusogenic due to strain and lateral tension at baseline that is relieved by fusion (Haque and Lentz, 2004; Kasson and Pande, 2007; Lee and Schick, 2008). Energetic calculations predict that the hemifusion diaphragm is more favorable than the stalk, but the diaphragm does not form spontaneously in DOPC membranes without lateral tension to pull the edges of the stalk (Chernomordik and Kozlov, 2003). The propensity of a hemifusion diaphragm to transition to a fusion pore, the penultimate stage in membrane fusion, also depends on lateral tension and spontaneous curvature of the lipids (Chernomordik et al., 1987; Cohen et al., 1980; Shillcock and Lipowsky, 2005). Therefore, the forces that create a diaphragm may very quickly lead to fusion pore opening, as has been observed in molecular dynamics simulations of fusion (Risselada et al., 2014). During fusion pore opening, the inner leaflets of the two membranes fuse and an aqueous channel opens between the membranes (Figure 1.4, v). As with all intermediate steps of membrane fusion, pore opening requires an input of energy (Cohen

and Melikyan, 2004). In models of fusion pores arising directly from hemifusion stalks, proteins may stabilize the stalk and mechanically drive opening of a pore, providing the required energy (Zimmerberg et al., 2006). Similar to hemifusion, fusion pores are stabilized by lipids with spontaneous curvature, but the curvature of the fusing leaflet and the effects of curved lipids are flipped compared to hemifusion (Markin and Albanesi, 2002). Negatively curved lipids, like PE, inhibit fusion pore formation and positively curved lipids, like lysoPC, promote fusion pores (Chernomordik and Kozlov, 2003).

Experimentally, fusion pores can be observed by conductance of solutes: initially ions (Zimmerberg et al., 1987) and upon expansion, fluorophores and other molecules of increasing size. Opening of a small fusion pore is likely reversible (Chernomordik et al., 2006; Melikyan et al., 1993) until an input of energy irreversibly expands the fusion pore from its highly curved "hourglass" shape to the less curved post-fusion membrane (Cohen and Melikyan, 2004). Wide fusion pore expansion completes membrane fusion.

1.7 Catalysis of Membrane Fusion by Proteins:

Cells use a cadre of proteins working in concert to overcome the kinetic barriers of membrane fusion for a myriad of cellular functions including vesicle trafficking, exocytosis, endosome maturation, syncytium formation, and mitochondrial remodeling. Viruses also use proteins to mediate fusion, but, to economize on limited genome space, most viruses use multiple copies of a single fusion protein (e.g. Retroviruses) while some use a small number of different fusion proteins (e.g. Herpesviruses) (White et al., 2008). The specifics of how viral fusion proteins enable fusion varies between viruses but the

mechanism is largely conserved. When an active fusion protein on the viral surface (Figure 1.5, ii) receives a "triggering" signal, it undergoes a conformational change that exposes and then inserts a hydrophobic "fusion peptide" or "fusion loop" into the host cell membrane (Figure 1.5, iii) (Harrison, 2015; White and Whittaker, 2016). This conformation is referred to as the "pre-hairpin intermediate" or "extended intermediate" where the viral fusion protein bridges the viral and cellular membranes (Bullough et al., 1994; Rey and Lok, 2018). The fusion protein then undergoes another conformational change, overcoming the hydration force to draw the membranes closer together and promote fusion (Chen et al., 1999). For HIV and other class I viral fusion proteins, the pre-hairpin folds back onto itself (Figure 1.5, iv) to become a hairpin, or six-helix bundle (6HB) (Figure 1.5, v), The exact relationship between viral fusion protein foldback and membrane rearrangements remains somewhat enigmatic due to their small size and short lifetime. Evidence from the best studied viral fusion protein, Influenza HA, suggests that pre-hairpin refolding into the 6HB promotes hemifusion. Then, further foldback brings the fusion peptide and transmembrane domains together to promote opening of a fusion pore (Figure 1.5, vi) (Armstrong et al., 2000; Kemble et al., 1994; Lai and Freed, 2015; Lee et al., 2017; Melikyan et al., 1995; Tamm, 2003).

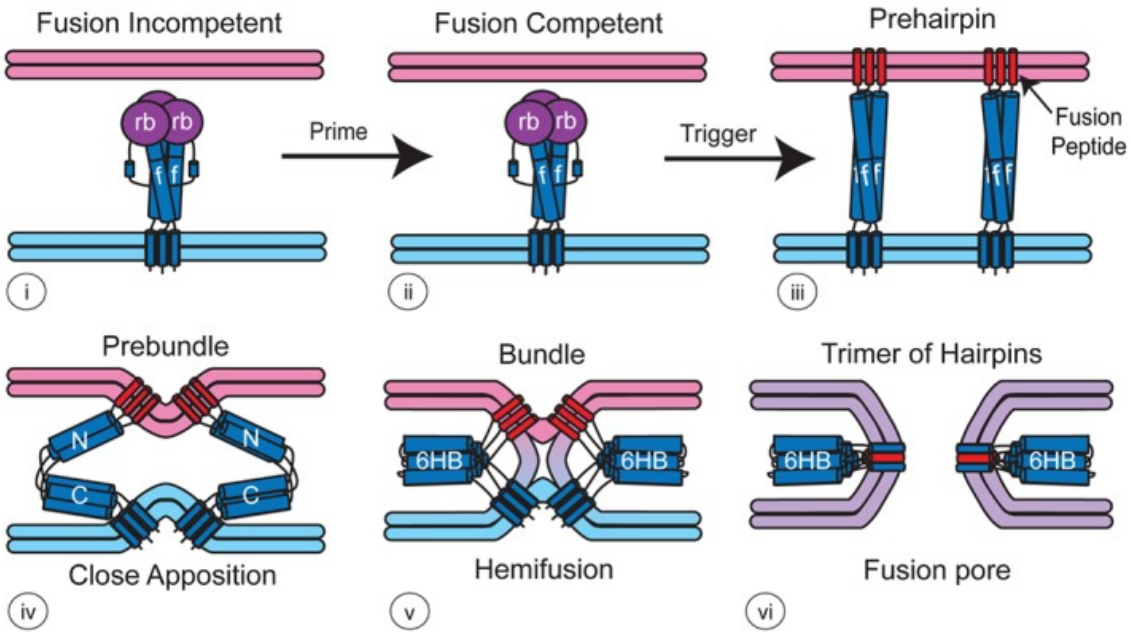

Figure 1.5: Model of membrane fusion driven by viral fusion proteins. The cartoon depicts fusion by a class I fusion protein but the process is similar for class II and III fusion proteins. A viral fusion protein is rendered active in a priming step (i). Priming of class I and II proteins generally involves proteolytic cleavage. The fusion competent protein (ii.) then responds to a fusion trigger by refolding into a prehairpin with fusion peptides inserted into the target membrane (iii.). The prehairpin folds back onto itself, drawing the membranes into close apposition (iv.) until it forms a six-helix bundle (6HB) and the membranes hemifuse (v.). Association of the fusion peptide and transmembrane domains promotes fusion pore opening (vi.) Adapted from White and Whittaker, 2016.

Interestingly, structurally dissimilar viral fusion proteins accomplish this same fusion mechanism with only small variations. These structural differences are formalized into three classes. Class I includes trimeric proteins primarily composed of α-helices that are activated by proteolytic cleavage (eg. Influenza HA, HIV Env, Paramyxovirus F).

Class II includes dimeric proteins primarily composed of β-sheets that are activated by proteolytic processing of a chaperone protein (eg. Flaviviruses and Alphaviruses). Finally, class III, which are likely an equilibrium of monomer and trimer, are composed of a mix of α-helix and β-sheet, and are not proteolytically activated (eg. Vesicular Stomatitis Virus G) (Albertini et al., 2012; Harrison, 2015; Rey and Lok, 2018; White et al., 2008). Proteolytic processing of class I and II proteins, whether during particle assembly/maturation or during entry, creates an active fusion protein that is sensitive to environmental triggers and able to perform the conformational changes described above. Many viral fusion proteins have separate receptor binding and fusion domains that are separated during activation (e.g. Influenza HA, HIV Env) (White et al., 2008). DNA viruses with larger genomes perform the same two functions with separate proteins (e.g. Herpesviruses, Poxviruses) (Eisenberg et al., 2012; Schmidt et al., 2012).

Cells assemble complexes of fusogenic and regulatory proteins to ensure proper timing of intracellular membrane fusion in vesicle trafficking. Viruses must accomplish the same regulation of fusion but without the luxury of multiple, distinct proteins. Instead, they use metastable fusion proteins to sense environmental changes and respond with conformational changes that drive membrane fusion (Harrison, 2015; White et al., 2008). In this context, a metastable state describes a protein folding energy minimum that is not the global minimum, but a kinetic barrier prevents it from adopting the more stable fold. Introduction of the environmental trigger removes this kinetic barrier and the protein is free to adopt the universally lowest energy fold, which is also the fusogenic conformation (Carr and Kim, 1993).

The fusion triggers of many viruses have been identified and range from low pH, calcium, and proteolytic cleavage, to receptor and coreceptor binding. These environmental changes are sensed by the fusion protein and translated into a conformational and/or dynamic change. Illustrating this, the Ebola Virus fusion protein, GP, has a complex fusion trigger involving all factors listed above: proteolytic cleavage by cathepsins, binding its receptor, Niemann-Pick C intracellular cholesterol transporter type I (NPC1), mildly acidic pH, apparently high calcium concentration, and perhaps yet another cryptic factor (Fénéant et al., 2019). The final trigger, low pH, is sensed by histidine and glutamate residues in the fusion domain, GP2 (Lee et al., 2016), which causes compaction of the fusion loop to form a hydrophobic surface that inserts into the host membrane and GP2 to fold back on itself (Gregory et al., 2014).

Some conformational changes of viral fusion proteins are reversible while others are not. Recent single molecule FRET studies of HIV Env (Alsahafi et al., 2019; Lu et al., 2019; Ma et al., 2018; Munro et al., 2014), Influenza HA (Das et al., 2018), and Ebola Virus GP (Das et al., 2020; Durham et al., 2020), illustrate that even in the absence of a fusion trigger, viral fusion proteins reversibly sample conformational states thought to be on pathway intermediate states and even the final, post-fusion state. For Influenza HA, the post-fusion state becomes irreversible after low pH treatment for 30 minutes at room temperature but this transition to irreversibility is quickened by the presence of receptor and a target membrane (Das et al., 2018; Leikina et al., 2002; Tatulian and Tamm, 1996).

Enveloped viruses must fuse with a host cell membrane to begin infection, but exactly which membrane depends on the availability of receptors and environmental

triggers. Within most organisms and tissues, the extracellular space is maintained at neutral pH at homeostasis and thus low pH triggered viruses must make their way to an acidic cellular compartment like endosomes or lysosomes for entry (Mercer et al., 2010; White and Whittaker, 2016). After binding cell surface receptors and/or attachment factors, viruses may enter the endocytic pathway via macropinocytosis or clathrin-mediated endocytosis. As vesicles mature and progress through the endocytic pathway from early endosomes to late endosomes and eventually to lysosomes, the pH decreases from 6.3 to 5.5 to 4.7 respectively (Casey et al., 2010). For viruses with a simple low pH fusion trigger, the virus traffics to an endosome of sufficiently low pH and then fuses. Beyond pH, endosome maturation also changes the proteins present, certain ion concentrations, and the lipid composition of the endolysosomes. These may introduce additional fusion triggers like a receptor, a protease, or a cation (Nathan et al., 2020; Straus et al., 2020). While not strictly a fusion trigger, the lipid composition of endolysosomes also contributes to fusion compartment determination as it has been shown that Semliki Forest Virus (SFV) and Hantavirus require a certain minimum concentration of cholesterol for efficient fusion (Kielian and Helenius, 1984; Kleinfelter et al., 2015; White and Helenius, 1980). Similarly, Influenza A fusion is enhanced by increasing cholesterol in the target membrane (Domanska et al., 2013). For both HIV and SFV, cholesterol concentration in the target membrane has been shown to influence the depth of fusion peptide insertion (Lai et al., 2012; Umashankar et al., 2008). Cholesterol has many effects on membranes, including maintenance of viscosity and phase separation, which have also been shown to influence membrane fusion (Yang et al., 2017,

2016b, 2016a). The importance of cholesterol in the target membrane very likely extends to fusion of many enveloped viruses as well even if it has not been explicitly studied.

Dogma states viruses that fuse at neutral pH and whose receptor and fusion trigger are present at the plasma membrane, such as HIV, can fuse with and enter at the plasma membrane (McClure et al., 1988; Stein et al., 1987). The reality may be more complicated as HIV pseudovirus particles have also been observed to fuse with an acidified endocytic compartment (Sood et al., 2016) so it may be more accurate that HIV is capable of fusion at the plasma membrane or within an early endosome but the cellular location of HIV fusion appears to depend on the cell type studied (Clotet-Codina et al., 2009; Dale et al., 2011; Herold et al., 2014) and availability of receptor (Padilla-Parra et al., 2012). This may also be the case with SARS-CoV-2: within tissues where fusion-triggering trypsin-like proteases are present (e.g. lung, small intestine), SARS-CoV-2 may be able to fuse with the plasma membrane of cells expressing its receptor, ACE2 (Hoffmann et al., 2020). In other tissues without cell surface trypsin-like proteases, the virus and its receptor may be endocytosed where cathepsin within endolysosomes promote cell entry (Walls et al., 2020).

1.8 Methods for studying viruses:

Arguably, the most important techniques for studying viruses are those for growing viruses and their models *in vitro*. Before the advent of molecular biology, viruses could be isolated from patient or environmental samples by culturing the filtered sample in competent cells. Viruses grown this way could then be plaque isolated by propagating material from a single plaque, presumably caused by a single infectious

particle, to obtain a pure virus line (Dulbecco and Vogt, 1954). While accessible to many clinical and research labs, culturing virus this way does not allow controlled genetic modification of the virus to study the effect of specific mutations. Forward genetics approaches were possible but imprecise (Desselberger, 2017).

The first solution to the problem of genetic intractability of viruses was the development of a reverse genetics system for Poliovirus in 1981 (Racaniello and Baltimore, 1981). This enabled production of replication competent viruses from transfection of cDNA clones of viral genomes which could be modified and mutated. A single plasmid containing the relatively small cDNA genomic clone of poliovirus (~7500 nucleotides) (Tavares et al., 2013) was sufficient for this simple, positive-sense RNA virus. Negative-sense, segmented, and larger genomes require more complicated systems. For negative-sense viruses, a positive-sense transcript of the components of the viral replication machinery must be supplied along with a negative-sense transcript of the genome. For segmented viruses, separate transcripts for each of the segments must be transfected. For large viral genomes, multiple reverse genetics approaches have been employed including cDNA expression from a Bacterial Artificial Chromosome (BAC), *in vitro* ligation of cDNA fragments, and use of a helper vaccinia virus (Almazán et al., 2014). Despite constant interest in Influenza A Virus, a reverse genetics system for the virus was not developed until 1999 due to the difficulties of replicating its segmented, negative-sense genome (Neumann et al., 1999). While reverse genetics viruses enable easier correlation of genotype with phenotype, they are self-replicating and thus require the same biosafety precautions as their parent virus (in the absence of attenuating

mutations or gene deletions). Pseudoviruses also allow genetic manipulation of viral proteins but are non-replicating and thus generally require a much lower biosafety level than the virus they model.

The name “pseudovirus” was first used to describe a virus particle from a mouse cell infected with polyoma virus which incorporated a segment of mouse DNA within the polyomavirus capsid (Michel et al., 1967). From this incidental finding, the field gained pseudoviruses as a versatile tool. The term applies to a viral particle that incorporates a non-viral piece of genetic material, whether DNA or RNA (Aposhian, 1975). This can be used to deliver a gene as a reporter of infection or to stably transduce cells. Pseudoviruses are generated by transfection of plasmids to produce the viral structural proteins and the non-viral genetic material with proper sequences for particle incorporation, transcription, translation, and/or genome integration. For many pseudoviral systems, the genes for viral structural proteins and the surface glycoproteins, including the fusion protein, are on separate plasmids, enabling “pseudotyping” of various fusion proteins onto a particle composed of the structural proteins of another virus (Steffen and Simmons, 2016). This allows straightforward comparisons of the effects of various fusion proteins on a common pseudoviral particle. While a somewhat more artificial system than viruses generated by reverse genetics, pseudoviruses offer more adaptation to specific experimental needs and applications extending beyond virology.

1.9 Viral Restriction Factors:

To counter viral infection, hosts have evolved multiple layers of immunity (Duggal and Emerman, 2012). While adaptive and cellular immunity are important for

controlling viral infections on the organismal level, this thesis will focus on cell-autonomous intrinsic immunity mediated by restriction factors. Restriction factors (RFs) are host proteins with direct antiviral activity defined by their ability to specifically inhibit at least one aspect of the viral replication cycle (Colomer-Lluch et al., 2018). Aside from their inhibitory properties, RFs are diverse in structure, localization and mechanism of action. Loosely, RFs may act against only one virus or many, bear signals of continual positive selection, and often are antagonized by viral factors, but only one or a subset of these properties may apply to a single RF (Blanco-Melo et al., 2012). Some restriction factors are constitutively expressed, like Serinc5 (Zutz et al., 2020), but classically, RFs are upregulated by Interferon (IFN) signaling, as for IFITMs (P. Li et al., 2017), APOBEC3G (Koning et al., 2009), and SAMHD1 (Zhaolong Li et al., 2020).

Present in nearly every cell type, type I IFNs are expressed upon detection of a virus-like, non-self molecular pattern, like dsRNA or dsDNA in the endosome or cytoplasm, by pattern recognition receptors including RIG-I and Toll-like receptors 3, 4, 7, 8, and 9 (Murira and Lamarre, 2016). Upon expression, type I IFNs initiate an anti-viral transcriptional program in the infected cell and its neighbors via autocrine and paracrine signaling (Fensterl and Sen, 2009). An optimal IFN response is essential for effective control of viral infection as both inadequate and excessive IFN levels are associated with pathology (Huang et al., 2019). As part of the anti-viral state induced by IFNs, IFN-stimulated genes (ISGs) are expressed, including ones for some restriction factors.

Serinc3 and Serinc5 are the restriction factors primarily examined in this dissertation but a brief overview of viral restriction factors is provided for contextualization and comparison.

APOBEC3G and 3F: APOBEC3G and 3F are cytidine deaminases from the larger AID/APOBEC family of enzymes (Colomer-Lluch et al., 2018). They restrict Hepatitis B virus (HBV) (Turelli et al., 2004; Vartanian et al., 2010), retrotransposons (Koito and Ikeda, 2013), and retroviruses, including HIV (Doehle et al., 2005) by inducing hypermutation of the viral genome. By catalyzing deamination of cytidine to uracil, APOBEC3G and 3F frequently create premature stop codons, leading to defective viral particles (Fan et al., 2010; Kobayashi et al., 2004; Mahieux et al., 2005; Mangeat et al., 2003). They can act within the nucleus and can incorporate into budding particles to reduce their ability to productively infect other cells. In the case of HIV, APOBEC3G incorporates into budding particles and induces hypermutation during reverse transcription (Bieniasz, 2004). However, APOBEC3G is antagonized by the HIV accessory protein, Vif (Mariani et al., 2003).

SAMHD1: Like APOBECs, SAMHD1 also acts on the viral genome but instead of inducing mutations, it depletes dNTPs required for reverse transcription of retroviruses. It is inducible by type I IFNs and antagonized by the HIV accessory protein Vpx (Descours et al., 2012; Hrecka et al., 2011; Laguette et al., 2011).

TRIMs: The TRIM family are E3 ubiquitin ligases that can inhibit multiple viral proteins and steps of the viral replication cycle (Nisole et al., 2005; Ozato et al., 2008) of Influenza A (Di Pietro et al., 2013), HIV (Tissot and Mechti, 1995), Hepatitis B (Gao et

al., 2009) and Hepatitis C (C. Yang et al., 2016). Perhaps best studied is the interaction between TRIM5α and HIV's capsid protein; TRIM5α lattices coat the post-entry viral capsid, destabilizing it and preventing effective reverse transcription(Ganser-Pornillos et al., 2011; Ganser-Pornillos and Pornillos, 2019; Li et al., 2016; Sakuma et al., 2007; Skorupka et al., 2019; Stremlau et al., 2006; Yu et al., 2020). The more recently identified E3 ubiquitin ligase RFs, MARCH2 and 8, also restrict HIV infection by lysosomal degradation of viral products but they target the fusion protein, Env, instead of Gag (Tada et al., 2015; Zhang et al., 2018).

Tetherin: Tetherin is a type I IFN inducible protein and as suggested by its name, tethers viral particles to the producing cell, preventing their release and infection of subsequent cells (Colomer-Lluch et al., 2018). It is antagonized by HIV-1 Vpu and other retroviral proteins (Blanco-Melo et al., 2016; Hotter et al., 2013; Neil et al., 2008; Van Damme et al., 2008; Waheed et al., 2008).

IFITMs: Interferon-inducible transmembrane proteins (IFITMs) restrict cell entry of enveloped viruses with all three classes of fusion proteins including HIV (Lu et al., 2011), Influenza A (Bailey et al., 2012; Brass et al., 2009; Huang et al., 2011), West Nile Virus (Gorman et al., 2016), Dengue Virus (Jiang et al., 2010), Vesicular Stomatitis Virus (Weidner et al., 2010), and SARS-CoV-2 (Shi et al., 2020) among others. As indicated in their name, their expression is stimulated by IFN treatment, including type I and type II IFNs (Perreira et al., 2013; Smith et al., 2014). The three isoforms, IFITM1, 2, and 3, localize to the plasma membrane and endolysosomes although this localization is easily disrupted by overexpression (Bailey et al., 2014). Regardless, colocalization of the

IFITM protein to the compartment of viral entry appears to be essential for IFITM-mediated restriction of cell entry (Suddala et al., 2019). All three IFITMs have been reported to restrict HIV although specificity may depend on the cell type studied. The most commonly suggested mechanism for IFITM restriction of viral entry is increasing host cell membrane order by modulating membrane curvature via an amphipathic helix, thus destabilizing the hemifusion state and preventing progression to full fusion (Chesarino et al., 2017; Desai et al., 2014; Diamond and Farzan, 2013; Li et al., 2013). Additionally, IFITMs can incorporate into viral particle membranes during budding and decrease infectivity of those particles (Compton et al., 2014).

Serincs: The Serinc family of transmembrane proteins was recently identified as retroviral restriction factors from a screen of HIV Nef interacting factors (Rosa et al., 2015; Usami et al., 2015). The family is composed of five paralogues but only Serinc5, and less frequently Serinc3, were found to inhibit HIV infection. In the setting of a cell infected with a strain of HIV that lacks Nef, Serincs localize to the plasma membrane and Serinc3 and 5 can incorporate into budding HIV particles. Serinc5 incorporation into Nef-deficient HIV particles decreases their ability to infect subsequent cells, implicating inhibition at the cell entry of the viral replication cycle (Rosa et al., 2015; Usami et al., 2015). While Serinc4 is unable to incorporate into budding particles under normal conditions, overexpression and inhibition of proteosomal degradation allows it to incorporate into particles where it inhibits cell entry to a similar degree as Serinc5 (Qiu et al., 2020). Oppositely, Serinc2 can incorporate into viral particles, to a slightly lower extent than Serinc5, but it does not restrict their ability to infect (Rosa et al., 2015;

Schulte et al., 2018). In cells infected with Nef-positive HIV, Nef antagonizes Serincs by targeting them to the lysosome for degradation (Rosa et al., 2015; Shi et al., 2018). Additionally, if Serincs escape degradation and successfully incorporate into budding HIV particles, Nef directly binds to an intraviral loop of Serinc5 and inactivates it (Dai et al., 2018; Trautz et al., 2016). Later reports showed Serinc5 also restricts Hepatitis B Virus (Liu et al., 2020) although the overwhelming interest in a new restriction factor for HIV means the effects of Serincs are best characterized against HIV.

Prior to their identification as restriction factors, Serincs were thought to contribute to the synthetic pathway of PS, hence the name Serine-incorporator shortened to Serinc (Inuzuka et al., 2005). Atypical for a viral restriction factor, sequences of Serincs do not show signatures of selection as would be expected for a protein interacting with a quickly evolving virus; perhaps their role in PS synthesis constrains their evolution (Murrell et al., 2016). Serincs are constitutively expressed in a wide variety of tissues including placenta, skeletal muscle, testis, spleen, thymus, and leukocytes (Xu et al., 2003). IFNα does not upregulate expression of Serinc5 but does increase protein localization on the plasma membrane (Passos et al., 2019).

Despite identification as an RF only 5 years ago, significant work has been done to elucidate the mechanism of Serincs' restriction of HIV infection. The accumulated evidence supports two non-exclusive theories: Serincs alter the viral membrane and/or Serincs alter the structure and activity of Env. There is a greater preponderance of evidence supporting the later, although the dearth of evidence supporting the former may

be due to the lack of widely accessible assays for examining lipid behavior. In the following, I review the literature on both hypotheses.

Given Serincs' role in PS biosynthesis, a tempting early hypothesis was that Serinc3 and 5 altered the lipid composition of regions of the plasma membrane where HIV particles bud and thus altered the composition of the viral envelope. However, this was thoroughly disproven by a study showing no changes in lipid composition of the producer cell or viral particles upon Serinc5 expression and incorporation (Trautz et al., 2017). As large transmembrane proteins, Serincs have ample surface area for lipid interactions and cryoEM structures of Drosophila and Human Serinc5 identified a lipid binding groove (Figure 1.6A and B). In the Drosophila structure, there was a density within the lipid binding groove that resembled the unusual lipid, cardiolipin, although this is not thought to be the physiological interaction. The stability of Drosophila and Human Serinc5 was enhanced by addition of cholesterol and phosphatidylserine, indicating these may be the more biologically relevant species. Interestingly, the Drosophila orthologue formed a star-shaped hexamer with the lipid binding groove in the protomer interface, implying a role for lipid-mediated oligomerization of Serinc5. However, the human orthologue was not observed to oligomerize so the relationship of lipid-mediated oligomerization to restriction remains uncertain (Pye et al., 2020). Further demonstrating the importance of Serinc-lipid interactions, the human Serinc5 was found to partition into detergent-resistant membranes and this partition was essential for restriction of HIV infection (Schulte et al., 2018). HIV Env is known to partition into ordered lipid domains (Schwarzer et al., 2014) and while detergent-resistant membranes are not always directly

comparable to ordered lipid domains, these data suggest Env and Serincs could colocalize on the plasma membrane and in the viral particle.

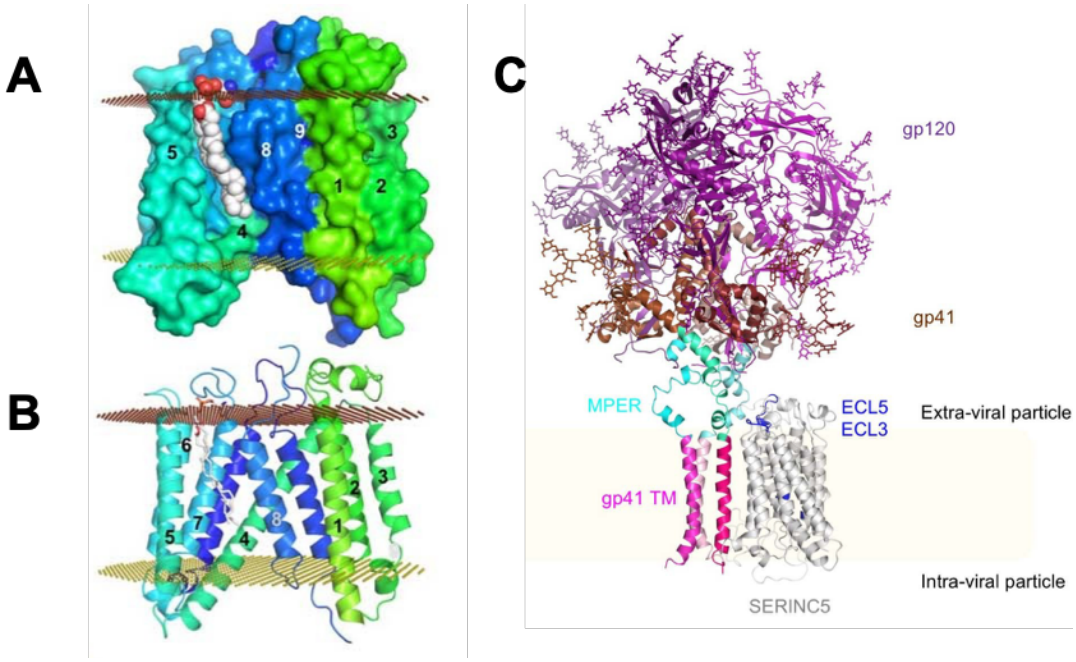

Figure 1.6: Serinc5 structure and potential interactions. Side views of Serinc5 as (**A.**) surface or (**B.**) ribbon representations. A lipid moiety occupies the lipid binding groove. Bilayer boundaries denoted by two planes. **C**. Speculative docking of HIV Env (PDB 6E8W and 5FUU) with Serinc5. HIV Env receptor binding domain, gp120, in purple; fusion domain, gp41, in brown and pink. Membrane proximal external region (MPER) of gp41 highlighted in cyan. Extracellular loops 3 and 5 of Serinc5 highlighted in blue. Adapted from Pye et al, 2020.

Multiple studies have mapped sequences for Serinc resistance to Env, specifically, the flexible V1/V2 and V3 loops within gp120 (Beitari et al., 2017; Pye et al., 2020;

Timilsina et al., 2020; Usami et al., 2015). Puzzlingly, the V1/V2 and V3 loops are near the gp120 apex (Pan et al., 2015), far away from the membrane and Serinc5. Additionally, multiple studies have observed conformational changes in Env, including changes to antibody sensitivity, upon Serinc5 incorporation into the viral particle (Schulte et al., 2018; Sood et al., 2017; Staropoli et al., 2019). These data suggest some form of interaction between Serinc3/5 and Env whether that be direct binding causing a conformational change (modeled in Figure 1.6C) or a more distal interaction mediated by another factor. Two groups have documented a Serinc5-mediated disruption of Env oligomerization within viral or cellular membranes with super resolution microscopy and bi-molecular complementation respectively (Chen et al., 2020; Zhang et al., 2019). While difficult to translate interactions observed by bi-molecular complementation to more transient interactions occurring *in vitro*, Zhang et al. do claim to detect a direct interaction between Serinc5 and Env.

Together, these results suggest Serinc5's mechanism of action may involve disruption of Env's function but do not exclude the possibility of alteration of the organization of the viral membrane. Changes to the viral membrane could be the intermediary that exerts Serinc5's effects on Env or may be an independent function of Serinc5. With the results contained in this dissertation, we hope to clarify these possible Serinc5 mechanisms of action.

Chapter 2. HIV-cell membrane fusion intermediates are restricted by Serincs as revealed by cryo electron and TIRF microscopy

Amanda E. Ward, Volker Kiessling, Owen Pornillos, Judith M. White, Barbie K. Ganser-Pornillos, Lukas K. Tamm (2020).

J. Biol. Chem. 295 (45): 15183-15195

2.1 Abstract

To enter a cell and establish infection, HIV must first fuse its lipid envelope with the host cell plasma membrane. While the process of HIV membrane fusion can be tracked by fluorescence microscopy, the 3D configuration of proteins and lipids at intermediate steps can only be resolved with cryo Electron Tomography (cryoET). However, cryoET of whole cells is technically difficult. To overcome this problem, we have adapted giant plasma membrane vesicles (or blebs) from native cell membranes expressing appropriate receptors as targets for fusion with HIV envelope glycoprotein-

expressing pseudovirus particles with and without Serinc host restriction factors. The fusion behavior of these particles was probed by TIRF microscopy on bleb-derived supported membranes. Timed snapshots of fusion of the same particles with blebs were examined by cryoET. The combination of these methods allowed us to characterize the structures of various intermediates on the fusion pathway and showed that when Serincs3 and 5 (but not Serinc2) were present, later fusion products were more prevalent, suggesting that Serinc3/5 act at multiple steps to prevent progression to full fusion. In addition, the antifungal amphotericin B, reversed Serinc restriction, presumably by intercalation into the fusing membranes. Our results provide a first high-resolution view of Serinc restriction of HIV-cell membrane fusion and thus extend current structural and functional information on Serinc as a lipid binding protein.

2.2 Introduction

To establish an infection, Human Immunodeficiency Virus (HIV) must enter the cell by fusing its lipid membrane with a host cell membrane (Melikyan, 2011). HIV membrane fusion is mediated by conformational rearrangements in the viral envelope protein, Env, that are induced by binding to receptor, CD4, and co-receptor, CCR5 or CXCR4 (Blumenthal et al., 2012). The process of HIV membrane fusion is thought to proceed through defined intermediate steps: receptor binding, hemifusion, and fusion pore opening and widening, similar to other enveloped viruses such as influenza (Chen, 2019). The earliest step, receptor binding, has been visualized with nanometer resolution by electron tomography of plastic sectioned cells (Sougrat et al., 2007) but subsequent steps have not been directly observed. Fusion of influenza virus with its much simpler

pH-sensitive fusion trigger has previously been studied by observing the merging of viral membrane envelopes with artificial liposomes using cryo Electron Tomography (cryoET) (Chlanda et al., 2016; Gui et al., 2016; Lee, 2010) but HIV's requirement for two cell surface membrane proteins to trigger fusion has made in vitro reconstitution difficult. In order to examine fusion of HIV at the plasma membrane with cryoET we have adapted giant plasma membrane vesicles (GPMVs or blebs) as model target membranes. Blebs are detached plasma membrane-derived vesicles that are much smaller than a cell and can easily be frozen in thin, vitreous ice required for cryoET. Blebs produced from cells expressing CD4 and CCR5 incorporate these full-length proteins along with their native lipid environment and post-translational modifications (Sezgin et al., 2012; Yang et al., 2017). Although we reported earlier that the final fusion product of Murine Leukemia Virus pseudoviruses bearing HIV Env and plasma membrane blebs can be visualized in projection by cryo Electron Microscopy (Yang et al., 2017), we show here that this system is ideally suited to image timed snapshots of 3D volumes, thus revealing multiple stages of the HIV fusion process by cryoET . In this study, we used a combination of cryoET and total internal reflection fluorescence (TIRF) microscopy with membrane blebs from HIV target cells to reveal various steps of fusion between two biological membranes, namely the HIV envelope and plasma membranes of susceptible cells. Tomograms of pseudovirus particles vitrified after different incubation times with $CD4^{+}/CCR5^{+}$ cell membrane blebs reveal a timeline of HIV fusion.

Serinc3 and Serinc5 are recently described viral restriction factors (Rosa et al., 2015; Usami et al., 2015) that are thought to block infection at cell entry, although the exact mechanism remains the subject of debate. Serincs comprise a family of five plasma

membrane proteins (Inuzuka et al., 2005) that, in the absence of the HIV accessory protein, Nef, can incorporate into budding viral particles and decrease the infectivity of those progeny viral particles (Zhang et al., 2017). While isoforms Serinc3 and Serinc5 can block infection of subsequent cells, other isoforms, including Serinc2, do not. Previous work has suggested that Serincs may act at the very earliest steps of membrane fusion by changing the conformation or clustering of unliganded Env (Chen et al., 2020), as evidenced by increased binding of broadly neutralizing antibodies to Env on Serinc5 containing viral particles (Beitari et al., 2017; Schulte et al., 2018; Sood et al., 2017). Serincs are integral membrane proteins that have been reported to be involved in lipid synthesis (Inuzuka et al., 2005). The structure of Serinc5 was solved recently, features a lipid binding groove involving four of its ten transmembrane helices, and is stabilized by cholesterol, cardiolipin, and phospholipids (Pye et al., 2020). Despite these observations, when incorporated into viruses, Serincs do not appear to detectably alter the composition of the viral membrane (Trautz et al., 2017). Some investigators have also suggested that Serinc incorporation may change the distribution of Env in the viral membrane (Firrito et al., 2018). Yet others have interpreted Serinc5's strong inhibition of infection to be indicative of an effect on fusion pore enlargement that would prevent delivery of the viral nucleocapsid into the cytosol (Rosa et al., 2015; Usami et al., 2015). This view was supported by the observation of impaired fusion pore formation using live cell imaging of HIV pseudovirus cell entry (Sood et al., 2017).

To elucidate at which step(s) Serincs might interfere with membrane fusion, we used a combination of TIRF microscopy and cryoET to monitor the evolution of fusion of viral particles with and without restricting and non-restricting Serinc isoforms in their

envelopes. With TIRF microscopy, we examine the fusion behavior of individual Serinc-containing and Serinc-lacking HIV pseudovirus particles to bleb-derived receptor- and co-receptor-containing supported planar plasma membranes (SPPMs) and find that Serinc3 and Serinc5, but not Serinc2, create bottlenecks to fusion at the hemifusion and at the pore expansion stage. Serinc3 and Serinc5, but not Serinc2, alter the progression of fusion and also reveal a subpopulation of new "cinched" structures not seen in the absence of Serincs. The combination of cryoET and TIRF microscopy on blebbed plasma membranes from receptor-expressing cells proved to be a powerful approach to reveal striking 3D images of membrane structures during restricted and unrestricted HIV fusion and thus provide the first structural as well as new functional insights on how Serincs restrict HIV entry into cells.

2.3 Results

Plasma Membrane Blebs as Models for Studying HIV Membrane Fusion

An ideal model target membrane for HIV fusion requires receptor, CD4, and co-receptor, CCR5 or CXCR4, in a lipid bilayer of size and geometry amenable to fluorescence and cryo-electron microscopies. Reconstitution of recombinant CD4 and CCR5 into proteoliposomes could produce such a model membrane but would be labor intensive, technically difficult, and still generate lipid bilayers lacking many components of the target biological membrane. Production of GPMVs or blebs from HeLa cells is relatively simple (Sezgin et al., 2012) and such vesicles can be derived from cells that express CD4 and CCR5 (Yang et al., 2017). Blebs also have the advantage of featuring the native lipid composition of the plasma membrane and full-length proteins with

mammalian post-translational modifications (Figure 2.1a). We have previously established that blebs and SPPMs are good models for studying fusion of single Murine Leukemia Virus particles pseudotyped with HIV Env in the absence of Serincs (Yang et al., 2017). To validate the fusion behaviors of HIV viral particles with and without Serincs for structural characterization by cryoET we therefore turn first to their characterization by TIRF microscopy.

We prepared blebs from HeLa cells expressing CD4 and CCR5 as described in the Methods section. Detached blebs were transformed from their spherical geometry into a SPPM by first depositing a lipid monolayer on a quartz slide via the Langmuir-Blodgett method, followed by spreading of the blebs on that monolayer (Yang et al., 2017) (see Methods). The resultant SPPM was then used as a target membrane with which to study single-particle fusion via TIRF microscopy (Figure 2.1b). We modified our prior single particle fusion assay by employing HIV pseudovirus particles bearing HIV Env and engineered to incorporate a freely diffusible mCherry content marker (Sood et al., 2016). When such particles were introduced into an SPPM from HeLa $CD4^+/CCR5^+$ cells, we observed videos such as the region of interest (ROI) shown in Figure 2.1c. A sudden appearance of punctate fluorescence indicates binding of the particle to the SPPM. The peak and mean intensities of the ROI shown in Figure 2.1c are plotted over time in Figure 2.1d. The fluorescence of the particle shown was stable over about 12 seconds and then gradually declined to background fluorescence due to fusion and release of soluble mCherry into the cleft between the supported membrane and the quartz slide. Many such intensity traces were aligned to the onset of fusion, characterized by a peak due to initial content movement within the evanescent excitation field, and averaged (Figure 2.1e).

This average intensity was fit to a release model as described in supplemental Figure 2.S1 where mCherry is released into the aqueous cleft and allowed to diffuse laterally. Given the similarity of intensity traces of slow decay events to other previously published descriptions of single-particle viral fusion (Floyd et al., 2008) and vesicle fusion (Alex J. B. Kreutzberger et al., 2017) to supported membranes, we interpreted events such as those shown in Figures 2.1c-e to represent stable binding followed by membrane fusion and release of viral contents. Of the particles that bind to SPPMs, a higher fraction undergo fusion to CD4- and CCR5-containing membranes than to receptor-lacking membranes prepared in the same manner, which indicates this process is HIV receptor dependent (Figure 2.1f).

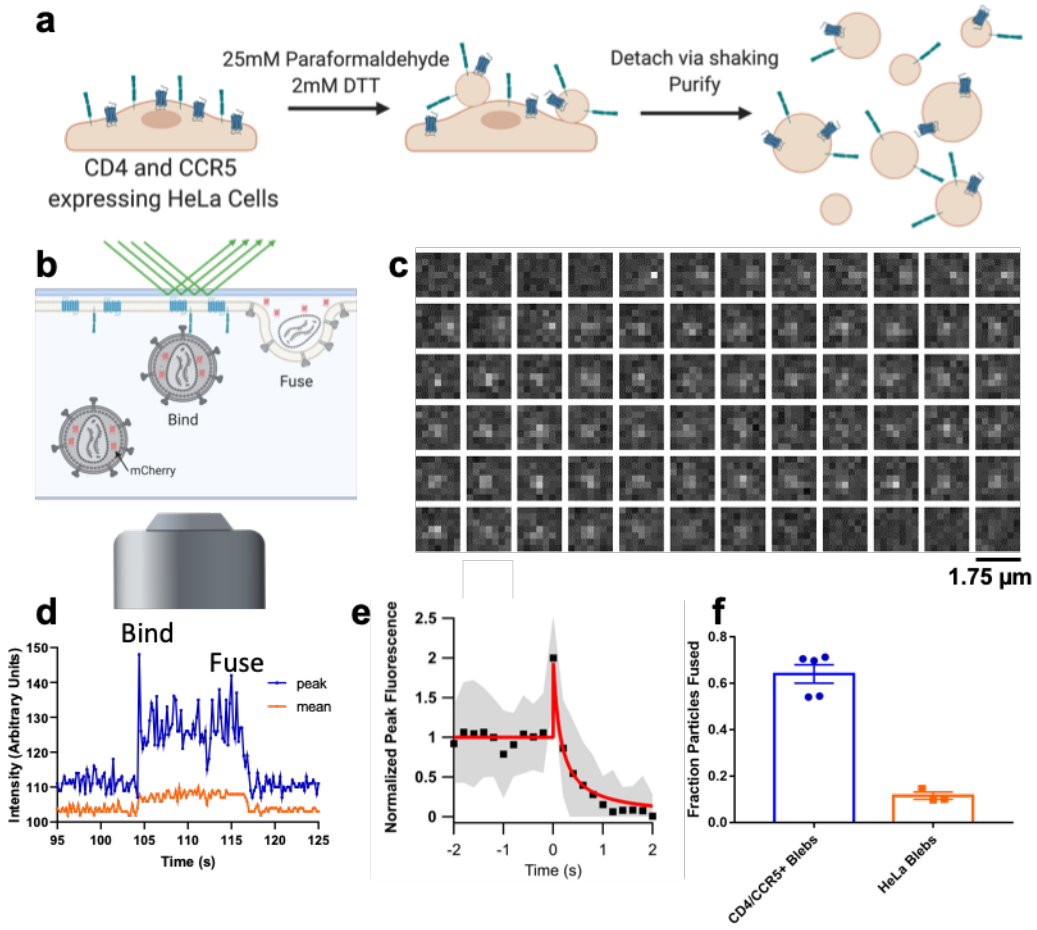

Figure 2.1: Membrane Blebs as a Model for Studying Viral Fusion. (a) Cartoon depicting protocol for making CD4 and CCR5 containing blebs from HeLa cells. Detached blebs are mixed with HIV pseudoviruses and frozen for cryoET or used to form a SPPM as shown in panel b. (b) Cartoon showing discrete steps of HIV fusion to a bleb-derived SPPM in a TIRF-based single-particle fusion assay. All pseudoviruses are grown with a genetically encoded soluble content marker, mCherry, that upon fusion diffuses out of the virus and into the cleft between the SPPM and the substrate (described in (Sood et al., 2016)) (c) Example micrographs of an HIV pseudovirus particle with a diffusible mCherry content marker fusing with a CD4 and CCR5 containing SPPM. Each box represents the same region separated in time by 0.2 seconds. (d) Fluorescence intensity of the same particle is plotted over time where "peak" is the intensity of the brightest pixel in the 7x7 region and "mean" is the average intensity of the same area. (e) 30 intensity traces of fusing particles were aligned to the increase in intensity at the onset of fusion, averaged (black squares show the mean, grey shaded area shows standard deviation), and fit to a release model as shown in Supplemental Figure 2.S1 (red line). (f) The fraction of stably bound particles that undergo fusion to SPPMs made with blebs from CD4 and CCR5 overexpressing HeLa cells or HeLa cells that do not express either. Each point represents a separately prepared bilayer. Error bars show SEM.

Observation of HIV Membrane Fusion by CryoET

Previous work has observed HIV particles bound to a T cell with multiple densities in between (Sougrat et al., 2007) but no work to date has directly observed

subsequent steps of HIV membrane fusion and cell entry by cryoET. To obtain detailed snapshots of HIV pseudovirus particles in the act of membrane fusion, we employed GPMVs/blebs as target membranes for studying HIV fusion by cryoET. To increase the likelihood of observing short-lived fusion intermediates between CD4- and CCR5-containing blebs and HIV pseudoviruses, we synchronized fusion by prebinding pseudoviruses to blebs at 4°C, raising the temperature to 37°C for defined, brief times, and then immediately freezing the samples for cryoET. As fusion of multiple pseudovirus particles and blebs proceeds, one would expect the resulting membraned structure to be larger than the starting components, which is confirmed by the data shown in Figure 2.2a (red bars). The diameter of membraned particles increased as the mixture of pseudovirus and bleb was warmed for a longer time before freezing. This increase was blocked by addition of the fusion inhibiting peptide T20, which binds to the N-terminal heptad repeat region of HIV gp41, the transmembrane and fusion promoting subunit of Env, and prevents the six-helix bundle formation that is required for fusion (Liu et al., 2005). Consistent with its described mechanism of action, T20 treated samples only showed receptor mediated binding events (Figure 2.2a, blue bars and Figure 2.2b). Samples without T20 that were warmed for 10 seconds before freezing showed multiple structures—receptor mediated binding, hemifusion and early fusion products—while samples that were warmed for 30 seconds showed only some residual receptor mediated binding events (Figure 2.2a). Receptor binding at the later time point may represent defective pseudovirus particles that are incapable of fusion and thus remain attached to the bleb when other pseudoviruses have fused and are indistinguishable from blebs. The majority of tomograms of samples warmed to 37°C for 30 seconds showed large

membraned particles that we deem late fusion products, which is consistent with measurement of those particle's diameters.

Examination of tomograms of T20 treated samples (Figure 2.2b and Supplementary Video 2.1) showed viral and target membranes in very close apposition but with a cleft between the densities characterizing the surfaces of both membranes. Additionally, densities extending from the viral membrane surface with a shape reminiscent of HIV Env (orange arrow) meet densities extending from the bleb membrane that intersect the Env-like density. There are no such densities in the area of closest approach of the two membranes. A similar scene was observed in tomograms of virus and bleb without T20 (Figure 2.2c and Supplementary Video 2.2) leading us to classify such interactions of virus and bleb as receptor mediated binding, an early step of HIV fusion. In samples frozen 10 seconds after warming, we also observed events where there was no cleft between the membrane surfaces, but the line and curvature of the inner leaflet surfaces of the viral and bleb membranes were still clearly demarcated and not interacting (Figure 2.2d and Supplementary Video 2.3). Based on the similarity of these events to those observed in previous studies of influenza A fusion with liposomes by cryoET (Chlanda et al., 2016) we classify these events as hemifusion.

We observed a third class of events where a single lipid bilayer surrounds contents of two different textures with a narrowing of the lipid bilayer around the transition between textures (Figure 2.2e). The texture of the smaller lobe is reminiscent of the darker texture seen in viruses (Figures 2.2b-d), and densities extend from the membrane around the smaller lobe that could be HIV Env. Similar events were previously observed for influenza A membrane fusion with liposomes and classified as an

early stage of fusion pore dilation (Lee, 2010) leading us to classify these events as an early fusion product, likely a step when the fusion pore is dilating and the viral matrix layer is dissociating. Similar events were also observed after Herpes Simplex Virus-1 fusion to the plasma membrane of whole cells (Maurer et al., 2008). In the samples warmed at 37°C for 30 seconds before freezing, we observe some virus particles binding to blebs (Figure 2.2a) but we mostly observe images such as seen in Figure 2.2f where there is a single, large membraned particle. Closer examination of the densities protruding from the membrane show multiple mushroom-like densities that may be HIV Env (orange arrows) and others that resemble the Ig-fold of CD4 (white arrows). Given the increase in particle size at 30 seconds and the presence of densities in the unified membrane that could be contributed by both virus and bleb, we interpret similar structures to be the result of pseudovirus-bleb full fusion, likely the products of multiple rounds of virus and bleb fusion.

Initial studies were performed with a HEK 293T-based packaging cell line that produces viral particles with 10-fold higher incorporation of HIV Env (Stano et al., 2017) (Figure 2.2b) but we did not observe any increased fusion, as reported by mCherry release, with high Env pseudoviruses vs. pseudoviruses produced from standard HEK 293T cells, so all subsequent studies were performed with SF162 HIV Env pseudoviruses produced from transiently transfected HEK 293T cells. In summary, using CD4- and CCR5-containing blebs as a target membrane to study HIV membrane fusion by cryoET, we have observed intermediates of HIV membrane fusion.

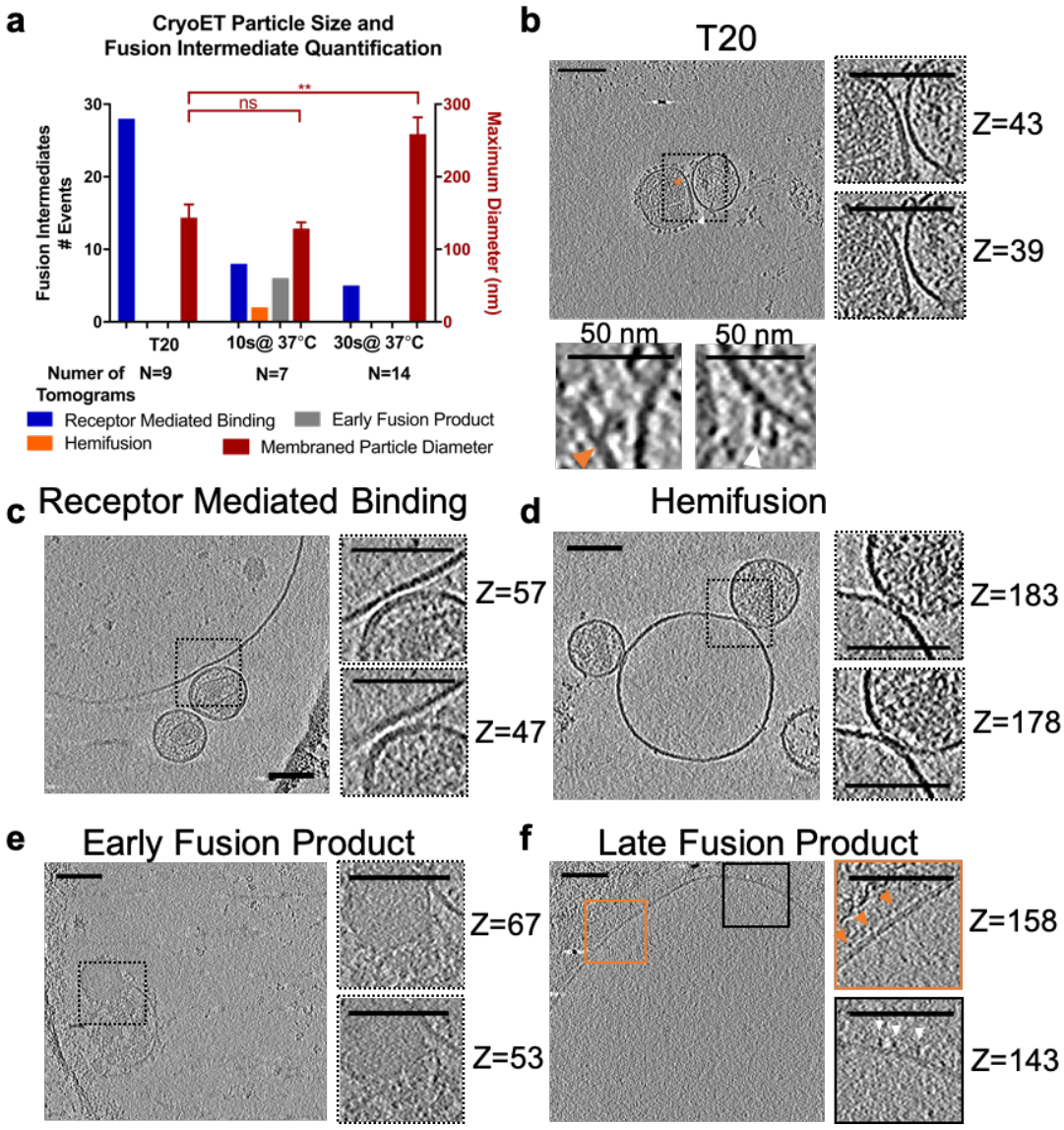

Figure 2.2: Observation of HIV Membrane Fusion Intermediate Structures by cryoET. (a) Membraned particle size and enumeration of fusion intermediates for each sample treatment. Spherical CD4 and CCR5 containing blebs were mixed with HIV pseudoviruses on ice and warmed to 37°C for the indicated time before freezing on a grid for cryoET. The number of intermediate structures observed for each condition (left y-axis) and the maximum diameter in the z-direction of membraned particles in a tomogram (red bars and right y-axis) were plotted. Data are from one set of matched

samples prepared and frozen at the same time and are taken from 109 similar tomograms. The number of tomograms for each treatment in this matched set is listed below the x-axis. Error bars represent SEM. Welch's t-test shown above data ** $p<0.01$, ns not significant. Examples of each type of event are shown in panels b-f. (b-f) Z-slices through tomograms of HIV pseudovirus and blebs. Additional slices at higher zoom are shown on the right and labeled with their slice number in the Z-direction. Tomograms are shown with cryoCARE denoising to enhance contrast for display. Scale bars are 100 nm unless otherwise indicated. Videos showing the complete tomograms and additional examples can be found in the supplemental data. (b) Tomogram of V4 High Env HIV pseudovirus and bleb mixture treated with 135 ng/mL T20. To highlight densities suggested to represent Env (orange arrow) or could potentially be CD4 (white arrow), higher magnification views are shown below with a 50nm scale bar. (c) Example tomogram showing characteristics used to classify receptor mediated binding events. The mixture of HIV pseudovirus and blebs with 40μM IP6 was warmed to 37°C for 10 seconds before freezing. Defocus was -10 μm. (d) Example tomogram showing characteristics used to classify hemifusion events. The mixture of HIV pseudovirus and blebs with 40μM IP6 was warmed to 37°C for 10 seconds before freezing. Defocus was -10 μm. (e) Example tomogram showing characteristics used to classify early fusion product events. The mixture of HIV pseudovirus and bleb was warmed to 37°C for 10 seconds before freezing. These types of events were relatively rare in the dataset. Defocus was -6 μm. (f) Example tomogram of HIV pseudoviruses and blebs warmed to 37°C for 30 seconds, which likely represents the product of multiple rounds of membrane fusion. Densities

extend from the membrane that resemble HIV Env (orange arrows) and CD4 (white arrows). Defocus was -6 μm.

Effects of Serincs on HIV membrane fusion

We next applied both TIRF microscopy and cryoET to study fusion of Serinc-containing HIV Env pseudoviruses. There was a decrease in Serinc2 and Serinc3-containing HIV pseudovirus particles binding to CD4- and CCR5-containing SPPMs as compared to pseudoviruses that did not incorporate Serincs (Serinc-lacking) but no significant difference for Serinc5-containing pseudoviruses (Figure 2.3a). However, of the particles that did bind, Serinc3- and Serinc5-containing pseudoviruses displayed impaired release of viral contents while Serinc2 pseudoviruses had a similar fusion probability to Serinc-lacking viruses (Figure 2.3b), as seen by Sood et al. for Serinc5 and Serinc2, respectively (Sood et al., 2017). The magnitude of Serinc3 and Serinc5 restriction was titratable with transfection of increasing amounts of Serinc plasmid (Supplemental Figure 2.S3a). For those viruses from Serinc-containing samples that did fuse, the kinetics of progression from binding to fusion pore opening were not appreciably different compared to those for Serinc-lacking pseudoviruses (Figure 2.3c). Kinetics of viral content release are similar to previously published measurement of influenza A fusion to supported bilayers (Floyd et al., 2008). The Serinc3 and Serinc5 particles that do fuse are a smaller subpopulation that could have lower Serinc incorporation. Infection of TZM-bl cells by the same preparations of HIV pseudovirus particles (Figure 2.3d) recapitulated the SPPM fusion results (Figure 2.3b) where Serinc3 and Serinc5 restricted HIV infection but Serinc2 did not, which is consistent with

previously published infection results (Beitari et al., 2017; Dai et al., 2018; Passos et al., 2019; Rosa et al., 2015; Schulte et al., 2018; Sharma et al., 2018; Shi et al., 2018; Sood et al., 2017; Trautz et al., 2017; Usami et al., 2015). Similarly, the size of membraned particles visualized by cryoET at 30 seconds after mixing of pseudovirus and blebs was notably smaller in tomograms of Serinc3 and Serinc5 containing pseudoviruses and blebs (Figure 2.3e). Even at the later, 30 second time point when most Serinc-lacking viruses had progressed to late fusion products (Figure 2.2a), we visualized many hemifusion and early fusion product events in tomograms with Serinc3 and Serinc5 pseudoviruses (Figure 2.3f).

Most tomograms of Serinc2 pseudoviruses looked very similar to the late fusion products seen with Serinc-lacking pseudoviruses at the same 30 second time point (Figure 2.3g); in 15 tomograms of Serinc2 samples, we observed only one early fusion product (Figure 2.3h). Strikingly, some of the early fusion products observed in Serinc3 (Figure 2.3i and 2.3j) and Serinc5 (Figure 2.3k and 2.3l) tomograms show a cinching of membraned particles and in the tomograms where viral capsids can be visualized, the capsid does not pass the narrowed section (Supplemental Figure 2.S4). Together, the higher resolution snapshots of Serinc-disrupted fusion obtained with cryoET and the information on the dynamic process of HIV pseudovirus fusion to SPPMs from TIRF microscopy, show that Serinc3 and Serinc5 incorporation increases the likelihood of observing hemifusion and abnormal early fusion products and inhibits the opening of fusion pores large enough for passage of soluble mCherry.

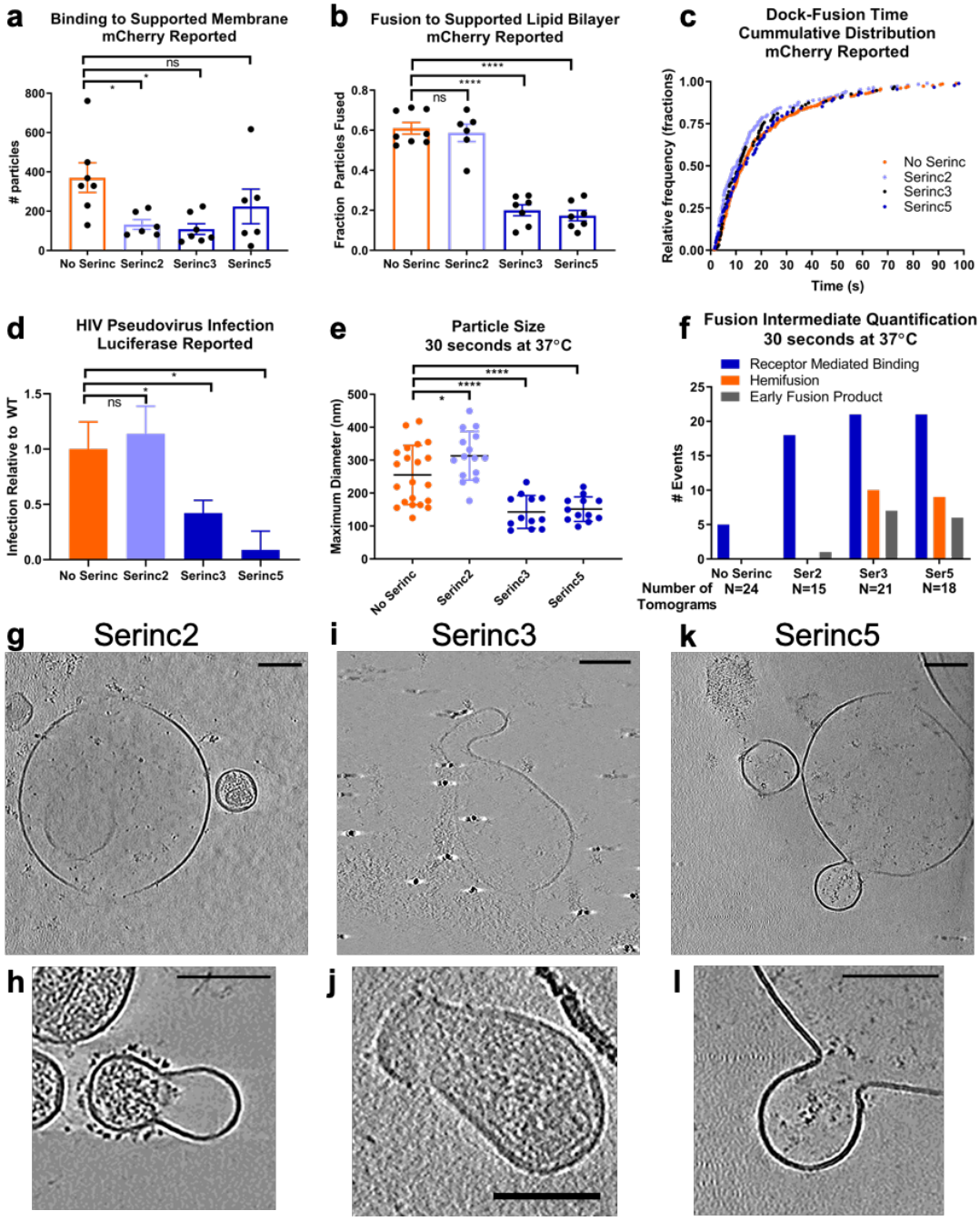

Figure 2.3: Serinc incorporation enhances the probability of observing hemifusion and abnormal early fusion products. (a) Number of HIV pseudovirus particles that bound to a CD4- and CCR5-containing SPPM. An equal amount of pseudovirus as measured by HIV p24 was introduced to bilayers and observed by TIRF microscopy for

13.3 minutes. HIV pseudovirus particles used in this experiment were labeled only with an mCherry content marker. Each point represents a separately prepared SPPM. Three separate preparations of each type of pseudovirus were examined. (b) Fraction of bound HIV pseudovirus particles that underwent fusion, as reported by loss of mCherry content marker. Each point represents a separately prepared SPPM. Data were collected from 5 experiments from 3 separate preparations of each type of pseudovirus. (c) Single-particle kinetics of pseudovirus fusion. The time between docking and the beginning of fusion, as reported by loss of mCherry signal, was measured for individual viral fusion events; each point represents an event. Events from five experiments and three separate HIV pseudovirus preparations are shown for each type. In total, 336 Serinc-lacking events, 187 Serinc2 events, 95 Serinc3 events, and 88 Serinc5 events are shown. (d) Infection of TZM-bl reporter cells by an equal amount of each type of HIV pseudovirus as measured by HIV p24. Data shown are from three separate preparations of pseudovirus and three infection experiments. For each experiment, the luciferase signal was normalized to the Serinc-lacking signal from a parallel preparation of virus examined in the same experiment. Error bars are SEM. (e) Maximum diameter in the z-direction of membraned particles in a tomogram after mixing with CD4- and CCR5-containing blebs and warming to 37°C for 30 seconds before freezing for cryoET. Each point represents a tomogram. Error bars show SEM. (f) Enumeration of fusion intermediate structures observed in tomograms of Serinc-lacking or Serinc-containing HIV pseudoviruses. The number of tomograms for each treatment is listed below the x-axis. (g-l) Z-slices through tomograms of Serinc-containing HIV pseudovirus and blebs that were warmed to 37°C for 30 seconds before freezing for cryoET. Tomograms are shown with cryoCARE

denoising to enhance contrast for display except where noted. Scale bars are 100 nm. (g) Representative image of tomograms of Serinc2 containing HIV pseudoviruses (h) the only early fusion product event observed in all tomograms of Serinc2 pseudoviruses and blebs. Both tomograms were prepared with 40μM IP6 and acquired at -10 μm defocus. (i-j) Representative images of early fusion products of Serinc3 containing pseudoviruses from different tomograms. i was acquired with -4 μm defocus and j was prepared with 40μM IP6, taken at -10 μm defocus, and is shown with non-anisotropic diffusion filtering. (k) Representative image of an early fusion product of Serinc5-containing pseudovirus and blebs. (l) an enlargement of the top image. The tomogram was taken at -5 μm defocus. Welch's two-tailed t-test shown above data $p<0.05$, $**p<0.01$, $****p<0.0001$, ns=not significant.

Perturbations of Membranes Rescues HIV Fusion from Serinc Restriction

To better understand the step at which Serinc3 and Serinc5 restrict HIV fusion, we incorporated a fluorescent lipid, Atto488-DMPE, into the membrane of HIV pseudoviruses (Figure 2.4a). Since membrane dyes have been reported to alter the efficiency and kinetics of viral fusion (Rawle et al., 2019), we selected a phospholipid conjugated to a non-membrane interacting fluorophore (Hughes et al., 2014) that should have less of an effect on fusion and indeed, we observed the same fusion efficiency for Serinc-lacking pseudoviruses whether they were or were not labeled with Atto488-DMPE (Supplemental Figure 2.S5). Fluorophore-conjugated phospholipids do not readily flip across a lipid bilayer (Blumenthal et al., 2002) so the dye is largely confined to the outer leaflet of the viral membrane (Supplemental Figure 2.S6). Upon lipid mixing of the viral

and target membranes, as occurs during hemifusion, the punctate fluorescence of the membrane dye diffuses into the bilayer (Supplemental Figure 2.S7). When dual mCherry and lipid labeled HIV pseudoviruses were allowed to fuse with a SPPM, no difference was seen in fusion probability between Serinc-lacking and Serinc-containing viruses as reported by the membrane dye (Figure 2.4b, green bars). However, incorporation of Atto488-DMPE increased the full fusion (content release) probability of Serinc3- and Serinc5-containing viruses, as reported by the mCherry content marker (Figure 2.4b, red bars compared to Figure 2.3b). This is in contrast to the behavior of mCherry singly-labeled particles where a clear diminution of content release was seen for Serinc3 and Serinc5-containing particles vs. Serinc-lacking particles (Figure 2.3b). Labeling the virus with Atto488-DMPE increases the speed of fusion pore opening of all types of pseudoviruses (Figure 2.4c) but there are no significant differences in the speed of lipid mixing, i.e. hemifusion, of Serinc-lacking and Serinc-containing pseudoviruses as reported by the membrane dye (Figure 2.4d). Changes in fusion probability and speed with Atto488-DMPE treated pseudovirus could be the result of changes in lipid order of the viral membrane.

The antifungal agent, Amphotericin B, is known to partition into membrane interfaces and to induce local changes in lipid order (Dufourc et al., 1984), as may occur in Atto488-DMPE treated viruses. We found that 1 μM of Amphotericin B increased HIV pseudovirus infection of TZM-bl cells for Serinc5 containing pseudovirus with a trend towards increase for Serinc3 containing particles. In contrast, Amphotericin B had little effect on the infectivity of Serinc-lacking or Serinc2 containing particles (Figure 2.4e). In the single-particle SPPM fusion assay, 1 μM Amphotericin B rescued fusion of

Serinc3 and Serinc5 containing pseudoviruses but had no effect on Serinc-lacking or Serinc2 pseudoviruses (Figure 2.4f). Therefore, it appears that perturbation of the viral membrane with lipophilic drugs such as Amphotericin B or incorporation of exogenous lipids such as Atto488-DMPE can rescue Serinc3- and Serinc5-restricted HIV membrane fusion.

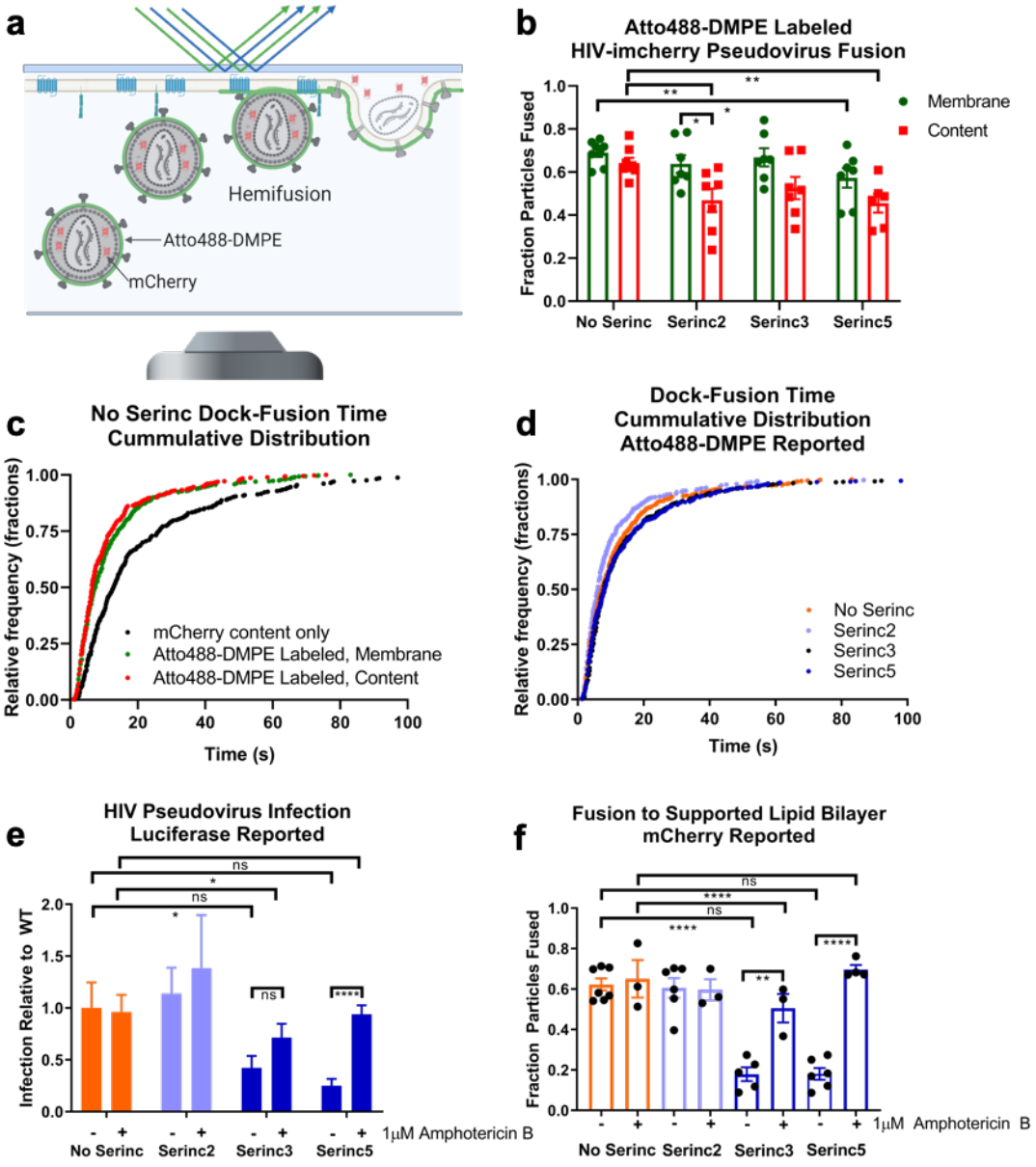

Figure 2.4: Perturbation of the viral membrane rescues HIV fusion and infection from Serinc restriction. (a) Cartoon depicting SPPM fusion experiment with double-labeled HIV pseudovirus. Since the vast majority of the Atto488-DMPE fluorescent membrane dye is in the outer leaflet of the viral membrane (supplemental data), both hemifusion and full fusion are reported as decay of the Atto488 fluorescence. Only full fusion is reported as decay of mCherry fluorescence. (b) Fraction of bound HIV pseudovirus particles that underwent fusion, as reported by loss of mCherry content marker (red) or lipid mixing, as reported by loss of Atto488 fluorescence from membrane dye (green). Data are from four separate experiments with two technical replicates for each. Error bars are SEM. Unpaired two-tailed t-test shown above data. All comparisons not shown are not significant. (c) Comparison of single-particle kinetics of Atto488-DMPE labeled vs. non-membrane labeled pseudovirus fusion. The time between docking and the beginning of fusion was measured for individual viral fusion events. Each point represents an event and events are from four experiments. In total, 462 mCherry content only (unlabeled) events, 536 membrane-reported fusion events from Atto488-DMPE labeled pseudovirus, and 330 content-reported fusion events from Atto488-DMPE labeled pseudovirus are shown. (d) Single-particle kinetics of Atto488-DMPE reported pseudovirus fusion. The time between docking and the beginning of lipid mixing was measured for individual viral fusion events; each point represents an event and events are from four experiments. In total, 536 Serinc-lacking events, 373 Serinc2 events, 459 Serinc3 events, and 485 Serinc5 events are shown. (e) Infection of Amphotericin B-treated TZM-bl cells by Serinc-containing or -lacking HIV pseudoviruses. Cells were pretreated with 1 μM Amphotericin B for 30 minutes before spinfection with HIV

pseudoviruses, also in media with 1 μM Amphotericin B. Data shown represent three separate preparations of pseudovirus and three infection experiments. Untreated data are replotted from Figure 2.3d for comparison. Error bars are SEM. Paired two-way t-test shown above data (f) Fraction of bound HIV pseudovirus particles that underwent fusion, as reported by loss of mCherry content marker. Each point represents a separately prepared SPPM. Untreated data are replotted from Figure 2.3b for comparison. Amphotericin B treated data were collected from 3 experiments from 3 separate preparations of each type of pseudovirus. Unpaired two-tailed t-test shown above data *$p<0.05$, **$p<0.01$, ****$p<0.0001$, ns=not significant.

2.4 Discussion

In this study, we demonstrated that plasma membrane blebs are very useful biological target membranes to study HIV membrane fusion with the powerful combination of cryoET and TIRF microscopy. The two methods assess structural intermediates and correlate them with functional states, respectively. The necessity of two membrane protein receptors to trigger HIV fusion previously made in vitro reconstitution of HIV fusion challenging but blebs from HIV target cells enable use of the full-length receptor (CD4) and co-receptor (CCR5) in multiple modalities. With such blebs, we have observed high-resolution snapshots of HIV membrane fusion intermediate structures and characterized the bottlenecks of HIV fusion caused by the HIV restriction factors, Serinc3 and Serinc5. This would likely not have been possible to achieve with whole cells because flash-frozen samples would have been too thick in most locations of

a cell to result in high resolution tomograms of a process that is rare and therefore hard to capture.

We observed an increase in the number and types of fusion intermediate structures visualized by cryoET in Serinc3 and Serinc5-containing samples (Figure 2.3f) as well as a strong defect in content release from Serinc3 and Serinc5-containing particles by TIRF (Figure 2.3b). This suggests that Serinc3/5 inhibit full fusion of HIV particles without targeting one particular step in the fusion process. It is already known that the energy required for each step during the fusion reaction increases along the fusion pathway (Cohen and Melikyan, 2004; Kawamoto and Shinoda, 2014), so it is plausible that Serinc3/5 increase the energy barriers between the intermediate states. Consequently, most particles are unable to complete the final step (pore expansion) but instead populate intermediate states. Broad energetic changes could also explain the abnormal, "cinched," early fusion products observed by cryoET that appear unable to fully dilate a fusion pore (Figure 2.3f, i, j, and l). These membrane structures are undetectable by TIRF microscopy because such wide fusion pores do not impede content (mCherry) release (Supplemental Figure 2.1) and could only be seen in the cryo electron tomograms of HIV target cell membrane blebs.

Examination of the kinetics of fusion by TIRF microscopy shows no slowing of lipid mixing (Figure 2.4d) or content release (Figure 2.3c) of Serinc-containing viruses that do fuse under these conditions. One possible explanation is that the transition state energies of hemifusion and small fusion pore opening are unchanged by Serinc3/5. Together with the observation of hemifusion and cinched early fusion product events in tomograms of Serinc3 and Serinc5 containing virus at the later, 30 second time point, it

may be that Serinc3/5 containing virus particles can complete the earlier intermediates of fusion but are slowed at later intermediate steps.

Interestingly, we discovered that treatment of HIV pseudoviruses with the membrane partitioning antifungal, Amphotericin B, has little effect on infection or fusion of Serinc-lacking pseudoviruses but increases infection and rescues fusion of Serinc3 and Serinc5 pseudoviruses, regardless of whether viral or target membranes are treated (Figure 2.4e and 2.4f). Since Amphotericin B partitions into membranes and thereby alters the headgroup structure of the lipids at the membrane-water interface, this finding indicates that Serinc's inhibitory activity on membrane fusion likely involves its interaction with the membrane interface. This view is supported by similar results that were obtained by the lipid headgroup altering fluorescent dye Atto488-DMPE. While it was recently shown that Serinc5 itself selectively binds certain lipids (Pye et al., 2020), our results strongly suggest that Serinc-lipid interactions are important for HIV restriction. How exactly this membrane interactive activity of Serinc relates to the recently described lipid binding grove on Serinc5 is not known and cannot be addressed with the methods employed in this study, but would be interesting to follow up on in future experiments.

In summary, we revealed three-dimensional structures of various intermediates on the pathway of HIV virion to plasma membrane fusion at resolutions not previously seen. We also demonstrated that the viral envelope-embedded restriction factors Serinc3 and Serinc5 arrest fusion at multiple of these intermediate structures suggesting an underlying mechanism with broad reaching changes to the energetics of fusion. These results provide a new dimension to explain the mechanism of Serinc's viral restriction function. In the

process, we also showed that plasma membrane blebs are useful for studying HIV membrane fusion in 3D by both cryoET and TIRF microscopy. The TIRF data on the dynamics of fusion and the static cryoET snapshots of multiple fusion intermediate structures complement each other. The methodology we developed could easily be used to study membrane fusion and cell entry of other viruses, other types of membrane fusion, and plasma membrane functions such as endocytosis, clustering of receptor signaling molecules, and potentially, conformational changes of ion-channels.

2.5 Materials and Methods

Cell lines, reagents, and plasmids: HEK 293T/17 cells (ATCC) were maintained in high glucose Dulbecco's Minimum Essential Media (Gibco) supplemented with 10% fetal bovine serum (Atlanta Biologicals), 1% antibiotic-antimycotic (Gibco), 1 mM sodium pyruvate (Gibco), and 2 mM glutamine (Gibco). V4 high HIV Envelope cells were a gift from Michael Zwick (Stano et al., 2017) and were maintained in the same medium as the HEK 293T/17 cells supplemented with 1 μg/mL puromycin (Gibco). HeLa cells (ATCC), TZM-bl cells (AIDS Reagents Program) and CD4 and CCR5 overexpressing HeLa cells (gift of David M. Rekosh, University of Virginia) were maintained in Iscove's Modified Dulbecco's Medium (Gibco) supplemented with 10% fetal bovine serum and 1% antibiotic/antimycotic. The medium of the CD4 and CCR5 overexpressing HeLa cells was supplemented with 0.5 mg/mL of G418 (Gibco), and 1 μg/mL puromycin. All cells were maintained at 37°C with 5% CO_2 atmosphere.

pHIV-luciferase, pHIV-Rev, and pHIV-pack were gifts of Wen Yuan (University of Virginia). pHIV-Env-SF162 was provided by the AIDS Reagent Program. pHIV-imCherry (Sergi et al., 2013) was a gift of Gregory Melikian (Emory University). pPBJ5-Serinc2-HA was a gift of Massimo Pizzato (University of Trento) and pPBJ5-Serinc3-HA and pPBJ5-Serinc5-HA were gifts of Heinrich Gottlinger (University of Massachusetts Medical School, Wooster).

HIV pseudovirus preparation: HIV pseudoviruses were produced by transfection of HEK 293T cells (ATCC) with Lipofectamine 2000 (Invitrogen) and the following amounts of plasmids per 10 cm dish: 13 μg pHIV-luciferase, 5 μg pHIV-pack, 4 μg pHIV-Env-SF162 (Cheng-Mayer et al., 1997; Stamatatos et al., 2000, 1998), 4 μg pHIV-imCherry, 1 μg pHIV-Rev and 4μg of pBJ5-Serinc2-HA (Rosa et al., 2015), pBJ5-Serinc3-HA (Usami et al., 2015), or pBJ5-Serinc5-HA (Usami et al., 2015) as indicated in text. "High Envelope" HIV pseudoviruses were produced in the previously described V4 cell line (Stano et al., 2017) with the same amounts of plasmids excluding pHIV-Env-SF162. Culture media was changed 4-6 hours after transfection to phenol-red free DMEM supplemented with 10% FBS, 1% antibiotic-antimycotic, 1 mM sodium pyruvate, and 2 mM glutamine. Culture supernatants were harvested 2 days after transfection and cleared by centrifuging 5000xg before passing through a 0.22 μm filter. HIV pseudoviruses were pelleted through a 25% sucrose-HME (20 mM HEPES, 20 mM morpholineethanesulfonic acid [MES], 130 mM NaCl, 1 mM EDTA [pH 7.4]) cushion as previously described (Hulseberg et al., 2019) and resuspended in buffer HME without sucrose. Pseudovirus preparations were further purified by density dependent

centrifugation on a discontinuous sucrose gradient composed of 65% sucrose-HME and 25% sucrose-HME spun 151,000xg for 18 hours. Pseudovirus was collected from the 65%/25% sucrose interface, diluted in buffer HME without sucrose, and repelleted through a 25% sucrose cushion. After resuspension in buffer HME without sucrose, the pseudovirus preparation was aliquoted and stored at -80°C. Additionally, the concentration of HIV p24 in each preparation was measured by ELISA (Toohey et al., 1995; Wehrly and Chesebro, 1997) and used to normalize the amount of pseudovirus added to downstream experiments. Each preparation of virus was checked for incorporation of Serincs by western blotting against the HA tag (Supplemental Figure 2.S8) with a Rat anti-HA antibody (3F10, Roche) normalized to p24 as detected by Human anti-HIV Immune Globulin (AIDS Reagent Program) (Cummins et al., 1991). For some preparations of virus, a small amount was surface biotinylated with sulfo-NHS-LB-biotin (Thermo Scientific) before western blotting with detection by streptavidin-IR680 (LiCor Biosciences).

Infection of TZM-bl cells (Derdeyn et al., 2000; Platt et al., 2009; Takeuchi et al., 2008; Wei et al., 2002) by HIV pseudoviruses was performed as previously described (Sarzotti-Kelsoe et al., 2014) and firefly luciferase activity was measured two days post-infection with the BriteLite reagent (Perkin Elmer) in a plate reader (Flex Station M5, Molecular Devices). Pelleted HIV pseudovirus preparations were diluted in Opti-MEM (Gibco) to the same concentration of p24 to ensure equal loading of viral particles. For infection assays performed with Amphotericin B (Bio Basic), cells were pre-treated with 1 μM Amphotericin B diluted in Opti-MEM or Opti-MEM alone for 30 minutes before HIV

pseudoviruses, diluted in 1 μM Amphotericin B in Opti-MEM or Opti-MEM alone, were added.

For some TIRF experiments, a fluorescent membrane label, Atto488-dimyristoylphosphatidylethanolamine (DMPE) (Millipore-Sigma), was incorporated into the viral membrane. Atto488-DMPE was dried on the bottom of a glass test tube to remove chloroform/methanol solvent and resuspended in buffer HB (20 mM HEPES, 150 mM NaCl [pH 7.4]) to a concentration of 1.8 μg/mL. HIV pseudovirus was diluted to a concentration of 2 μg/mL, as measured by p24, in buffer HB and mixed in a 1:3.5 ratio with the dye suspension. The mixture was incubated at room temperature in the dark for 2 hours on a rotary spinner. To remove free Atto488-DMPE, the HIV pseudovirus mixture was diluted up to 1.5 mL in buffer HB and pelleted by spinning at 21,000xg for 1 hour at 4°C. The viral pellet was washed in an additional 1.5 mL of buffer HB and pelleted again. Atto488-DMPE labeled HIV pseudoviruses were used within 24 hours. For TIRF experiments with Atto488-DMPE labeled virus, the chamber with the SPPM was washed with 3 mL of buffer HB and allowed to equilibrate before pseudovirus was introduced.

Plasma Membrane Bleb Preparation: Blebs were produced from HeLa cells (ITCC) or HeLa cells overexpressing CD4 and CCR5 by previously published methods(Sezgin et al., 2012; Yang et al., 2017). Briefly, when cells reached 90% confluence, they were washed twice with blebbing buffer (10 mM HEPES, 150 mM NaCL, 2 mM CaCl2, pH 7.4) and blebbing was induced by replacing buffer on the cells with 5 mL of 25 mM formaldehyde (J.T.Baker) and 2 mM Dithiothreitol (DTT) diluted in blebbing buffer and

incubating the cells at 37°C, 5% CO_2 for 45 minutes. After 45 minutes, blebs were detached from cells by shaking on a radial shaker at room temperature for 1 hour before the supernatant was collected and cleared of large cell debris by centrifuging and 100xg for 10 minutes. Blebs were pelleted at 20,000xg for 1 hr and washed twice in blebbing buffer without DTT or formaldehyde. Blebs used for cryoET were washed and resuspended in blebbing buffer without calcium and filtered through an 800nm filter. For select cryoET experiments, 40uM inositol hexaphosphate (IP6) was added to wash and resuspension buffers.

TIRF Supported Lipid Bilayer Fusion Assay:

Supported planar plasma membranes derived from blebs were prepared as previously described (Kalb et al., 1992; Wagner and Tamm, 2000; Yang et al., 2017). Quartz slides were cleaned in piranha solution (95% H_2SO_4 and 30% H_2O_2 in a 3:1 ratio) and rinsed in 12 liters of deionized water. Next, a lipid monolayer composed of 4:1 brain phosphatidylcholine and cholesterol (Avanti Polar Lipids) with 3% 1,2-dimyristoyl-*sn*-glycero-3-phosphoethanolamine-PEG3400-triethoxysilane was deposited on the quartz slide by the Langmuir-Blodgett method. A chloroform solution of the lipid mixture was applied to a Nima 611 Langmuir-Blodgett trough and after letting the solvent evaporate for 10 minutes, the lipid layer was compressed at a rate of 10 cm^2/min to a pressure of 32 mN/m. A cleaned, rinsed, and dried quartz slide was rapidly dipped (68 mm/min) and slowly removed (5 mm/min) from the trough and then dried in a desiccator chamber overnight.

The slide was then assembled into a custom-built microscopy flow cell (Appendix B) and plasma membrane blebs diluted in blebbing buffer without DTT or formaldehyde were flowed in to form the outer leaflet of the supported planar plasma membrane. After 2 hours at room temperature, the flow cell was washed with multiple volumes of blebbing buffer, then multiple volumes of HME buffer, and transferred to a prism-based TIRF microscope. The sample was excited with a 561nm diode laser (OBIS 561 nm LS, Coherent) at an angle of 72 degrees from normal and emission light was filtered through a dichroic mirror (DC565, Semrock) and a band-pass filter (BP605/50, Semrock). For double labeled (membrane and content) experiments, the sample was excited with both a 488 nm (OBIS 488 nm LX, Coherent) laser and the 561nm laser. Emission light from both labels was filtered by a dichroic mirror (DC-Di-493/574, Semrock) before the combined light was split in two bands by an optosplit (Optosplit II, Andor Technology) equipped with a dichroic mirror (DC562, Semrock) and two band pass filters (BPS525/50 and BP607/70, Semrock). Video was recorded by an EMCCD (DV887ESC-BV, Andor Technology) in frame transfer mode with an exposure time of 0.2 s for 13.3 minutes as a dilution of HIV pseudovirus totaling 16 ng of p24 as measured by ELISA was flowed into the chamber. Laser intensity, shutter, and camera were controlled by a custom LabView program (National Instruments).

Intensities of single particles over time were extracted with a custom-built LabView program and classified as representing binding without fusion or binding with fusion based on the following criteria: a rapid increase in intensity followed by multiple frames of similar intensity without translation of the particle more than 4 pixels was classified as

binding. If the intensity of the particle remained the same for the duration of the acquisition or slowly bleached over 10 seconds or more, this was considered binding without fusion. If the intensity of a bound particle decreased to background in one frame (0.2 s), this was considered an unbinding event. If the intensity of a bound particle decreased to background with a characteristic curve as shown in Figure 2.1e, it was classified as binding with fusion.

CryoET of HIV Pseudoviruses and Membrane Blebs: Temperature was used to synchronize HIV membrane fusion before freezing. HIV pseudovirus particles were mixed with 10 nm colloidal gold fiducials and CD4 and CCR5 containing membrane blebs in a thin walled PCR tube on ice for 1 minute. The PCR tube was then transferred to a heat block set at 37°C for either 10 or 30 seconds. The HIV/bleb/gold mixture was rapidly transferred to a C-Flat 2/2-3C or Quantifoil 2/2 grid (Electron Microscopy Sciences), previously glow discharged with amylamine (Sigma), blotted, and frozen in liquid ethane before storage in liquid nitrogen. To aid the visualization of viral capsids, 40 μM inositol-hexakisphosphate (IP6) (Dick et al., 2018) was added to the membrane blebs before freezing for some samples as it is expected to leak out of blebs (Skinkle, 2019). The grids were imaged on a Titan Krios electron microscope operating at 300 kV equipped with a Falcon 3 detector and controlled by Tomography 4.0 software (ThermoFisher Scientific). Bidirectional tilt series of regions of interest were acquired with 2 degree increments from -60° to +60°. Magnification was 29,000X, which yielded a pixel size of 0.288 nm.

Tilt series images were motion corrected with MotionCor2 (Zheng et al., 2017) (5 by 5 patch for 10 iterations with a tolerance of 0.5) and tomograms were reconstructed in IMOD (Mastronarde and Held, 2017). High tilt views that were obstructed were excluded. Gold fiducials were used for alignment. Aligned tilt stacks were binned by 4 and back projected to create tomograms. To enhance contrast for display, tomograms were denoised by cryoCARE (Buchholz et al., 2018) with the following parameters: binned by 6, training volumes: 1200, validation volumes: 120, volume dimensions: 64x64x64, training epochs: 200, steps per epoch: 75.

Classification criteria for HIV fusion intermediate structures shown by cryoET. Receptor mediated binding: One membraned vesicle must be approximately 100-150nm in diameter and show a continuous, medium density texture inside the membrane; we classify this as a viral particle. The target membrane vesicle can be any size and must have a less regular and lower density texture inside. At least one instance where a dark, linear density extends between viral and target membranes is required. This distinguishes particles that may be close by chance from those that are interacting. We did not distinguish between loose binding or tight binding.

Hemifusion: Using the same definition of viral particle and target membrane above, hemifusion is defined such that there is at least one section through a tomogram (binned by 4) where the densities of the outer lipid leaflets of viral and target membranes are indistinguishable but the curvature of the inner leaflet is unchanged.

Early Fusion Product: There must be only one contiguous membrane and it cannot be spherical but rather have some sort of narrowing. There must be either 1) demarcation of different textures within the volume surrounded by the membrane, 2) clear evidence of viral products like a capsid within the membrane, or 3) virus-like membrane proteins in a lobe of approximately 100nm in diameter.

Late Fusion Product: There must be only one contiguous membrane and it must be spherical without focal narrowing. It must be much larger than a virus (>200nm diameter). It must have some evidence of viral proteins whether that is characteristic Env-like densities in the membrane or virus-like textured density inside.

Acknowledgements:

We thank Dr. Marie-Louise Hammarskjold and Dr. David Rekosh for the gift of CD4 and CCR5 overexpressing HeLa cells and Dr. Heinrich Gottlinger, Dr. Gregory Melikyan, and Dr. Massimo Pizzato for the gift of pBJ5-Serinc plasmids. The following reagents were obtained through the NIH AIDS Reagent Program, Division of AIDS, NIAID, NIH: TZM-bl cells (Cat# 8129) from Dr. John C. Kappes and Dr. Xiaoyun Wu, pCAGGS SF162 gp160 from Drs. L. Stamatatos and C. Cheng-Mayer, Anti-HIV Immune Globulin (HIVIG) from NABI and NHLBI (Cat# 3957), and Anti-HIV-1 p24 Monoclonal (183-H12-5C) (Cat#3537) from Dr. Bruce Chesebro and Kathy Wehrly. Thank you to Dr. Kelly Dryden and the University of Virginia Molecular Electron Microscopy Core for training and assistance with cryoET. The University of Virginia Research Computing is acknowledged for high performance computing time. Cartoons were created with

BioRender.com. This work was supported by US National Institutes of Health Grants R01 AI030557 to LKT, F30 HD101348 to AEW, and P50 AI150464 to BKG.

2.6 Supplemental Figures and Video Legends:

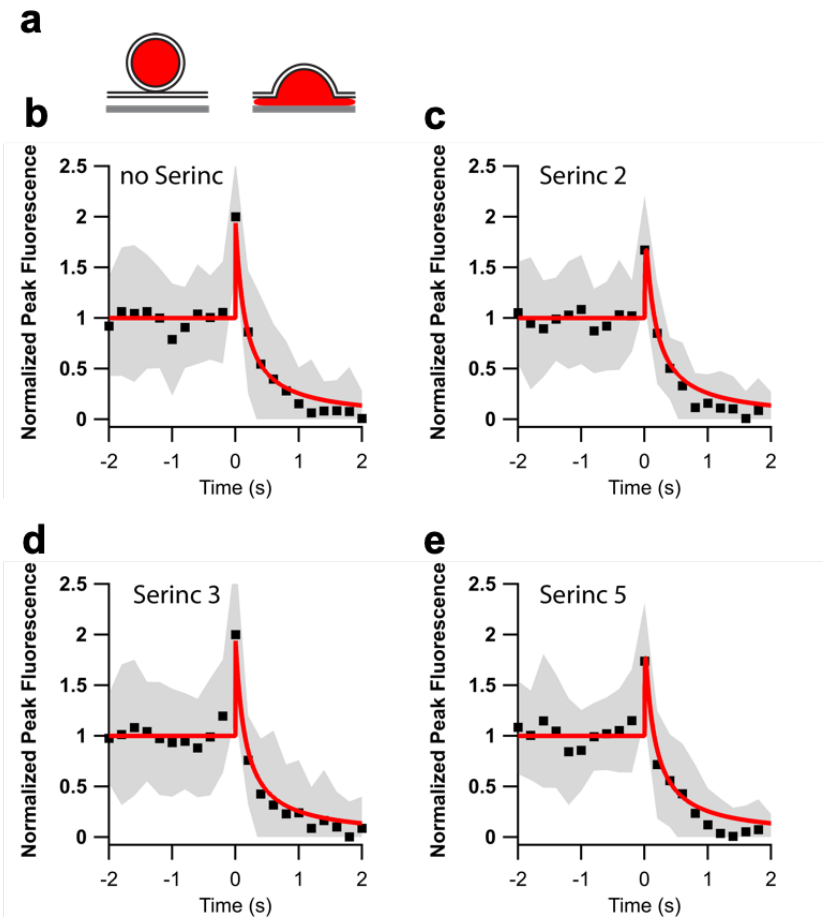

Fig. 2.S1. Model of mCherry content release from HIV pseudoviruses during fusion. (a) Cartoon of pseudovirus mCherry content release model. We assume the mCherry content is freely mobile within the virus and is released into the aqueous cleft between SPPM and quartz slide at the onset of fusion pore opening with a specific release rate k_r. Within the cleft, mCherry diffuses in 2-dimensions with a characteristic diffusion coefficient D (0.1 $\mu m^2/s$). Other numerical parameters of the model include the radius of the viral particle R (55 nm) and the characteristic penetration depth d_p of the evanescent field at the quartz/water interface. The release rate k_r, was adjusted for each type of

pseudovirus (no Serinc: (1000 s^{-1}, Serinc 2: 100 s^{-1}, Serinc 3: 1000 s^{-1}, Serinc 5: 200 s^{-1}). The model is a simplified, one step release model, based on the more complex release model of secretory vesicles described in detail in Kreutzberger et al., 2017 (b-e). Average content release traces of HIV mCherry pseudoviruses with model calculations based on the parameters above. Individual fusion events for each virus were aligned to the peak at the onset of fusion and intensities were normalized to the "binding state" before fusion. Aligned and normalized traces were averaged and the mean (black squares) and standard deviation (grey shaded area) were plotted. (b) Serinc-lacking pseudovirus content release. Average represents 35 individual fusion events. (c) Serinc2 pseudovirus content release. Average represents 32 individual fusion events. (d) Serinc3 pseudovirus content release. Average represents 32 individual fusion events. (e) Serinc5 pseudovirus content release. Average represents 39 individual fusion events.

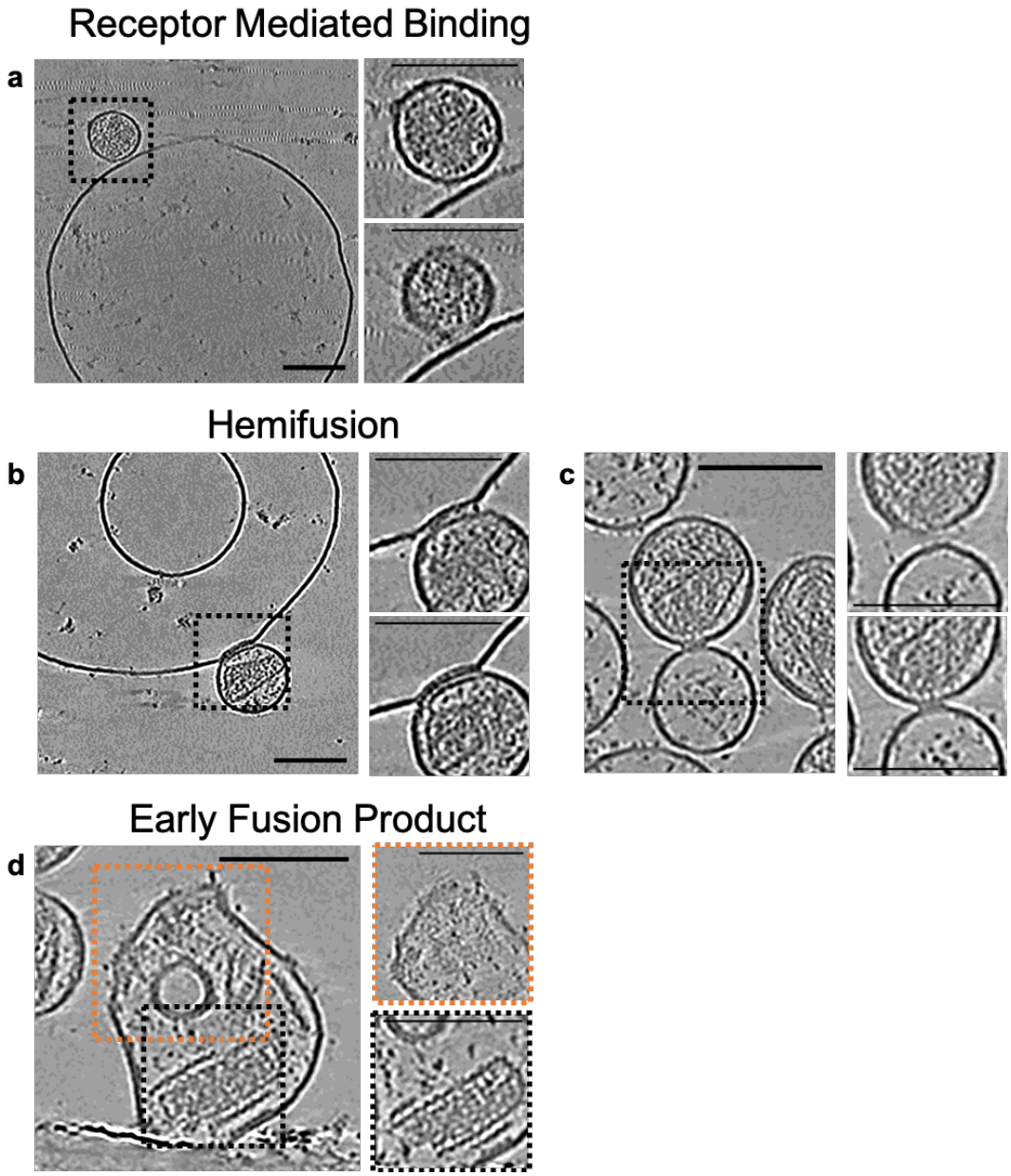

Fig. 2.S2. Additional examples of HIV pseudovirus-bleb fusion intermediates. All samples were supplemented with IP6. Tomograms were all prepared with additional IP6 and are shown with cryoCARE denoising to enhance contrast for display. Scale bars are 100nm. (a) Example of receptor mediated binding (b) example of hemifusion with a wider area of contact (c) example of hemifusion with a narrower contact (d) Early fusion where a viral capsid and an enclosed vesicle can be seen. Many blebs are multilamellar

(like the bleb in panel b) whereas viruses are never multilamellar. Additional views of the boxed areas at different slices in the z direction are shown to the right.

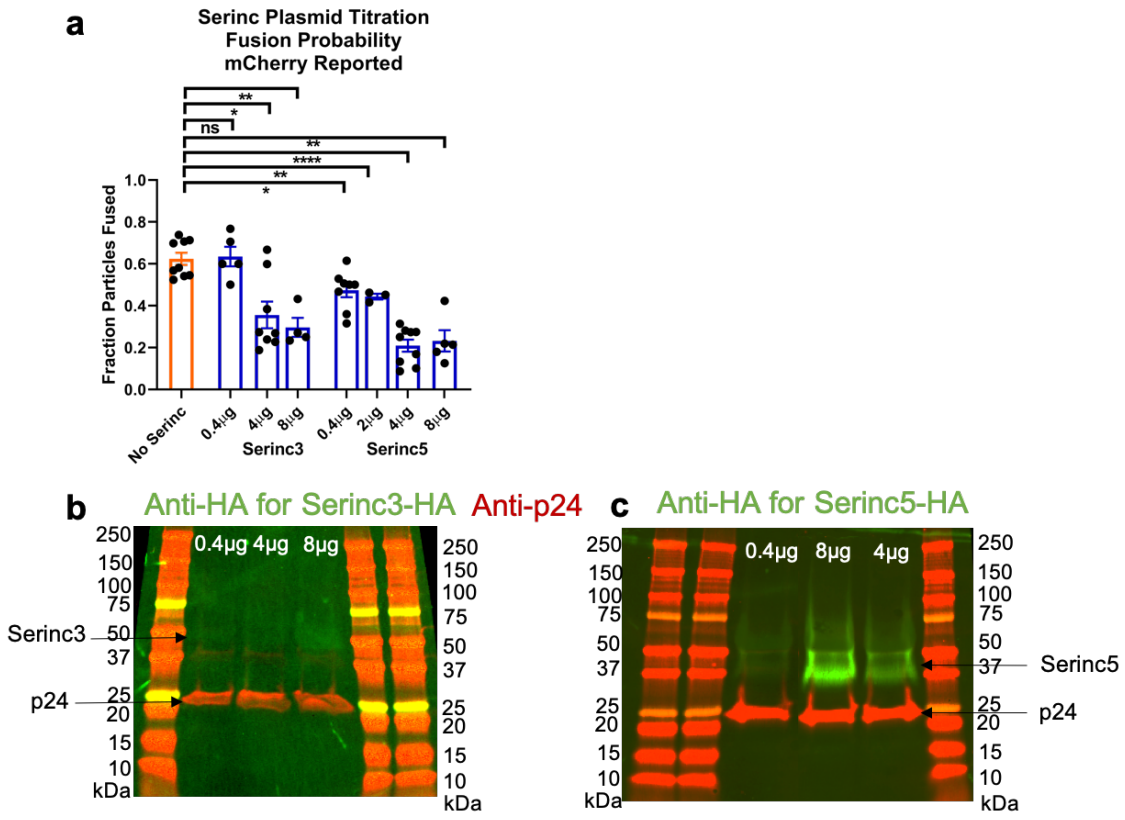

Fig. 2.S3. Titration of Serinc3 and Serinc5's viral incorporation and inhibition of viral content release. (a) Fraction of bound HIV pseudovirus particles that underwent fusion, as reported by loss of mCherry content marker. Each point represents a separately prepared bilayer. No Serinc and 4 µg data reproduced from Figure 2.3b for comparison. All other data collected from 3 experiments and 1 preparation of HIV pseudovirus. (b,c) The pBJ5 Serinc plasmids are expressed as C-terminal fusion proteins with an HA tag which was used for detection of Serinc incorporation in HIV pseudoviruses by western blot (green channel). The concentration of p24 in each preparation was measured by ELISA and a roughly normalized amount of pseudovirus was loaded. p24 was detected

by mouse anti-p24 (red channel). The expected molecular weights are 53kDa and 47kDa for Serinc3 and Serinc5 respectively. (b) Titration Serinc3 incorporation into HIV pseudoviruses. The mass of pBJ5-Serinc3-HA plasmid transfected per 10 cm^2 plate is indicated for each lane. (c) Titration Serinc5 incorporation into HIV pseudoviruses. The mass of pBJ5-Serinc5-HA plasmid transfected per 10 cm^2 plate is indicated for each lane. The density of Serinc5 bands is consistently higher than the density of Serinc3 bands for an equivalent amount of virus (see Figure 2.S7).

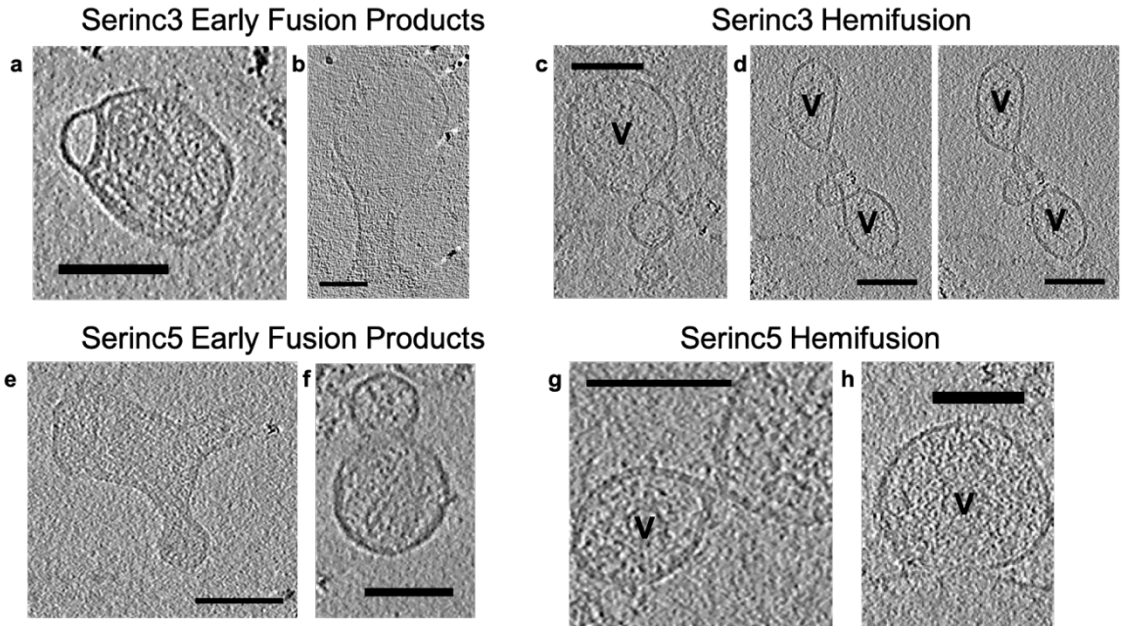

Fig. 2.S4. Additional examples of tomograms of Serinc3- and Serinc5-disrupted HIV fusion events. All images are single z-slices through tomograms of HIV pseudoviruses mixed with CD4/CCR5-containing blebs and warmed to 37°C for 30 seconds before freezing. All scale bars are 100 nm. "v" designates a viral particle. (a) Serinc3 HIV pseudovirus mixed with blebs. Defocus = -10 μm. (b) Serinc3 HIV pseudovirus mixed with blebs. Defocus = -4 μm. (c) Serinc3 HIV pseudovirus mixed with blebs. Defocus = -4 μm. (d) Serinc3 HIV pseudovirus mixed with blebs. Defocus = -4 μm. (e) Serinc5 HIV

pseudovirus mixed with blebs. Defocus = -4 μm. (f) Serinc3 HIV pseudovirus mixed with blebs. Defocus = -10 μm. (g) Serinc5 HIV pseudovirus mixed with blebs. Defocus = -4 μm. (h) Serinc5 HIV pseudovirus mixed with blebs. Defocus = -4 μm.

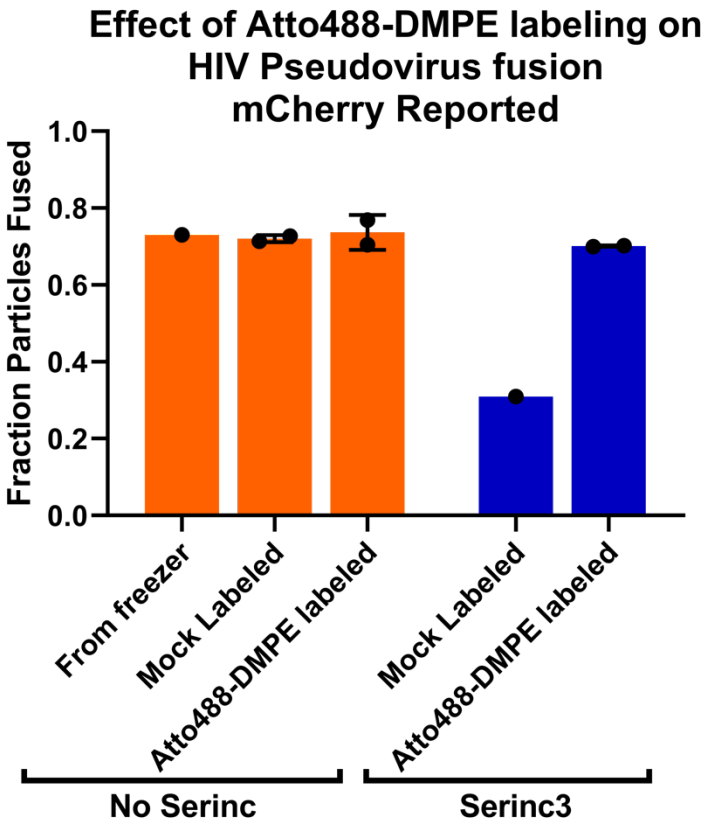

Fig. 2.S5. Atto488-DMPE labeling does not affect fusion of Serinc-lacking particles, but increases fusion of Serinc3-containing particles. Fraction of bound HIV pseudovirus particles that underwent fusion, as reported by loss of mCherry content marker. Each point represents a separately prepared SPPM. Data are paired repeats from a single experiment. The same preparation of HIV pseudovirus was used for each set of conditions (Serinc-lacking or Serinc3, respectively). The virus for the "No Serinc from freezer" condition was thawed immediately before the experiment, diluted in buffer, and

added directly to the SPPM without modification. The mock labeled conditions were treated with the same buffers, incubations, and centrifugations alongside the Atto488-DMPE labeled pseudovirus but without the addition of the lipid. Error bars are SD.

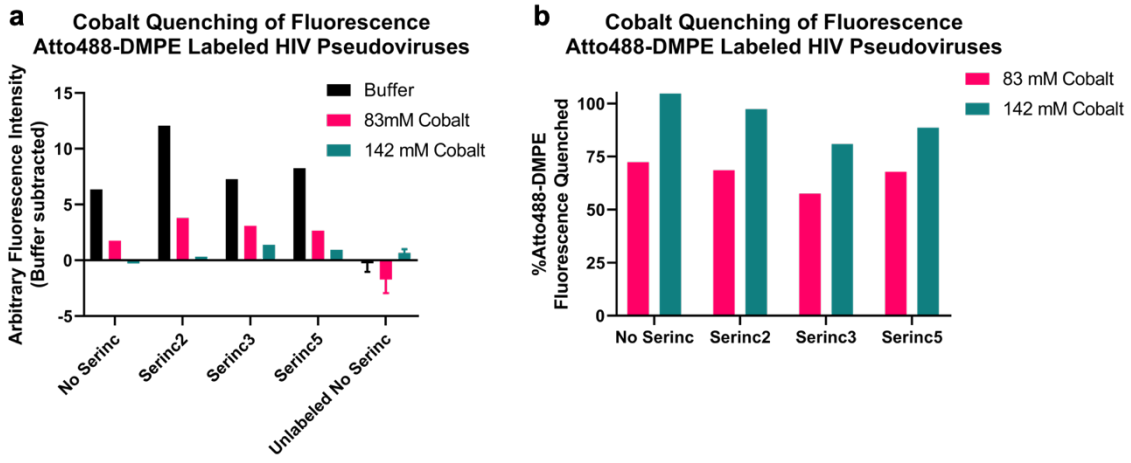

Fig. 2.S6. Atto488-DMPE is mostly confined to the outer leaflet of the viral membrane. HIV pseudoviruses were labeled with Atto488-DMPE as described in the Methods section and fluorescence was measured in a plate reader (Exc 488nm, Em 514nm, Cutoff 505nm) before and after addition of cobalt chloride to quench solvent accessible fluorophores. (a) Arbitrary fluorescence intensity (buffer fluorescence subtracted) of HIV pseudoviruses before and after cobalt addition. Data are from one experiment. Error bars show SD for 2 replicates of unlabeled No Serinc virus (b) The same data as in panel a represented as percent of original fluorescence remaining after cobalt addition.

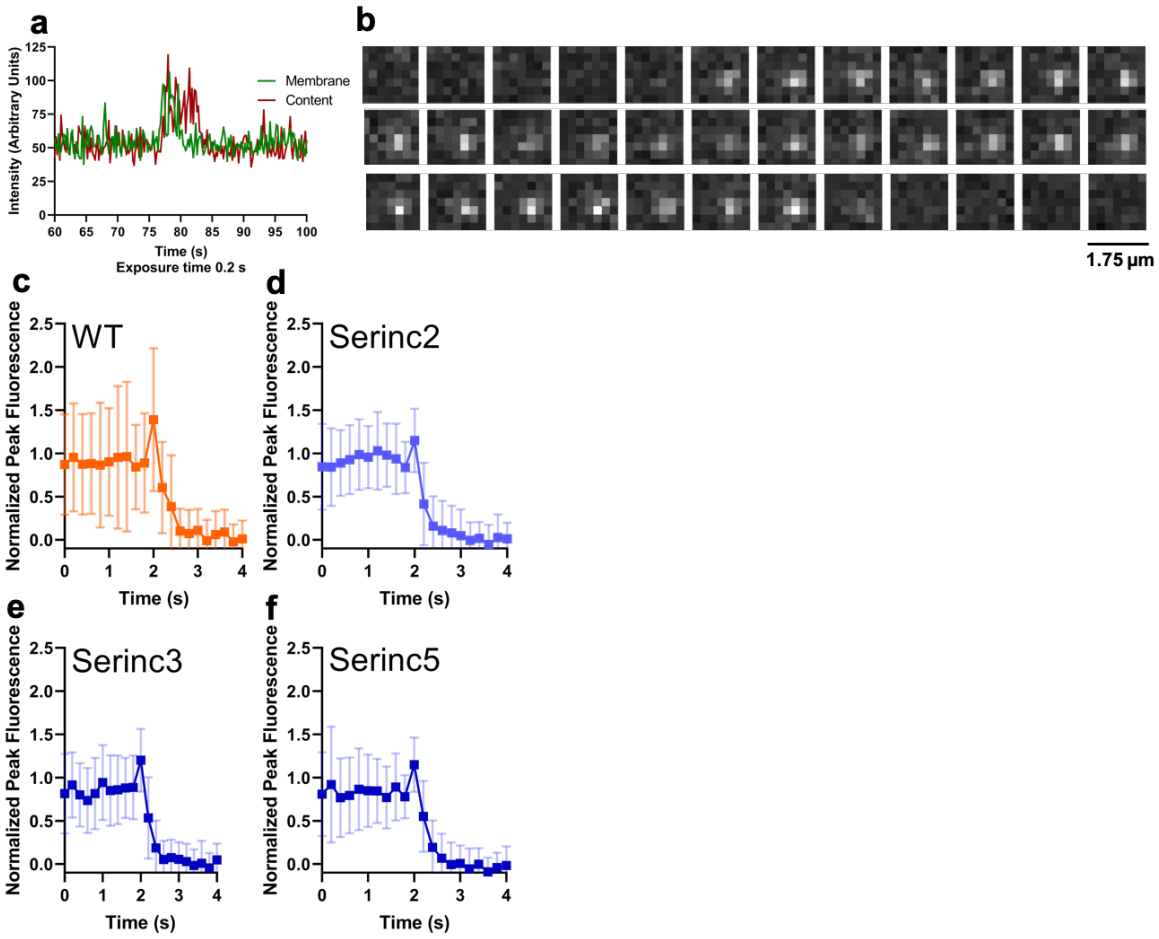

Fig. 2.S7. Average lipid mixing traces of HIV mCherry pseudoviruses labeled with Atto488-DMPE. (a) Fluorescence intensity of a dual labeled (mCherry and Atto488-DMPE) HIV pseudovirus particle fusing with an SPPM. (b) Example micrographs of the membrane label for the particle shown in panel a. Each box represents the same region separated in time by 0.2 seconds. (c-f) Individual events for each virus were aligned and normalized in the same manner as the content release traces where events were aligned to peak at the onset of fusion and intensities were normalized such that "binding" before fusion was set to one and "baseline" after fusion was set to zero. Aligned and normalized traces were averaged together and the mean (squares) and SD were plotted. Dissipation of the Atto488-DMPE after lipid mixing would be expected to occur quickly via 2-

dimensional diffusion of labeled lipids within the larger SPPM. The smaller peaks we observe could be due to changes in the direction of the fluorescence dipole as the spherical viral membrane collapses into the planar SPPM, as described by (Kiessling et al., 2010). Averaged lipid mixing trace of Atto488-DMPE labeled (c) Serinc-lacking (d) Serinc2 (e) Serinc3 (d) Serinc5 mCherry pseudoviruses.

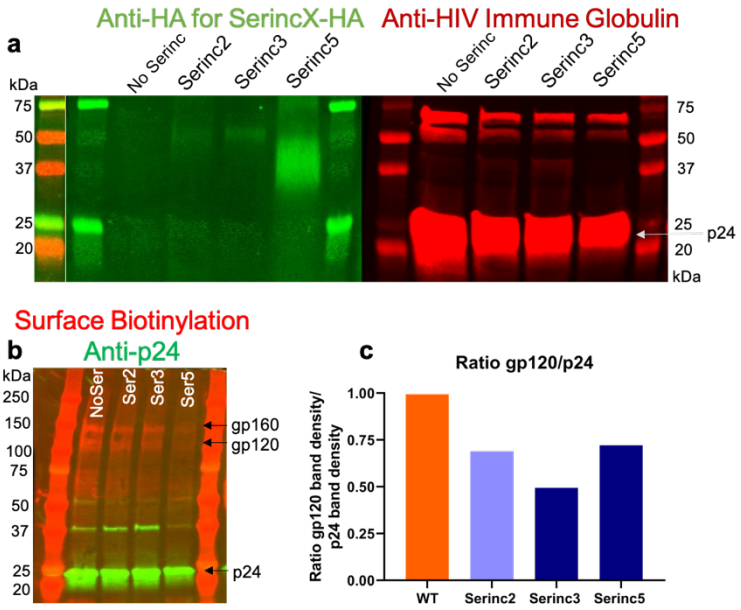

Fig. 2.S8. Protein incorporation into HIV pseudoviruses and effects on HIV pseudovirus fusion. (a) The pBJ5 Serinc plasmids are expressed as C-terminal fusion proteins with an HA tag which was used for detection of Serinc incorporation in HIV pseudoviruses by western blot (green channel). The concentration of p24 in each preparation was measured by ELISA and a normalized amount of pseudovirus was loaded. p24 was detected by HIV Immune Globulin (red channel) and used for normalization. Expected molecular weights of Serincs: Serinc2 51kDa, Serinc3 53kDa, Serinc5 47kDa. (b) To assess surface glycoprotein incorporation, an equal amount of

virus as measured by p24 ELISA was surface biotinylated by sulfo-NHS-succinimide ester before western blotting and detection by streptavidin-IR680 (red channel). (c) Quantification of the ratio of the gp120 and p24 bands shown in b.

Movie S1 (separate file). Z-slices through tomograms of HIV pseudovirus and blebs treated with fusion inhibitor, T20. The video shows slices through the 3D volume of the same tomogram as Figure 2.2b, moving from the bottom to the top. The pseudovirus and bleb mixture was treated with 135 ng/mL T20. Tomogram is shown with non-anisotropic diffusion filtering to enhance contrast for display. Scale bars are 100 nm.

Movie S2 (separate file). Z-slices through tomograms of HIV pseudovirus and blebs showing receptor mediated binding. The video shows slices through the 3D volume of the same tomogram as Figure 2.2c, moving from the bottom to the top. The pseudovirus and bleb mixture was warmed to 37°C for 10 seconds before freezing. Tomogram is shown with cryoCARE denoising to enhance contrast for display. Scale bars are 100 nm.

Movie S3 (separate file). Z-slices through tomograms of HIV pseudovirus and blebs showing hemifusion. The video shows slices through the 3D volume of the same tomogram as Figure 2.2d, moving from the bottom to the top. The pseudovirus and bleb mixture was warmed to 37°C for 10 seconds before freezing. Tomogram is shown with cryoCARE denoising to enhance contrast for display. Scale bars are 100 nm.

Movie S4 (separate file). Z-slices through tomograms of Serinc2-containing HIV pseudovirus and blebs. The video shows slices through the 3D volume of the same tomogram as Figure 2.3g, moving from the bottom to the top. The pseudovirus and bleb

mixture was warmed to 37°C for 30 seconds before freezing. Tomogram is shown with cryoCARE denoising to enhance contrast for display. Scale bars are 100 nm.

Movie S5 (separate file). Z-slices through tomograms of Serinc3-containing HIV pseudovirus and blebs. The video shows slices through the 3D volume of the same tomogram as Figure 2.3h, moving from the bottom to the top. The pseudovirus and bleb mixture was warmed to 37°C for 30 seconds before freezing. Tomogram is shown with cryoCARE denoising to enhance contrast for display. Scale bars are 100 nm.

Movie S6 (separate file). Z-slices through tomograms of Serinc5-containing HIV pseudovirus and blebs. The video shows slices through the 3D volume of the same tomogram as Figure 2.3i, moving from the bottom to the top. The pseudovirus and bleb mixture was warmed to 37°C for 30 seconds before freezing. Tomogram is shown with cryoCARE denoising to enhance contrast for display. Scale bars are 100 nm**.**

CHAPTER 3: Serinc5 restricts HIV membrane fusion by altering lipid order and tension in the viral membrane

Manuscript in preparation.

3.1 Abstract:

The host restriction factor, Serinc5, incorporates into budding HIV particles and inhibits their infection by an incompletely understood mechanism. We have previously reported that Serinc5 but not its paralogue, Serinc2, blocks HIV cell entry by membrane fusion, specifically by inhibiting fusion pore formation and dilation. A compelling body of work suggests Serinc5 may alter the conformation and clustering of the HIV fusion protein, Env, although these changes would be expected to disrupt earlier steps in fusion than pore dilation. To contribute an additional perspective to the developing model of Serinc5 restriction, we assessed Serinc2 and Serinc5's effects on HIV pseudoviral membranes. Using a previously established TIRF-based single particle fusion assay, we found that pre-treatment with exogenous phosphatidylethanolamine (PE) rescued HIV pseudovirus fusion from restriction by Serinc5. This effect was specific for PE and did

not depend on acyl chain length or saturation. Additionally, Serinc5 was found to increase the portion of the viral membrane in an ordered phase by both fluorescence lifetime imaging with an order and tension sensitive dye, FLIPPER-TR, and by measuring pseudoviral membrane thickness via cryoEM. Together, these data suggest Serinc5 alters multiple interrelated properties of the viral membrane—order, rigidity, line tension, and lateral tension—which are predicted to alter the energies of fusion intermediates to disfavor fusion completion. Understanding the mechanism of Serinc5 restriction could enable the development of novel antivirals that exploit the same viral weaknesses.

3.2 Introduction:

Serinc5 is a recently described host restriction factor that incorporates into budding HIV particles and inhibits infection at the cell entry step (Rosa et al., 2015; Usami et al., 2015). While it is known to inhibit multiple steps of membrane fusion—hemifusion, fusion pore opening, and fusion pore dilation (Sood et al., 2017; Ward et al., 2020)—, the exact mechanism by which it does so remains uncertain. Many studies have focused on the interaction between Serinc5 and the HIV fusion protein, Env, demonstrating that Serinc5 alters Env conformation (Schulte et al., 2018; Staropoli et al., 2019), antibody binding (Beitari et al., 2017; Sood et al., 2017) and clustering (Chen et al., 2020). However, alterations in Env cannot fully explain the observed fusion defects induced by Serinc5 incorporation. In current models of viral membrane fusion, progression through early intermediate steps is driven by rearrangements of the viral fusion protein (Harrison, 2015; White and Whittaker, 2016) but the penultimate step,

fusion pore dilation, is driven by membrane tension and curvature (Kozlov and Chernomordik, 2015). Disruption of fusion pore dilation as we previously observed (Ward et al., 2020), suggests Serinc5 may alter properties of the viral membrane.

While it has already been shown that Serinc5 does not change the composition of the viral membrane (Trautz et al., 2017), there are levels of organization of the membrane which could be altered to change local concentrations of lipids. In model membranes, the composition of the HIV membrane was shown to support liquid-liquid phase separation (Huarte et al., 2016); areas enriched in saturated phospholipids, cholesterol and sphingolipids with a more ordered packing of lipid acyl chains called liquid-ordered (L_o) domains coexisting with liquid-disordered (L_d) domains where unsaturated phospholipids, less cholesterol and fewer sphingolipids pack in a more disordered manner (Feigenson, 2006). As a consequence of ordered packing, membranes in an L_o phase have a higher lateral pressure and are several Angstroms thicker than membranes in an L_d phase (Levental et al., 2020). These two parameters can be reported by specific fluorescent membrane probes (Ashdown and Owen, 2015; Colom et al., 2018; Niko et al., 2016) and more recently, heterogeneity of membrane thickness was directly observed by cryoEM (Cornell et al., 2020; Heberle et al., 2020). Additionally, the host plasma membrane, from which the viral membrane is derived, has an asymmetric composition of lipids where phosphatidylethanolamine (PE) and phosphatidylserine (PS) are actively sequestered on the inner leaflet and are only present on the outer leaflet in times of cellular stress (Lorent et al., 2020). In the HIV membrane, PS and PE are detectable in the outer leaflet of the membrane (Amara and Mercer, 2015; Callahan et al., 2003; Chua

et al., 2019; Huarte et al., 2016) and thus the asymmetry of the plasma membrane is assumed to be lost in viral particles.

Previously, we have shown that membrane fusion of Serinc5-containing HIV pseudoviruses is restored by incorporation of the exogenous lipid, Atto488-Dimyristoyl PE (DMPE), and the lipophilic antifungal drug, amphotericin B, while fusion of HIV particles containing the non-restricting paralogue, Serinc2, are unaffected (Ward et al., 2020). These data suggest Serinc5 restriction may be dependent on the lipid environment of the viral membrane. To address the hypothesis that Serinc5 alters lipid bilayer properties of the HIV envelope, we systematically investigate the chemical and physical properties of lipids required to overcome restriction by Serinc5 and the effects of Serinc5 incorporation on the order of the membrane of pseudoviral particles.

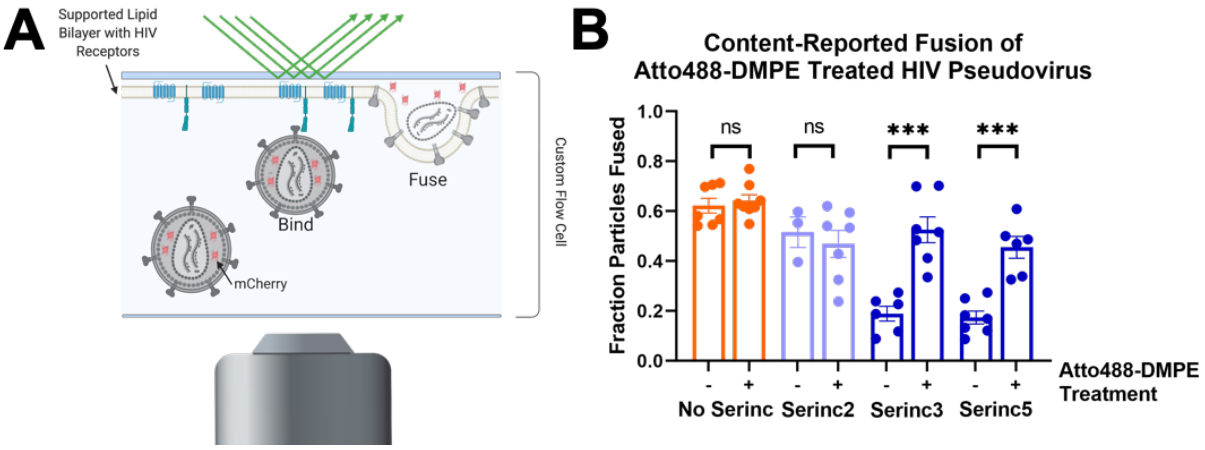

Figure 3.1: A. Diagram of TIRF-based single HIV pseudovirus particle fusion assay. Pseudovirus binding to a supported planar plasma membrane containing receptor and co-receptor is reported as a sudden appearance of bright puncta that remains stationary for several frames. Fusion is reported as a decrease in fluorescence over several frames as a genetically encoded content marker, mCherry, diffuses away. **B**. Incorporation of

Atto488-DMPE increases fusion of HIV pseudovirus particles containing Serinc3 and Serinc5 but does not affect fusion of particles containing Serinc2 or No Serincs. Data reproduced from Ward et al, 2020, with permission. *** $p<0.001$. Each data point represents the fraction of particles fused on a separately prepared bilayer. Each condition includes data from at least three distinct preparations of pseudovirus.

3.3 Results:

Treatment of HIV pseudovirus particles with exogenous PE restores membrane fusion, regardless of acyl chain length or saturation.

We used a previously described total internal reflection fluorescence (TIRF)-based, single-particle fusion assay to examine the effects of pretreatment of HIV pseudovirus particles with exogenous lipids (Figure 3.1A). Briefly, binding of pseudovirus particles engineered to incorporate an mCherry content marker to a supported planar plasma membrane containing CD4 and CCR5 is reported as the sudden appearance of punctate fluorescence. After remaining stably bound for several frames, the particle either fuses, as reported by a decay of fluorescence as the mCherry content diffuses away over multiple frames of recorded video, or becomes unbound from the membrane, reported by a sudden drop in fluorescence intensity back to baseline over a single frame. We previously used this assay to study fusion of HIV pseudoviruses labeled with Atto488-DMPE and found incorporation of the fluorescent lipid specifically increased fusion of Serinc5-containing HIV pseudoviruses (Figure 3.1B). DMPE modified at the headgroup with Atto488 is chemically distinct from unmodified DMPE so we assessed the effects of exogenous unmodified DMPE on fusion of HIV pseudoviruses incorporating Serinc5, Serinc2, or No

Serinc (Figure 3.2). Additionally, we compared the effects of acyl chain length and saturation by examining the fusion of pseudoviruses pre-treated with dipalmitoyl (DP), dioleoyl (DO), and palmitoyl-oleoyl (PO) PE. Both saturated (DMPE and DPPE) and unsaturated (DOPE) lipids increased fusion of Serinc5-containing pseudoviruses with only minimal effect on Serinc2 and No Serinc pseudoviruses. This indicates the restoration of fusion of Serinc5-containing pseudoviruses upon PE pretreatment is not caused by the Atto488 modification that was previously used, but is a function of the PE headgroup independent of acyl chain length or saturation. To further prove that the PE headgroup is critical to counteract the fusion restriction of Serinc5, we pretreated particles with palmitoyl-oleoyl-phosphatidylcholine (POPC) or POPS and found that these lipids had no effect on fusion of any of the pseudoviruses tested. While fewer particles incorporated fluorescently labeled PC than PE or PS (Supplemental Figure 3.S1A) and the amount of PC incorporated was lower than PE or PS (Supplemental Figure 3.S1B), PS incorporation was equal to PE incorporation yet still failed to increase fusion of Serinc5-containing particles, indicating the specificity of PE in overcoming Serinc5-restriction of HIV membrane fusion. Due to their smaller headgroup and hydrogen bonding capability, PEs are known to alter the lateral pressure profile and hence membrane tension in lipid bilayers (Fan et al., 2016).

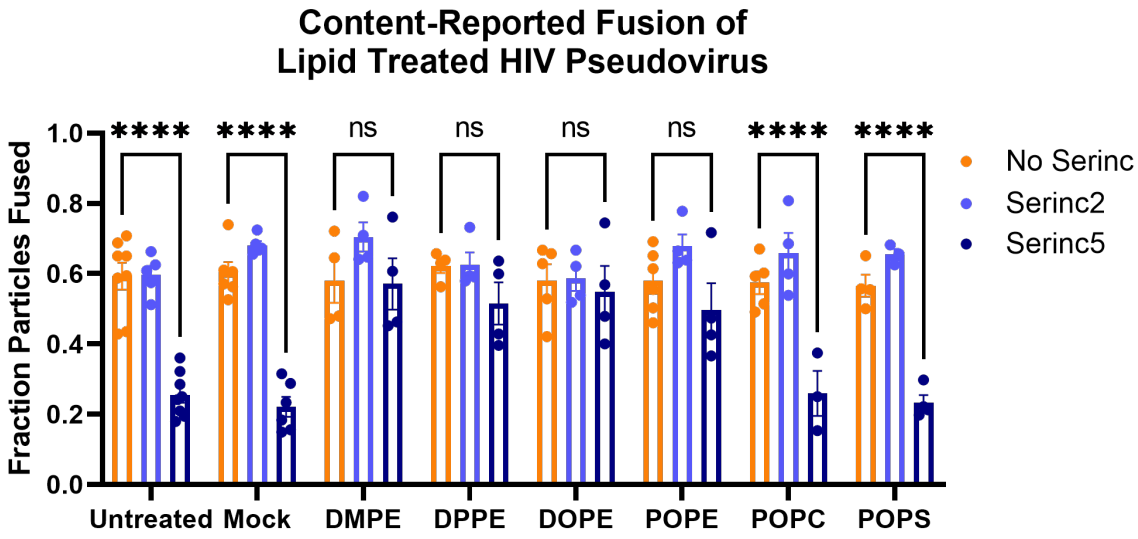

Figure 3.2: PE pretreatment of HIV pseudoviruses specifically overcomes restriction of fusion of Serinc5-containing particles. HIV pseudoviruses with or without Serincs were treated with the lipids listed on the X-axis, separated from free lipids, and fusion in a single-particle assay was assessed. A two-way ANOVA test was conducted to examine the statistical significance of the effects of Serinc incorporation and lipid treatment on HIV pseudovirus fusion. There was a statistically significant interaction between the two factors, $F(14, 88)=4.894$, $p<0.001$. Tukey's multiple comparisons test showed significant differences in the means of the comparisons shown above (**** $p<0.0001$, ns not significant). None of the No Serinc-Serinc2 comparisons were significant. Each data point represents the fraction of particles fused on a separately prepared bilayer. Each condition includes data from at least three distinct preparations of pseudovirus.

Serinc5 increases the portion of the viral membrane in an ordered lipid state

In order to examine if Serinc5 changes the order and tension of the lipid bilayer in the HIV envelope, we labeled pseudovirus particles with the fluorescent membrane dye

FLIPPER-TR. This push-pull fluorescent probe changes wavelength (red-shifted excitation) and has a longer lifetime in membranes with increased lipid order and higher lateral pressure (Colom et al., 2018; Dal Molin et al., 2015; Licari et al., 2020). FLIPPER-TR has been used as a reporter of membrane order not only in lipid model membranes but also in a variety of biological membranes in cells (Colom et al., 2018; Dal Molin et al., 2015; Goujon et al., 2019). To calibrate the FLIPPR-TR method for application to pseudoviruses, we first measured the fluorescence lifetimes of large unilamellar vesicles (LUVs) stained with FLIPPER-TR (Figure 3.3, left). LUVs were made of ternary lipid compositions previously reported to exist as all L_o, all L_d, or co-existing L_o/L_d phases (De Almeida et al., 2003; Ionova et al., 2012). As expected, we observed long, short, and intermediate average lifetimes for L_o, L_d, and L_o/L_d LUVs, respectively (Figure 3.3, left). HIV pseudoviruses were stained with FLIPPR-TR and imaged in the same manner by fluorescence lifetime (FL) microscopy. The lifetime of the dye in pseudovirus membranes without Serincs was similar to LUVs with coexisting L_o and L_d phases whereas the lifetime in pseudovirus membranes with Serinc5 was more comparable to LUVs in the L_o phase (Figure 3.3, right).

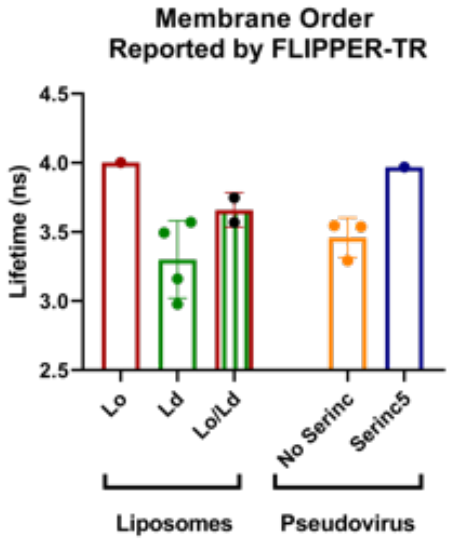

Figure 3.3: Fluorescence lifetimes of the lipid order sensitive membrane dye, FLIPPER-TR, in liposomes of defined lipid composition and in HIV pseudovirus particles. Liposomes of compositions known to exist solely in L_o (35/40/25, SM/chol/POPC), solely L_d (25/5/70, SM/chol/POPC), or as a mixture of L_o and L_d (40/20/40, SM/chol/POPC) phases were used as standards for comparison. Lifetimes were determined by FL microscopy and average lifetimes of a given field of view are plotted on the y-axis after background subtraction. Each data point is a field of view within a single sample.

Increased membrane order is usually accompanied by an increase in membrane thickness. However, it is not trivial to measure membrane thickness in biological membrane samples, especially if the membrane itself contains coexisting areas of variable thickness. This problem can be overcome by applying cryo-EM to LUVs and, under favorable conditions, to plasma membrane-derived blebs as has been recently shown by Heberle et al., 2020 and Cornell et al, 2020. In order to detect membrane

thickness changes in the envelopes of native HIV pseudovirus particles, we flash-froze such particles with Serinc2, Serinc5, or No Serincs and imaged them by cryoEM. The distance between the two lines of density, or "troughs," produced by the bilayer was measured in 5 nm membrane segments as described previously (Heberle et al., 2020). To calibrate our measurements of viral membrane thickness and to confirm consistency with published results, we added LUVs of a composition that is known to support coexistence of L_o and L_d domains (Figure 3.4A). In agreement with previously published data, we observed thicker and thinner portions of the lipid bilayer, indicative of coexisting L_o and L_d domains in the LUV model membranes. We also observed variations in thickness within the membrane envelopes of individual HIV pseudovirus particles although the height differences of thicker and thinner portions of the membrane were not as dramatic as in LUVs (Figure 3.4A). The majority of the membrane area of HIV pseudoviruses with Serinc2 appears thinner, and therefore, may be in a phase resembling the L_d phase of pure lipid LUVs (Figure 3.4A). In pseudoviruses containing Serinc5, we also observed a variation in the thickness of the membrane, but in this case a larger portion of the Serinc5-containing membrane appears thicker, resembling the L_o phase of pure lipid LUVs (Figure 3.4A). The mean bilayer thicknesses were similar for No Serinc and Serinc2 pseudoviruses but the distribution of Serinc5 pseudoviruses skewed towards thicker membranes (Figure 3.4B). This skewed distribution may be attributable to the known per particle variability in Serinc5 incorporation (Sood et al., 2017). The distribution of particle sizes is comparable for HIV pseudoviruses with and without Serincs and we detected no relationship between particle size and mean membrane thickness (Supplemental Figure 3.S2). Examining membrane thickness at a higher level

of granularity, the pseudoviral membrane segments did not fall into two easily discernible populations like the 2-phase LUV controls, but they were more broadly distributed than a single phase LUV (Figure 3.4C). These distributions include all segments from all particles within a preparation and thus collapses measurements taken on single particles to a bulk measurement. Similar to the per particle mean membrane thickness distributions, the Serinc5 distribution skews to a larger bilayer thickness.

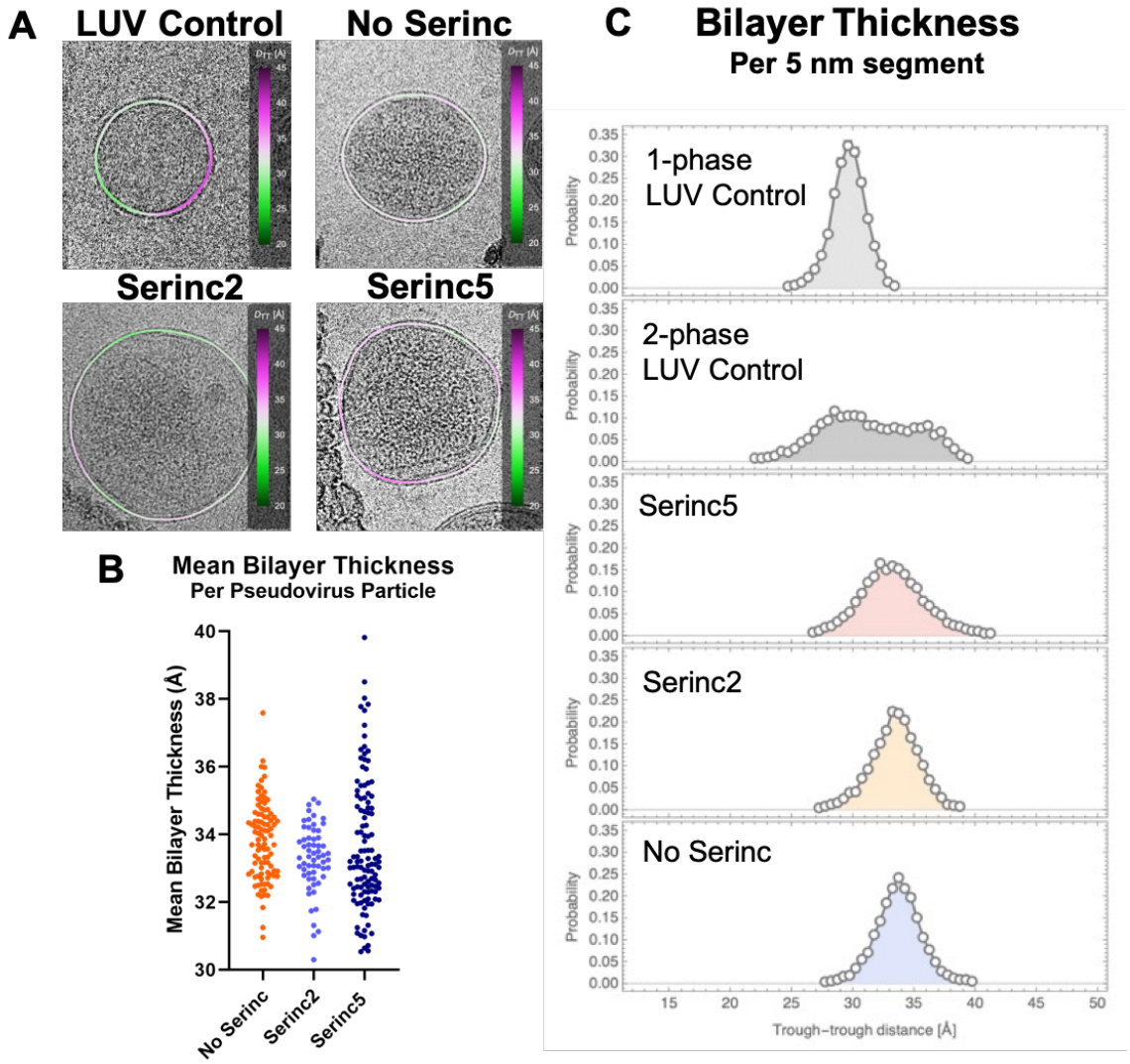

Figure 3.4: Serinc5 incorporation heterogeneously increases membrane thickness of HIV pseudovirus particles , as measured by cryoEM. **A**. Example micrographs with membrane thickness (D_{TT}) overlay of HIV pseudoviruses or LUVs composed of a 20/40/35/5 ratio of Chol/DPPC/DOPC/POPG as LUV control. The measured distances between intensity troughs (D_{TT}) for 5 nm segments of the membranes were plotted as a smoothed, colored overlay according to the scale on the right side of the image. **B.** Distributions of the mean membrane thickness of HIV pseudovirus particles. Each point represents one pseudovirus particle. **C.** Distribution of membrane thickness (D_{TT}) measurements of 5 nm segments of HIV pseudovirus or LUV membranes. 1-phase LUV control composed of DOPC and 2-phase LUV control composed of a 20/40/40 ratio of Chol/DPPC/DOPC. LUV distributions reproduced from Heberle et al., 2020. No Serinc and Serinc5 conditions include data from two independent preparations of pseudovirus. Serinc2 condition includes data from one preparation of pseudovirus.

3.4 Discussion:

In this study, we sought to understand the mechanism by which Serincs might restrict HIV Env-mediated membrane fusion and hence entry of HIV particles into cells. We previously established that Serincs 3 and 5, but not Serinc2, inhibit fusion pore opening and constrict the widening of the fusion "neck" of virus particles fusing with plasma membranes that were derived from HIV receptor and co-receptor expressing cells (Ward et al., 2020). The constricted fusion necks could not be explained by Serinc3/5's possible function as a lipid binding or translocating integral membrane protein (Pye et al., 2020; Trautz et al., 2017), nor by the observation that Serincs may alter Env

conformation or clustering (Beitari et al., 2017; Chen et al., 2020; Schulte et al., 2018; Sood et al., 2017; Staropoli et al., 2019). In an attempt to reveal how Serincs may inhibit virus entry, we employed recently described fluorescence and cryoEM methods to assess the importance of the viral membrane to the mechanism of Serinc5's inhibition of HIV membrane fusion. Our observation via two modalities that Serinc5 increases the order of HIV pseudoviral membranes (Figures 3.3 and 3.4) provides an important perspective for developing a complete understanding of Serinc5's function.

As a result of increased order, the Serinc5 viral membrane is stiffer, which increases the energy required to bend it into highly curved intermediates like hemifusion stalks, diaphragms, and fusion pores (Figure 3.5). Increased membrane stiffness has been shown to have an inhibitory effect on polyethylene glycol (PEG)-induced fusion (Fan et al., 2016). Additionally, increasing the area of the membrane in ordered domains alters line tension between domains and lateral tension in the viral membrane. Previous work has shown that in phase separated viral and target membranes, minimization of the energy of line tension drives HIV gp41-mediated fusion and that altering the circumference of ordered domains in the target membrane promotes or inhibits fusion as well (S.-T. Yang et al., 2016). Applying this simplified model to study the effect of increased ordered domain area in a viral membrane of 110 nm diameter, we found that increasing the fraction of the membrane in an ordered domain first increases and then sharply decreases the contribution of line tension to the free energy change of fusion (Supplemental Figure 3.S3). Thus, increased ordered domain area in a viral particle would be expected to decrease fusion. The final step of fusion, fusion pore expansion, is known to be dependent on lateral tension in the membrane (Kliesch et al., 2017; Kozlov

and Chernomordik, 2015; Shillcock and Lipowsky, 2005; Staykova et al., 2011). Using a tension-sensitive membrane probe (Colom et al., 2018; Dal Molin et al., 2015; Licari et al., 2020), we have demonstrated that tension is decreased in membranes of Serinc5 virus particles (Figure 3.3). Decreased lateral tension would be expected to inhibit fusion pore expansion resulting in the increased frequency with which we observed "early fusion products" with cinched membranes (Ward et al., 2020).

Our observation that PE selectively increases fusion of Serinc5-containing viruses (Figure 3.2) is further demonstration of the importance of altered membrane tension for Serinc5-mediated fusion inhibition. PE is known to enhance membrane fusion, especially when preferentially incorporated into the exterior leaflet of the membrane (Chernomordik and Kozlov, 2005; Churchward et al., 2008; Kreutzberger et al., 2017). As a wedge-shaped molecule, PE induces frustrated negative curvature in the pre-fusion membrane, increasing lateral tension in the headgroup region (Fan et al., 2016). Furthermore, if the curvature of ordered and disordered domains differ, their interface would be highly curved (Baumgart et al., 2003). PE's intrinsic curvature may enable it to partition to the domain boundary, thereby altering the energetic contribution of line tension to the fusion reaction although this is speculative. The specific increase in fusion of Serinc5-containing viruses demonstrates that Serinc5 alters membrane tension, which is reversed by addition of exogenous PE.

We have also observed coexistence of ordered and disordered domains in HIV pseudoviral membranes which, to our knowledge, is the first time phase separation has been directly observed in a viral membrane. Bulk measurements of lipid order of HIV particles has shown it is largely ordered but depends on the producing cell line (Lorizate

et al., 2009). Phase separation has been observed in supported lipid bilayers made from viral membrane lipid extracts (Huarte et al., 2016) but never intact viral particles.

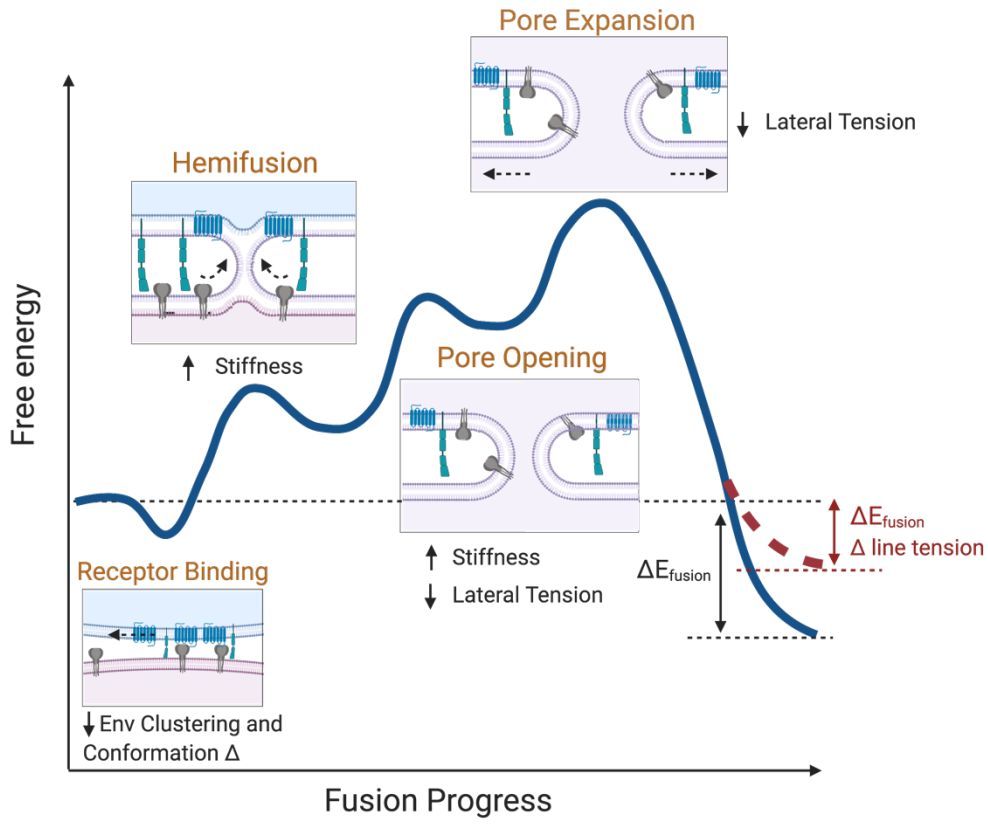

Figure 3.5: Theoretical model of energetic changes to fusion resulting from Serinc5-induced ordering of the viral membrane. The free energy change of intermediate steps along the fusion reaction (orange titles) is shown by the blue line. Proposed effects of Serinc5-induced alteration of membrane order are listed in black below each intermediate state although many of these properties are inter-related. The effect of increased order on the contribution of line tension to the energetics of fusion is shown by the red dashed line. Intermediate states are written in orange letters. Proposed effects of Serinc5-induced membrane alterations written in black under the applicable intermediate state or in red for the global changes.

It was known that both Env and Serinc5 partition into ordered membrane domains (Schulte et al., 2018; Schwarzer et al., 2014) and that Serinc5 disrupts clustering on Env in the viral membrane (Chen et al., 2020). If clustering in the mature viral envelope is driven by confinement of Env to ordered domains, increasing the area of ordered domains could result in a loss of clustering. This is similar to the observation of lipid domain-driven clustering of Influenza A hemagglutinin (Domanska et al., 2015; Goronzy et al., 2018) but HIV particles have only 7-10 trimers per particle (Klein and Bjorkman, 2010; Zhu et al., 2006, 2003) as compared to Influenza's 300-400 trimers per particle (Harris et al., 2006; Yamaguchi et al., 2008) making HIV even more reliant on Env clustering for efficient fusion. Furthermore, the conformation of Env is known to be dependent on its lipid environment (Salimi et al., 2020). Thus Serinc5-induced alteration of the local lipid environment would also be expected to cause conformational changes in Env as have been observed (Schulte et al., 2018; Staropoli et al., 2019). It is telling that the strongest effect of Serinc5 incorporation on antibody binding to Env is on antibodies directed to the membrane proximal external region (MPER) (Beitari et al., 2017; Sood et al., 2017). Many monoclonal antibodies that recognize MPER also include the neighboring lipid headgroups in the binding site (Chen et al., 2014; Rantalainen et al., 2020) so altered membrane thickness and local composition would also be expected to affect anti-MPER binding. As noted previously, changes in the function of Env would only be expected to affect the early steps of membrane fusion that are dependent on conformational rearrangements of Env. Changes to the properties of the viral membrane could also explain the observed defects in progression of the later stages of fusion.

Previously, we hypothesized that Serinc5 would need to cause "broad energetic changes" to the membrane fusion process to accumulate arrested intermediates at every step, as we observed (Ward et al., 2020). With the data presented in this work, we provide details as to how Serinc5 can alter one property of the virus and disrupt nearly every aspect of fusion, lending context to previous work in the field.

3.5 Materials and Methods:

Cell lines, reagents, and plasmids: HEK 293T/17 cells (ATCC) were maintained in high glucose Dulbecco's Minimum Essential Media (Gibco) supplemented with 10% fetal bovine serum (Atlanta Biologicals), 1% antibiotic-antimycotic (Gibco), 1 mM sodium pyruvate (Gibco), and 2 mM glutamine (Gibco). CD4 and CCR5 overexpressing HeLa cells (gift of David M. Rekosh, University of Virginia) were maintained in Iscove's Modified Dulbecco's Medium (Gibco) supplemented with 10% fetal bovine serum and 1% antibiotic/antimycotic with 0.5 mg/mL of G418 (Gibco), and 1 μg/mL puromycin. All cells were maintained at 37°C with 5% CO_2 atmosphere.

pHIV-luciferase, pHIV-Rev, and pHIV-pack were gifts of Wen Yuan (University of Virginia). pHIV-Env-SF162 was provided by the AIDS Reagent Program. pHIV-imCherry (Sergi et al., 2013) was a gift of Gregory Melikian (Emory University). pPBJ5-Serinc2-HA was a gift of Massimo Pizzato (University of Trento) and pPBJ5-Serinc5-HA was a gift of Heinrich Gottlinger (University of Massachusetts Medical School, Worcester).

The following compounds were purchased from Avanti Polar Lipids and used without modification: brain phosphatidylcholine (bPC), egg sphingomyelin (SM), 1-palmitoyl-2-oleoyl-sn-glycero-3-phosphoethanolamine (POPE), 1,2-dioleoyl-sn-glycero-3-phosphoethanolamine (DOPE), 1,2-dimyristoyl-sn-glycero-3-phosphoethanolamine (DMPE), 1,2-dipalmitoyl-sn-glycero-3-phosphoethanolamine (DPPE), 1-palmitoyl-2-oleoyl-glycero-3-phosphocholine (POPC), 1,2-dipalmitoyl-sn-glycero-3-phosphocholine (DPPC), 1-palmitoyl-2-oleoyl-sn-glycero-3-phospho-L-serine (POPS), 1-palmitoyl-2-oleoyl-sn-glycero-3-phospho-(1'-rac-glycerol) (POPG), 1-palmitoyl-2-{6-[(7-nitro-2-1,3-benzoxadiazol-4-yl)amino]hexanoyl}-sn-glycero-3-phosphocholine (NBD-PC), 1-palmitoyl-2-{6-[(7-nitro-2-1,3-benzoxadiazol-4-yl)amino]hexanoyl}-sn-glycero-3-phosphoserine (NBD-PS), and 1-palmitoyl-2-{6-[(7-nitro-2-1,3-benzoxadiazol-4-yl)amino]hexanoyl}-sn-glycero-3-phosphoethanolamine (NBD-PE). Cholesterol was purchased from Sigma-Aldrich. 1,2-dimyristoyl-*sn*-glycero-3-phosphoethanolamine-PEG3400-triethoxysilane (DPS) was synthesized as described previously (Wagner and Tamm, 2000).

HIV pseudovirus preparation: HIV pseudoviruses were produced as described before by transfection of HEK 293T cells (ATCC) with Lipofectamine 2000 (Invitrogen) and the following amounts of plasmids per 10 cm dish: 13 μg pHIV-luciferase, 5 μg pHIV-pack, 4 μg pHIV-Env-SF162 (Cheng-Mayer et al., 1997; Stamatatos et al., 2000, 1998), 4 μg pHIV-imCherry, 1 μg pHIV-Rev and 4μg of pBJ5-Serinc2-HA (Rosa et al., 2015) or pBJ5-Serinc5-HA (Usami et al., 2015) as indicated in text. Culture media was changed 4-6 hours after transfection to phenol-red free DMEM supplemented with 10% FBS, 1% antibiotic-antimycotic, 1 mM sodium pyruvate, and 2 mM glutamine. Culture

supernatants were harvested 2 days after transfection and cleared by centrifuging 5000xg before passing through a 0.22 μm filter. HIV pseudoviruses were pelleted through a 25% sucrose-HME (20 mM HEPES, 20 mM morpholineethanesulfonic acid [MES], 130 mM NaCl, 1 mM EDTA [pH 7.4]) cushion as previously described (Hulseberg et al., 2019) and resuspended in buffer HME without sucrose. Pseudovirus preparations for cryoEM were further purified by density dependent centrifugation on a discontinuous sucrose gradient composed of 65% sucrose-HME and 25% sucrose-HME spun 151,000xg for 18 hours. Pseudovirus was collected from the 65%/25% sucrose interface, diluted in buffer HME without sucrose, and repelleted through a 25% sucrose cushion. After resuspension in buffer HME without sucrose, the pseudovirus preparation was aliquoted and stored at -80°C. Additionally, the concentration of HIV p24 in each preparation was measured by ELISA (Toohey et al., 1995; Wehrly and Chesebro, 1997) and used to normalize the amount of pseudovirus added to downstream experiments.

Lipid pre-treatment of viruses: 10^{-10} moles of the indicated lipid were dried on the bottom of a glass test tube to remove chloroform/methanol solvent and resuspended by vigorous vortexing in buffer HB (20 mM HEPES, 150 mM NaCl [pH 7.4]) to yield a concentration of 1.4 μM. 21 ng of HIV pseudovirus, as measured by p24 ELISA, was mixed with the lipid suspension. The mixture was incubated at room temperature for 2 hours on a rotary spinner. To remove free lipid, the HIV pseudovirus mixture was diluted up to 1.5 mL in buffer HB and pelleted by spinning at 21,000xg for 1 hour at 4°C before final resuspension in buffer HB. Lipid-treated HIV pseudoviruses were used within 24 hours.

Large unilamellar vesicle preparation: Chloroform stocks of desired lipids were mixed and the solvent was evaporated under a gentle stream of nitrogen gas. The resulting lipid film was desiccated under vacuum for at least one hour before resuspension in buffer appropriate to the experiment to a final concentration of 1 mM. After vortexing at room temperature, the lipid suspension was subjected to 10 freeze/thaw cycles in liquid nitrogen and warm water before extrusion through two 100 nm polycarbonate membranes (Avestin). Resulting LUVs were stored at 4°C and used within 24 hours of extrusion.

Plasma membrane bleb preparation: Blebs were produced from HeLa cells overexpressing CD4 and CCR5 by previously published methods (Sezgin et al., 2012; Yang et al., 2017). Briefly, when cells reached 90% confluence, they were washed twice with blebbing buffer (10 mM HEPES, 150 mM NaCl, 2 mM $CaCl_2$, pH 7.4) and blebbing was induced by replacing buffer on the cells with 5 mL of 25 mM formaldehyde (J.T.Baker) and 2 mM dithiothreitol (DTT) diluted in blebbing buffer and incubating the cells at 37°C, 5% CO_2 for 1 hour. After an hour, blebs were detached from cells by shaking on a radial shaker at room temperature for 1 hour before the supernatant was collected and cleared of large cell debris by centrifuging at 100xg for 10 minutes. Blebs were pelleted at 20,000xg for 1 hour and washed twice in blebbing buffer without DTT or formaldehyde.

TIRF supported lipid bilayer fusion assay: Supported planar plasma membranes derived from blebs were prepared as previously described (Kalb et al., 1992; Wagner and

Tamm, 2000; Yang et al., 2017). Quartz slides were cleaned in piranha solution (95% H_2SO_4 and 30% H_2O_2 in a 3:1 ratio) and rinsed in 12 liters of deionized water. Next, a lipid monolayer composed of 4:1 brain phosphatidylcholine and cholesterol (Avanti Polar Lipids) with 3% 1,2-dimyristoyl-*sn*-glycero-3-phosphoethanolamine-PEG3400-triethoxysilane was deposited on the quartz slide by the Langmuir-Blodgett method. A chloroform solution of the lipid mixture was applied to a Nima 611 Langmuir-Blodgett trough and after letting the solvent evaporate for 10 minutes, the lipid layer was compressed at a rate of 10 cm^2/min to a pressure of 32 mN/m. A cleaned, rinsed, and dried quartz slide was rapidly dipped (68 mm/min) and slowly removed (5 mm/min) from the trough and then dried in a desiccator chamber overnight.

The slide was then assembled into a custom-built microscopy flow cell and plasma membrane blebs diluted in blebbing buffer without DTT or formaldehyde were flowed in to form the outer leaflet of the supported planar plasma membrane. After 1-2 hours at room temperature, the flow cell was washed with multiple volumes of blebbing buffer, then multiple volumes of buffer HB, and transferred to a prism-based TIRF microscope (Zeiss AxioObserver Z1). The sample was excited with a 561nm diode laser (OBIS 561 nm LS, Coherent) at an angle of 72 degrees from normal and emission light was filtered through a dichroic mirror (DC565, Semrock) and a band-pass filter (BP605/50, Semrock). Video was recorded by an EMCCD (DV887ESC-BV, Andor Technology) in frame transfer mode with an exposure time of 0.2 s for 13.3 minutes as a dilution of HIV pseudovirus totaling 21 ng of p24 as measured by ELISA was flowed into the chamber.

Laser intensity, shutter, and camera were controlled by a custom LabView program (National Instruments).

Intensities of single particles over time were extracted with a custom-built LabView program and classified as representing binding without fusion or binding with fusion based on the criteria described in Ward et al, 2020.

FLIM data acquisition and analysis: HIV pseudoviruses and LUVs were stained with 500 nM FLIPPER-TR for 3 hours at room temperature before pelleting at 26,200xg at 4°C for 1 hour to remove free dye. Pseudoviruses and LUVs were resuspended in buffer HB and added to a coverslip cleaned with piranha solution and treated with CellTak. After liposomes and pseudoviruses were allowed to adhere for 30 minutes, unbound sample was washed in buffer HB before fixation with 4% formaldehyde for 10 minutes, quenching with 1% glycine for 5 minutes and washing in buffer HB before mounting in Prolong Gold antifade (Invitrogen). Stained and mounted samples were imaged on a Leica Stellaris8 microscope with FALCON software. Background was subtracted and lifetime for the field of view was fit with two components. Only the longer component is displayed.

CryoEM of HIV pseudovirus particles: C-Flat 2/2-3C or 1.2/1.3-3C grids (Electron Microscopy Sciences) were glow discharged at 10 mA for 90 seconds. A suspension of HIV pseudovirus in buffer HME was applied and blotted from the grid before freezing in liquid nitrogen cooled ethane. For initial experiments, LUVs composed of 20/40/35/5

Chol/DPPC/DOPC/POPG were spiked into the pseudovirus suspension before freezing to serve as internal standards for quality control. The grids were imaged on a Titan Krios electron microscope operating at 300 kV equipped with a K3/GIF (Gatan) and controlled by EPU software (ThermoFisher Scientific). Magnification was 33,000X, which yielded a pixel size of 2.7 Å. As described in Heberle et al., 2020, the optimal total dose was set at 13.8 e/Å^2. Micrographs were motion corrected with MotionCorr2 (Zheng et al., 2017) (10 by 10 patch for 10 iterations with a tolerance of 0.5, dose weighted) before analysis of trough-to-trough distance as described previously (Heberle et al., 2020).

3.6 Supplemental Figures:

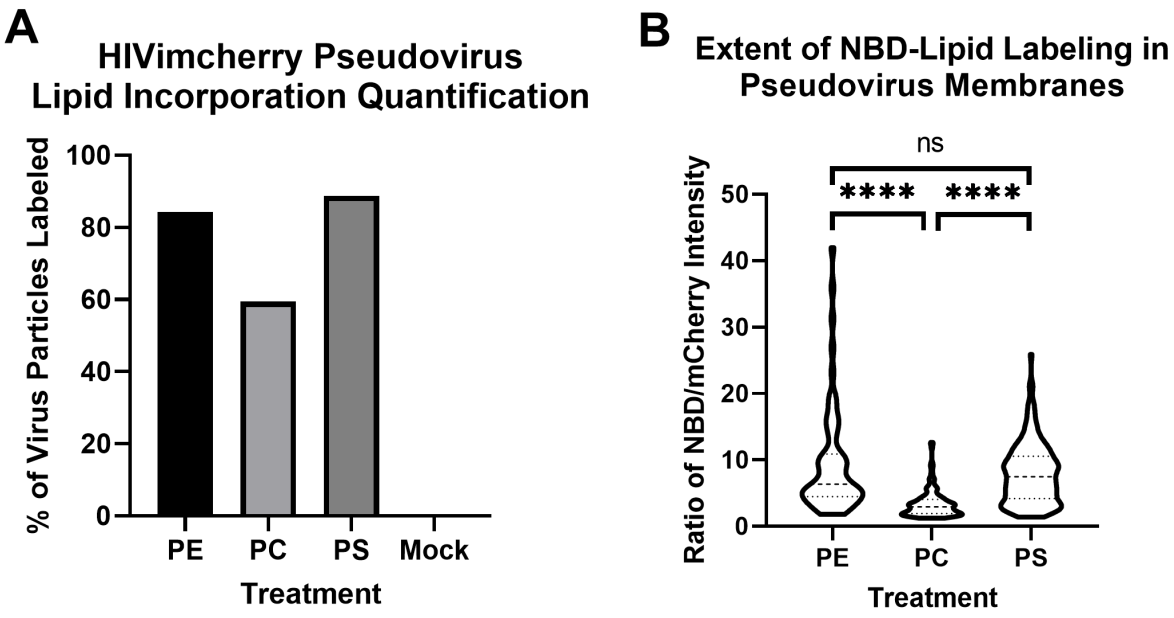

Supplemental Figure 3.S1: Incorporation of exogenous lipids into HIV pseudoviruses. HIV pseudoviruses were treated with an NBD acyl chain version of the phospholipid listed on the X-axis. **A.** The percentage of particles (defined as mCherry

fluorescent region of interest) exhibiting NBD fluorescence. **B.** The ratio of NBD to mCherry fluorescence intensity of the particles that had incorporated NBD-lipid is plotted as a proxy for relative amount of exogenous lipid incorporated into the viral membrane. The dashed line is the median and the dotted lines are quartiles. **** $p<0.0001$, ns not significant.

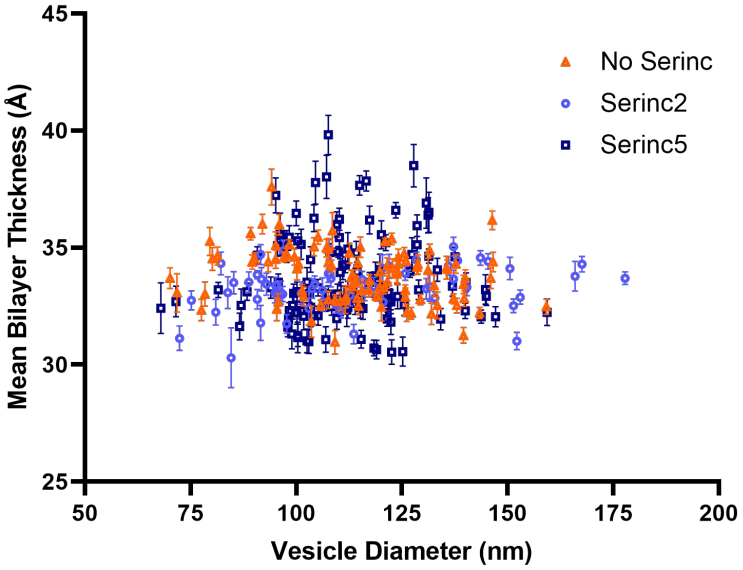

Supplemental Figure 3.S2: Relationship between size distribution and membrane thickness for HIV pseudoviruses imaged by cryoEM. The diameter of the pseudovirus membrane contour was plotted against the mean bilayer thickness for each particle analyzed in Figure 3.4.

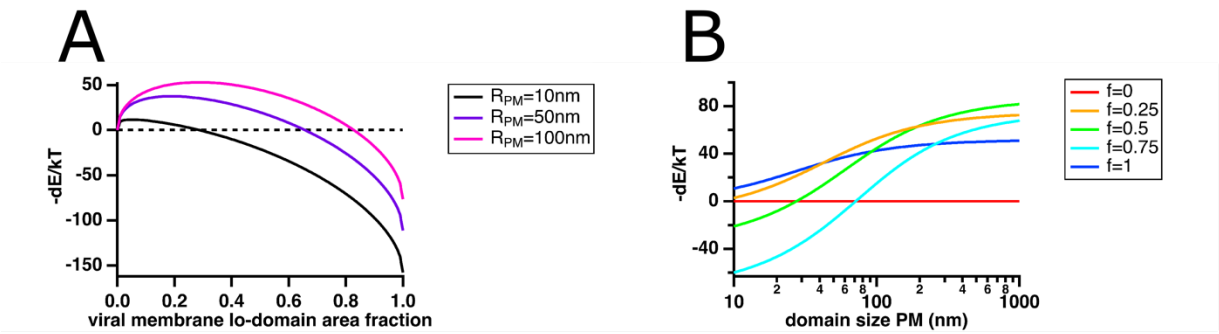

Supplemental Figure 3.S3: Contribution of line tension to energy change of fusion. Based on the model described in Yang et al., 2016, the effect of increasing the fraction of the viral membrane in a single ordered domain on the contribution of line tension to the energy change of fusion is plotted in panel **A**. The radius of the virus was held constant at 55 nm and the radius of domains in the plasma membrane were varied from 10 to 100 nm as shown in the key. Positive values of -dE/kT (above the x-axis) favor fusion. In panel **B**, the effect of increasing domain fraction and size in the plasma membrane is plotted. The radius and L_o domain area fraction of the viral membrane are held constant at 55 nm and 0.5 respectively.

CHAPTER 4: Fluid semi-supported lipid bilayers for cryo-electron microscopy

4.1 Abstract:

Supported lipid bilayers (SLBs) on hydrophilic solid substrates are useful model systems with a simplified planar geometry for studying membranes and their functions. To take advantage of the recent advances in cryo Electron Microscopy (cryoEM) we have developed a method to create SLBs on commercially available holey carbon grids used for cryoEM. These membranes span the carbon support film and its holes and thus, we have named them semi-supported lipid bilayers (SSLBs). SSLBs have similar properties to SLBs and we show that lipids in SSLBs can phase separate and diffuse freely over the carbon film and the holes. Like other SLBs, SSLBs can be created with a range of lipid and protein compositions, including asymmetric leaflet compositions, biological membrane preparations, and recombinant integral membrane proteins. Additionally, we demonstrate the utility of SSLBs for studying membrane protein oligomerization, membrane association of soluble proteins, and membrane deformation by protein assemblies. While not amenable to all cryoEM-based applications, SSLBs allow higher-resolution visualization of membrane behavior and processes.

4.2 Introduction:

Lipid membranes and their emergent properties influence the structure, assembly, and function of membrane proteins, which in turn, cooperatively contribute to the organization of the membrane (Cournia et al., 2015; Levental et al., 2020). Supported lipid bilayers (SLBs) are useful models for observing these behaviors of lipids and proteins in controlled, reconstituted systems (Tamm and McConnell, 1985). Their planar geometry simplifies many experiments and they have been created with a broad range of compositions—synthetic lipids, recombinant membrane proteins, and biological preparations of membranes (Richards et al., 2016; Sezgin et al., 2020; Yang et al., 2017)—representative of the diverse physiological functions they have been used to model. SLBs are amenable to observation with a variety of techniques ranging from fluorescence microscopy (Floyd et al., 2008; Kiessling et al., 2017; Liu et al., 2017), electrophysiology (Khan et al., 2017), surface plasmon resonance (Barros et al., 2016; Terrettaz et al., 1993), quartz crystal microbalance (Cho et al., 2010; Nielsen and Otzen, 2019), to atomic force microscopy (AFM) (Levy and Milhiet, 2013), allowing the observation of phenomena across scales and modalities. However, the most common modality, fluorescence microscopy, is limited in resolution by the Abbe diffraction limit of visible light (Abbe, 1873). Certain super-resolution techniques are able to achieve resolutions below this theoretical limit (B. Huang et al., 2010) and AFM routinely achieves sub-nanometer resolution (Ando, 2019; Uchihashi and Scheuring, 2018) but cryo Electron Microscopy (cryoEM) allows yet higher resolution than either of these techniques. In this work we aim to adapt SLBs to take advantage of the recent advances in cryoEM.

CryoEM allows observation of fully hydrated biological samples frozen in very thin vitreous ice and has been used to image small vesicles (Wytrwal et al., 2014), suspensions of membrane proteins in small membrane mimetics (detergent micelles (Linke, 2009), vesicles (Liu and Sigworth, 2014), nanodiscs (Kern et al., 2019; Ritchie et al., 2009; Schuler et al., 2013), and lipodisqs (Knowles et al., 2009)), ion-milled cellular lamellae (Albert et al., 2020; Bykov et al., 2017; Guo et al., 2018), and lipid monolayers (Bischler et al., 1998; Hemming et al., 1995)), which have yielded a wealth of information about membrane protein structure, protein-lipid interactions, and lipid organization in membranes. Most of these cryoEM modalities are well suited to determination of high-resolution structures, but are either highly artificial systems divorced from larger biological assemblies or, like cryo Electron Tomography (cryoET) of focused ion beam (FIB) milled cells, are low throughput. While cryoET is a powerful technique for visualizing protein structures and assemblies *in situ*, it can be difficult to interpret data about one protein of interest in a busy cellular environment (Turk and Baumeister, 2020). Here we describe a method to create fluid semi-supported lipid bilayers (SSLBs) on EM grids to serve as a complementary and more accessible technique for reconstituting biological phenomena and studying membranes by cryoEM. While SSLBs are a more artificial system than cellular cryoET and not well suited for high resolution protein structure determination, reconstitution allows observation of biological assemblies under controlled conditions where the effect of a single factor can be assayed.

Pore spanning membranes have been prepared on specially fabricated aluminum, gold, and silicon oxide supports with regularly patterned holes for fluorescence and

atomic force microscopies (Hennesthal et al., 2002; Schwenen et al., 2015; Sibold et al., 2020; Steltenkamp et al., 2006) so we adapted these methods for commercially available holey carbon grids used for cryoEM. Lipid monolayers have been deposited on grids to serve as templates for crystals (Chiu et al., 1997; Lévy et al., 1999; Uzgiris and Kornberg, 1983; Yeager et al., 2013) or as a substrate for protein complex purification (Janknecht et al., 1991). For these techniques, a solution of lipids in a volatile organic solvent is added to a droplet of water to apply lipids at the air/water interface with a spontaneous orientation of hydrophobic tails towards air and with hydrophilic heads towards the water. The aligned lipids are then deposited onto a hydrophobic carbon support film on an electron microscopy sample grid with tails facing the support. Others have used a Langmuir-Blodgett trough in a similar manner although they dipped a grid through the air/water interface in the Langmuir-Blodgett method. This created bilayers in holes of the support separated by areas of monomer over the support, similar to black lipid membranes (Mcalduff et al., 2002).

We aimed to create a continuous bilayer amenable to protein incorporation from various membrane preparations (Figure 4.1A) and thus modified these techniques, flipping the orientation of the monolayer by converting a hydrophobic holey carbon film into a positively charged hydrophilic surface and using a Langmuir trough to orient lipids and control lateral pressure as we deposit a lipid monolayer by gently placing a grid on the air/water interface (Figure 4.1B). Additionally, we use a tethered silane-modified PEG cushion to create a water filled cleft between lipid monolayer and carbon film to ensure membrane proteins in the bilayer are unconstrained by irregularities in the surface of the carbon film (Wagner and Tamm, 2000). The polymer supported monolayer is dried

before a second leaflet is created by vesicle fusion in the presence of calcium (Kalb et al., 1992). This sequential construction of a lipid bilayer allows creation of asymmetric membranes and allows customization as needed for an experiment. In this paper, we demonstrate construction of protein-free asymmetric lipid bilayers, plasma membrane-derived asymmetric lipid bilayers, and membranes incorporating a recombinant integral membrane protein. We evaluate the quality of these bilayers based on their mobility, ability to phase separate, incorporation of known lipids and proteins, and reconstitution of biochemical assemblies. We also demonstrate their application to study protein association and assembly on lipid bilayers as relevant for antimicrobial peptide development and elucidation of the mechanism of membrane bending during HIV budding.

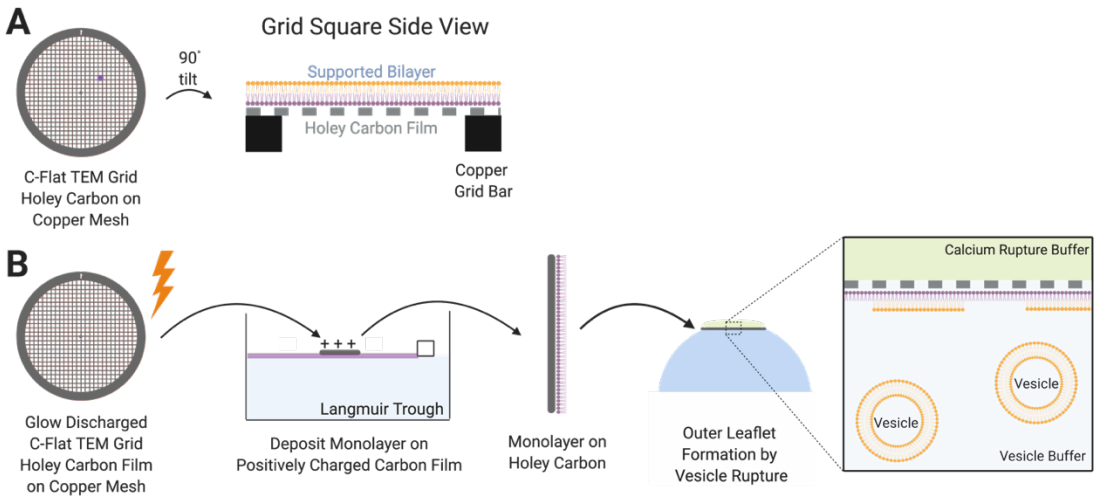

Figure 4.1: Schematic of semi-supported lipid bilayers on EM grids and general protocol for their preparation. A. Cartoon of an EM copper grid and side view of a square showing the end result: a semi-supported lipid bilayer with different lipid compositions in the two leaflets spanning carbon-supported and free-standing areas over

the carbon holes. **B.** Cartoon of the method for the preparation of the semi-supported lipid bilayer by sequential formation of a supported lipid monolayer on a Langmuir trough and formation of the distal monolayer by vesicle, proteoliposome, or plasma membrane bleb fusion on commercially available EM grids with holey carbon films.

4.3 Results:

Leaflet asymmetry and phase separation in fluid SSLBs on EM grids

To confirm that we had constructed a supported bilayer as we aimed to, we observed the EM grid bilayer via confocal fluorescence microscopy, a modality where membrane appearance and behavior is well characterized (Honigmann et al., 2010; Kiessling et al., 2015b; Sibold et al., 2020). In a bilayer composed of a fluorescent lipid mixture known to phase separate (33:40:20:2:2 brain phosphatidylcholine (bPC): brain sphingomyelin (bSM):cholesterol (chol):biotin-Dipalmitoylphosphatidylethanolamine (DPPE):Rhodamine-DPPE +3% DPS) we observed areas of bright fluorescence that spanned holes in the carbon support film but not the copper grid bars (Figure 4.2A). Within the bright squares, there are approximately circular areas of darkness where the fluorescent lipid is excluded which are likely ordered lipid domains. These domains are highly mobile and we have observed them fuse together into larger domains (Supplemental Video 1). The same grid was vitrified and imaged by cryoEM (Figure 4.2B). Ni-DGS, a nickel chelating lipid, was previously incorporated into the outer leaflet of the bilayers to provide contrast for cryoEM. Micrographs of SSLBs made with the phase separated mixture showed continuous dark areas of higher electron density that span holes in the carbon support film. Within the bilayer areas, there are areas of even

higher density where the Ni-lipid is concentrated in domains (white arrows). Lipid domains are expected to be preserved in flash frozen samples for cryoEM as vitrification occurs so rapidly that even water molecules cannot undergo a phase transition (Dubochet et al., 1987). The areas of highest density, thought to be ordered domains, are absent from SLBs prepared from a mixture of lipids that does not phase separate (Figure 4.2C). In both phase separated and non-phase separated grids, the bilayer is not perfectly continuous as shown by the edges of the nickel-containing second leaflet (Figure 4.2B and C, black arrows), but importantly, the bilayer does span holes in the carbon support film without discernable changes.

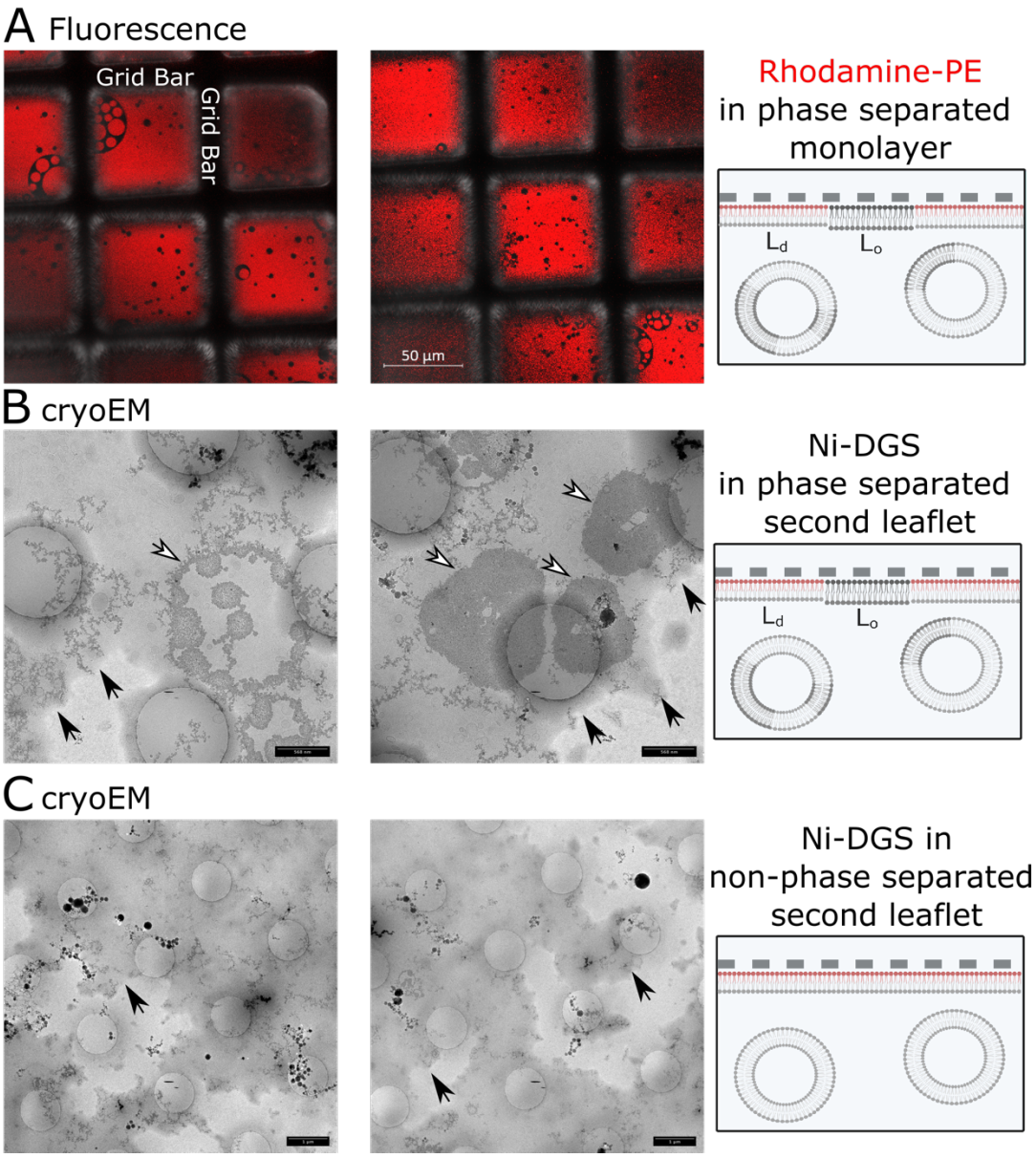

Figure 4.2: Semi-supported lipid bilayers on holey carbon films exhibit similar properties as bilayers on continuous supports. A. Confocal fluorescence images of a SLB grid suspended in buffer in a petri dish with coverslip glass bottom. The monolayer is composed of bPC:bSM:chol:Biotin-DPPE:Rhodamine-DPPE:DPS in a 33:40:20:2:2:3 ratio. The second leaflet was formed from 50 nm small unilamellar vesicles (SUVs) composed of bPC:bSM:chol:Ni-DGS in a 38:40:20:2 ratio. Overlay of red, Rhodamine-PE fluorescence, and gray, differential interference contrast (DIC) micrographs. Scale bar

is 50 μm and grid spacing is the same between images. **B.** Same grid as in A vitrified and imaged by cryoEM. Black arrows, edge of bilayer. White arrows, dark patches with an increased concentration of Ni-DGS. Carbon foil holes are 1.2 μm in diameter for scale. **C.** SLB grid prepared in parallel with grid shown in A and B. The first leaflet monolayer is composed of bPC:cholesterol:Rhodamine-DPPE:DPS in a 72:20:5:3 ratio. The second leaflet monolayer was formed from 50 nm SUVs composed of bPC:cholesterol:Ni-DGS in a 78:20:2 ratio. Black arrows, edge of bilayer. Circular holes in carbon film are 1.2 μm in diameter for scale.

SSLBs on EM grids incorporate plasma membrane components

To demonstrate the utility of SSLBs for reconstituting preparations of biological membranes, we used plasma membrane blebs to form the second leaflet of the bilayer as has previously been done for more conventional applications of SLBs (Ward et al., 2020; Yang et al., 2017). To easily confirm that plasma membrane proteins are incorporated into the SLBs on grids, blebs were surface biotinylated before their addition to the monolayer. The sulfo-NHS-LC-biotin reagent used is membrane impermeable and attaches a biotin and chemical linker to primary amines, which would include proteins and phosphatidylethanolamine (PE) exposed on the outer leaflet of bleb membranes. Bilayer incorporation of biotinylated components was detected by binding streptavidin-gold nanoparticles before freezing and imaging by cryoEM (Figure 4.3A). In the bilayers made from biotinylated blebs, gold nanoparticles were observed both over carbon and in grid holes (Figure 4.3B). Fewer gold nanoparticles were observed in SLBs created from blebs that had not been biotinylated (Figure 4.3C) but were not completely absent. This

is due to difficulties of washing a fragile membrane to fully remove unbound nanoparticles. These representative micrographs are supported statistically by the larger number of gold nanoparticles observed over holes in the carbon support (Figure 4.3D) and in fields of view containing hole and carbon support (Figure 4.3E). While biotinylation cannot report on which orientation or conformation proteins adopt upon SSLB incorporation, these data show plasma membrane components are incorporated into SSLBs on holey carbon grids. Based on previous experience, with very similar systems in a conventional SLB format, we think that most gold particles attached to the carbon-distal side of the membrane.

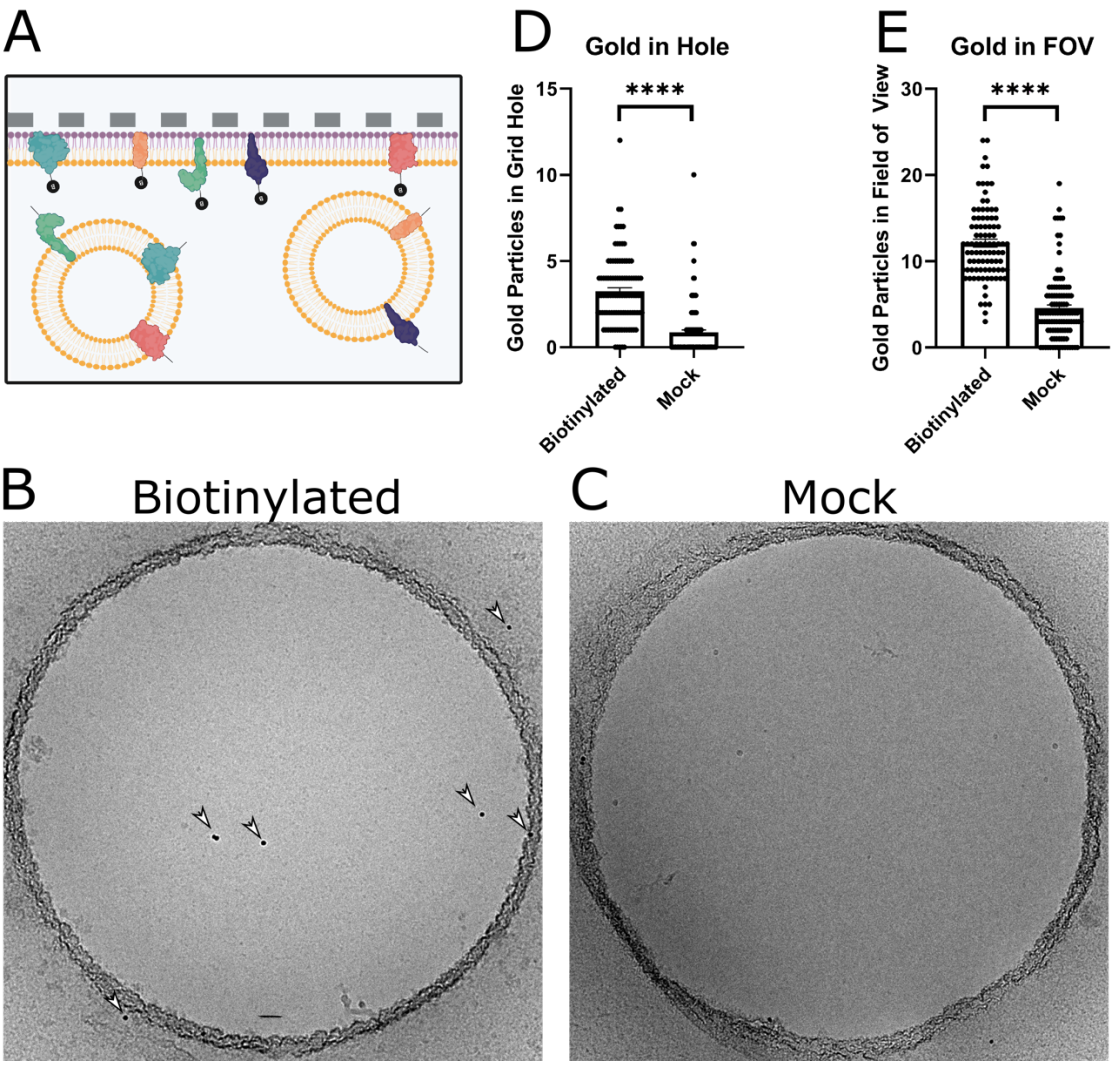

Figure 4.3. SSLB on grids can incorporate plasma membrane components. A. Cartoon depicting formation of an SSLB formed from a monolayer composed of bPC:cholesterol:DPS in a 77:20:3 ratio and a second leaflet formed from plasma membrane blebs that had been surface biotinylated by EZ-link Sulfo-NHS-LC-Biotin or mock treated. After SSLBs were formed and unincorporated excess blebs were washed away, streptavidin-gold 5 nm nanoparticles were added to both types of grids. Unbound gold was washed before vitrification. **B.** and **C.** Example micrographs of membranes made from biotinylated or mock treated blebs. White arrows point to streptavidin gold

nanoparticles. Hole diameter is 1.2 μm for scale. **D.** The number of gold particles visible in a carbon foil hole was counted in 101 and 111 exposures of biotinylated and mock treated grids respectively. Data are combined from three separate experiments. **E.** In the same images as D, the number of gold particles visible in the entire field of view (25,000x magnification centered on foil hole) were counted. These counts include gold nanoparticles over carbon and in the foil hole. **** $p<0.0001$ by unpaired t-test with Welch's correction.

SSLBs containing a recombinant integral membrane protein

OprG is a protein in the outer membrane of the bacterium, *Pseudomonas aeruginosa,* that adopts the β-barrel fold typical of bacterial outer membrane porins and transporters (Kucharska et al., 2015). The lumen of the β-barrel is too narrow to conduct its cargo, uncharged amino acids, and thus the active form of the channel is thought to be a higher-order oligomer, likely a trimer (Sanganna Gari et al., 2018). While the individual channel is too small to be reliably distinguished by cryoEM, the trimer is predicted to be 6 nm in diameter (Figure 4.4B), well within the resolution range of the modality. We created symmetric SSLBs on holey carbon grids from proteoliposomes containing OprG (Figure 4.4A) and imaged them by automated acquisition for single-particle analysis. In this dataset, we collected approximately 800 micrographs like the one shown in Figure 4.4C where the most immediately recognizable features are ice contaminants (distinguished by sharp Fresnel edges) but also contain an abundance of uniform rings of density of approximately 6 nm diameter (Figure 4.4D). Interestingly, we also observe two or three conjoined rings in these micrographs (Figure 4.4E). With automated particle picking of

the ringed densities in this dataset, we generated 2D class averages that show a round density of approximately 6 nm in diameter containing three opacities arranged in a triangle (Figure 4.4F). This agrees with the predicted configuration of an OprG trimer based on previous NMR structures (Kucharska et al., 2015; Sanganna Gari et al., 2018); the three circular opacities are likely the barrel lumens and the ring-like density surrounding them is likely contributed by their flexible extracellular loops. Additionally, some of the classes showed two conjoined rings (Figure 4.4F, right-most column), which may be the higher order oligomers previously seen in crosslinking experiments (Sanganna Gari et al., 2018).

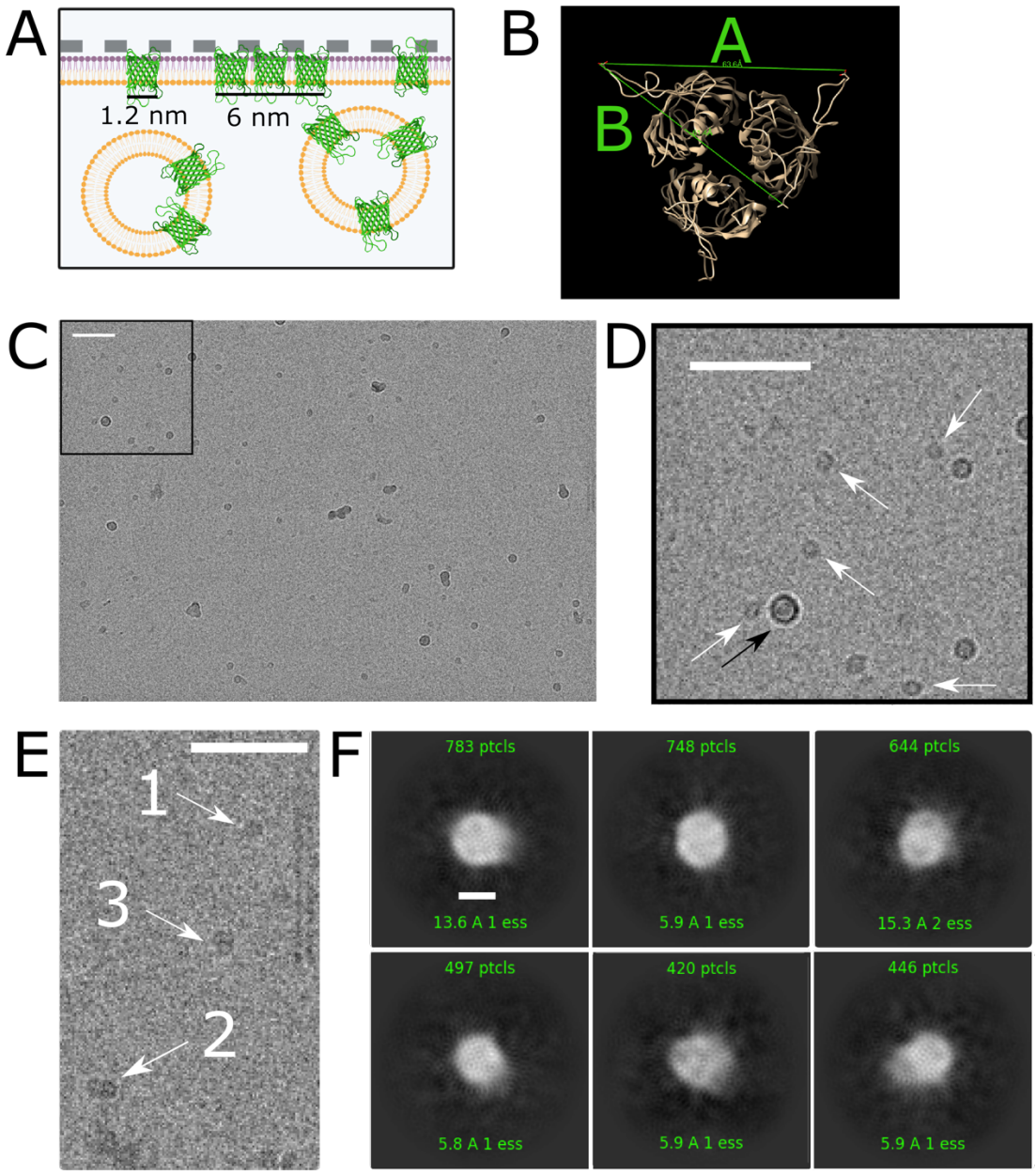

Figure 4.4: Semi-supported lipid bilayers containing a reconstituted integral membrane protein. A. Cartoon showing formation of an SSLB from proteoliposomes containing the outer membrane protein OprG from *P. aeruginosa*. Proteoliposomes composed of eggPC and eggPA in a 20:1 ratio were added to a monolayer of the same composition with 3 mol% DPS. **B.** Model of OprG trimer as described in Sanganna Gari et al., 2018. Diameter and side length of the trimer were measured as 63.6 (distance A)

and 61.4 Å (distance B) respectively. **C.** Example micrograph of a semi-supported lipid bilayer containing OprG. Scale bar 50 nm. **D**. Enlarged area of panel C showing round densities thought to be multimers of OprG (white arrows). Note ice contaminant is larger and has more defined Fresnel edges (black arrow). Scale bar 50 nm. **E.** Enlargement of a second micrograph with examples of single, double, and triple rings (white arrows). Scale bar 50 nm. **G**. 2D classes of OprG. Scale bar 60 Å. Number of particles (ptcls) contributing to a class and effective sample size (ess) calculated by cryoSPARC.

Application of SSLBs: Antimicrobial peptide assembly on SSLBs

SSLBs on holey carbon grids can also be used to study protein association with and assembly on membranes. Peptide 1 (P1) is an antimicrobial peptide derived from the N-terminus of the human chemokine, CXCL10, that is known to interact with membranes (more details in Appendix A). Unstructured in solution, P1 adopts a β-strand secondary structure upon association with membranes (Figure A.4) but its tertiary and quaternary structures are unknown. To better understand the structural changes that follow membrane association, we added P1 to a symmetric SSLB composed of *E. coli* polar lipids (PL) (Figure 4.5A) and observed the formation of round densities of approximately 50 nm in diameter, indicating an association containing many peptides (Figure 4.5B and C). Interestingly, the round densities were irregular in shape but relatively uniform in size and are mostly absent from areas of the grid that lack a bilayer. The peptide in solution in the absence of a bilayer did not produce these round densities (Figure 4.5D and E) indicating this multimerization is membrane dependent.

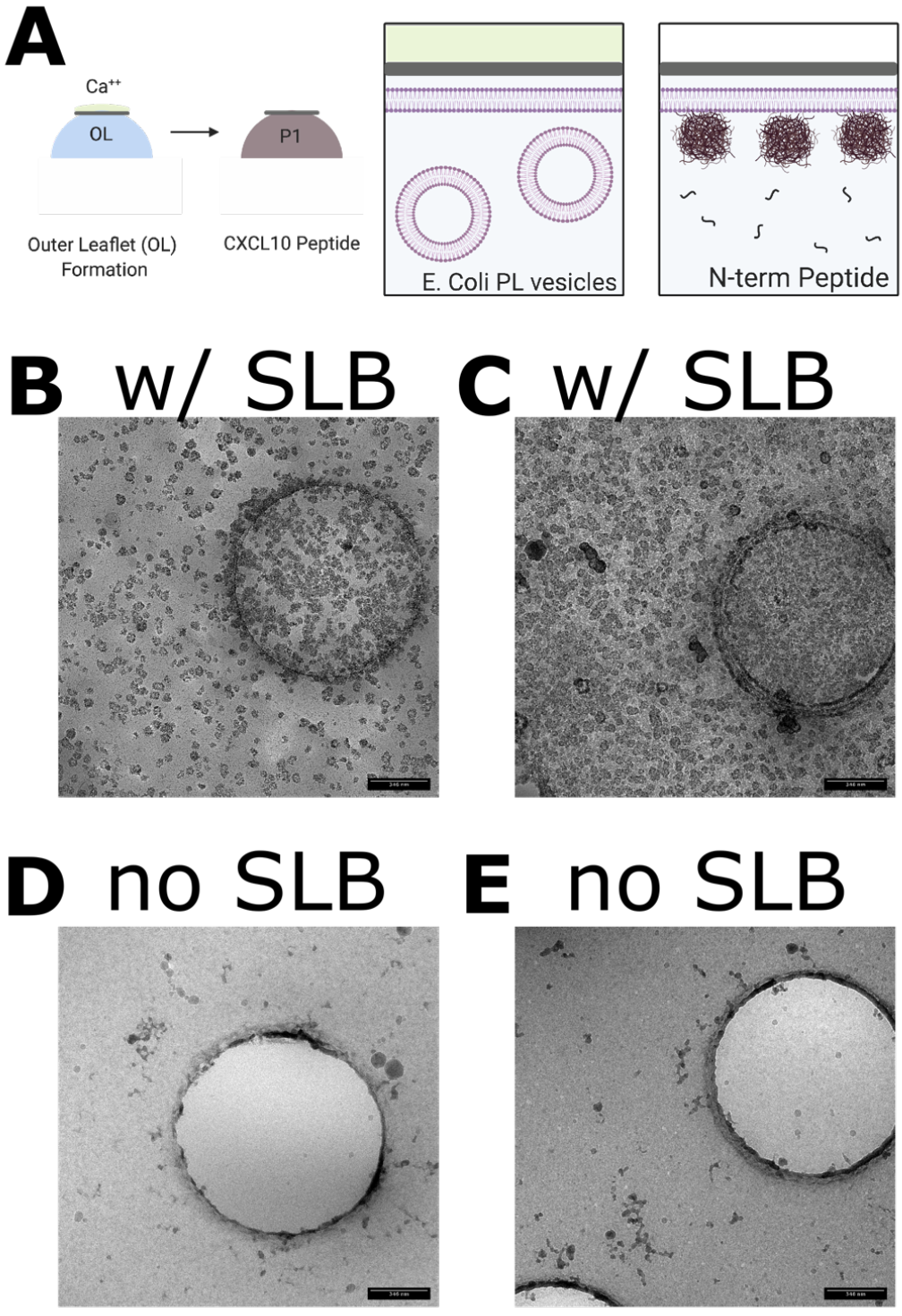

Figure 4.5: An antimicrobial peptide derived from the N-terminus of CXCL10 multimerizes in the presence of semi-supported lipid bilayers. A. Cartoon showing

sequential bilayer formation followed by peptide addition. The peptide is mostly disordered in solution but becomes more ordered upon interaction with membranes. **B and C**. Micrographs of CXCL10 peptide 1 in RPMI medium+5.5mg/mL bovine serum albumin (BSA) with symmetric semi-supported lipid bilayers composed of *E. coli* polar lipid extracts. **D and E.** Peptide 1 in RPMI+5.5mg/mL BSA frozen on a grid without a lipid bilayer. Darker densities over carbon are residual ethane from vitrification. Holes in carbon film are 1.2 μm for scale, scale bars are 350 nm.

Application of SSLBs: Reconstitution of HIV Gag assembly at the plasma membrane

SSLBs on holey carbon grids can also be used to reconstitute assembly of and possible precursors to budding HIV particles. To create a progeny viral particle, HIV's proteins and RNA genome associate on the plasma membrane of an infected cell, inducing curvature and recruiting host factors that aid in assembly and budding (Briggs and Kräusslich, 2011; Ganser-Pornillos et al., 2012; Sundquist and Kräusslich, 2012). Viral assembly is an intricate process known to be regulated by lipid composition, asymmetry, and phase separation in the plasma membrane (Favard et al., 2019; Sengupta et al., 2019; Wen et al., 2016) as well as other host and viral factors (Lippincott-Schwartz et al., 2017). Traditional supported lipid bilayers are useful for reconstitution of this process (Barros et al., 2016) but budding particles appear as diffraction limited spots by fluorescence microscopy and the support material may not allow membrane curvature induced by the assembly of many copies of the main HIV structural polyprotein, Gag. To assess the suitability of SSLBs on EM grids for further studies reconstituting HIV

assembly and budding, we created a simplified construct that replaced MA, the N-terminal domain of Gag, with a His tag and expressed it in *E. coli* (Figure 4.6A). This construct is expected to bind Ni-DGS present in the semi-supported lipid bilayer but an additional assembly cofactor, inositol hexakisphosphate (IP6), is required to observe round areas of increased density of a comparable size to a viral particle (Figure 4.6B and C). Identically prepared membranes without IP6 show diffuse density attributable to the Ni-DGS but no similarly round features (Figure 4.6D and E). IP6 is known to stabilize Gag (Dick et al., 2018) and has previously been used to reconstitute Gag assembly *in vitro* (Kucharska et al., 2019). Therefore, SSLBs reproduce known phenomena and reveal a possible configuration of an early intermediate of HIV budding.

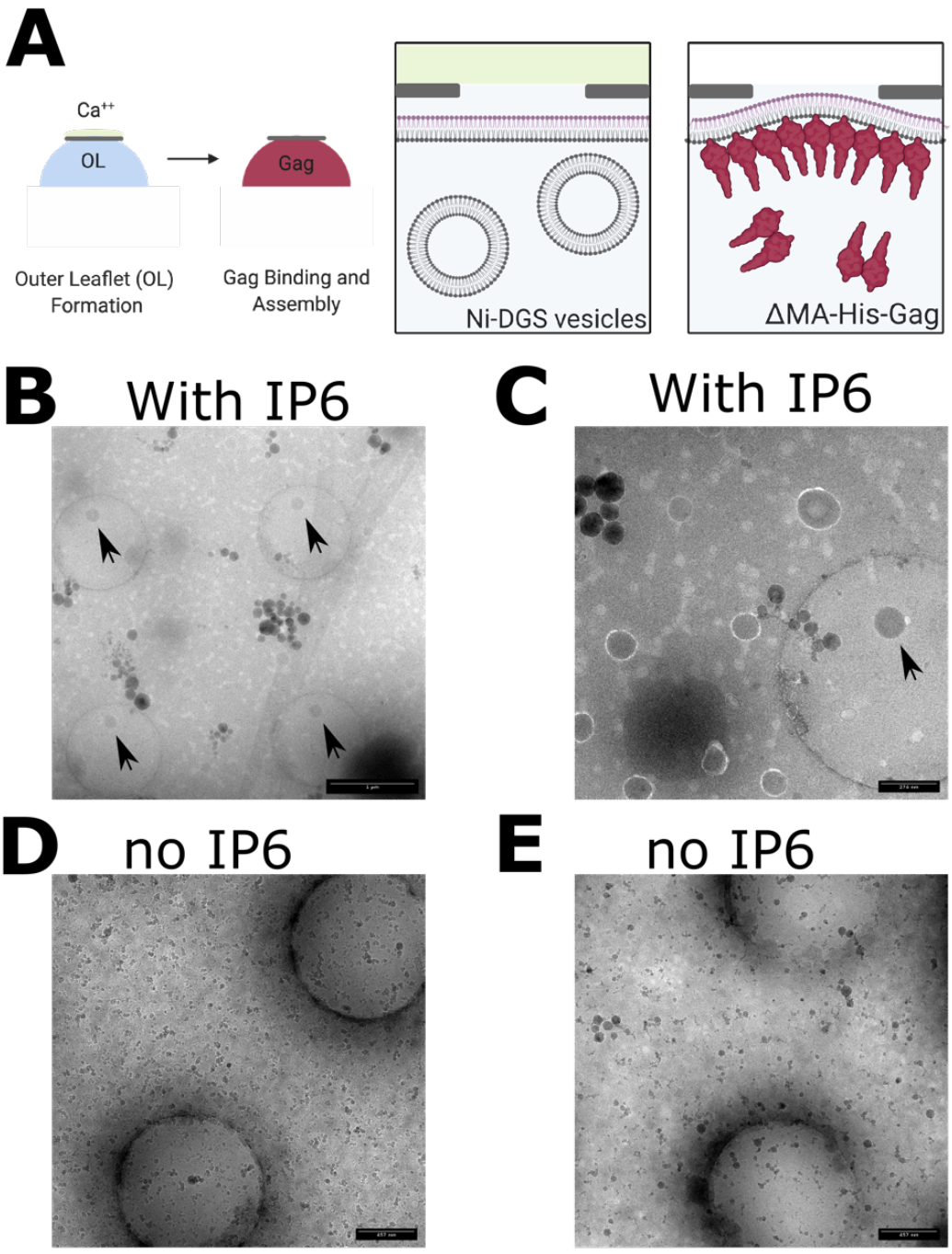

Figure 4.6: HIV Gag creates round features on semi-supported lipid bilayers in the presence of inositol hexakisphosphate, IP6. A. Cartoon showing formation of a semi-supported lipid bilayer from a monolayer composed of 78:20:2 bPC:chol:NBD-DPPE +3% DPS and LUVs composed of 76:20:2:2 bPC:chol:Rh-DOPE:Ni-DGS. The inclusion

of Ni-DGS in the outer leaflet enables the HIV Gag construct with an N-terminal His tag to associate with the membrane. **B and C.** Micrographs of HIV Gag associating with semi-supported lipid bilayers in the presence of 40 μM IP6. Black arrows point towards round areas approximately 150 nm in diameter with higher density. Over the carbon support, these round areas are typically surrounded by a "halo" of low density. **D and E.** Micrographs of HIV Gag associating with semi-supported lipid bilayers in the absence of IP6. Round areas of higher density are not seen in these samples. Holes in carbon film are 1.2 μm for scale.

4.4 Discussion:

Building on previously described technologies, we have developed a method for constructing semi-supported lipid bilayers on holey carbon supports for cryoEM. The described method produces contiguous areas of lipid bilayers that span holes in the carbon support film (Figure 4.2) and can incorporate membrane proteins (Figures 4.3 and 4.4) that show similar structure and oligomerization to that described in SLBs (Figure 4.4). Moreover, sequential formation of lipid mono and then bilayers, allows asymmetric SSLBs (Figure 4.2). Biological membranes are asymmetric in composition (Lorent et al., 2020; Op den Kamp, 1979; Van Meer et al., 2008) whereas most membrane models, including nanodiscs, lipodiscs, and proteoliposomes, are symmetric. Lipid asymmetry is essential for multiple biological functions (Clarke et al., 2020) and thus SSLBs may provide a more realistic model of biological membranes than others commonly used for cryoEM. It should be noted that SSLBs are not fully contiguous across the entire grid but rather form patches within grid squares, the edges of which can be seen as borders of

discontinuous density (Figures 4.2B and 4.2C, black arrows). With screening, these patches are easily identified and abundant enough to allow automated image acquisition (Figure 4.4). While bilayer edges may alter lipid order or protein behavior near them, these effects should be less significant in bilayers spanning tens of microns than those described for <10 nanometer diameter lipodisqs and nanodiscs (Thonghin et al., 2018).

In support of our claim that we have constructed SSLBs, we observed specific lipid incorporation in both monolayers and bilayers (Rh-DPPE and Ni-DGS, respectively) as imaged by fluorescence and cryo electron microscopies (Figure 4.2). Additionally, in SSLBs we have observed liquid-liquid phase separation (Figure 4.2A and 4.2B) and rapid lipid diffusion (Supplemental Video 1), which are well-documented phenomena characteristic of more traditional supported lipid bilayers, (Crane and Tamm, 2004; Honigmann et al., 2010; Kiessling et al., 2009; Lingwood et al., 2008; Wan et al., 2008). Phase separation has been imaged by cryoEM in spherical model membranes (Cornell et al., 2020; Heberle et al., 2020) but the current work likely represents the first observation of phase separation by cryoEM in a planar bilayer. The areas of higher electron density that we interpret to be lipid domains appear more spiculate (Figure 4.2B) than the perfectly round and smooth domains visible by fluorescence microscopy (Figure 4.2A) and predicted by line tension. While we do not expect cryo preservation to alter the appearance of lipid domains, we have no evidence to dismiss this possibility. Nanometer scale lipid domains in supported lipid bilayers imaged with the higher resolution of AFM can appear smooth or similarly spiculate, depending on the membrane composition and temperature (Bhojoo et al., 2018; Botet-Carreras et al., 2019; Chiantia et al., 2006; Gumí-Audenis et al., 2016; Vázquez et al., 2021). Additionally, within domains we observe

smaller areas of contrasting density that would be too small to observe with fluorescence microscopy but similar domains-within-domains are regularly seen with AFM (Bhojoo et al., 2018; Botet-Carreras et al., 2019; Gumí-Audenis et al., 2016; Vázquez et al., 2021). The consistency between the appearance of lipid domains in SSLBs by fluorescence and cryo electron microscopies with previous observations of phase separated membranes by fluorescence and AFM suggest that SSLBs are bilayers with similar properties to SLBs.

Membrane proteins can be incorporated into supported lipid bilayers by fusing proteoliposomes or biological membrane preparations, like plasma membrane blebs, on a supported monolayer (Diaz et al., 2008; Richards et al., 2016; Wagner and Tamm, 2001, 2000). Maintaining protein conformation, orientation, and diffusion in the bilayer can be a challenge although all are aided by introduction of a polymer cushion, which minimizes protein adsorption to the support material and creates space for protein domains below the bilayer (Wagner and Tamm, 2000). In SSLBs, free-standing membranes over holes in the support material would not be expected to have similar issues but we have included a PEG-based cushion to minimize adsorption over the supported areas.

As planar bilayers, SSLBs are well suited to model biological membranes with low curvature, like the plasma membrane. To further demonstrate the suitability of SSLBs for studying plasma membrane processes, we have shown that a commonly used plasma membrane preparation can form SSLBs and incorporates biotinylated membrane proteins (Figure 4.3). However, detection of biotinylation cannot report on whether proteins incorporate with the correct tertiary or quaternary structure.

To confirm that protein conformation is preserved in SSLBs, we studied a membrane protein for which the structure and oligomerization are known, *P. aeruginosa*

OprG (Kucharska et al., 2015; Sanganna Gari et al., 2018). 2D class averages revealed a ring of density with the expected diameter, containing three circular opacities (Figure 4.4E), which are likely the lumens of the three β-barrels that compose a trimeric channel. This agrees well with the published structures and suggests that at least a portion of proteins incorporate into SSLBs with proper tertiary and quaternary structure. Additionally, we observed "fused rings" of densities (Figure 4.4E and 4.4F, right-most column) which may be a minor population of even larger assemblies of OprG, as previously observed by cross-linking (Sanganna Gari et al., 2018). However, as a 25.5 kDa protein, OprG is near the lower size limit for single-particle cryoEM so in this particular application, we may underestimate the proportion of monomers or dimers. This would likely not be an issue for application of the technique to larger membrane proteins. Harnessing the capabilities of single-particle cryoEM for the study of a heterogeneous population of membrane protein oligomers will allow visualization of oligomers and quantification of the relative frequency of oligomerization states.

In addition to membrane proteins, SSLBs can also be used to study the interactions of soluble proteins with membranes. Antimicrobial peptide (AMP) interactions with membranes have been studied by AFM (Juhaniewicz and Sek, 2015; Mularski et al., 2016; Pittman et al., 2018) and produced important mechanistic insights but cryoEM has become the more accessible technique. Classically, AMPs are unstructured in aqueous buffers and adopt a more ordered conformation upon interaction with membranes (Yeaman and Yount, 2003). The AMP, P1 follows this pattern as well (Figure A.4) and we have visualized round assemblies of P1 of approximately 50 nm on SSLBs (Figure 4.5B and 4.5C) that are not observed in solution (Figure 4.5D and 4.5E).

Direct observation of the effect of AMPs on membranes in this way helps clarify potential mechanisms of action.

In a second application of SSLBs, we have demonstrated that SSLBs reproduce IP6-induced initiation of HIV Gag assembly on the plasma membrane of an infected cell (Figure 4.6). Round areas of higher density with diameter slightly larger than an HIV particle were observed in the presence of the assembly co-factor, IP6 (Figure 4.6B), but not observed in membranes without IP6 (Figure 4.6C), where Gag is capable of binding the membrane but likely cannot assemble. In IP6-treated samples, a "halo" of low density surrounded the areas of high density. Nickel chelating lipids contribute electron density and their bulky headgroups would be excluded from areas of high curvature, like the boundary between different curvatures, giving rise to a ring of low density. This indirectly suggests these areas of HIV Gag assembly may be capable of inducing membrane curvature although further studies with cryoET would be required to demonstrate that.

In summary, we have developed a method for creating semi-supported lipid bilayers on commercially available holey carbon EM grids that can be easily modified to suit a range of experiments examining membrane and protein behavior.

4.5 Materials and Methods:

Reagents: The following compounds were purchased from Avanti Polar Lipids and used without modification: brain phosphatidylcholine (bPC), egg phosphatidylcholine (egg PC), egg L-α-phosphatidic acid (egg PA), brain sphingomyelin (bSM), 1,2-dipalmitoyl-sn-glycero-3-phosphoethanolamine-N-(lissamine rhodamine B sulfonyl) (Rh-DPPE), 1,2-dipalmitoyl-sn-glycero-3-phosphoethanolamine-N-(7-nitro-2-1,3-benzoxadiazol-4-yl) (NBD-DPPE), 1,2-dipalmitoyl-sn-glycero-3-phosphoethanolamine-N-(cap biotinyl) sodium salt (Biotin-DPPE), 1,2-dioleoyl-sn-glycero-3-[(N-(5-amino-1-carboxypentyl)iminodiacetic acid)succinyl] Nickel (Ni-DGS), and *E. coli* polar lipid extract (*E. coli* PL). Cholesterol and streptavidin-coated 10 nm gold nanoparticles were purchased from Sigma-Aldrich. 1,2-dimyristoyl-*sn*-glycero-3-phosphoethanolamine-PEG3400-triethoxysilane (DPS) was synthesized as described previously (Wagner and Tamm, 2000). Peptides were prepared as described in Appendix A and diluted in phenol-red free Roswell Park Memorial Institute (RPMI) 1640 medium (Gibco) with 5.5 mg/mL bovine serum albumin (BSA, Sigma-Aldrich)

EM grid preparation and monolayer deposition with Langmuir trough:

A chloroform solution of a lipid mixture containing 3% DPS was applied to a Nima 611 Langmuir-Blodgett trough and after letting the solvent evaporate for 10 minutes, the lipid layer was compressed at a rate of 10 cm^2/min to a pressure of 32 mN/m. C-Flat 1.2/1.3-300 mesh holey carbon grids (Electron Microscopy Sciences) were glow discharged at 20 mA for 45 seconds with amylamine (Sigma) immediately before monolayer deposition. Grids were held with PTFE-coated tweezers as they were delicately placed carbon side

down on the compressed lipid monolayer on the trough. The grid was removed from the trough with tweezers with an adhering water droplet. This water droplet was allowed to evaporate before the grid with the transferred lipid monolayer was stored in a desiccator for at least 16 hours before use.

Bilayer formation by vesicle fusion:

Parafilm was spread over an empty pipette tip box to create a clean and portable surface to hold up to 96 droplets. The appropriate membrane preparation for the experiment (LUVs, blebs, or proteoliposomes) was diluted 1:10 in appropriate buffer and a 30 μL droplet was placed on the parafilm. Grids with transferred lipid monolayers were placed monolayer side down on the droplet and 3 μL of calcium rupture buffer (75 mM $CaCl_2$, 10 mM HEPES, pH 7.4) was carefully pipetted on the opposite side of the grid. Grids were incubated in this manner for 1-2 hours at room temperature before washing by sequentially tapping the grid on droplets of experiment appropriate buffer.

Vitrification and cryoEM imaging:

After bilayer formation, washing, and additional steps as appropriate for the experiment, 3 μL of additional buffer was pipetted on top of the membrane, the grid was blotted on the opposite side and plunged into liquid ethane before storage in liquid nitrogen. All data was acquired on a Tecnai F20 EM operating at 120 kV and cryogenic temperature with a field emission gun and a CCD camera except for the OprG single particle analysis dataset.

SUV and LUV preparation:

Chloroform stocks of desired lipids were mixed and the solvent was evaporated under a gentle stream of nitrogen gas. The resulting lipid film was desiccated under vacuum for at least one hour before resuspension in buffer appropriate to the experiment to a final concentration of 1 mM. After vortexing at room temperature, the lipid suspension was subjected to 10 freeze/thaw cycles in liquid nitrogen and warm water before extrusion through two, 50 nm polycarbonate membranes (Avestin) for SUVs or 100 nm membranes for LUVs. SUVs and LUVs were stored at 4 °C and used within 24 hours of extrusion.

Plasma membrane bleb preparation, biotinylation, and SSLB formation:

CD4 and CCR5 overexpressing HeLa cells (gift of David M. Rekosh, University of Virginia) were maintained at 37 °C with 5% CO_2 atmosphere in Iscove's Modified Dulbecco's Medium (Gibco) supplemented with 10% fetal bovine serum, 1% antibiotic/antimycotic, 0.5 mg/mL of G418 (Gibco), and 1 µg/mL puromycin.

Blebs were produced from CD4+/CCR5+ HeLa cells by previously published methods (Sezgin et al., 2012; Yang et al., 2017). Briefly, when cells reached 90% confluence, they were washed twice with blebbing buffer (10 mM HEPES, 150 mM NaCL, 2 mM $CaCl_2$, pH 7.4) and blebbing was induced by replacing buffer on the cells with 5 mL of 25 mM formaldehyde (J.T.Baker) and 2 mM Dithiothreitol (DTT) diluted in blebbing buffer and incubating the cells at 37°C, 5% CO_2 for 1 hour. After 1 hour, blebs were detached from cells by shaking on a radial shaker at room temperature for 1 hour before the supernatant was collected and cleared of large cell debris by centrifuging at 100xg for 10 minutes.

Blebs were pelleted at 20,000xg for 1 hour and washed twice in blebbing buffer without formaldehyde or DTT before being resuspended in phosphate buffered saline with or without 2 mg/mL surface biotinylating agent, sulfo-NHS-LC-biotin (Thermo Fisher Scientific). Biotinylation was allowed to proceed at room temperature for 30 minutes before the blebs were pelleted at 21,000xg for 1 hour and resuspended in blebbing buffer without formaldehyde or DTT.

SSLBs were formed on grids by diluting blebs (biotinylated or mock biotinylated) 1:10 in blebbing buffer without formaldehyde or DTT followed by washing in the same buffer. All grids were incubated with streptavidin-gold nanoparticles diluted 1:50 in blebbing buffer without formaldehyde or DTT for 30 minutes at room temperature before additional washing in blebbing buffer without formaldehyde or DTT. The grids were frozen after the second round of washing.

***P. aeruginosa* OprG proteoliposome preparation:**

OprG protein was expressed and purified in a urea-denatured form and refolded n-dodecylphosphocholine (Anatrace) as described previously (Kucharska et al., 2015). Liposomes were made by suspending a dried film of 3 μmol of egg PC and 0.15 μmol of egg PA in 20 μL of a 0.18 mM micellar solution of n-dodecylphosphocholine (Anatrace) in water containing 1 nmol OprG (protein-to-lipid ratio 1:3150, detergent to lipid ratio 1:875). Samples were vortexed for 10 seconds, followed by sonication in a bath sonicator for 15 minutes, twice, then dehydrated in vacuo. Dried films were resuspended in 200 μL of 12 mM stachyose, 12 mM HEPES (pH 7.5), then vortexed for

10 seconds, followed by sonication in a water bath at room temperature for 15 minutes and repeated by another round of 10 second vortexing and 15 minute sonication. SSLBs were formed on grids by diluting proteoliposomes 1:10 in 12 mM HEPES (pH 7.5) and washing in the same buffer. The grids were frozen after washing without additional reagents.

SSLB grids containing OprG were imaged on a Titan Krios EM operating at 300 kV equipped with a K3/GIF (Gatan) direct electron detector and controlled by EPU software (ThermoFisher Scientific). Magnification was 81,000X, which yielded a pixel size of 1.08 Å. CryoSPARC was used for all data processing (Punjani et al., 2017). Micrographs were motion corrected and their contrast transfer function (CTF) was estimated. 2D class averages were generated from manually picked particles and used as templates for automated particle picking. 2D class averages were calculated from automatically picked particles.

Peptide assembly on SSLBs:

SSLBs were formed on grids by diluting LUVs composed of *E. coli* polar lipid extract 1:10 in RPMI media with 5.5 mg/mL BSA and washing in the same buffer. The grids were then incubated in 8 μM of Peptide 1 (described in Appendix A) diluted in RPMI+BSA for 30 minutes before a second round of washing and vitrification for cryoEM.

Gag protein preparation and assembly on SSLBs:

E. coli transformed with the ΔMA-6xHis-Gag construct were grown in Luria Bertani (LB) broth, pelleted, and resuspended in 50 mM Tris pH 8.3/1 M LiCl with protease inhibitor cocktail. Bacteria were lysed with deoxycholate and lysozyme on ice before sonication with a tip sonicator. Insoluble material was pelleted at 18,000 RPM for 45 minutes and the resulting supernatant was filtered (0.8 μm) before affinity purification with nickel-NTA resin. The protein was eluted from the resin in fractions with 50 mM Tris pH 8.3/1 M LiCl with an increasing concentration of imidazole up to 300 mM. Fractions containing the protein of interest were combined and dialyzed against 20 mM Tris pH 8.0/500 mM NaCl/2 mM β-mercaptoethanol (β-ME) overnight. The protein was passed over a Q anion exchange column and eluted in fractions with 20 mM Tris pH 8.0/1.5 M NaCl/2 mM β-ME. The eluted protein was concentrated in a spin concentrator with 5000 molecular weight cutoff before dialysis against 20 mM Tris pH 8.0/500 mM NaCl overnight. The protein was kept at 4°C or flash frozen and stored at -80°C.

SSLBs were formed on grids by diluting LUVs composed of 76:20:2:2 bPC:chol:Rh-DOPE:Ni-DGS in 20 mM Tris pH 8.0/500 mM NaCl and washing in the same buffer. The SSLB was incubated with 1mg/mL of ΔMA-6xHis-Gag at room temperature for 1 hour in the same buffer with or without 40 μm IP6. The grids were washed in buffer with or without 40 μm IP6 before freezing.

4.6 Supplemental Video Legend:

Supplemental Video 1: Lipid domains are mobile and capable of fusion in phase separated SSLBs. Confocal fluorescence images of a the same grid as Figure 4.2A, suspended in buffer in a petri dish with coverslip glass bottom. A white arrow points towards an example of domain fusion. The monolayer is composed of bPC:bSM:chol:Biotin-DPPE:Rhodamine-DPPE:DPS in a 33:40:20:2:2:3 ratio. The second leaflet was formed from 50 nm small unilamellar vesicles composed of bPC:bSM:chol:Ni-DGS in a 38:40:20:2 ratio. Overlay of red, Rhodamine-PE fluorescence, and gray, differential interference contrast (DIC) micrographs. Scale bar is 50 μm. Acquisition time scale was 3.9 frames per second, video sped up 10X.

Chapter 5: Discussion and Summary

We have produced data on the development of model membranes and their use for studying immunity to pathogens. Specifically, we have demonstrated that blebs incorporating appropriate receptors can be used to study viral membrane fusion by cryoET and TIRFm. Then, we characterized uninhibited and Serinc3/5-interrupted HIV fusion with both methods which revealed that Serinc3 and Serinc5 inhibit multiple intermediate steps of membrane fusion. While earlier fusion intermediates are morphologically similar between Serinc5-containing and -lacking pseudoviruses, the penultimate "early fusion product" of Serinc5-containing particles showed a cinched fusion pore as if unable to fully dilate. Additionally, treatment with Atto488-DMPE or amphotericin B selectively increased fusion of Serinc3 and Serinc5 pseudoviruses. This rescue of fusion in Serinc5-containing pseudoviruses was repeatable with all chain lengths and saturations of unmodified PE but not with PC or PS. From these data, we hypothesized that the viral lipid environment may be important for Serinc5 function. To that end, we examined the effect of Serinc incorporation on lipid order in the viral membrane by cryoEM and fluorescence lifetime microscopy. Both techniques showed an increase in the portion of the viral membrane in an ordered domain in pseudoviruses incorporating Serinc5. Therefore, we suggest that by increasing membrane order, Serinc5 alters the energetics of fusion, leading to the accumulation of stalled fusion intermediates, including the striking semi-dilated fusion pores we observed.

We built on previously-described techniques to develop a method for creating semi-supported lipid bilayers (SSLBs) on holey carbon EM grids and then demonstrated

their utility for observing lipid phase separation, membrane protein multimerization, and association and assembly of soluble proteins on membranes. Most of these applications of SSLBs supported larger collaborative projects, one of which is described in Appendix A.

5.1 Further studies and applications of semi-supported lipid bilayers:

We have described a method for constructing SSLBs and provided evidence of their similarity to conventionally-prepared supported lipid bilayers. More direct evidence of specific bilayer formation could be obtained with electron (Carlemalm and Wieslander, 1975; Hui, 1977) or x-ray diffraction (Tyler et al., 2015), although both would require additional expertise and/or instrumentation. Since the membranes are vitrified so quickly that even water molecules cannot rearrange into crystals (Dubochet et al., 1987), the disordered packing of lipids inherent in some biological membranes is expected to be preserved. While this is a benefit of the technique that allows higher fidelity modeling of biological membranes, it may hinder the usefulness of diffractive techniques that rely on regular spacings of atoms.

While we were originally motivated to develop another method for observing viral or intracellular membrane fusion by cryoEM, SSLBs are adaptable and could be useful for studying nearly any process involving a membrane. It is beyond the scope of this thesis to demonstrate the full range of their applications but we expect the technique to be of interest to cell biologists, membrane biophysicists, and structural biologists. SSLBs are not useful for structural biology because the membrane imparts an orientation on particles, making 3D structure determination impossible. However, we envision

SSLBs to be a complementary method for structural biologists to demonstrate the relevance of structures solved in membrane mimetics to bilayers of more physiological compositions.

SSLBs are particularly well-suited for studying membrane trafficking. Many important membrane processes, like endo/exocytosis, involve protein complexes and vesicles on a scale of hundreds of nanometers which appear as diffraction-limited spots by fluorescence microscopy (Alberts et al., 2002a, 2002b). Visualizing localizations of protein densities with cryoEM will enable a greater understanding of these processes. The unique advantage of SSLBs is their suitability to study the deformation of the free-standing portion of the membrane. While we have shown micrographs that implicate the induction of membrane curvature by HIV Gag, further studies could use cryoET to directly observe membrane curvature. We have used HIV Gag to induce curvature but there are also many cellular proteins involved in membrane trafficking that induce curvature including clathrin, COPI/II, caveolins, BAR domain proteins, and ESCRT proteins (McMahon and Boucrot, 2015). Previously, large-scale induction of curvature by these proteins was studied in unilamellar vesicles (Dodonova et al., 2015; Kroppen et al., 2020; McCullough et al., 2018) but the rigidity of support material under conventional SLBs limited their use for these studies. With cryoET of SSLBs, induction of membrane curvature, both large and small, can be assessed. Additionally, asymmetric leaflet composition is essential for stabilization of membrane curvature (McMahon and Boucrot, 2015). While some techniques have been described for selectively enriching or depleting certain lipid species from the outer leaflet of vesicles (Chiantia et al., 2011; Doktorova et al., 2018; Steinkühler et al., 2018), SSLBs offer more precise control of the composition

of both leaflets. This allows titration of certain lipid species and observation of their effects on various phenomena, as has similarly been done with conventional SLBs (Kreutzberger et al., 2017; Kreutzberger et al., 2015).

5.2 Further studies and applications of blebs as target membranes for studying viral fusion by cryoET:

In this dissertation, we synchronized HIV fusion with temperature by mixing pseudoviruses and blebs on ice in a PCR tube, transferring the tube to a heat block at 37°C for 10 or 30 seconds, and then freezing as rapidly as possible. These methods were adequate for comparing the dramatic differences between fusion of Serinc5-containing or -lacking pseudoviruses but could be improved on. If the kinetics of viral fusion were to be studied with greater subtlety, a temperature jump device could be used to precisely raise the temperature of a sample on an EM grid with a pulse of light less than a second before freezing (Chestnut et al., 1992; S. Li et al., 2017; Yoder et al., 2020). Additionally, receptor and co-receptor binding are sufficient for triggering HIV fusion, but fusion of many other viruses is dependent on the introduction of soluble chemical factors like pH or calcium (Harrison, 2015; White and Whittaker, 2016). Fusion could be triggered in a virus and bleb mixture on an EM grid by the addition of a low pH or calcium-containing buffer. Combining both methods, a laser pulse could be used to release caged protons (Costello et al., 2012) already present in a virus and bleb mixture at a precise interval before freezing to allow even greater temporal control of fusion triggering and freezing.

5.3 Further studies to substantiate our model of Serinc5-mediated restriction of HIV membrane fusion:

We have demonstrated that Serinc5 alters the order and organization of the HIV viral membrane to disrupt fusion and interpreted this in terms of the energetics of fusion to explain the mechanism of Serinc5's restriction of HIV. While the model we present is consistent with previously-published studies of Serinc5, it could be further substantiated by additional studies on the interactions between Serinc5, Env, and the viral membrane.

Domain partitioning of Env in blebs with or without Serincs could be used to support the speculation that an increase in the portion of the viral membrane in an ordered domain would decrease Env clustering. The ratio of Env in ordered versus disordered domains under various conditions would be assessed as done previously for CD4 and CCR5 (Yang et al., 2017). These conditions should include treatment with exogenous PE, amphotericin B, and linactants that are known to change the shape and size of domains (Yang et al., 2015). Our proposed model predicts that blebs containing Serinc5 would have a larger portion of the viral membrane in ordered domains and a greater distance between Env trimers in those domains. Notably, the viral membrane is enriched in cholesterol as compared to blebs, so if Serinc5's alteration of lipid order is dependent on a high concentration of cholesterol, no changes to order would be observed in Serinc5-containing blebs. While not compatible with the experiments described above, this too would be an interesting observation deserving of further study.

Similarly, to assess the interaction of Serinc5, Env, and the viral membrane in a pseudovirus particle, one could build on the work of Chen et al., 2020 by treating Serinc5-containing HIV pseudoviruses with exogenous PE, amphotericin B, or linactants

and observing Env clustering via super-resolution microscopy. If PE and amphotericin B restore Env clustering like they restore fusion of Serinc5 pseudoviruses, it would suggest that Serinc5's disruption of Env clustering is dependent on viral membrane lipid order. This would be further supported if PE or amphotericin B treatment decreases lipid order of Serinc5-containing pseudoviruses as reported by FLIPPER-TR.

We have also speculated that Serinc5 alterations of viral membrane order would induce conformational changes in Env. This could be directly assessed with subtomogram averaging (STA) of Env on HIV pseudovirus particles with and without Serinc5. STA is a method for obtaining higher resolution views of repeated features in a tomogram by iteratively extracting subvolumes, aligning them to a template, and averaging their intensities (Wan and Briggs, 2016). Not only would STA produce structures of Env in these two conditions, but it also would define the locations of Env trimers on the surface of the viral particle. From these, nearest-neighbor distances could be computed to assess Env clustering. Moreover, the viral membrane immediately surrounding Env would be included in the resulting average. If Serinc5 does force Env into a thicker membrane, a change in the thickness of the bilayer immediately surrounding Env should be detectable by STA. We have attempted STA on tomograms of V4 High Env HIV pseudoviruses like those in Figure 2.2b, but the alignment of particles to the template was dominated by the missing wedge of information inherent in tomography and thus unlikely to produce high-quality results (Schmid and Booth, 2008). Further optimization of sample preparation and imaging conditions for STA may alleviate this issue. While STA of HIV Env is possible (Ze Li et al., 2020), it remains extremely difficult.

5.4 Contextualization of proposed Serinc5 mechanism of action within the current understanding of viral restriction factors:

Alteration of viral membrane properties has been known to inhibit fusion of a broad variety of viruses and the same may be true of Serinc-mediated alterations. Serinc5 restriction of Hepatitis B Virus (Liu et al., 2020) and Influenza A Virus (IAV) has been described (Diehl et al., 2019). However, Serinc5 activity against other enveloped viruses depended on the pseudoviral system studied (Diehl et al., 2019) and is of uncertain biological relevance. Considering the breadth of viruses blocked by similar restriction factors, it is very likely that Serincs do not act against only a few viruses, but the scope of study has not allowed the identification of the full breadth of Serincs' activity. Following from this, only Serinc3 and Serinc5 have been shown to have antiviral activity, but perhaps the other Serinc family members, Serinc1, Serinc2, and Serinc4, show antiviral activity against yet unidentified viruses or in unidentified environments. For instance, Serinc4 is prevented from incorporating into HIV particles by a high level of proteasomal degradation, even at baseline in the uninfected cell (Qiu et al., 2020). Many viruses are known to alter proteasomal activity to avoid immune detection and boost translation of viral proteins. Additionally, interferon (IFN) signaling changes the composition and catalytic activity of the proteasome (McCarthy and Weinberg, 2015). Therefore, it is possible Serinc4 may be active under certain conditions or against enveloped viruses that alter proteasomal degradation.

Alteration of membrane properties has also been proposed as the mechanism of action of IFN-induced transmembrane proteins (IFITMs), a family of restriction factors with activity against many enveloped viruses (Chesarino et al., 2017; Guo et al., 2020; Li

et al., 2013; Suddala et al., 2019). IFITM activity has been best characterized in cellular membranes where colocalization to the membraned compartment of entry and alteration of membrane order are required for restriction (Chesarino et al., 2017; Li et al., 2013). In model membranes, IFITM3 inhibits fusion by partitioning into L_d domains, inducing negative curvature, and increasing membrane order (Guo et al., 2020). More similar to the described functions of Serincs, IFITMs can also incorporate into budding HIV particles and decrease their infectivity (Compton et al., 2014; Tartour et al., 2017, 2014). However, the effect of IFITMs on viral membranes has not yet been directly demonstrated. Both Serinc5 and IFITM3 have been described to oligomerize and cluster under certain conditions, but Serincs and IFITMs are structurally very different. Serincs are large proteins with 10-13 transmembrane domains while IFITMs are small proteins with only one transmembrane domain and an amphipathic helix (Chen et al., 2020; Kummer et al., 2019; Pye et al., 2020; Rahman et al., 2020). IFITM-mediated alteration of membrane properties is dependent on its amphipathic helix (Chesarino et al., 2017) but an analogous domain in Serinc5 is not apparent. This raises the question of how Serinc5 induces ordering of membranes. The data presented in this thesis cannot directly address this question but leave it for future studies. Speculating based on the structure of Serinc5 and its stabilization with exogenous cholesterol addition (Pye et al., 2020), Serinc5 may locally concentrate cholesterol in its annular lipids, leading to a more ordered packing of lipids in its vicinity. Serinc5 clustering, as has been observed in viral particles (Chen et al., 2020), could extend the effects of short-range associations with cholesterol and coalesce into larger ordered domains on the scale of tens of nanometers. This would not be mediated by a specific domain as described for IFITMs (Chesarino et al., 2017), but

rather a cooperative stabilization of Serinc5 and ordered membrane domains—a common theme for membrane proteins (Levental et al., 2020).

5.5 Altered viral membrane order as a therapeutic target:

The alteration of membrane properties to prevent viral membrane fusion is a common mechanism shared by IFITM3, Serinc5, and some potential broad-spectrum antiviral compounds in development (Vigant et al., 2015). These compounds fall into three categories: cholesterol-depleting agents, rigid amphipathic fusion inhibitors (RAFIs), and lipid oxidation agents. Cholesterol is essential for maintaining membrane fluidity and its depletion has been shown to be inhibitory for HIV (Campbell et al., 2002; Liao et al., 2001; Viard et al., 2002), IAV (Domanska et al., 2013; Fedson, 2013; Sun and Whittaker, 2003), and other viruses (Kleinfelter et al., 2015; Umashankar et al., 2008; Van Duijl-Richter et al., 2015). Statins are a class of FDA-approved drugs that inhibit cholesterol synthesis and have been associated with lower disease severity of Ebola Virus infection (Johansen et al., 2015; Shrivastava-Ranjan et al., 2018). Statins have also been associated with lower disease severity of IAV infection but the significance of this effect is debated (Fedson, 2013, 2006; Haidari et al., 2007; Mehrbod et al., 2014). The proprietary compound SP01A from Samaritan Pharmaceuticals was reported to reduce cellular cholesterol and HIV viral load when given as adjunctive antiretroviral therapy in a Phase I/II clinical trial although the results are not publicly available (Teissier et al., 2011).

RAFIs are compounds with an inverted cone shape that insert into membranes (Vigant et al., 2015, 2010). While their exact mechanism of action is not certain, RAFIs

are thought to work by inducing curvature in the viral membrane that destabilizes fusion intermediates (Melikyan, 2010; Nieto-Garai et al., 2018; Speerstra et al., 2018; St. Vincent et al., 2010). They show antiviral activity with little cytotoxicity at nanomolar concentrations *in vitro* but have not yet been tested *in vivo* (Speerstra et al., 2018).

Lipid oxidizers, or type II photosensitizers, incorporate into membranes and generate singlet oxygen radicals upon exposure to visible light. These radicals oxidize carbon-carbon double bonds in unsaturated acyl chains and introduce a hydrophilic hydroperoxy group, leading to increased positive curvature and decreased fluidity of bilayers (Vigant et al., 2015). Without the lipid homeostatic mechanisms present in cellular membranes, viruses cannot repair the oxidative damage and thus viral treatment with lipid oxidizers is irreversible but cell-cell fusion is unaffected (Vigant et al., 2013). Several of these compounds exhibit broad antiviral activity with low nanomolar IC_{50} concentrations against enveloped viruses *in vitro* and *in vivo* (Vigant et al., 2014; Wolf et al., 2010).

The discovery of Serinc5's alteration of the viral membrane to block fusion and prevent infection lends further support to the development of antivirals targeting membrane properties. Further study of the mechanism by which Serinc5 alters lipid order may provide a new strategy for the design of membrane-altering antivirals.

5.6 Summary:

In this work, we have developed two model membrane systems, characterized the defect in HIV membrane fusion due to Serinc3 and Serinc5, and demonstrated that Serinc5 alters viral membrane order to disrupt fusion. Our investigation of Serincs

provides context to previous work in the field and a critical piece of Serinc5's mechanism of action. With further study, these results could inform the design of new antivirals. More immediately, the tools we developed can be used to study membrane fusion and other membrane processes.

Appendix A: Characterization of anti-microbial peptides derived from CXCL10

Introduction:

Bacterial resistance to clinically available antibiotics is a global threat of increasing concern (Livermore, 2004; Morehead and Scarbrough, 2018; The Lancet, 2009). Towards addressing this issue, the World Health Organization (WHO) has committed to a five-pronged Global Action Plan where one prong is the development of novel antibiotics (WHO, 2015). Antimicrobial peptides (AMPs) are produced by organisms for host defense and have been studied for decades as a potential source of new antibiotics (Lei et al., 2019). Over 3,000 natural and synthetic peptides have been described, of which, seven have been approved by the Food and Drug Administration (Chen and Lu, 2020). The nearly unlimited combinatorial space of peptides, further expanded by chemical modifications (Porto et al., 2018; Rathinakumar et al., 2009; Torres et al., 2019), position AMPs as a rich source of potential antibiotics.

Classical AMPs are cationic amphiphiles that are unstructured in solution and adopt an α-helical secondary structure in hydrophobic environments. The peptide, melittin, is a prototypical α-helical AMP–although it is far too toxic to be of clinical use (Y. Huang et al., 2010). More broadly, however, AMPs are diverse in structure with many examples that form β-strands (Dong et al., 2019) or remain unstructured (Takahashi et al., 2010). Their cationic residues are thought to interact with the negative charge of lipid headgroups, and their hydrophobic faces with the bilayer interior, leading to the disruption of bacterial cell membranes (Y. Huang et al., 2010; Lei et al., 2019). Although the mechanism of action for AMPs depends on the specific peptide studied, it is generally

thought to involve permeabilization of the cell membrane, antagonism of membrane processes, and/or recruitment of immune cells (Guha et al., 2019; Shagaghi et al., 2018; Shenkarev et al., 2011). The lack of clear structure-to-function relationships that confer antimicrobial activity contributes to the complexity of optimizing AMPs for clinical use (Chen and Lu, 2020).

The human chemokine, CXCL10, in addition to its immune signaling capabilities, has been found to exhibit broad antimicrobial activity against Gram-positive and -negative bacteria (Cole et al., 2001; Crawford et al., 2017, 2010; Oppenheim et al., 2003), including multidrug resistant clinical isolates (Crawford et al., 2017) and *B. anthracis* spores (Crawford et al., 2009). Further investigations have revealed two possible mechanisms of antimicrobial activity of CXCL10: 1) a likely interaction between the N-terminus of CXCL10 and the bacterial membrane protein, FtsX, and 2) a non-specific interaction between the C-terminal amphipathic helix and bacterial cell membranes (Margulieux et al., 2016). Peptides derived from the C-terminus of chemokines CCL13, CCL20, CXCL4, and CXCL9 have been shown to retain the antimicrobial activity of the parent protein (Crawford et al., 2019) and thus we hypothesized that peptides derived from the C-terminus of CXCL10 may also have broad antimicrobial activity. Additionally, a C-terminally truncated version of CXCL10 retained antimicrobial activity (Margulieux et al., 2016) and thus we hypothesize that peptides derived from the N-terminus will also be antimicrobial. In the following study, we examined the suitability of peptides derived from the N- and C-terminal regions of CXCL10 as novel antibiotics.

Results:

Both N- and C-terminal CXCL10 peptides show broad antimicrobial activity.

For the purposes of this study, we compared the bactericidal activities of the N- and C-terminal peptides (P1 and P9, respectively) that are expected to show antimicrobial activity with that of a peptide derived from the middle of CXCL10, P5, that is not expected to be antimicrobial. (Figure A.1A). P1 and P9 each killed a broad, yet unique, range of multidrug resistant bacteria in hypotonic buffer while P5 showed no activity against any of the strains tested (Figure A.1B). The tested panel of multidrug-resistant bacteria included Gram-negative (*Salmonella typhi, Shigella flexneri, Acinetobacter baumannii, Enterobacter cloacae, Pseudomonas aeruginosa*) and Gram-positive (*Enterococcus faecium, Staphylococcus aureus*) organisms that cause disease in humans. P1 and P9 demonstrated differing activity against the isolates examined: P1 potently killed the two Gram-positive organisms, whereas P9 showed less activity against *E. faecium* and no activity against *S. aureus*. While both P1 and P9 were potent antimicrobials against some Gram-negative organisms (*S. typhi, S. flexneri*), P9 demonstrated greater activity than P1 against *A. baumanii* and *P. aeruginosa*. Some of these trends were replicated when the assay was performed in isotonic Roswell Park Memorial Institute (RPMI) medium; P1 is still much more active than P9 against *S. aureus* and P1 still potently inhibits *S. typhi* and *E. cloacae,* although P9 activity is lost against *S. typhi*, *E. cloacae*, and *P. aeruginosa* (Figure A.1C).

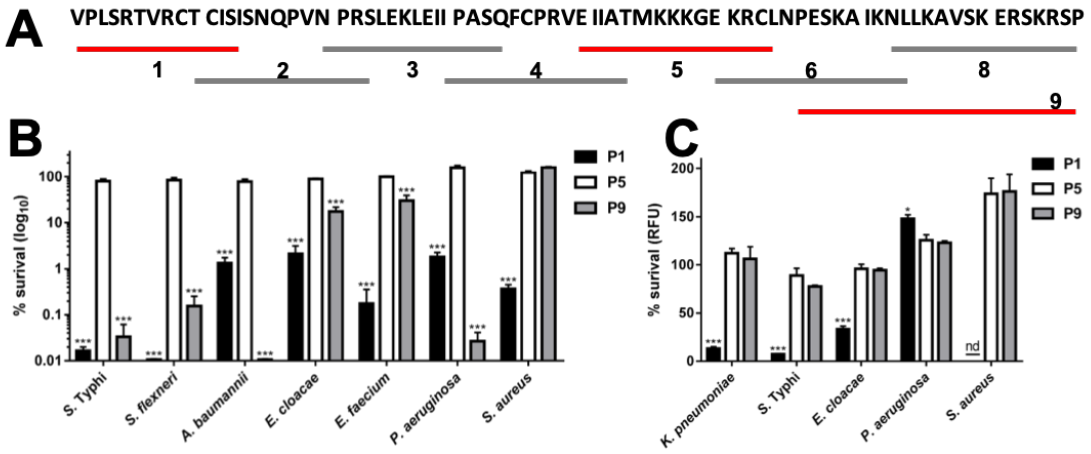

Figure A.1: Bacterial survival after CXCL10 peptide treatment. A. Schematic depicting the division of CXCL10 into peptides; the three peptides examined in this study are denoted with red bars. **B**. Bactericidal activity of P1, P5, and P9 in hypotonic buffer against multidrug resistant panel. Killing of the indicated bacterial pathogen upon exposure to 1.4 μM (MDR *A. baumannii*), 2.8 μM (MDR *S. flexneri* and MDR *S.* Typhi), 5.6 μM (MDR *P. aeruginosa*), 11.2 μM (MRSA and VRE), or 16.8 μM (MDR *Enterobacter cloacae*), peptide P1, P5, or P9 in 10 mM potassium phosphate buffer supplemented with 1% Tryptic Soy Broth as measured by colony-forming unit (cfu) determination. Data expressed as % survival (log_{10}) relative to the species-matched untreated control, represent the mean ± SEM. n = 3. **C**. Bactericidal activity as measured using the fluorescent viability reagent alamarBlue. Indicated bacteria were treated with 50 μM P1, P5, or P9 in RPMI medium against selection of multidrug resistant organisms. Data expressed as % survival as above and are from three replicate experiments. Error bars are SEM. nd, none detected. *** $p < 0.001$ by one-way ANOVA with Dunnett's multiple comparisons post hoc test.

CXCL10-derived peptides show minimal toxicity against human cells.

While P1 and P9 are able to decrease bacterial viability, their suitability as potential antimicrobial therapy depends on their toxicity against eukaryotic cells as well. For example, the peptide, melittin, found in bee venom, potently kills both bacterial and eukaryotic cells by permeabilizing their plasma membranes, making it unsuitable as an antibiotic. As a well-studied peptide with a known mechanism of action, we used it as a control for studies of CXCL10 peptide toxicity against human cells. When added to red blood cells (RBCs), melittin permeabilizes the cellular membrane, releasing pigmented hemoglobin into the supernatant which is detectable by increased absorbance at 540 nm (Figure A.2A, black diamond). When CXCL10 peptides at a range of concentrations are added to RBCs, hemolysis is nearly undetectable for most conditions (Figure A.2A). Very low hemolytic activity of CXCL10 peptides is encouraging for their suitability as antimicrobial therapy, although RBCs are highly specialized cells that lack typical organelles and do not perform the same functions as most human cell types. To assess peptide toxicity against a more typical human cell, we observed CXCL10 peptide activity against Human Embryonic Kidney (HEK293T/17) cells. After peptide treatment, viability was assessed by staining with the LIVE/DEAD kit components, calcein-AM and ethidium homodimer, as has been described previously (Apostol et al., 2003; Fifre et al., 2006). Echoing the hemolysis data, P5 and P9 at all concentrations tested had no effect on cell viability although P1 slightly reduced viability in a concentration dependent manner (Figure A.2B). However, cytotoxicity by P1 was much smaller than that of melittin and P1-treated samples showed >75% viability at concentrations up to 20 μM.

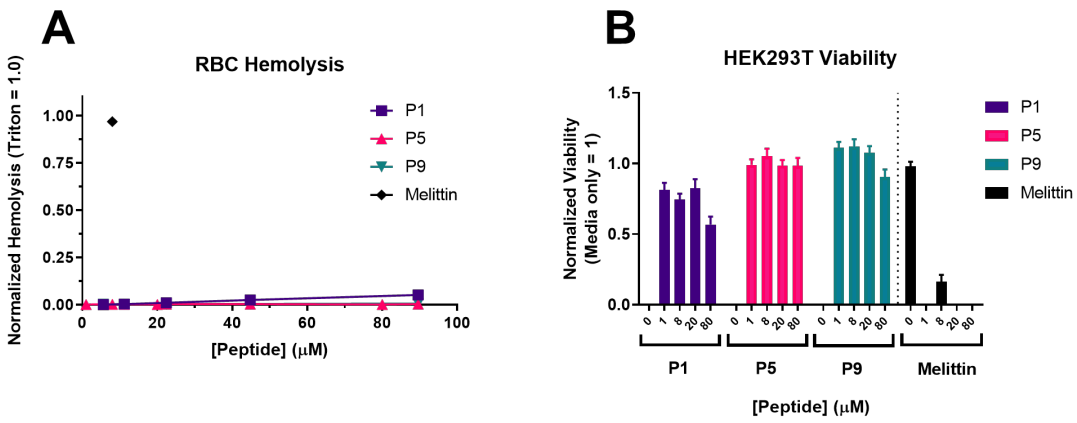

Figure A.2: CXCL10-derived peptides show low toxicity against human cells. A. Human red blood cells (RBCs) in RPMI medium were treated with peptides at the concentration shown on the X-axis, and hemolysis was assessed relative to the complete permeabilization of RBC membranes with Triton X-100. Data points represent mean values from at least three replicate experiments. Error bars are SEM and plotted for all data points. B. Viability of peptide-treated HEK293T cells in RPMI medium as assessed by the ratio of calcein-AM to ethidium homodimer staining and normalized to media alone condition (Melittin, 0μM). Data are mean with SEM from at least three replicate experiments.

CXCL10-derived peptides permeabilize LUVs.

Membrane permeabilization is a principal mechanism by which antimicrobial peptides kill bacteria (Mahlapuu et al., 2016). To test if CXCL10-derived peptides can permeabilize bacteria-like and/or eukaryotic-like model membranes, we assessed dye leakage from large unilamellar vesicles (LUVs). P1 and P9 permeabilized LUVs of all compositions in a concentration dependent manner up to a plateau. For all four

compositions tested, P1 permeabilized most potently, followed by P9 and finally P5 which showed low permeabilization of all compositions of LUVs (Figure A.3). There are subtle differences in the concentration dependence for each LUV composition but generally, the extent of permeabilization was independent of composition. If selective permeabilization of bacterial but not eukaryotic membranes were the major mechanism of action of CXCL10 peptides, there should be stark differences in permeabilization between the bacteria-like *E. coli* PL and PE:PG LUVs (Figure A.3A and A.3C), and the eukaryotic-like membranes containing cholesterol (Figure A.3B and A.3D); these differences were not observed. While LUVs model simplified lipid compositions of cellular bilayers fairly well, they do not reproduce additional factors such as curvature or protein composition. Based on these data, P1, and to a lesser extent P9, can interact with and permeabilize protein-free lipid bilayers. The discrepancy between effective bacterial killing with low eukaryotic cell toxicity and comparable permeabilization of bacterial and eukaryotic-like LUVs suggest that selective permeabilization of bacterial membranes may contribute to, but is not the entirety of the mechanism of action of P1 or P9. Additional factors may regulate the activity of P1 and P9.

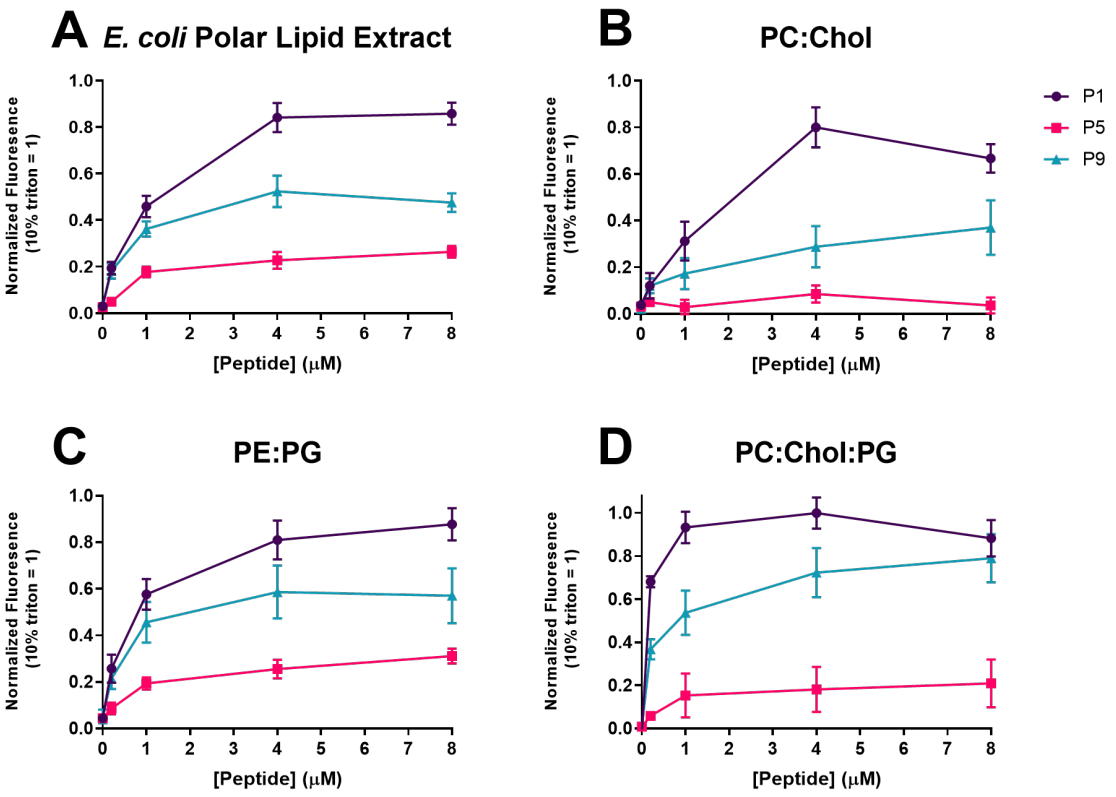

Figure A.3: Permeabilization of LUVs of differing composition by CXCL10-derived peptides. LUVs loaded with a self-quenching concentration of the soluble fluorophore calcein were treated with CXCL10-derived peptides in hypotonic phosphate buffer at concentrations listed on the X-axis. Permeabilization was detected by increased fluorescence as calcein is diluted in the bulk buffer and dequenches. Data are normalized to Triton X-100 detergent treatment and are from at least 4 separate experiments. LUVs were composed of **A**. *E. coli* polar lipid (PL) extract, **B.** 4:1 molar ratio of brain phosphatidylcholine (brainPC):cholesterol, **C.** 7:3 molar ratio of dioleoylphosphatidylethanolamine (DOPE) DOPE to palmitoyloleoylphosphatidylglycerol (POPG), or **D**. 5:2:3 molar ratio of brainPC:cholesterol:POPG.

Classical AMPs adopt an α-helical secondary structure although β-strand and unordered AMPs have been described as well. We used circular dichroism (CD) spectroscopy to assess the secondary structure of P1 and P9 in buffer or membrane mimetic environments. In aqueous buffer, both P1 and P9 are largely unordered (Figure A.4A and A.4B, black lines) but their spectra shift with the addition of the organic solvent, trifluoroethane (TFE), or *E. coli* PL LUVs (Figure A.4A and A.4B). Using the SELCON3 algorithm to estimate the fraction of residues in a specific secondary structure from CD spectra, we quantified the fraction of unordered residues in P1 and P9 (Figure A.4C and A.4D). The fraction of unordered residues in P1 is unchanged by TFE addition, but steadily decreases with increasing concentration of LUVs (Figure A.4C). In contrast, the fraction of unordered residues in P9 drastically decreases with TFE addition and is similarly decreased by all concentrations of LUVs (Figure A.4D). The increased order in P1 upon increasing LUV addition tracks with increasing adoption of a β-strand secondary structure (Figure A.4E). Similarly, the increased order in P9 upon TFE addition is due to adoption of an α-helical secondary structure (Figure A.4F). While the fraction of unordered residues in P9 does not change dramatically with increasing concentration of LUVs, the fraction of α-helical residues does. These data suggest that both peptides become more ordered in membranes although P1 primarily adopts a β-strand secondary structure whereas P9 is more like a classical, α-helical AMP. Hydrophobicity as supplied by TFE is sufficient for P9 to become helical but hydrophobicity alone is not sufficient for P1 to increase its β-strand content.

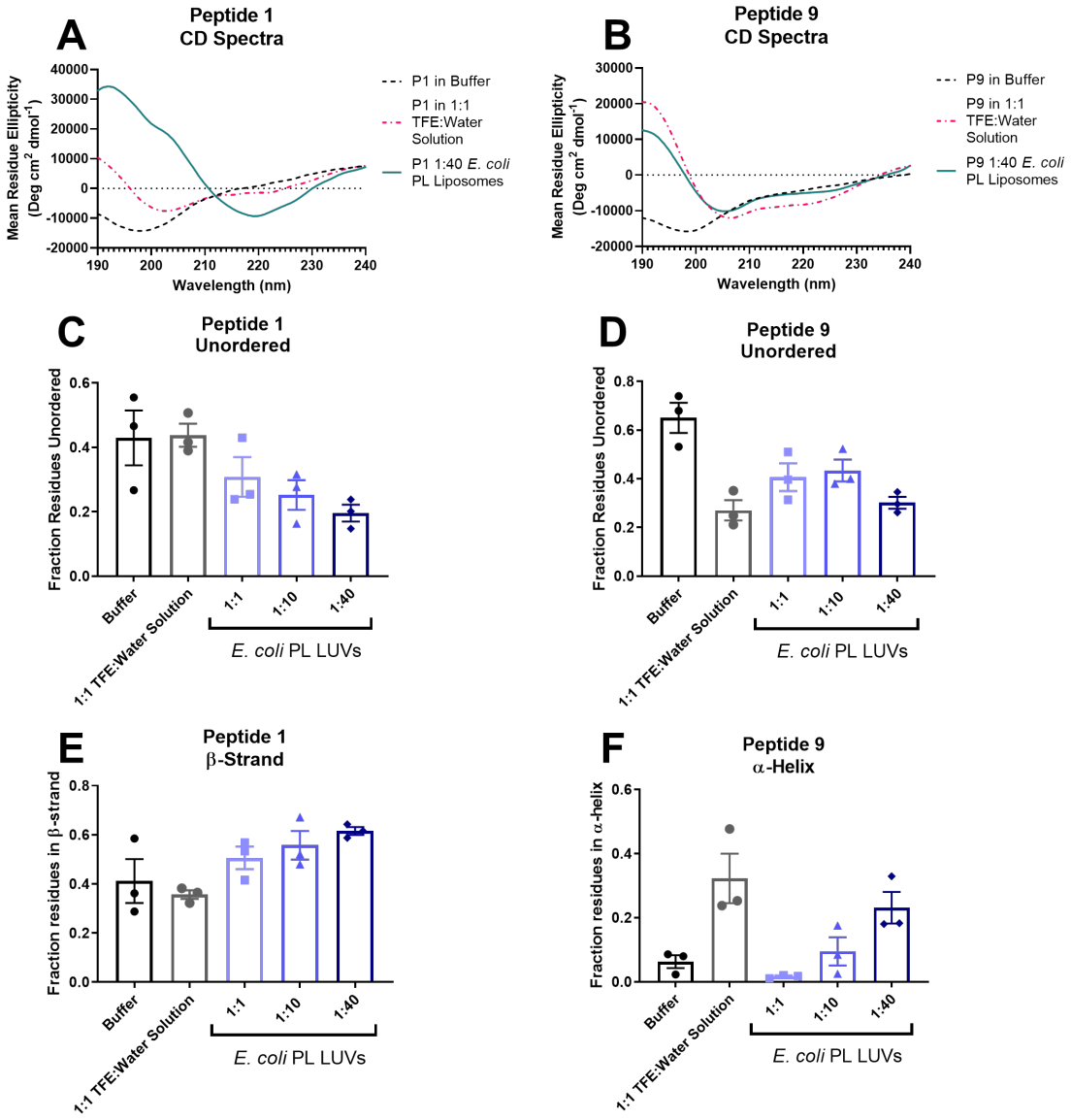

Figure A.4: Secondary structure of P1 and P9 in membrane mimetics. A. and B. CD spectra of P1 and P9 in hypotonic phosphate buffer (black lines), a 1:1 trifluoroethane (TFE) and water mixture (pink lines), or LUVs composed of *E. coli* polar lipid extract (teal lines). Lines are the average of six spectra from at least three separate experiments with LOWESS smoothing. **C-F.** SELCON3 estimates from CD spectra of the fraction of residues in a secondary structure. In addition to the conditions shown in panels A and B,

LUVs were titrated to give the peptide to lipid molar ratios listed below the X-axis. Each point is a prediction from the average of two spectra from the same sample. Data are from three separate experiments. Mean and SEM are plotted for each. **C. and D.** Prediction of fractions of unordered residues **E.** Predictions of the fraction of P1 residues in a β-strand-like fold. **F.** Predictions of the fraction of P9 residues in an α-helix-like fold.

Discussion:

The increasing prevalence of infections caused by multidrug-resistant organisms is an issue of great concern, which may be partially alleviated by the development of novel antibiotics. In this work, we have demonstrated that peptides derived from the N- and C-terminus of CXCL10 (P1 and P9, respectively) show broad antimicrobial activity against Gram-negative and -positive multidrug-resistant bacterial pathogens (Figure A.1B and 1C) with minimal toxicity against human cells (Figure A.2). These *in vitro* results are encouraging, and will be followed by *in vivo* experiments demonstrating therapeutic utility (e.g. improved bacterial clearance, decreased mortality, decreased weight loss, etc.) in an animal model of bacterial infection.

Building on previous reports of CXCL10's dual mechanisms of action (Crawford et al., 2011; Margulieux et al., 2016), we have begun to investigate the apparently distinct mechanisms of actions of P1 and P9. With LUV permeability experiments (Figure A.3) and CD spectroscopy (Figure A.4), we have demonstrated that P1 and P9 are capable of interacting with lipid bilayers and change conformation upon doing so— hallmarks of AMPs (Huan et al., 2020). While both peptides are capable of permeabilizing LUVs to a greater extent than the inactive control peptide, P5, P1 does so more potently than P9

(Figure A.3). This apparent difference in potency could be explained by the higher portion of lysine residues in P9 than in P1 (5 vs 0), which are known to favor lipid translocation across bilayers rather than true permeabilization (Kol et al., 2001). In support of this, alanine scan mutations demonstrated the importance of all five lysines in P9 for antimicrobial activity (data not shown). However, P5 which does not kill bacteria also has three lysines; thus, lipid translocation via lysine residues may contribute to, but is not the sole mechanism of action of P9. Most cationic AMPs are thought to act by binding the higher proportion of negatively charged lipids, like PG, in bacterial membranes. We did observe increased potency of P1 and P9 in membranes containing PG (Figure 3D) as compared to a similar composition that lacked PG (Figure A.3B) but the difference was not large enough to explain selective permeabilization of bacterial but not eukaryotic membranes.

An alternative model for AMP activity is depolarization rather than permeabilization of membranes (Mahlapuu et al., 2016). Upon interaction with membranes, some AMPs are thought to collapse the membrane potential, thereby inhibiting respiration and disrupting osmotic regulation. Eventually, these changes would be expected to lead to membrane permeabilization and membrane permeabilization also collapses membrane potential so these two models are not completely distinct (Yeaman and Yount, 2003). Membrane depolarization by CXCL10 peptides could be assessed using the potentiometric probe, DiSC3-5. This fluorescent probe accumulates on hyperpolarized membranes to self-quenching concentrations and upon depolarization, dissociates from membranes resulting in an increase in fluorescence (Shapiro, 1994;

Singh and Nicholls, 1985). Further studies of the effect of CXCL10 peptides on membrane potential may be important for elucidating their mechanisms of action.

Yet another described mechanism of action of some AMPs is the collapse of bacterial proteostasis by targeting aggregation prone regions in the bacterial proteome with an amyloidogenic peptide (Khodaparast et al., 2018). While the data presented on P1 is limited and thus concluding on its mechanism of action is speculative, the available data are consistent with bactericidal activity via amyloid formation on bacterial membranes. While mostly unstructured in aqueous buffer, P1 adopts a β-strand in the presence of lipid bilayers (Figure A.4A, A.4C, and A.4D). The hydrophobic environment of TFE is not sufficient to induce this transformation so the conformational switch may be the addition of an organizing surface, like LUVs, for multimerization and the formation of β-sheets. Consistent with these data, P1 in RPMI+5.5 BSA mg/mL, as imaged by cryoEM, had no discernable features but when P1 in the same medium was added to supported lipid bilayers composed of *E. coli* PL, electron-dense round features of similar size but variable shape were visualized (Figure 4.5). The similar sizes suggest some ordering principle in the formation of these multimers, such as amyloid formation, but the lack of a defined structure disfavors a specific interaction interface. These data may also indicate the formation of membrane pores as has been described for other β-strand AMPs (Lipkin and Lazaridis, 2015; Rausch et al., 2007, 2005). The detection of an amyloid specific fold with the fluorescent amyloid probe, Thioflavin T, may help distinguish between these two possible mechanisms (Xue et al., 2017). If P1 did adopt an amyloid-like fold upon association with bacterial or bacterial-like membranes, it could

suggest P1 kills bacteria by targeting aggregation prone regions of the bacterial proteome as has been described by Khodaparast et al., 2018.

In summary, we have demonstrated that P1 and P9 are capable of permeabilizing membranes and that both peptides undergo structural changes upon interaction with membranes, typical characteristics of AMPs. Our *in vitro* demonstration of the broad antibacterial activity and low cytotoxicity of P1 and P9 makes both of them promising potential therapeutics deserving of additional study.

Materials and Methods:

Reagents: The following compounds were purchased from Avanti Polar Lipids and used without modification: brain phosphatidylcholine (brainPC), *E. coli* polar lipid extract (*E. coli* PL), 1-palmitoyl-2-oleoyl-sn-glycero-3-phosphoethanolamine (POPE), and 1,2-dioleoyl-sn-glycero-3-phospho-(1'-rac-glycerol) (DOPG). Cholesterol and bovine serum albumin (BSA) were purchased from Sigma-Aldrich. Peptides were custom synthesized by GenScript by solid-state, microwave-assisted peptide synthesis and purified by high pressure liquid chromatography (HPLC) before lyophilization.

Bacterial strains used in this study:

K. pneumoniae	BL13802 (CFSAN044570)
A. baumannii	AR0304
P. aeruginosa	AR0231

S. typhi	BL31130 (CFSAN059647)
S. flexneri	BL28504 (CFSAN059650)
E. faecium	AR0575
E. cloacae	BL36213 (CFSAN059636)
S. aureus	LAC (USA300)

Bacterial killing assays: Bacteria were inoculated from glycerol stocks into Luria Bertani (LB) broth and grown overnight at 37°C with shaking. A portion of the culture was diluted in fresh LB and grown to an OD_{600} of 0.6. The culture was then diluted in either RPMI (Gibco) or hypotonic media (10mM H_2KPO_4 with 1% tryptic soy broth) and mixed CXCL10 peptides at the concentration indicated in a 96 well plate. The plate was incubated at 37°C with shaking for 2 hours. To determine CFUs, bacteria were diluted in sterile saline and plated on LB agar. Treatment counts (CFU/ml) were divided by the average counts for the untreated control for the specific strain to determine % survival. To determine killing by alamarBlue staining, each well was diluted 1:2 in fresh 2x LB, divided into triplicates, and transferred to a new 96-well plate. 10% (v/v) of alamarBlue Cell Viability Reagent (ThermoFisher) was added to each prepared well and incubated in the dark at 37°C without shaking. As alamar Blue is reduced by live, metabolically active bacteria, it generates a fluorescent product and also changes color by eye. The incubation was allowed to proceed until the untreated control showed adequate color change. Fluorescence (Exc 530/10 nm, Emis 590/20 nm) was measured in a PerkinElmer VICTOR Multilabel Counter. All wells were blanked by subtracting the average signal from wells containing buffer alone + alamarBlue. Treatment wells (peptide, vehicle, etc.)

were normalized to the strain-specific untreated controls for that particular experiment to calculate % survival.

Fluorescent content LUV preparation: Chloroform stocks of desired lipids were mixed and the solvent was evaporated under a gentle stream of nitrogen gas. The resulting lipid film was desiccated under vacuum for at least one hour before resuspension in potassium phosphate buffer with calcein (10mM H_2KPO_4, 75mM calcein, pH 7.4) to a final concentration of 1mM. After vortexing at room temperature, the lipid suspension was subjected to 10 freeze/thaw cycles in liquid nitrogen and warm water before extrusion through a 200nm nanosizer (T&T Scientific). LUVs were separated from free dye by size exclusion with a PD-10, Sephadex G-25 column (GE LifeSciences), followed by pelleting and washing twice with phosphate buffer without calcein at 100,000 xg at 4°C for 1 hour. LUVs were stored at 4°C and used within 24 hours of extrusion.

LUV permeability assay: The concentration of LUVs was adjusted to be roughly equivalent based on their fluorescence intensity (Exc 485 nm Emis 538 nm) and 90 μL of the adjusted LUV suspension was added to each well of a clear-bottom, 96-well plate. The fluorescence intensity of each well was measured as baseline ($I_{baseline}$) in a SpectraMax M5 plate reader (Molecular Devices). Peptides were diluted in potassium phosphate buffer (10mM H_2KPO_4, pH 7.4) and added to the appropriate well. The fluorescence intensity of each well was measured again, 15 minutes after the addition of peptides. LUVs were then fully permeabilized by the addition of 10% Triton X-100 and

the maximum fluorescence intensity was measured (I_{max}). The normalized fluorescence intensity was calculated for each well with the following equation:

$$I_{normalized} = \frac{I - I_{baseline}}{I_{max} - I_{baseline}}$$

CD spectra acquisition and analysis: Peptides were dissolved in potassium phosphate buffer (10mM H_2KPO_4, pH 7.4) and diluted to a final concentration of 20.83 μM with 50% (v/v) Trifluoroethane (TFE) in water, LUVs in potassium phosphate buffer, or buffer only and incubated at 37°C for 1 hour. The mixtures were transferred to 2 or 0.5 mm quartz cuvettes and spectra were collected from 190 to 250 nm with a wavelength step of 1 nm in either a JASCO J-1500 or an AVIV model 215 spectropolarimeter. Two spectra for each sample were collected at room temperature and averaged. Spectra were analyzed and converted to mean residue molar ellipticity with DichroWeb using the SELCON3 algorithm (Sreerama and Woody, 1993; Whitmore and Wallace, 2008). Mean residue molar ellipticity was calculated with the following equation:

$$\Delta\boldsymbol{\varepsilon} = \boldsymbol{\theta} * \frac{(\mathbf{0.1} * \boldsymbol{M})}{(\boldsymbol{L} * \boldsymbol{C} * \mathbf{3298})}$$

Where Δε is mean residue ellipticity in degrees cm^2 $dmol^{-1}$ $residue^{-1}$. θ is the measured ellipticity in millidegrees. M is mean residue weight given by the peptide's weight in daltons/the number of peptide bonds (the number of residues minus one). L is the pathlength of the cuvette given in cm. C is the concentration of the peptide in g/L.

Hemolysis assay: Human venous blood was drawn from consenting donors in accordance with an approved IRB protocol. RBCs were then separated from other blood

components by a Ficoll gradient as previously described (Ragland and Criss, 2019). RBCs were then washed three times in phosphate buffered saline (Gibco), with pelleting at 1000xg for 10 minutes at 4°C. After the final wash, the supernatant was carefully removed and an adequate volume of RPMI + 5.5 mg/mL BSA was added to yield a 10% (v/v) solution of RBCs. Peptides or controls (medium alone or 20% Triton X-100) were diluted in the same medium in a v-bottom 96-well plate and the RBC solution was added to each well with mixing. The plate was covered and incubated at 37°C for 1 hour before centrifuging at 500 xg for 5 minutes to pellet intact RBCs. The resulting supernatant was carefully transferred to a clear-bottom 96-well plate and the absorbance at 540 nm was measured in a SpectraMax M5 plate reader (Molecular Devices). Normalized hemolysis was calculated relative to Triton X-100 condition with the following formula:

$$Hemolysis_{normalized} = \frac{A - A_{medium}}{A_{Triton} - A_{medium}}$$

Cell viability assay:

HEK 293T/17 cells (ATCC) were maintained in high glucose Dulbecco's Minimum Essential Media (Gibco) supplemented with 10% fetal bovine serum (Atlanta Biologicals), 1% antibiotic-antimycotic (Gibco), 1 mM sodium pyruvate (Gibco), and 2 mM glutamine (Gibco). For viability assays, cells were cultured in clear, cell-culture-treated, 48-well plates overnight in the same medium and environmental conditions. Growth media was removed and cells were washed with phosphate buffered saline (PBS). Peptides diluted in RPMI + 5.5 mg/mL BSA were incubated with cells for 1 hour at 37°C. Medium was then aspirated and cells were stained with LIVE/DEAD kit

components (ThermoFisher) according to the manufacturer directions. Fluorescence of each well was measured in a SpectraMax M5 plate reader (Molecular Devices) in well scan mode. Fluorescence from two wavelengths (Exc1 488 nm Em1 508 nm Cutoff1 495 nm; Exc2, 528 nm Em2 617 nm, Cutoff2 610 nm) was measured and intensity of all tiles in a well was summed. The ratio of intensities in green/red channels for a well was normalized to the ratio from untreated control wells which received only RPMI + BSA.

Appendix B: Design, rapid prototyping, and usage of a modular chamber for TIRF microscopy

Introduction:

Total Internal Reflect Fluorescence (TIRF) Microscopy is a diffraction-limited, widefield illumination technique that improves on the signal-to-noise ratio of epifluorescence by exclusively exciting fluorophores within approximately 100 nm of a support material of higher refractive index than the sample (Tamm, 1993). This can be accomplished one of two ways: objective based TIRF and prism-based TIRF. Both rely on altering the angle of incidence of the excitation light but use different optic configurations to achieve it. In an objective based TIRF microscope, the excitation light is translated from the optical axis at the back focal plane of the microscope such that it is incident upon the sample coverslip at or above the critical angle at which it is totally internally reflected. In contrast, prism-based TIRF uses a prism in contact with the support material and cut on the correct angle to bend the excitation light to the critical angle in the support material. As the prisms used for this are quartz, this means the support material must be quartz as well to achieve internal reflection at the support material/aqueous sample interface rather than at the prism/support material interface (Martin-Fernandez et al., 2013). While there are many iterations of this general design (Chen et al., 2013), the simplest requires the sample to be enclosed on the bottom by coverglass suitable for the objective and by a quartz slide (to match the refractive index of the prism) on top. The distance separating them must be less than the focal length of the objective to ensure focus at the correct plane. Additionally for TIRF of supported

lipid bilayers, the quartz slide must be useable in the Langmuir-Blodgett trough so the sample chamber for prism-based TIRF must be able to be disassembled and reassembled.

Dr. Volker Kiessling had machined an aluminum and Teflon sample chamber for prism-based TIRF that met these criteria but the design could be improved upon. In this original design, the TIRF chambers were composed of an aluminum frame that held a quartz slide and a second aluminum and teflon piece glued to a glass coverslip. Both sides were held together around the quartz slide by four screws. Firstly, the design required at least 1.2 mL of sample and/or buffers to fill. For abundant or concentrated samples this was no issue but for scarce and expensive samples, this limited the number of samples that could be examined. Second, two small channels in the Teflon piece could be accessed by a 26 gauge needle bent at a 90 degree angle to exchange buffers but this channel could become blocked by the glue. Difficulties accessing these flow channels frequently led to backflow of buffers and leakage. Third, the coverglass frequently cracked during use, leading to leakage of sample and requiring frequent maintenance of the chambers to replace broken glass. Finally, the four screws holding the chamber together received daily wear as the chambers were assembled and disassembled repeatedly and exposed to corrosive buffers. Corrosion and thread stripping meant the screws did not reliably create a water tight chamber, also leading to leakage and sample loss. Experience with the previous chambers motivated the following design criteria:

1) Glass coverslip and quartz slide are held at a set distance compatible with the focal length of a 63X objective.

2) Aqueous buffers can be rapidly exchanged from the water-tight chamber without leaking
3) The volume of sample required to fill imaging chamber is minimized
4) The chamber is easily assembled and disassembled
5) Only infrequent maintenance is required

To achieve this, I designed the new chambers in CAD, compared various materials and additive manufacturing (3D printing) methods, and tested performance against the criteria listed above. Here, I narratively describe the iterative design process followed by excerpts from the provisional patent filing of the final design.

The initial design used disc magnets to hold two cassettes together around a coverslip, a flow insert with tubing attachments, and the quartz slide. Each part was modified several times but the overarching concept remained. The disc magnets were replaced with bar magnets (Figure B.1, column 1-10 vs 11-12) to deliver more force (2.3lbs vs. 0.3lbs) and ensure adequate pressure for a water-tight seal. The rigid tubes in the initial design attached well to flexible tubing but the flow insert itself did not form a water-tight seal and thus was replaced with a rubber-like polymer, TangoBlack. This required redesign of how buffers would be exchanged through the chamber (Figure B.1, columns 5-9). Rather than flexible tubing attached to a rigid tube, a semi-rigid intravenous (IV) catheter was inserted into the flexible TangoBlack flow insert. The inclusion of an IV catheter as the tubing adaptor also allowed luer lock connections to more complicated tubing to regulate the flow of multiple reagents in and out of the chamber. All of the luer lock tubing, stopcocks, etc. used for these purposes were past expiration date surplus infusion supplies

acquired from the hospital medical equipment recycling center. With a few iterations to adjust the width of the flow insert (Figure B.1, columns 5-9), the coverglass and quartz were at an acceptable distance such that the objective could focus on the quartz. This design met the criteria listed above and is shown in more detail in Figure B.2.

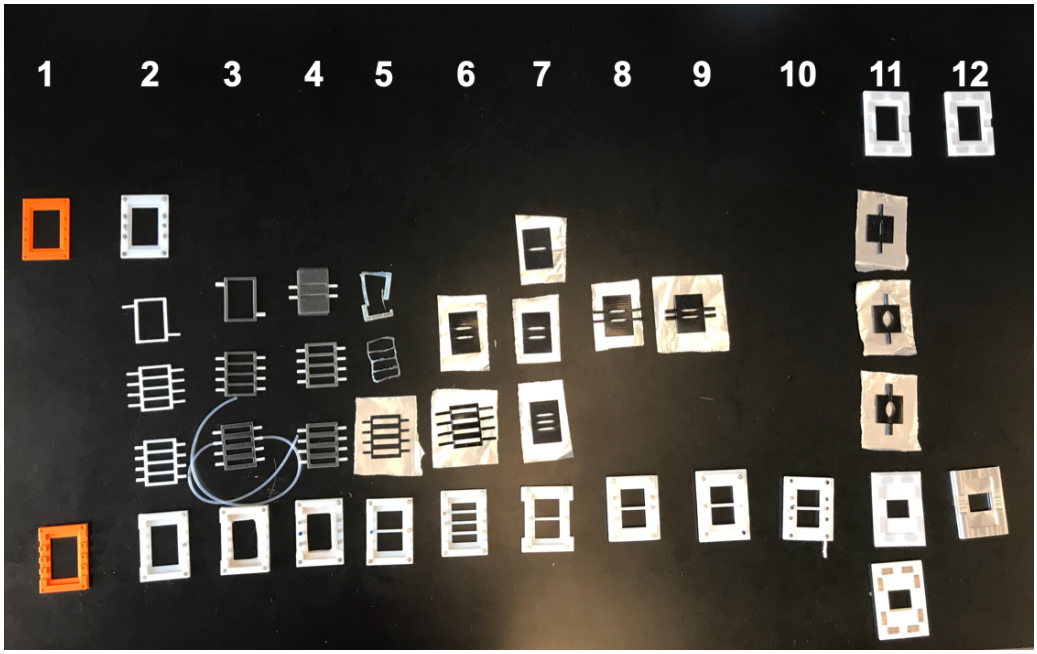

Figure B.1. Prototyping a modular 3D printed sample chamber for TIRFm. Objects are arranged chronologically from left to right. The multiple parts that composed an assembly are grouped into a column. Aluminum foil was placed under parts in columns 5-11 to create contrast between a black object and the black background. Parts that remained unchanged in the subsequent iteration of an assembly are not duplicated; thus the top-most object in column 2 is included in the assemblies in columns 3-10.

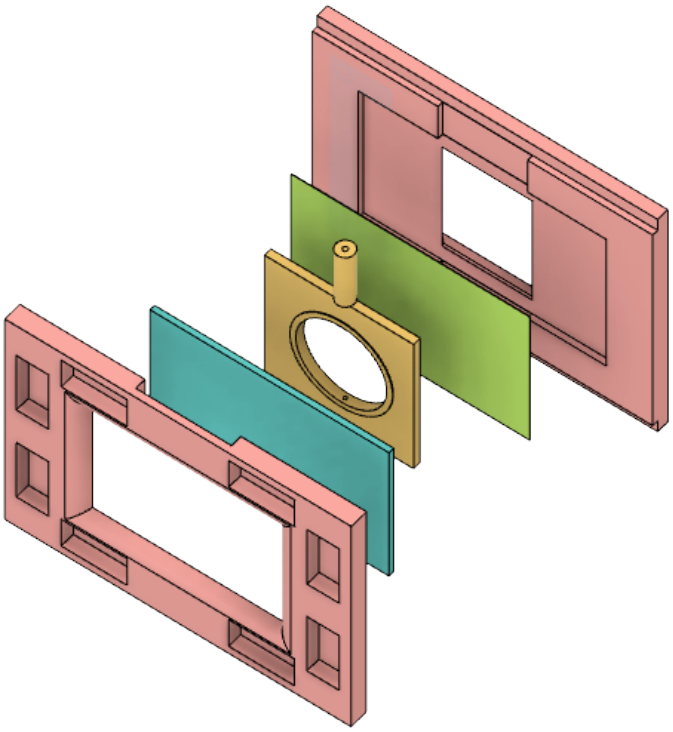

Figure B.2. Exploded-view CAD rendering of final assembly. The 3D printed flow insert (yellow) is held between a quartz slide (teal) and glass coverslip (green) by a bar magnets in two halves of a rigid cassette (pink)

The third design criterion, minimize volume required to fill the chamber, comes at the expense of area available for observation. The acceptability of this compromise may depend on the goals of the experiment and thus I took advantage of the modularity of the sample chamber and designed flow inserts with various configurations. For experiments where maximizing viewable area is higher priority than minimizing sample volume, the flow insert with circular area (Figure B.3, yellow) can be used with no other modification of the chamber. For the opposite case, the flow insert with the more narrow channel could

be used (Figure B.3, orange). For most experiments, a compromise between both is preferable (Figure B.3, red) and anecdotally, this shape allows even flow of fluids in the chamber, an important quality for creating supported lipid bilayers on Langmuir-Blodgett monolayers. Expanding on the idea of modularity, I also designed an insert with two inlets and two outlets for an experiment observing the mixing of two reagents or to accommodate simultaneous data acquisition with a microprobe for pH (Figure B.3, green). Additionally, to increase throughput by observing two samples on one slide, I created a flow insert with two separate channels (Figure B.4, blue). Observing two samples on one slide is one approach to maximizing throughput for the single-particle TIRF assay described in chapters 2 and 3 but I also developed a secondary approach to increase throughput of lipid monolayer deposition on quartz with the Langmuir-Blodgett trough described below.

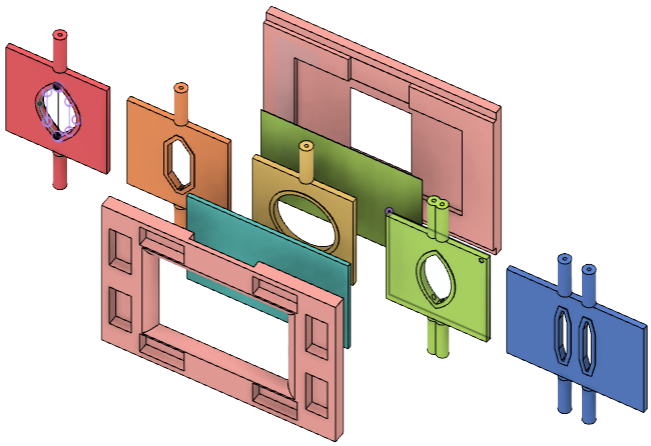

Figure B.3. Exploded-view CAD rendering of assembly, demonstrating modularity and adaptability of the flow insert. Five examples of flow inserts suited for different purposes are shown side by side. Only one can be used a time.

Excerpt from Provisional Patent:

"An aspect of an embodiment of the present invention provides, among other things, a TIRF sample chamber that can be 3D printed inexpensively and efficiently. An aspect of an embodiment of the present invention provides among other things, an improved design to simplify and improve aspects related to: cleaning/repairing, decreasing the volume of sample required, and incorporating luer lock tubing for easy liquid exchange through the chamber. In an aspect of an embodiment the chamber may be composed of three 3D printed parts, 16 small bar magnets, a glass coverslip and a quartz slide. Additionally, an aspect of an embodiment of the present invention provides, among other things, a design providing modularity that allows the inner-most part, the "flow insert", to be adapted to the requirements of different samples. For example, some experiments can be performed with just one "in" flow port and one "out" flow port but to examine the mixing of two components requires two "in" flow ports. This may be achieved by swapping the flow insert for one with two "in" flow ports while the rest of the chamber may remain the same.

An aspect of an embodiment of the present invention provides, among other things, a 3D printed sample chamber for total-internal reflection fluorescence microscopy, and related method of use and manufacture.

An aspect of an embodiment of the present invention provides, among other things, 3D printed microscopy chambers, and related methods of use and manufacture.

An aspect of an embodiment of the present invention provides, among other things, an approach whereby the total cost of the chamber is about $20-$25 and all parts

are reusable. TIRF microscopy is used by many fields including cell biology, physiology, and biophysics and a low-cost sample chamber could be of interest to those who use it.

An aspect of various embodiments of the present invention may provide a number of novel and nonobvious features, elements, advantages, and characteristics, such as but not limited thereto, the following:

1. An aspect of an embodiment of the present invention provides, among other things, the capability of manufacturing of a sample chamber by 3D printing.

2. An aspect of an embodiment of the present invention provides, among other things, a sample chamber that may be completely closed except for the inlet and outlet so it can be used with both upright and inverted microscopy without any modification.

3. An aspect of an embodiment of the present invention provides, among other things, a sample chamber that may be easily assembled and disassembled. This means, for example but not limited thereto, the glass coverslip and/or quartz slide can be separately treated or modified in a myriad of way. Examples of potential modifications may include, but not limited thereto:

    a. Culturing cells or tissues on the quartz slide.

    b. Protein binding for measurement of binding kinetics.

    c. Microarray of DNA, RNA, or proteins.

    d. Charge deposition with plasma treatment.

    e. Material deposition or modification (sialyation, oxide deposition, etc.)

    f. Micropatterning or etching.

4. An aspect of an embodiment of the present invention provides, among other things, a sample chamber that is modular so slides, coverslips, flow gaskets, optical elements, sensors, and more can be incorporated as needed to accommodate a broad range of experiments. The case may include magnet closure that fits into common microscopy stages and provides a constant base for nearly all possible variations.

Design and prototyping of a multisubstrate holder for Langmuir-Blodgett monolayer deposition:

Developed by Dr. Katharine Blodgett, the first woman to earn a PhD in physics from Cambridge ("Katharine Burr Blodgett," 1980), the Langmuir-Blodgett trough is a device for depositing a single molecule thick Langmuir-Blodgett film by slowly dipping a substrate through a monomolecular film of amphiphiles layered on top of water. Langmuir-Blodgett troughs are commercially available with a motorized arm to control the speed of substrate dipping although most only hold one substrate at a time. I designed and prototyped a substrate dipper that can dip up to 6 quartz slides, glass coverslips, or silicon wafers at a time. Laterally expanding the design of the manufactured substrate holder allows three substrates to be dipped at once. In the manufactured holder, a spring clip holds the substrate in place but to simplify the design and allow a second layer of substrates on the back, the new design uses 10x5x2 mm magnets to hold the substrate in place; a magnet is inserted into a hollow space in each of the three prongs and a second magnet is used to hold a substrate to that prong. A cushion is used between the exterior magnets and substrate for delicate substrates that can crack or scratch. With a long post, the new dipper design fits into the round adaptor for the trough and can be used without

any other physical modification. To accommodate the increased surface area, the rate of compression of the lipid surface must also be increased to ensure maintenance of a constant pressure.

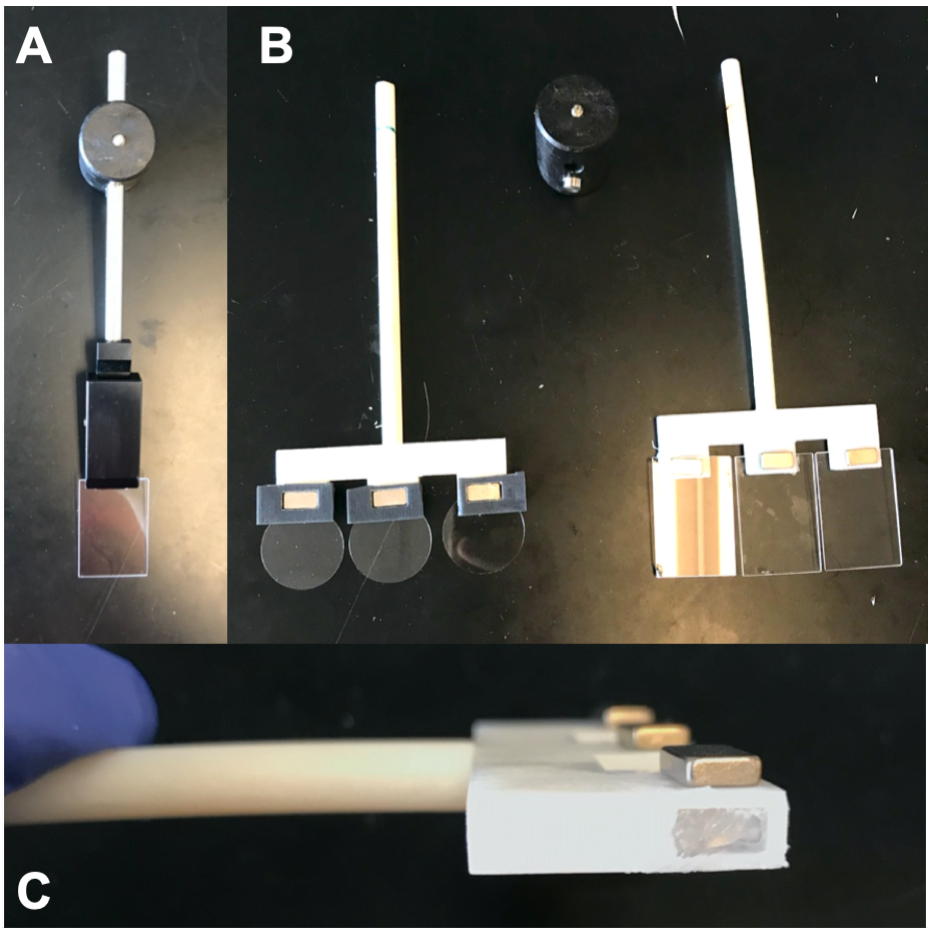

Figure B.4 Multisubstrate holder for Langmuir-Blodgett film deposition. A. Commercially available substrate holder with single substrate. The holder attaches to the dipping mechanism of the Langmuir-Blodgett trough by the black, round piece. **B.** Multisubstrate holders with three substrates each. The post of the substrate holder inserts into the black, round piece. **C.** Side view of multisubstrate dipper showing the hollowed compartment where a bar magnet is inserted to produce an attractive force with the external bar magnet that holds the substrate in place.

References:

Abbe E. 1873. Beiträge zur Theorie des Mikroskops und der mikroskopischen Wahrnehmung: I. Die Construction von Mikroskopen auf Grund der Theorie. *Arch für mikroskopische Anat* **9**:413–418. doi:10.1007/BF02956173

Ackerman DG, Feigenson GW. 2015. Lipid bilayers: Clusters, domains and phases. *Essays Biochem* **57**:33–42. doi:10.1042/BSE0570033

Aeffner S, Reusch T, Weinhausen B, Salditt T. 2012. Energetics of stalk intermediates in membrane fusion are controlled by lipid composition. *Proc Natl Acad Sci U S A* **109**:E1609-1618. doi:10.1073/pnas.1119442109

Akabori K, Nagle JF. 2015. Structure of the DMPC lipid bilayer ripple phase. *Soft Matter* **11**:918–926. doi:10.1039/c4sm02335h

Albert S, Wietrzynski W, Lee CW, Schaffer M, Beck F, Schuller JM, Salomé PA, Plitzko JM, Baumeister W, Engel BD. 2020. Direct visualization of degradation microcompartments at the ER membrane. *Proc Natl Acad Sci U S A* **117**:1069–1080. doi:10.1073/pnas.1905641117

Albertini AA, Mérigoux C, Libersou S, Madiona K, Bressanelli S, Roche S, Lepault J, Melki R, Vachette P, Gaudin Y. 2012. Characterization of Monomeric Intermediates during VSV Glycoprotein Structural Transition. *PLoS Pathog* **8**:e1002556. doi:10.1371/journal.ppat.1002556

Alberts B, Johnson A, Lewis J, Raff M, Roberts K, Walter P. 2002a. Transport into the Cell from the Plasma Membrane: Endocytosis.

Alberts B, Johnson A, Lewis J, Raff M, Roberts K, Walter P. 2002b. Transport from the Trans Golgi Network to the Cell Exterior: Exocytosis.

Almazán F, Sola I, Zuñiga S, Marquez-Jurado S, Morales L, Becares M, Enjuanes L. 2014. Coronavirus reverse genetic systems: Infectious clones and replicons. *Virus Res* **189**:262–270. doi:10.1016/j.virusres.2014.05.026

Alsahafi N, Bakouche N, Kazemi M, Richard J, Ding S, Bhattacharyya S, Das D, Anand SP, Prévost J, Tolbert WD, Lu H, Medjahed H, Gendron-Lepage G, Ortega Delgado GG, Kirk S, Melillo B, Mothes W, Sodroski J, Smith AB, Kaufmann DE, Wu X, Pazgier M, Rouiller I, Finzi A, Munro JB. 2019. An Asymmetric Opening of HIV-1 Envelope Mediates Antibody-Dependent Cellular Cytotoxicity. *Cell Host Microbe* **25**:578-587.e5. doi:10.1016/j.chom.2019.03.002

Amara A, Mercer J. 2015. Viral apoptotic mimicry. *Nat Rev Microbiol* **13**:461–469. doi:10.1038/nrmicro3469

Ando T. 2019. High-speed atomic force microscopy. *Curr Opin Chem Biol*. doi:10.1016/j.cbpa.2019.05.010

Anthony SJ, Epstein JH, Murray KA, Navarrete-Macias I, Zambrana-Torrelio CM, Solovyov A, Ojeda-Flores R, Arrigo NC, Islam A, Khan SA, Hosseini P, Bogich TL, Olival KJ, Sanchez-Leon MD, Karesh WB, Goldstein T, Luby SP, Morse SS, Mazet JAK, Daszak P, Lipkin WI. 2013. A strategy to estimate unknown viral diversity in mammals. *MBio* **4**. doi:10.1128/mBio.00598-13

Aposhian HV. 1975. Pseudovirions in Animals, Plants, and BacteriaStructure and Assembly. Springer US. pp. 155–218. doi:10.1007/978-1-4684-2709-7_3

Apostol BL, Kazantsev A, Raffioni S, Illes K, Pallos J, Bodai L, Slepko N, Bear JE, Gertler FB, Hersch S, Housman DE, Marsh JL, Thompson LM. 2003. A cell-based assay for aggregation inhibitors as therapeutics of polyglutamine-repeat disease and

validation in Drosophila. *Proc Natl Acad Sci U S A* **100**:5950–5955. doi:10.1073/pnas.2628045100

Armstrong RT, Kushnir AS, White JM. 2000. The transmembrane domain of influenza hemagglutinin exhibits a stringent length requirement to support the hemifusion to fusion transition. **151**:425–437.

Arumugam S, Petrov EP, Schwille P. 2015. Cytoskeletal pinning controls phase separation in multicomponent lipid membranes. *Biophys J* **108**:1104–1113. doi:10.1016/j.bpj.2014.12.050

Ashdown GW, Owen DM. 2015. Imaging membrane order using environmentally sensitive fluorophores. *Methods Mol Biol* **1232**:115–122. doi:10.1007/978-1-4939-1752-5_10

Bailey CC, Huang IC, Kam C, Farzan M. 2012. Ifitm3 Limits the Severity of Acute Influenza in Mice. *PLoS Pathog*. doi:10.1371/journal.ppat.1002909

Bailey CC, Zhong G, Huang I-C, Farzan M. 2014. IFITM-Family Proteins: The Cell's First Line of Antiviral Defense. *Annu Rev Virol* **1**:261–283. doi:10.1146/annurev-virology-031413-085537

Baltimore D. 1971. Expression of animal virus genomes. *Bacteriol Rev*. doi:10.1128/mmbr.35.3.235-241.1971

Bangham AD, Horne RW. 1964. Negative staining of phospholipids and their structural modification by surface-active agents as observed in the electron microscope. *J Mol Biol* **8**:660–668. doi:10.1016/S0022-2836(64)80115-7

Barros M, Heinrich F, Datta SAK, Rein A, Karageorgos I, Nanda H, Lösche M. 2016. Membrane Binding of HIV-1 Matrix Protein: Dependence on Bilayer Composition and Protein Lipidation. *J Virol* **90**:4544–4555. doi:10.1128/jvi.02820-15

Basáñez G, Goñi FM, Alonso A. 1998. Effect of single chain lipids on phospholipase C-promoted vesicle fusion. A test for the stalk hypothesis of membrane fusion. *Biochemistry* **37**:3901–3908. doi:10.1021/bi9728497

Bauer B, Davidson M, Orwar O. 2009. Proteomic analysis of plasma membrane vesicles. *Angew Chemie - Int Ed* **48**:1656–1659. doi:10.1002/anie.200803898

Baumgart T, Hammond AT, Sengupta P, Hess ST, Holowka DA, Baird BA, Webb WW. 2007. Large-scale fluid/fluid phase separation of proteins and lipids in giant plasma membrane vesicles. *Proc Natl Acad Sci U S A* **104**:3165–3170. doi:10.1073/pnas.0611357104

Baumgart T, Hess ST, Webb WW. 2003. Imaging coexisting fluid domains in biomembrane models coupling curvature and line tension. *Nature* **425**:821–824. doi:10.1038/nature02013

Beitari S, Ding S, Pan Q, Finzi A, Liang C. 2017. Effect of HIV-1 Env on SERINC5 Antagonism. *J Virol* **91**. doi:10.1128/JVI.02214-16

Bhojoo U, Chen M, Zou S. 2018. Temperature induced lipid membrane restructuring and changes in nanomechanics. *Biochim Biophys Acta - Biomembr* **1860**:700–709. doi:10.1016/j.bbamem.2017.12.008

Bieniasz PD. 2004. Intrinsic immunity: A front-line defense against viral attack. *Nat Immunol* **5**:1109–1115. doi:10.1038/ni1125

Bischler N, Balavoine F, Milkereit P, Tschochner H, Mioskowski C, Schultz P. 1998. Specific interaction and two-dimensional crystallization of histidine tagged yeast RNA polymerase I on nickel-chelating lipids. *Biophys J* **74**:1522–1532.

doi:10.1016/S0006-3495(98)77864-6
Blanco-Melo D, Venkatesh S, Bieniasz PD. 2016. Origins and Evolution of tetherin, an Orphan Antiviral Gene. *Cell Host Microbe* **20**:189–201. doi:10.1016/j.chom.2016.06.007
Blanco-Melo D, Venkatesh S, Bieniasz PD. 2012. Intrinsic Cellular Defenses against Human Immunodeficiency Viruses. *Immunity*. doi:10.1016/j.immuni.2012.08.013
Blumenthal R, Durell S, Viard M. 2012. HIV entry and envelope glycoprotein-mediated fusion. *J Biol Chem* **287**:40841–9. doi:10.1074/jbc.R112.406272
Blumenthal R, Gallo SA, Viard M, Raviv Y, Puri A. 2002. Fluorescent lipid probes in the study of viral membrane fusion. *Chem Phys Lipids* **116**:39–55. doi:10.1016/S0009-3084(02)00019-1
Botet-Carreras A, Montero MT, Domènech Ò, Borrell JH. 2019. Effect of cholesterol on monolayer structure of different acyl chained phospholipids. *Colloids Surfaces B Biointerfaces* **174**:374–383. doi:10.1016/j.colsurfb.2018.11.040
Brass AL, Huang IC, Benita Y, John SP, Krishnan MN, Feeley EM, Ryan BJ, Weyer JL, van der Weyden L, Fikrig E, Adams DJ, Xavier RJ, Farzan M, Elledge SJ. 2009. The IFITM Proteins Mediate Cellular Resistance to Influenza A H1N1 Virus, West Nile Virus, and Dengue Virus. *Cell* **139**:1243–1254. doi:10.1016/j.cell.2009.12.017
Brian AA, McConnell HM. 1984. Allogeneic stimulation of cytotoxic T cells by supported planar membranes. *Proc Natl Acad Sci U S A*. doi:10.1073/pnas.81.19.6159
Briggs JAG, Kräusslich HG. 2011. The molecular architecture of HIV. *J Mol Biol*. doi:10.1016/j.jmb.2011.04.021
Brown DA, London E. 2000. Structure and function of sphingolipid- and cholesterol-rich membrane rafts. *J Biol Chem* **275**:17221–17224. doi:10.1074/jbc.R000005200
Buchholz T-O, Jordan M, Pigino G, Jug F. 2018. Cryo-CARE: Content-Aware Image Restoration for Cryo-Transmission Electron Microscopy Data.
Bullough PA, Hughson FM, Skehel JJ, Wiley DC. 1994. Structure of influenza haemagglutinin at the pH of membrane fusion. *Nature* **371**:37–43. doi:10.1038/371037a0
Bykov YS, Schaffer M, Dodonova SO, Albert S, Plitzko JM, Baumeister W, Engel BD, Briggs JA. 2017. The structure of the COPI coat determined within the cell. *Elife* **6**. doi:10.7554/eLife.32493
Callahan MK, Popernack PM, Tsutsui S, Truong L, Schlegel RA, Henderson AJ. 2003. Phosphatidylserine on HIV Envelope Is a Cofactor for Infection of Monocytic Cells. *J Immunol* **170**:4840–4845. doi:10.4049/jimmunol.170.9.4840
Campbell SM, Crowe SM, Mak J. 2002. Virion-associated cholesterol is critical for the maintenance of HIV-1 structure and infectivity. *AIDS*. doi:10.1097/00002030-200211220-00004
Carlemalm E, Wieslander Å. 1975. Electron diffraction studies of biological membrane and lipids. *Nature* **254**:537–538. doi:10.1038/254537a0
Carr CM, Kim PS. 1993. A spring-loaded mechanism for the conformational change of influenza hemagglutinin. *Cell* **73**:823–832. doi:10.1016/0092-8674(93)90260-W
Casares D, Escribá P V., Rosselló CA. 2019. Membrane lipid composition: Effect on membrane and organelle structure, function and compartmentalization and therapeutic avenues. *Int J Mol Sci* **20**. doi:10.3390/ijms20092167

Casey JR, Grinstein S, Orlowski J. 2010. Sensors and regulators of intracellular pH. *Nat Rev Mol Cell Biol*. doi:10.1038/nrm2820

Chen B. 2019. Molecular Mechanism of HIV-1 Entry. *Trends Microbiol*. doi:10.1016/j.tim.2019.06.002

Chen CH, Lu TK. 2020. Development and challenges of antimicrobial peptides for therapeutic applications. *Antibiotics*. doi:10.3390/antibiotics9010024

Chen J, Frey G, Peng H, Rits-Volloch S, Garrity J, Seaman MS, Chen B. 2014. Mechanism of HIV-1 neutralization by antibodies targeting a membrane-proximal region of gp41. *J Virol* **88**:1249–58. doi:10.1128/JVI.02664-13

Chen J, Skehel JJ, Wiley DC. 1999. N- and C-terminal residues combine in the fusion-pH influenza hemagglutinin HA2 subunit to form an N cap that terminates the triple-stranded coiled coil. *Proc Natl Acad Sci U S A* **96**:8967–8972. doi:10.1073/pnas.96.16.8967

Chen M, Zaytseva N V, Wu Q, Li M, Fang Y. 2013. Microplate-compatible total internal reflection fluorescence microscopy for receptor pharmacology. **102**:193702. doi:10.1063/1.4805041

Chen Y-C, Sood C, Marin M, Aaron J, Gratton E, Salaita K, Melikyan GB. 2020. Super-Resolution Fluorescence Imaging Reveals That Serine Incorporator Protein 5 Inhibits Human Immunodeficiency Virus Fusion by Disrupting Envelope Glycoprotein Clusters. *ACS Nano* acsnano.0c02699. doi:10.1021/acsnano.0c02699

Cheng-Mayer C, Liu R, Landau NR, Stamatatos L. 1997. Macrophage tropism of human immunodeficiency virus type 1 and utilization of the CC-CKR5 coreceptor. *J Virol* **71**:1657–1661.

Chernomordik L, Chanturiya A, Green J, Zimmerberg J. 1995. The hemifusion intermediate and its conversion to complete fusion: regulation by membrane composition. *Biophys J* **69**:922–929. doi:10.1016/S0006-3495(95)79966-0

Chernomordik L V., Kozlov MM. 2008. Mechanics of membrane fusion. *Nat Struct Mol Biol*. doi:10.1038/nsmb.1455

Chernomordik L V., Kozlov MM. 2005. Membrane hemifusion: Crossing a chasm in two leaps. *Cell*. doi:10.1016/j.cell.2005.10.015

Chernomordik L V., Kozlov MM. 2003. Protein-lipid interplay in fusion and fission of biological membranes. *Annu Rev Biochem* **72**:175–207. doi:10.1146/annurev.biochem.72.121801.161504

Chernomordik L V., Melikyan GB, Chizmadzhev YA. 1987. Biomembrane fusion: a new concept derived from model studies using two interacting planar lipid bilayers. *BBA - Rev Biomembr*. doi:10.1016/0304-4157(87)90016-5

Chernomordik L V., Zimmerberg J, Kozlov MM. 2006. Membranes of the world unite! *J Cell Biol*. doi:10.1083/jcb.200607083

Chesarino NM, Compton AA, McMichael TM, Kenney AD, Zhang L, Soewarna V, Davis M, Schwartz O, Yount JS. 2017. IFITM3 requires an amphipathic helix for antiviral activity. *EMBO Rep* **18**. doi:10.15252/embr.201744100

Chestnut MH, Siegel DP, Burns JL, Talmon Y. 1992. A temperature jump device for time resolved cryotransmission electron microscopy. *Microsc Res Tech* **20**:95–101. doi:10.1002/jemt.1070200110

Chiantia S, Kahya N, Ries J, Schwille P. 2006. Effects of ceramide on liquid-ordered domains investigated by simultaneous AFM and FCS. *Biophys J* **90**:4500–4508.

doi:10.1529/biophysj.106.081026
Chiantia S, Schwille P, Klymchenko AS, London E. 2011. Asymmetric GUVs prepared by MβCD-mediated lipid exchange: An FCS study. *Biophys J* **100**:L1–L3. doi:10.1016/j.bpj.2010.11.051
Chiu W, Avila-Sakar AJ, Schmid MF. 1997. Electron crystallography of macromolecular periodic arrays on phospholipid monolayers. *Adv Biophys* **34**:161–172. doi:10.1016/S0065-227X(97)89638-4
Chlanda P, Mekhedov E, Waters H, Schwartz CL, Fischer ER, Ryham RJ, Cohen FS, Blank PS, Zimmerberg J. 2016. The hemifusion structure induced by influenza virus haemagglutinin is determined by physical properties of the target membranes. *Nat Microbiol* **1**:16050. doi:10.1038/nmicrobiol.2016.50
Cho NJ, Frank CW, Kasemo B, Höök F. 2010. Quartz crystal microbalance with dissipation monitoring of supported lipid bilayers on various substrates. *Nat Protoc* **5**:1096–1106. doi:10.1038/nprot.2010.65
Chua BA, Ngo JA, Situ K, Morizono K. 2019. Roles of phosphatidylserine exposed on the viral envelope and cell membrane in HIV-1 replication. *Cell Commun Signal*. doi:10.1186/s12964-019-0452-1
Churchward MA, Rogasevskaia T, Brandman DM, Khosravani H, Nava P, Atkinson JK, Coorssen JR. 2008. Specific lipids supply critical negative spontaneous curvature-an essential component of native Ca2+-triggered membrane fusion. *Biophys J* **94**:3976–3986. doi:10.1529/biophysj.107.123984
Clarke RJ, Hossain KR, Cao K. 2020. Physiological roles of transverse lipid asymmetry of animal membranes. *Biochim Biophys Acta - Biomembr*. doi:10.1016/j.bbamem.2020.183382
Clotet-Codina I, Bosch B, Senserrich J, Fernández-Figueras MT, Peña R, Ballana E, Bofill M, Clotet B, Esté JA. 2009. HIV endocytosis after dendritic cell to T cell viral transfer leads to productive virus infection. *Antiviral Res* **83**:94–98. doi:10.1016/j.antiviral.2009.03.009
Cohen FS, Melikyan GB. 2004. The Energetics of Membrane Fusion from Binding, through Hemifusion, Pore Formation, and Pore Enlargement. *J Membr Biol* **199**:1–14. doi:10.1007/s00232-004-0669-8
Cohen FS, Zimmerberg J, Finkelstein A. 1980. Fusion of phospholipid vesicles with planar phospholipid bilayer membranes: II. Incorporation of a vesicular membrane marker into the planar membrane. *J Gen Physiol* **75**:251–70. doi:10.1085/jgp.75.3.251
Cole AM, Ganz T, Liese AM, Burdick MD, Liu L, Strieter RM. 2001. Cutting Edge: IFN-Inducible ELR − CXC Chemokines Display Defensin-Like Antimicrobial Activity . *J Immunol* **167**:623–627. doi:10.4049/jimmunol.167.2.623
Collins MD, Keller SL. 2008. Tuning lipid mixtures to induce or suppress domain formation across leaflets of unsupported asymmetric bilayers. *Proc Natl Acad Sci U S A* **105**:124–128. doi:10.1073/pnas.0702970105
Colom A, Derivery E, Soleimanpour S, Tomba C, Molin MD, Sakai N, González-Gaitán M, Matile S, Roux A. 2018. A fluorescent membrane tension probe. *Nat Chem* **10**:1118–1125. doi:10.1038/s41557-018-0127-3
Colomer-Lluch M, Ruiz A, Moris A, Prado JG. 2018. Restriction Factors: From Intrinsic Viral Restriction to Shaping Cellular Immunity Against HIV-1. *Front Immunol*.

doi:10.3389/fimmu.2018.02876
Compton AA, Bruel T, Porrot F, Mallet A, Sachse M, Euvrard M, Liang C, Casartelli N, Schwartz O. 2014. IFITM Proteins Incorporated into HIV-1 Virions Impair Viral Fusion and Spread. *Cell Host Microbe* **16**:736–747. doi:10.1016/J.CHOM.2014.11.001
Cornell CE, Black RA, Xue M, Litz HE, Ramsay A, Gordon M, Mileant A, Cohen ZR, Williams JA, Lee KK, Drobny GP, Keller SL. 2019. Prebiotic amino acids bind to and stabilize prebiotic fatty acid membranes. *Proc Natl Acad Sci U S A* **116**:17239–17244. doi:10.1073/pnas.1900275116
Cornell CE, Mileant A, Thakkar N, Lee KK, Keller SL. 2020. Direct imaging of liquid domains in membranes by cryo-electron tomography. *Proc Natl Acad Sci U S A* **117**:19713–19719. doi:10.1073/PNAS.2002245117
Costello DA, Lee DW, Drewes J, Vasquez KA, Kisler K, Wiesner U, Pollack L, Whittaker GR, Daniel S. 2012. Influenza virus-membrane fusion triggered by proton uncaging for single particle studies of fusion kinetics. *Anal Chem* **84**:8480–8489. doi:10.1021/ac3006473
Cournia Z, Allen TW, Andricioaei I, Antonny B, Baum D, Brannigan G, Buchete NV, Deckman JT, Delemotte L, del Val C, Friedman R, Gkeka P, Hege HC, Hénin J, Kasimova MA, Kolocouris A, Klein ML, Khalid S, Lemieux MJ, Lindow N, Roy M, Selent J, Tarek M, Tofoleanu F, Vanni S, Urban S, Wales DJ, Smith JC, Bondar AN. 2015. Membrane Protein Structure, Function, and Dynamics: a Perspective from Experiments and Theory. *J Membr Biol*. doi:10.1007/s00232-015-9802-0
Crane JM, Tamm LK. 2004. Role of cholesterol in the formation and nature of lipid rafts in planar and spherical model membranes. *Biophys J* **86**:2965–2979. doi:10.1016/S0006-3495(04)74347-7
Crawford MA, Burdick MD, Glomski IJ, Boyer AE, Barr JR, Mehrad B, Strieter RM, Hughes MA. 2010. Interferon-inducible CXC chemokines directly contribute to host defense against inhalational anthrax in a murine model of infection. *PLoS Pathog* **6**. doi:10.1371/journal.ppat.1001199
Crawford MA, Fisher DJ, Leung LM, Lomonaco S, Lascols C, Cannatelli A, Giani T, Rossolini GM, Doi Y, Goodlett DR, Allard MW, Sharma SK, Khan E, Ernst RK, Hughes MA. 2017. CXC chemokines exhibit bactericidal activity against multidrug-resistant gram-negative pathogens. *MBio* **8**. doi:10.1128/mBio.01549-17
Crawford MA, Lowe DE, Fisher DJ, Stibitz S, Plaut RD, Beaber JW, Zemansky J, Mehrad B, Glomski IJ, Strieter RM, Hughes MA. 2011. Identification of the bacterial protein FtsX as a unique target of chemokine-mediated antimicrobial activity against Bacillus anthracis. *Proc Natl Acad Sci U S A* **108**:17159–17164. doi:10.1073/pnas.1108495108
Crawford MA, Margulieux KR, Singh A, Nakamoto RK, Hughes MA. 2019. Mechanistic insights and therapeutic opportunities of antimicrobial chemokines. *Semin Cell Dev Biol*. doi:10.1016/j.semcdb.2018.02.003
Crawford MA, Zhu Y, Green CS, Burdick MD, Sanz P, Alem F, O'Brien AD, Mehrad B, Strieter RM, Hughes MA. 2009. Antimicrobial effects of interferon-inducible CXC chemokines against Bacillus anthracis spores and bacilli. *Infect Immun* **77**:1664–1678. doi:10.1128/IAI.01208-08
Cummins LM, Weinhold KJ, Matthews TJ, Langlois AJ, Perno CF, Condie RM, Allain

JP. 1991. Preparation and characterization of an intravenous solution of IgG from human immunodeficiency virus-seropositive donors. *Blood* **77**:1111–7.

Czogalla A, Grzybek M, Jones W, Coskun Ü. 2014. Validity and applicability of membrane model systems for studying interactions of peripheral membrane proteins with lipids. *Biochim Biophys Acta - Mol Cell Biol Lipids* **1841**:1049–1059. doi:10.1016/j.bbalip.2013.12.012

Dai W, Usami Y, Wu Y, Göttlinger H. 2018. A Long Cytoplasmic Loop Governs the Sensitivity of the Anti-viral Host Protein SERINC5 to HIV-1 Nef. *Cell Rep* **22**:869–875. doi:10.1016/j.celrep.2017.12.082

Dal Molin M, Verolet Q, Colom A, Letrun R, Derivery E, Gonzalez-Gaitan M, Vauthey E, Roux A, Sakai N, Matile S. 2015. Fluorescent flippers for mechanosensitive membrane probes. *J Am Chem Soc* **137**:568–571. doi:10.1021/ja5107018

Dale BM, McNerney GP, Thompson DL, Hubner W, De Los Reyes K, Chuang FYS, Huser T, Chen BK. 2011. Cell-to-cell transfer of HIV-1 via virological synapses leads to endosomal virion maturation that activates viral membrane fusion. *Cell Host Microbe* **10**:551–562. doi:10.1016/j.chom.2011.10.015

Daleke DL. 2003. Regulation of transbilayer plasma membrane phospholipid asymmetry. *J Lipid Res*. doi:10.1194/jlr.R200019-JLR200

Daněk M, Angelini J, Malínská K, Andrejch J, Amlerová Z, Kocourková D, Brouzdová J, Valentová O, Martinec J, Petrášek J. 2020. Cell wall contributes to the stability of plasma membrane nanodomain organization of Arabidopsis thaliana FLOTILLIN2 and HYPERSENSITIVE INDUCED REACTION1 proteins. *Plant J* **101**:619–636. doi:10.1111/tpj.14566

Danielli JF, Davson H. 1935. A contribution to the theory of permeability of thin films. *J Cell Comp Physiol* **5**:495–508. doi:10.1002/jcp.1030050409

Das DK, Bulow U, Diehl WE, Durham ND, Senjobe F, Chandran K, Luban J, Munro JB. 2020. Conformational changes in the Ebola virus membrane fusion machine induced by pH, Ca2+, and receptor binding. *PLoS Biol* **18**. doi:10.1371/journal.pbio.3000626

Das DK, Govindan R, Nikić-Spiegel I, Krammer F, Lemke EA, Munro JB. 2018. Direct Visualization of the Conformational Dynamics of Single Influenza Hemagglutinin Trimers. *Cell* **174**:926-937.e12. doi:10.1016/j.cell.2018.05.050

De Almeida RFM, Fedorov A, Prieto M. 2003. Sphingomyelin/phosphatidylcholine/cholesterol phase diagram: Boundaries and composition of lipid rafts. *Biophys J* **85**:2406–2416. doi:10.1016/S0006-3495(03)74664-5

Deamer D, Bangham AD. 1976. Large volume liposomes by an ether vaporization method. *BBA - Biomembr*. doi:10.1016/0005-2736(76)90483-1

Derdeyn CA, Decker JM, Sfakianos JN, Wu X, O'Brien WA, Ratner L, Kappes JC, Shaw GM, Hunter E. 2000. Sensitivity of human immunodeficiency virus type 1 to the fusion inhibitor T-20 is modulated by coreceptor specificity defined by the V3 loop of gp120. *J Virol* **74**:8358–67. doi:10.1128/jvi.74.18.8358-8367.2000

Desai TM, Marin M, Chin CR, Savidis G, Brass AL, Melikyan GB. 2014. IFITM3 restricts influenza A virus entry by blocking the formation of fusion pores following virus-endosome hemifusion. *PLoS Pathog* **10**:e1004048. doi:10.1371/journal.ppat.1004048

Descours B, Cribier A, Chable-Bessia C, Ayinde D, Rice G, Crow Y, Yatim A, Schwartz

O, Laguette N, Benkirane M. 2012. SAMHD1 restricts HIV-1 reverse transcription in quiescent CD4 + T-cells. *Retrovirology* **9**:87. doi:10.1186/1742-4690-9-87

Desselberger U. 2017. Reverse genetics of rotavirus. *Proc Natl Acad Sci U S A*. doi:10.1073/pnas.1700738114

Di Pietro A, Kajaste-Rudnitski A, Oteiza A, Nicora L, Towers GJ, Mechti N, Vicenzi E. 2013. TRIM22 Inhibits Influenza A Virus Infection by Targeting the Viral Nucleoprotein for Degradation. *J Virol* **87**:4523–4533. doi:10.1128/jvi.02548-12

Diamond MS, Farzan M. 2013. The broad-spectrum antiviral functions of IFIT and IFITM proteins. *Nat Rev Immunol*. doi:10.1038/nri3344

Diaz AJ, Albertorio F, Daniel S, Cremer PS. 2008. Double cushions preserve transmembrane protein mobility in supported bilayer systems. *Langmuir* **24**:6820–6826. doi:10.1021/la800018d

Dick RA, Zadrozny KK, Xu C, Schur FKM, Lyddon TD, Ricana CL, Wagner JM, Perilla JR, Ganser-Pornillos BK, Johnson MC, Pornillos O, Vogt VM. 2018. Inositol phosphates are assembly co-factors for HIV-1. *Nature*. doi:10.1038/s41586-018-0396-4

Diehl WE, Guney MH, Kyawe PP, White JM, Pizzato M, Luban J. 2019. Influence of different glycoproteins and of the virion core on SERINC5 antiviral activity. *bioRxiv*. doi:10.1101/780577

Dietrich C, Bagatolli LA, Volovyk ZN, Thompson NL, Levi M, Jacobson K, Gratton E. 2001. Lipid rafts reconstituted in model membranes. *Biophys J* **80**:1417–1428. doi:10.1016/S0006-3495(01)76114-0

Dodonova SO, Diestelkoetter-Bachert P, Von Appen A, Hagen WJH, Beck R, Beck M, Wieland F, Briggs JAG. 2015. A structure of the COPI coat and the role of coat proteins in membrane vesicle assembly. *Science (80-)* **349**:195–198. doi:10.1126/science.aab1121

Doehle BP, Schäfer A, Wiegand HL, Bogerd HP, Cullen BR. 2005. Differential Sensitivity of Murine Leukemia Virus to APOBEC3-Mediated Inhibition Is Governed by Virion Exclusion. *J Virol* **79**:8201–8207. doi:10.1128/jvi.79.13.8201-8207.2005

Doktorova M, Heberle FA, Eicher B, Standaert RF, Katsaras J, London E, Pabst G, Marquardt D. 2018. Preparation of asymmetric phospholipid vesicles for use as cell membrane models. *Nat Protoc* **13**:2086–2101. doi:10.1038/s41596-018-0033-6

Domanska MK, Dunning RA, Dryden KA, Zawada KE, Yeager M, Kasson PM. 2015. Hemagglutinin Spatial Distribution Shifts in Response to Cholesterol in the Influenza Viral Envelope. *Biophys J* **109**:1917–24. doi:10.1016/j.bpj.2015.09.014

Domanska MK, Wrona D, Kasson PM. 2013. Multiphasic effects of cholesterol on influenza fusion kinetics reflect multiple mechanistic roles. *Biophys J* **105**:1383–1387. doi:10.1016/j.bpj.2013.08.003

Dong N, Wang C, Zhang T, Zhang L, Xue C, Feng X, Bi C, Shan A. 2019. Bioactivity and bactericidal mechanism of histidine-rich β-hairpin peptide against gram-negative bacteria. *Int J Mol Sci* **20**. doi:10.3390/ijms20163954

Dubochet J, Adrian M, Chang J-J, Lepault J, McDowall AW. 1987. Cryoelectron Microscopy of Vitrified SpecimensCryotechniques in Biological Electron Microscopy. Springer Berlin Heidelberg. pp. 114–131. doi:10.1007/978-3-642-72815-0_5

Dufourc EJ, Smith ICP, Jarrell HC. 1984. Interaction of amphotericin B with membrane lipids as viewed by 2H-NMR. *Biochim Biophys Acta - Biomembr* **778**:435–442. doi:10.1016/0005-2736(84)90391-2

Duggal NK, Emerman M. 2012. Evolutionary conflicts between viruses and restriction factors shape immunity. *Nat Rev Immunol*. doi:10.1038/nri3295

Dulbecco R, Vogt M. 1954. Plaque formation and isolation of pure lines with poliomyelitis viruses. *J Exp Med* **99**:167–182. doi:10.1084/jem.99.2.167

Durham ND, Howard AR, Govindan R, Senjobe F, Fels JM, Diehl WE, Luban J, Chandran K, Munro JB. 2020. Real-Time Analysis of Individual Ebola Virus Glycoproteins Reveals Pre-Fusion, Entry-Relevant Conformational Dynamics. *Viruses* **12**:103. doi:10.3390/v12010103

Eeman M, Deleu M. 2010. From biological membranes to biomimetic model membranes. *Biotechnol Agron Soc Environ*.

Efrat A, Chernomordik L V., Kozlov MM. 2007. Point-like protrusion as a prestalk intermediate in membrane fusion pathway. *Biophys J* **92**:L61-3. doi:10.1529/biophysj.106.103341

Eggeling C, Ringemann C, Medda R, Schwarzmann G, Sandhoff K, Polyakova S, Belov VN, Hein B, Von Middendorff C, Schönle A, Hell SW. 2009. Direct observation of the nanoscale dynamics of membrane lipids in a living cell. *Nature* **457**:1159–1162. doi:10.1038/nature07596

Eisenberg RJ, Atanasiu D, Cairns TM, Gallagher JR, Krummenacher C, Cohen GH. 2012. Herpes virus fusion and entry: A story with many characters. *Viruses*. doi:10.3390/v4050800

Fan J, Ma G, Nosaka K, Tanabe J, Satou Y, Koito A, Wain-Hobson S, Vartanian J-P, Matsuoka M. 2010. APOBEC3G Generates Nonsense Mutations in Human T-Cell Leukemia Virus Type 1 Proviral Genomes In Vivo. *J Virol* **84**:7278–7287. doi:10.1128/jvi.02239-09

Fan ZA, Tsang KY, Chen SH, Chen YF. 2016. Revisit the Correlation between the Elastic Mechanics and Fusion of Lipid Membranes. *Sci Rep* **6**:1–10. doi:10.1038/srep31470

Fantini J, Barrantes FJ. 2013. How cholesterol interacts with membrane proteins: an exploration of cholesterol-binding sites including CRAC, CARC, and tilted domains. *Front Physiol* **4**:31. doi:10.3389/fphys.2013.00031

Favard C, Chojnacki J, Merida P, Yandrapalli N, Mak J, Eggeling C, Muriaux D. 2019. HIV-1 Gag specifically restricts PI(4,5)P2 and cholesterol mobility in living cells creating a nanodomain platform for virus assembly. *Sci Adv* **5**:eaaw8651. doi:10.1126/sciadv.aaw8651

Fedson DS. 2013. Treating influenza with statins and other immunomodulatory agents. *Antivir Res* **99**:417–435. doi:10.1016/j.antiviral.2013.06.018

Fedson DS. 2006. Pandemic influenza: a potential role for statins in treatment and prophylaxis. *Clin Infect Dis* **43**:199–205. doi:10.1086/505116

Feigenson GW. 2006. Phase behavior of lipid mixtures. *Nat Chem Biol*. doi:10.1038/nchembio1106-560

Fénéant L, Szymańska-de Wijs KM, Nelson EA, White JM. 2019. An exploration of conditions proposed to trigger the Ebola virus glycoprotein for fusion. *PLoS One* **14**:e0219312. doi:10.1371/journal.pone.0219312

Fensterl V, Sen GC. 2009. Interferons and viral infections. *BioFactors*. doi:10.1002/biof.6

Fifre A, Sponne I, Koziel V, Kriem B, Yen Potin FT, Bihain BE, Olivier JL, Oster T, Pillot T. 2006. Microtubule-associated protein MAP1A, MAP1B, and MAP2 proteolysis during soluble amyloid β-peptide-induced neuronal apoptosis: Synergistic involvement of calpain and caspase-3. *J Biol Chem* **281**:229–240. doi:10.1074/jbc.M507378200

Firrito C, Bertelli C, Vanzo T, Chande A, Pizzato M. 2018. SERINC5 as a New Restriction Factor for Human Immunodeficiency Virus and Murine Leukemia Virus. *Annu Rev Virol* **5**:323–340. doi:10.1146/annurev-virology-092917-043308

Floyd DL, Ragains JR, Skehel JJ, Harrison SC, van Oijen AM. 2008. Single-particle kinetics of influenza virus membrane fusion. *Proc Natl Acad Sci USA* **105**:15382–15387. doi:10.1073/pnas.0807771105

Fujimoto T, Parmryd I. 2017. Interleaflet coupling, pinning, and leaflet asymmetry-major players in plasma membrane nanodomain formation. *Front Cell Dev Biol*. doi:10.3389/fcell.2016.00155

Ganser-Pornillos BK, Chandrasekaran V, Pornillos O, Sodroski JG, Sundquist WI, Yeager M. 2011. Hexagonal assembly of a restricting TRIM5α protein. *Proc Natl Acad Sci U S A* **108**:546–550. doi:10.1073/pnas.1013426108

Ganser-Pornillos BK, Pornillos O. 2019. Restriction of HIV-1 and other retroviruses by TRIM5. *Nat Rev Microbiol*. doi:10.1038/s41579-019-0225-2

Ganser-Pornillos BK, Yeager M, Pornillos O. 2012. Assembly and architecture of HIV. *Adv Exp Med Biol* **726**:441–465. doi:10.1007/978-1-4614-0980-9_20

Gao B, Duan Z, Xu W, Xiong S. 2009. Tripartite motif-containing 22 inhibits the activity of hepatitis B virus core promoter, which is dependent on nuclear-located RING domain. *Hepatology* **50**:424–433. doi:10.1002/hep.23011

Gawrisch K, Ruston D, Zimmerberg J, Parsegian VA, Rand RP, Fuller N. 1992. Membrane dipole potentials, hydration forces, and the ordering of water at membrane surfaces. *Biophys J* **61**:1213–1223. doi:10.1016/S0006-3495(92)81931-8

Gerstle Z, Desai R, Veatch SL. 2018. Giant Plasma Membrane Vesicles: An Experimental Tool for Probing the Effects of Drugs and Other Conditions on Membrane Domain StabilityMethods in Enzymology. Academic Press Inc. pp. 129–150. doi:10.1016/bs.mie.2018.02.007

Goiko M, De Bruyn JR, Heit B. 2016. Short-Lived Cages Restrict Protein Diffusion in the Plasma Membrane. *Sci Rep* **6**. doi:10.1038/srep34987

Gorman MJ, Poddar S, Farzan M, Diamond MS. 2016. The Interferon-Stimulated Gene Ifitm3 Restricts West Nile Virus Infection and Pathogenesis . *J Virol* **90**:8212–8225. doi:10.1128/jvi.00581-16

Goronzy IN, Rawle RJ, Boxer SG, Kasson PM. 2018. Cholesterol enhances influenza binding avidity by controlling nanoscale receptor clustering. *Chem Sci* **9**:2340–2347. doi:10.1039/c7sc03236f

Gorter E, Grendel F. 1925. On bimolecular layers of lipoids on the chromocytes of the blood. *J Exp Med* **41**:439–444. doi:10.1084/jem.41.4.439

Goujon A, Colom A, Straková K, Mercier V, Mahecic D, Manley S, Sakai N, Roux A, Matile S. 2019. Mechanosensitive Fluorescent Probes to Image Membrane Tension in Mitochondria, Endoplasmic Reticulum, and Lysosomes. *J Am Chem Soc*

141:3380–3384. doi:10.1021/jacs.8b13189
Gregory SM, Larsson P, Nelson EA, Kasson PM, White JM, Tamm LK. 2014. Ebolavirus Entry Requires a Compact Hydrophobic Fist at the Tip of the Fusion Loop. *J Virol* **88**:6636–6649. doi:10.1128/jvi.00396-14
Guha S, Ghimire J, Wu E, Wimley WC. 2019. Mechanistic Landscape of Membrane-Permeabilizing Peptides. *Chem Rev*. doi:10.1021/acs.chemrev.8b00520
Gui L, Ebner JL, Mileant A, Williams JA, Lee KK. 2016. Visualization and Sequencing of Membrane Remodeling Leading to Influenza Virus Fusion. *J Virol*. doi:10.1128/JVI.00240-16
Gumí-Audenis B, Costa L, Carlá F, Comin F, Sanz F, Giannotti MI. 2016. Structure and nanomechanics of model membranes by atomic force microscopy and spectroscopy: Insights into the role of cholesterol and sphingolipids. *Membranes (Basel)*. doi:10.3390/membranes6040058
Guo Q, Lehmer C, Martínez-Sánchez A, Rudack T, Beck F, Hartmann H, Pérez-Berlanga M, Frottin F, Hipp MS, Hartl FU, Edbauer D, Baumeister W, Fernández-Busnadiego R. 2018. In Situ Structure of Neuronal C9orf72 Poly-GA Aggregates Reveals Proteasome Recruitment. *Cell* **172**:696-705.e12. doi:10.1016/J.CELL.2017.12.030
Guo X, Steinkühler J, Marin M, Li X, Lu W, Dimova R, Melikyan G. 2020. Interferon-Induced Transmembrane Protein 3 Blocks Fusion of Diverse Enveloped Viruses by Locally Altering Mechanical Properties of Cell Membranes. *bioRxiv* 2020.06.25.171280. doi:10.1101/2020.06.25.171280
Haidari M, Ali M, Casscells SW, Madjid M. 2007. Statins block influenza infection by down-regulating Rho/rho kinase pathway.
Haque E, Lentz BR. 2004. Roles of Curvature and Hydrophobic Interstice Energy in Fusion: Studies of Lipid Perturbant Effectst. *Biochemistry* **43**:3507–3517. doi:10.1021/bi035794j
Harris A, Cardone G, Winkler DC, Heymann JB, Brecher M, White JM, Steven AC. 2006. Influenza virus pleiomorphy characterized by cryoelectron tomography. *Proc Natl Acad Sci U S A* **103**:19123–19127. doi:10.1073/pnas.0607614103
Harrison SC. 2015. Viral membrane fusion. *Virology* **479–480**:498–507. doi:10.1016/j.virol.2015.03.043
Hatfull GF. 2015. Dark Matter of the Biosphere: the Amazing World of Bacteriophage Diversity. *J Virol* **89**:8107–8110. doi:10.1128/jvi.01340-15
Heberle FA, Doktorova M, Scott HL, Skinkle AD, Waxham MN, Levental I. 2020. Direct label-free imaging of nanodomains in biomimetic and biological membranes by cryogenic electron microscopy. *Proc Natl Acad Sci U S A* **117**:19943–19952. doi:10.1073/PNAS.2002200117
Heinemann F, Vogel SK, Schwille P. 2013. Lateral Membrane Diffusion Modulated by a Minimal Actin Cortex **104**:1465–1475. doi:10.1016/j.bpj.2013.02.042
Hemming SA, Bochkarev A, Darst SA, Kornberg RD, Ala P, Yang DSC, Edwards AM. 1995. The Mechanism of Protein Crystal Growth from Lipid Layers. *J Mol Biol* **246**:308–316. doi:10.1006/jmbi.1994.0086
Hennesthal C, Drexler J, Steinem C. 2002. Membrane-suspended nanocompartments based on ordered pores in Alumina. *ChemPhysChem* **3**:885–889. doi:10.1002/1439-7641(20021018)3:10<885::AID-CPHC885>3.0.CO;2-9
Hernandez JM, Kreutzberger AJB, Kiessling V, Tamm LK, Jahn R. 2014. Variable

cooperativity in SNARE-mediated membrane fusion. *Proc Natl Acad Sci U S A* **111**:12037–12042. doi:10.1073/pnas.1407435111

Herold N, Anders-Osswein M, Glass B, Eckhardt M, Muller B, Krausslich H-G. 2014. HIV-1 Entry in SupT1-R5, CEM-ss, and Primary CD4+ T Cells Occurs at the Plasma Membrane and Does Not Require Endocytosis. *J Virol* **88**:13956–13970. doi:10.1128/jvi.01543-14

Hoffmann M, Kleine-Weber H, Schroeder S, Krüger N, Herrler T, Erichsen S, Schiergens TS, Herrler G, Wu NH, Nitsche A, Müller MA, Drosten C, Pöhlmann S. 2020. SARS-CoV-2 Cell Entry Depends on ACE2 and TMPRSS2 and Is Blocked by a Clinically Proven Protease Inhibitor. *Cell* **181**:271-280.e8. doi:10.1016/j.cell.2020.02.052

Honigmann A, Walter C, Erdmann F, Eggeling C, Wagner R. 2010. Characterization of horizontal lipid bilayers as a model system to study lipid phase separation. *Biophys J* **98**:2886–2894. doi:10.1016/j.bpj.2010.03.033

Hotter D, Sauter D, Kirchhoff F. 2013. Emerging role of the host restriction factor tetherin in viral immune sensing. *J Mol Biol*. doi:10.1016/j.jmb.2013.09.029

Hrecka K, Hao C, Gierszewska M, Swanson SK, Kesik-Brodacka M, Srivastava S, Florens L, Washburn MP, Skowronski J. 2011. Vpx relieves inhibition of HIV-1 infection of macrophages mediated by the SAMHD1 protein. *Nature* **474**:658–661. doi:10.1038/nature10195

Huan Y, Kong Q, Mou H, Yi H. 2020. Antimicrobial Peptides: Classification, Design, Application and Research Progress in Multiple Fields. *Front Microbiol*. doi:10.3389/fmicb.2020.582779

Huang B, Babcock H, Zhuang X. 2010. Breaking the diffraction barrier: Super-resolution imaging of cells. *Cell*. doi:10.1016/j.cell.2010.12.002

Huang IC, Bailey CC, Weyer JL, Radoshitzky SR, Becker MM, Chiang JJ, Brass AL, Ahmed AA, Chi X, Dong L, Longobardi LE, Boltz D, Kuhn JH, Elledge SJ, Bavari S, Denison MR, Choe H, Farzan M. 2011. Distinct patterns of IFITM-mediated restriction of filoviruses, SARS coronavirus, and influenza A virus. *PLoS Pathog*. doi:10.1371/journal.ppat.1001258

Huang J, Feigenson GW. 1999. A microscopic interaction model of maximum solubility of cholesterol in lipid bilayers. *Biophys J*. doi:10.1016/S0006-3495(99)77369-8

Huang Y, Dai H, Ke R. 2019. Principles of Effective and Robust Innate Immune Response to Viral Infections: A Multiplex Network Analysis. *Front Immunol* **10**:1736. doi:10.3389/fimmu.2019.01736

Huang Y, Huang J, Chen Y. 2010. Alpha-helical cationic antimicrobial peptides: Relationships of structure and function. *Protein Cell*. doi:10.1007/s13238-010-0004-3

Huarte N, Carravilla P, Cruz A, Lorizate M, A, Nieto-Garai J, Kräusslich H-GG, Jesús P-G, Jose R-I, Nieva JLL. 2016. Functional organization of the HIV lipid envelope. *Sci Rep* **6**:34190. doi:10.1038/srep34190

Hughes LD, Rawle RJ, Boxer SG. 2014. Choose Your Label Wisely: Water-Soluble Fluorophores Often Interact with Lipid Bilayers. *PLoS One* **9**:e87649. doi:10.1371/journal.pone.0087649

Hui SW. 1977. Electron diffraction studies of membranes. *BBA - Rev Biomembr*. doi:10.1016/0304-4157(77)90002-8

Hulseberg CE, Fénéant L, Wijs KMS, Kessler NP, Nelson EA, Shoemaker CJ, Schmaljohn CS, Polyak SJ, White JM. 2019. Arbidol and Other Low-Molecular-Weight Drugs That Inhibit Lassa and Ebola Viruses. *J Virol* **93**:e02185-18. doi:10.1128/JVI.02185-18

International Committee on Taxonomy of Viruses. 2012. Virus Taxonomy: Classification and Nomenclature of Viruses, Ninth Report of the International Committee on Taxonomy of Viruses.

Inuzuka M, Hayakawa M, Ingi T. 2005. Serinc, an Activity-regulated Protein Family, Incorporates Serine into Membrane Lipid Synthesis. *J Biol Chem* **280**:35776–35783. doi:10.1074/jbc.M505712200

Ionova I V., Livshits VA, Marsh D. 2012. Phase diagram of ternary cholesterol/palmitoylsphingomyelin/ palmitoyloleoyl-phosphatidylcholine mixtures: Spin-label EPR study of lipid-raft formation. *Biophys J* **102**:1856–1865. doi:10.1016/j.bpj.2012.03.043

Jacobson K, Mouritsen OG, Anderson RGW. 2007. Lipid rafts: At a crossroad between cell biology and physics. *Nat Cell Biol*. doi:10.1038/ncb0107-7

Janknecht R, De Martynoff G, Lou J, Hipskind RA, Nordheim A, Stunnenberg HG. 1991. Rapid and efficient purification of native histidine-tagged protein expressed by recombinant vaccinia virus. *Proc Natl Acad Sci U S A* **88**:8972–8976. doi:10.1073/pnas.88.20.8972

Jiang D, Weidner JM, Qing M, Pan X-B, Guo H, Xu C, Zhang X, Birk A, Chang J, Shi P-Y, Block TM, Guo J-T. 2010. Identification of Five Interferon-Induced Cellular Proteins That Inhibit West Nile Virus and Dengue Virus Infections. *J Virol* **84**:8332–8341. doi:10.1128/jvi.02199-09

Johansen LM, DeWald LE, Shoemaker CJ, Hoffstrom BG, Lear-Rooney CM, Stossel A, Nelson E, Delos SE, Simmons JA, Grenier JM, Pierce LT, Pajouhesh H, Lehár J, Hensley LE, Glass PJ, White JM, Olinger GG. 2015. A screen of approved drugs and molecular probes identifies therapeutics with anti-Ebola virus activity. *Sci Transl Med* **7**. doi:10.1126/scitranslmed.aaa5597

Juhaniewicz J, Sek S. 2015. Atomic force microscopy and electrochemical studies of melittin action on lipid bilayers supported on gold electrodes. *Electrochim Acta* **162**:53–61. doi:10.1016/j.electacta.2014.10.039

Kalb E, Frey S, Tamm LK. 1992. Formation of supported planar bilayers by fusion of vesicles to supported phospholipid monolayers. *Biochim Biophys Acta - Biomembr* **1103**:307–316. doi:10.1016/0005-2736(92)90101-Q

Kasson PM, Pande VS. 2007. Control of membrane fusion mechanism by lipid composition: Predictions from ensemble molecular dynamics. *PLoS Comput Biol* **3**:2228–2238. doi:10.1371/journal.pcbi.0030220

Katharine Burr Blodgett. 1980. . *Phys Today* **33**:107–107. doi:10.1063/1.2913969

Kawamoto S, Shinoda W. 2014. Free energy analysis along the stalk mechanism of membrane fusion. *Soft Matter* **10**:3048–3054. doi:10.1039/c3sm52344f

Kelly C V, Kober M-MT, Kinnunen P, Reis DA, Orr BG, Holl MM. 2009. Pulsed-laser creation and characterization of giant plasma membrane vesicles from cells. *J Biol Phys* **35**:279–295. doi:10.1007/s10867-009-9167-7

Kemble GW, Danieli T, White JM. 1994. Lipid-anchored influenza hemagglutinin promotes hemifusion, not complete fusion. *Cell* **76**:383–391. doi:10.1016/0092-

8674(94)90344-1
Kern DM, Oh S, Hite RK, Brohawn SG. 2019. Cryo-EM structures of the DCPIB-inhibited volume-regulated anion channel LRRC8A in lipid nanodiscs. *Elife* **8**. doi:10.7554/eLife.42636
Khan MS, Dosoky NS, Mustafa G, Patel D, Berdiev B, Williams JD. 2017. Electrophysiology of Epithelial Sodium Channel (ENaC) Embedded in Supported Lipid Bilayer Using a Single Nanopore Chip. *Langmuir* **33**:13680–13688. doi:10.1021/acs.langmuir.7b02404
Khodaparast Ladan, Khodaparast Laleh, Gallardo R, Louros NN, Michiels E, Ramakrishnan R, Ramakers M, Claes F, Young L, Shahrooei M, Wilkinson H, Desager M, Mengistu Tadesse W, Nilsson KPR, Hammarström P, Aertsen A, Carpentier S, Van Eldere J, Rousseau F, Schymkowitz J. 2018. Aggregating sequences that occur in many proteins constitute weak spots of bacterial proteostasis. *Nat Commun* **9**:866. doi:10.1038/s41467-018-03131-0
Kielian MC, Helenius A. 1984. Role of cholesterol in fusion of Semliki Forest virus with membranes. *J Virol* **52**:281–283. doi:10.1128/jvi.52.1.281-283.1984
Kiessling V, Crane JM, Tamm LK. 2006. Transbilayer effects of raft-like lipid domains in asymmetric planar bilayers measured by single molecule tracking. *Biophys J* **91**:3313–3326. doi:10.1529/biophysj.106.091421
Kiessling V, Domanska MK, Tamm LK. 2010. Single SNARE-mediated vesicle fusion observed in vitro by polarized TIRFM. *Biophys J*. doi:10.1016/j.bpj.2010.10.022
Kiessling V, Liang B, Kreutzberger AJB, Tamm LK. 2017. Planar Supported Membranes with Mobile SNARE Proteins and Quantitative Fluorescence Microscopy Assays to Study Synaptic Vesicle Fusion. *Front Mol Neurosci* **10**:72. doi:10.3389/fnmol.2017.00072
Kiessling V, Liang B, Tamm LK. 2015a. Reconstituting SNARE-mediated membrane fusion at the single liposome level. *Methods Cell Biol* **128**:339–363. doi:10.1016/BS.MCB.2015.02.005
Kiessling V, Tamm LK. 2003. Measuring distances in supported bilayers by fluorescence interference-contrast microscopy: Polymer supports and SNARE proteins. *Biophys J* **84**:408–18. doi:10.1016/S0006-3495(03)74861-9
Kiessling V, Wan C, Tamm LK. 2009. Domain coupling in asymmetric lipid bilayers **1788**:64–71. doi:10.1016/j.bbamem.2008.09.003
Kiessling V, Yang ST, Tamm LK. 2015b. Supported Lipid Bilayers as Models for Studying Membrane Domains. *Curr Top Membr* **75**:1–23. doi:10.1016/bs.ctm.2015.03.001
Klein JS, Bjorkman PJ. 2010. Few and Far Between: How HIV May Be Evading Antibody Avidity. *PLoS Pathog* **6**:e1000908. doi:10.1371/JOURNAL.PPAT.1000908
Kleinfelter LM, Jangra RK, Jae LT, Herbert AS, Mittler E, Stiles KM, Wirchnianski AS, Kielian M, Brummelkamp TR, Dye JM, Chandran K. 2015. Haploid Genetic Screen Reveals a Profound and Direct Dependence on Cholesterol for Hantavirus Membrane Fusion. *MBio* **6**:e00801. doi:10.1128/mBio.00801-15
Kliesch TT, Dietz J, Turco L, Halder P, Polo E, Tarantola M, Jahn R, Janshoff A. 2017. Membrane tension increases fusion efficiency of model membranes in the presence of SNAREs. *Sci Rep* **7**. doi:10.1038/s41598-017-12348-w

Knowles TJ, Finka R, Smith C, Lin YP, Dafforn T, Overduin M. 2009. Membrane proteins solubilized intact in lipid containing nanoparticles bounded by styrene maleic acid copolymer. *J Am Chem Soc* **131**:7484–7485. doi:10.1021/ja810046q

Kobayashi M, Takaori-Kondo A, Shindo K, Abudu A, Fukunaga K, Uchiyama T. 2004. APOBEC3G Targets Specific Virus Species. *J Virol* **78**:8238–8244. doi:10.1128/jvi.78.15.8238-8244.2004

Koito A, Ikeda T. 2013. Intrinsic immunity against retrotransposons by APOBEC cytidine deaminases. *Front Microbiol*. doi:10.3389/fmicb.2013.00028

Kol MA, de Kroon A, Rijkers D, Killian J, de Kruijff B. 2001. Membrane-spanning peptides induce phospholipid flop: a model for phospholipid translocation across the inner membrane of E. coli. *Biochemistry* **40**. doi:10.1021/BI010627+

Koning FA, Newman ENC, Kim E-Y, Kunstman KJ, Wolinsky SM, Malim MH. 2009. Defining APOBEC3 Expression Patterns in Human Tissues and Hematopoietic Cell Subsets. *J Virol* **83**:9474–9485. doi:10.1128/jvi.01089-09

Kozlov MM, Chernomordik L V. 2015. Membrane tension and membrane fusion. *Curr Opin Struct Biol*. doi:10.1016/j.sbi.2015.07.010

Kreutzberger Alex J. B., Kiessling V, Liang B, Seelheim P, Jakhanwal S, Jahn R, Castle JD, Tamm LK. 2017. Reconstitution of calcium-mediated exocytosis of dense-core vesicles. *Sci Adv* **3**:e1603208. doi:10.1126/sciadv.1603208

Kreutzberger Alex J.B., Kiessling V, Liang B, Yang S-T, Castle JD, Tamm LK. 2017. Asymmetric Phosphatidylethanolamine Distribution Controls Fusion Pore Lifetime and Probability. *Biophys J* **113**:1912–1915. doi:10.1016/J.BPJ.2017.09.014

Kreutzberger AJB, Kiessling V, Tamm LK. 2015. High Cholesterol Obviates a Prolonged Hemifusion Intermediate in Fast SNARE-Mediated Membrane Fusion. *Biophys J* **109**:319–329. doi:10.1016/j.bpj.2015.06.022

Kroppen B, Teske N, Yambire KF, Denkert N, Mukherjee I, Tarasenko D, Jaipuria G, Zweckstetter M, Milosevic I, Steinem C, Meinecke M. 2020. Cooperativity of membrane-protein and protein–protein interactions control membrane remodeling by epsin 1 and affects clathrin-mediated endocytosis. *Cell Mol Life Sci*. doi:10.1007/s00018-020-03647-z

Kucharska I, Ding P, Zadrozny KK, Dick RA, Summers MF, Ganser-Pornillos BK, Pornillos O. 2019. Biochemical Reconstitution of HIV-1 Assembly and Maturation. *J Virol* **94**. doi:10.1128/jvi.01844-19

Kucharska I, Seelheim P, Edrington T, Liang B, Tamm LK. 2015. OprG Harnesses the Dynamics of its Extracellular Loops to Transport Small Amino Acids across the Outer Membrane of Pseudomonas aeruginosa. *Structure* **23**:2234–2245. doi:10.1016/j.str.2015.10.009

Kummer S, Avinoam O, Kräusslich H-G. 2019. IFITM3 Clusters on Virus Containing Endosomes and Lysosomes Early in the Influenza A Infection of Human Airway Epithelial Cells. *Viruses* **11**:548. doi:10.3390/v11060548

Kuzmin PI, Zimmerberg J, Chizmadzhev YA, Cohen FS. 2001. A quantitative model for membrane fusion based on low-energy intermediates. *Proc Natl Acad Sci U S A* **98**:7235–7240. doi:10.1073/pnas.121191898

Laguette N, Sobhian B, Casartelli N, Ringeard M, Chable-Bessia C, Ségéral E, Yatim A, Emiliani S, Schwartz O, Benkirane M. 2011. SAMHD1 is the dendritic- and myeloid-cell-specific HIV-1 restriction factor counteracted by Vpx. *Nature*

474:654–657. doi:10.1038/nature10117
Lai AL, Freed JH. 2015. The Interaction between Influenza HA Fusion Peptide and Transmembrane Domain Affects Membrane Structure. *Biophys J* **109**:2523–2536. doi:10.1016/j.bpj.2015.10.044
Lai AL, Moorthy AE, Li Y, Tamm LK. 2012. Fusion activity of HIV gp41 fusion domain is related to its secondary structure and depth of membrane insertion in a cholesterol-dependent fashion. *J Mol Biol* **418**:3–15. doi:10.1016/j.jmb.2012.02.010
Lasic DD. 1988. The mechanism of vesicle formation. *Biochem J* **256**:1–11. doi:10.1042/bj2560001
Lee AG. 2011. Lipid-protein interactionsBiochemical Society Transactions. Biochem Soc Trans. pp. 761–766. doi:10.1042/BST0390761
Lee J, Gregory SM, Nelson EA, White JM, Tamm LK. 2016. The roles of histidines and charged residues as potential triggers of a conformational change in the fusion loop of ebola virus glycoprotein. *PLoS One*. doi:10.1371/journal.pone.0152527
Lee J, Nyenhuis DA, Nelson EA, Cafiso DS, White JM, Tamm LK. 2017. Structure of the Ebola virus envelope protein MPER/TM domain and its interaction with the fusion loop explains their fusion activity. *Proc Natl Acad Sci U S A*. doi:10.1073/pnas.1708052114
Lee JY, Schick M. 2008. Calculation of free energy barriers to the fusion of small vesicles. *Biophys J* **94**:1699–1706. doi:10.1529/biophysj.107.119511
Lee KK. 2010. Architecture of a nascent viral fusion pore **29**:1299–1311. doi:10.1038/emboj.2010.13
Lei J, Sun LC, Huang S, Zhu C, Li P, He J, Mackey V, Coy DH, He QY. 2019. The antimicrobial peptides and their potential clinical applications. *Am J Transl Res*.
Leikin S, Parsegian VA, Rau DC, Rand RP. 1993. Hydration forces. *Annu Rev Phys Chem* **44**:369–395. doi:10.1146/annurev.pc.44.100193.002101
Leikina E, Ramos C, Markovic I, Zimmerberg J, Chernomordik L V. 2002. Reversible stages of the low-pH-triggered conformational change in influenza virus hemagglutinin. *EMBO J* **21**:5701–5710. doi:10.1093/emboj/cdf559
Lentz BR, Lee JK. 1999. Poly(ethylene glycol) (PEG)-mediated fusion between pure lipid bilayers: A mechanism in common with viral fusion and secretory vesicle release? *Mol Membr Biol*. doi:10.1080/096876899294508
Levental I, Levental KR, Heberle FA. 2020. Lipid Rafts: Controversies Resolved, Mysteries Remain. *Trends Cell Biol*. doi:10.1016/j.tcb.2020.01.009
Levental KR, Levental I. 2015. Giant Plasma Membrane Vesicles: Models for Understanding Membrane Organization. *Curr Top Membr* **75**:25–57. doi:10.1016/bs.ctm.2015.03.009
Levy D, Milhiet PE. 2013. Imaging of transmembrane proteins directly incorporated within supported lipid bilayers using atomic force microscopy. *Methods Mol Biol* **950**:343–357. doi:10.1007/978-1-62703-137-0_19
Lévy D, Mosser G, Lambert O, Moeck GS, Bald D, Rigaud JL. 1999. Two-dimensional crystallization on lipid layer: A successful approach for membrane proteins. *J Struct Biol* **127**:44–52. doi:10.1006/jsbi.1999.4155
Li K, Markosyan RM, Zheng Y-M, Golfetto O, Bungart B, Li M, Ding S, He Y, Liang C, Lee JC, Gratton E, Cohen FS, Liu S-L. 2013. IFITM Proteins Restrict Viral Membrane Hemifusion. *PLoS Pathog* **9**:e1003124.

doi:10.1371/journal.ppat.1003124
Li P, Shi ML, Shen WL, Zhang Z, Xie DJ, Zhang XY, He C, Zhang Y, Zhao ZH. 2017. Coordinated regulation of IFITM1, 2 and 3 genes by an IFN-responsive enhancer through long-range chromatin interactions. *Biochim Biophys Acta - Gene Regul Mech* **1860**:885–893. doi:10.1016/j.bbagrm.2017.05.003
Li S, Raychaudhuri S, Watanabe S. 2017. Flash-and-freeze: A novel technique to capture membrane dynamics with electron microscopy. *J Vis Exp* **2017**. doi:10.3791/55664
Li YL, Chandrasekaran V, Carter SD, Woodward CL, Christensen DE, Dryden KA, Pornillos O, Yeager M, Ganser-Pornillos BK, Jensen GJ, Sundquist WI. 2016. Primate TRIM5 proteins form hexagonal nets on HIV-1 capsids. *Elife* **5**. doi:10.7554/eLife.16269
Li Zhaolong, Huan C, Wang H, Liu Y, Liu X, Su X, Yu J, Zhao Z, Yu X, Zheng B, Zhang W. 2020. TRIM 21-mediated proteasomal degradation of SAMHD 1 regulates its antiviral activity . *EMBO Rep* **21**. doi:10.15252/embr.201847528
Li Ze, Li W, Lu M, Bess J, Chao CW, Gorman J, Terry DS, Zhang B, Zhou T, Blanchard SC, Kwong PD, Lifson JD, Mothes W, Liu J. 2020. Subnanometer structures of HIV-1 envelope trimers on aldrithiol-2-inactivated virus particles. *Nat Struct Mol Biol* **27**:726–734. doi:10.1038/s41594-020-0452-2
Liao Z, Cimakasky LM, Hampton R, Nguyen DH, Hildreth JEK. 2001. Lipid rafts and HIV pathogenesis: Host membrane cholesterol is required for infection by HIV type 1. *AIDS Res Hum Retroviruses*. doi:10.1089/088922201300343690
Licari G, Strakova K, Matile S, Tajkhorshid E. 2020. Twisting and tilting of a mechanosensitive molecular probe detects order in membranes. *Chem Sci* **11**:5637–5649. doi:10.1039/d0sc02175j
Lichtenberg D, Goñi FM, Heerklotz H. 2005. Detergent-resistant membranes should not be identified with membrane rafts. *Trends Biochem Sci* **30**:430–436. doi:10.1016/j.tibs.2005.06.004
Lin CM, Li CS, Sheng YJ, Wu DT, Tsao HK. 2012. Size-dependent properties of small unilamellar vesicles formed by model lipids. *Langmuir* **28**:689–700. doi:10.1021/la203755v
Lingwood D, Ries J, Schwille P, Simons K. 2008. Plasma membranes are poised for activation of raft phase coalescence at physiological temperature. *Proc Natl Acad Sci U S A* **105**:10005–10010. doi:10.1073/pnas.0804374105
Linke D. 2009. Chapter 34 Detergents. An OverviewMethods in Enzymology. Academic Press Inc. pp. 603–617. doi:10.1016/S0076-6879(09)63034-2
Lipkin RB, Lazaridis T. 2015. Implicit Membrane Investigation of the Stability of Antimicrobial Peptide β-Barrels and Arcs. *J Membr Biol* **248**:469–486. doi:10.1007/s00232-014-9759-4
Lippincott-Schwartz J, Freed EO, Van Engelenburg SB. 2017. A Consensus View of ESCRT-Mediated Human Immunodeficiency Virus Type 1 Abscission. *Annu Rev Virol* **4**:309–325. doi:10.1146/annurev-virology-101416-041840
Liu HY, Grant H, Hsu HL, Sorkin R, Bošković F, Wuite G, Daniel S. 2017. Supported Planar Mammalian Membranes as Models of in Vivo Cell Surface Architectures. *ACS Appl Mater Interfaces*. doi:10.1021/acsami.7b07500
Liu S, Lu H, Niu J, Xu Y, Wu S, Jiang S. 2005. Different from the HIV Fusion Inhibitor C34, the Anti-HIV Drug Fuzeon (T-20) Inhibits HIV-1 Entry by Targeting Multiple

Sites in gp41 and gp120. *J Biol Chem* **280**:11259–11273. doi:10.1074/jbc.M411141200

Liu Y, Sigworth FJ. 2014. Automatic cryo-EM particle selection for membrane proteins in spherical liposomes. *J Struct Biol* **185**:295–302. doi:10.1016/j.jsb.2014.01.004

Liu Y, Wang H, Zhang J, Yang J, Bai L, Zheng B, Zheng T, Wang Y, Li J, Zhang W. 2020. SERINC5 Inhibits the Secretion of Complete and Genome-Free Hepatitis B Virions Through Interfering With the Glycosylation of the HBV Envelope. *Front Microbiol* **11**. doi:10.3389/fmicb.2020.00697

Livermore DM. 2004. The need for new antibiotics. *Clin Microbiol Infect Suppl* **10**:1–9. doi:10.1111/j.1465-0691.2004.1004.x

Lorent JH, Levental KR, Ganesan L, Rivera-Longsworth G, Sezgin E, Doktorova M, Lyman E, Levental I. 2020. Plasma membranes are asymmetric in lipid unsaturation, packing and protein shape. *Nat Chem Biol* **16**:644–652. doi:10.1038/s41589-020-0529-6

Lorizate M, Brügger B, Akiyama H, Glass B, Müller B, Anderluh G, Wieland FT, Kräusslich HG. 2009. Probing HIV-1 membrane liquid order by Laurdan staining reveals producer cell-dependent differences. *J Biol Chem* **284**:22238–22247. doi:10.1074/jbc.M109.029256

Lu J, Pan Q, Rong L, Liu S-L, Liang C. 2011. The IFITM Proteins Inhibit HIV-1 Infection. *J Virol* **85**:2126–2137. doi:10.1128/jvi.01531-10

Lu M, Ma X, Castillo-Menendez LR, Gorman J, Alsahafi N, Ermel U, Terry DS, Chambers M, Peng D, Zhang B, Zhou T, Reichard N, Wang K, Grover JR, Carman BP, Gardner MR, Nikić-Spiegel I, Sugawara A, Arthos J, Lemke EA, Smith AB, Farzan M, Abrams C, Munro JB, McDermott AB, Finzi A, Kwong PD, Blanchard SC, Sodroski JG, Mothes W. 2019. Associating HIV-1 envelope glycoprotein structures with states on the virus observed by smFRET. *Nature* **568**:415–419. doi:10.1038/s41586-019-1101-y

Lwoff A, Horne R, Tournier P. 1962. A system of viruses. *Cold Spring Harb Symp Quant Biol* **27**:51–55. doi:10.1101/SQB.1962.027.001.008

Ma X, Lu M, Gorman J, Terry DS, Hong X, Zhou Z, Zhao H, Altman RB, Arthos J, Blanchard SC, Kwong PD, Munro JB, Mothes W. 2018. HIV-1 Env trimer opens through an asymmetric intermediate in which individual protomers adopt distinct conformations. **7**. doi:10.7554/eLife.34271

Mahieux R, Suspène R, Delebecque F, Henry M, Schwartz O, Wain-Hobson S, Vartanian JP. 2005. Extensive editing of a small fraction of human T-cell leukemia virus type 1 genomes by four APOBEC3 cytidine deaminases. *J Gen Virol* **86**:2489–2494. doi:10.1099/vir.0.80973-0

Mahlapuu M, Håkansson J, Ringstad L, Björn C. 2016. Antimicrobial peptides: An emerging category of therapeutic agents. *Front Cell Infect Microbiol*. doi:10.3389/fcimb.2016.00194

Malinin VS, Lentz BR. 2004. Energetics of Vesicle Fusion Intermediates: Comparison of Calculations with Observed Effects of Osmotic and Curvature Stresses. *Biophys J* **86**:2951–2964. doi:10.1016/S0006-3495(04)74346-5

Mangeat B, Turelli P, Caron G, Friedli M, Perrin L, Trono D. 2003. Broad antiretroviral defence by human APOBEC3G through lethal editing of nascent reverse transcripts. *Nature* **424**:99–103. doi:10.1038/nature01709

Mapar M, Jõemetsa S, Pace H, Zhdanov VP, Agnarsson B, Höök F. 2018. Spatiotemporal Kinetics of Supported Lipid Bilayer Formation on Glass via Vesicle Adsorption and Rupture. *J Phys Chem Lett* **9**:5143–5149. doi:10.1021/acs.jpclett.8b02092

Margulieux KR, Fox JW, Nakamoto RK, Hughes MA. 2016. CXCL10 acts as a bifunctional antimicrobial molecule against Bacillus anthracis. *MBio* **7**. doi:10.1128/mBio.00334-16

Mariani R, Chen D, Schröfelbauer B, Navarro F, König R, Bollman B, Münk C, Nymark-McMahon H, Landau NR. 2003. Species-specific exclusion of APOBEC3G from HIV-1 virions by Vif. *Cell* **114**:21–31. doi:10.1016/S0092-8674(03)00515-4

Markin VS, Albanesi JP. 2002. Membrane fusion: Stalk model revisited. *Biophys J* **82**:693–712. doi:10.1016/S0006-3495(02)75432-5

Markin VS, Kozlov MM, Borovjagin VL. 1984. On the theory of membrane fusion. The stalk mechanism. *Gen Physiol Biophys* **3**:361–77.

Martin-Fernandez ML, Tynan CJ, Webb SED. 2013. A "pocket guide" to total internal reflection fluorescence. *J Microsc* **252**:16–22. doi:10.1111/jmi.12070

Mastronarde DN, Held SR. 2017. Automated tilt series alignment and tomographic reconstruction in IMOD. *J Struct Biol* **197**:102–113. doi:10.1016/j.jsb.2016.07.011

Maurer UE, Sodeik B, Grünewald K. 2008. Native 3D intermediates of membrane fusion in herpes simplex virus 1 entry. *Proc Natl Acad Sci U S A* **105**:10559–10564. doi:10.1073/pnas.0801674105

Mcalduff DE, Heng YM, Ottensmeyer FP. 2002. Freestanding lipid bilayers as substrates for electron cryomicroscopy of integral membrane proteins. *J Microsc* **205**:113–117. doi:10.1046/j.0022-2720.2001.00999.x

McCarthy MK, Weinberg JB. 2015. The immunoproteasome and viral infection: A complex regulator of inflammation. *Front Microbiol*. doi:10.3389/fmicb.2015.00021

McClure MO, Marsh M, Weiss RA. 1988. Human immunodeficiency virus infection of CD4-bearing cells occurs by a pH-independent mechanism. *EMBO J* **7**:513–8. doi:10.1002/j.1460-2075.1988.tb02839.x

McCullough J, Frost A, Sundquist WI. 2018. Structures, Functions, and Dynamics of ESCRT-III/Vps4 Membrane Remodeling and Fission Complexes. *Annu Rev Cell Dev Biol*. doi:10.1146/annurev-cellbio-100616-060600

McMahon HT, Boucrot E. 2015. Membrane curvature at a glance. *J Cell Sci* **128**:1065–1070. doi:10.1242/jcs.114454

Meers P, Ali S, Erukulla R, Janoff AS. 2000. Novel inner monolayer fusion assays reveal differential monolayer mixing associated with cation-dependent membrane fusion. *Biochim Biophys Acta - Biomembr* **1467**:227–243. doi:10.1016/S0005-2736(00)00224-8

Meher G, Chakraborty H. 2019. Membrane Composition Modulates Fusion by Altering Membrane Properties and Fusion Peptide Structure. *J Membr Biol*. doi:10.1007/s00232-019-00064-7

Mehrbod P, Omar AR, Mohd H-B, Haghani A, Ideris A. 2014. Mechanisms of action and efficacy of statins against influenza. *Biomed Res Int* **2014**:872370. doi:10.1155/2014/872370

Melikyan GB. 2011. Membrane Fusion Mediated by Human Immunodeficiency Virus Envelope Glycoprotein. *Curr Top Membr* **68**:81–106. doi:10.1016/B978-0-12-385891-7.00004-0

Melikyan GB. 2010. Driving a wedge between viral lipids blocks infection. *Proc Natl Acad Sci U S A*. doi:10.1073/pnas.1012748107

Melikyan GB, Niles WD, Peeples ME, Cohen FS. 1993. Influenza hemagglutinin-mediated fusion pores connecting cells to planar membranes: Flickering to final expansion. *J Gen Physiol* **102**:1131–49. doi:10.1085/jgp.102.6.1131

Melikyan GB, White JM, Cohen FS. 1995. GPI-anchored influenza hemagglutinin induces hemifusion to both red blood cell and planar bilayer membranes. *J Cell Biol* **131**:679–691. doi:10.1083/jcb.131.3.679

Mercer J, Lee JE, Saphire EO, Freeman SA. 2020. SnapShot: Enveloped Virus Entry. *Cell* **182**:786-786.e1. doi:10.1016/j.cell.2020.06.033

Mercer J, Schelhaas M, Helenius A. 2010. Virus entry by endocytosis. *Annu Rev Biochem*. doi:10.1146/annurev-biochem-060208-104626

Merrill AH. 2008. SphingolipidsBiochemistry of Lipids, Lipoproteins and Membranes. Elsevier. pp. 363–397. doi:10.1016/B978-044453219-0.50015-5

Michel MR, Hirt B, Weil R. 1967. Mouse cellular DNA enclosed in polyoma viral capsids (pseudovirions). *Proc Natl Acad Sci U S A* **58**:1381–1388. doi:10.1073/pnas.58.4.1381

Microbiology by numbers. 2011. . *Nat Rev Microbiol*. doi:10.1038/nrmicro2644

Morehead MS, Scarbrough C. 2018. Emergence of Global Antibiotic Resistance. *Prim Care - Clin Off Pract*. doi:10.1016/j.pop.2018.05.006

Mularski A, Wilksch JJ, Hanssen E, Strugnell RA, Separovic F. 2016. Atomic force microscopy of bacteria reveals the mechanobiology of pore forming peptide action. *Biochim Biophys Acta - Biomembr* **1858**:1091–1098. doi:10.1016/j.bbamem.2016.03.002

Müller P, Herrmann A. 2002. Rapid transbilayer movement of spin-labeled steroids in human erythrocytes and in liposomes. *Biophys J*. doi:10.1016/S0006-3495(02)75496-9

Munro JB, Gorman J, Ma X, Zhou Z, Arthos J, Burton DR, Koff WC, Courter JR, Smith AB, Kwong PD, Blanchard SC, Mothes W, Mothes W. 2014. Conformational dynamics of single HIV-1 envelope trimers on the surface of native virions. *Science* **346**:759–63. doi:10.1126/science.1254426

Murira A, Lamarre A. 2016. Type-I interferon responses: From friend to foe in the battle against chronic viral infection. *Front Immunol*. doi:10.3389/fimmu.2016.00609

Murrell B, Vollbrecht T, Guatelli J, Wertheim JO. 2016. The Evolutionary Histories of Antiretroviral Proteins SERINC3 and SERINC5 Do Not Support an Evolutionary Arms Race in Primates. *J Virol* **90**:8085–9. doi:10.1128/JVI.00972-16

Nathan L, Lai AL, Millet JK, Straus MR, Freed JH, Whittaker GR, Daniel S. 2020. Calcium Ions Directly Interact with the Ebola Virus Fusion Peptide to Promote Structure-Function Changes That Enhance Infection. *ACS Infect Dis* **6**:250–260. doi:10.1021/acsinfecdis.9b00296

Neil SJD, Zang T, Bieniasz PD. 2008. Tetherin inhibits retrovirus release and is antagonized by HIV-1 Vpu. *Nature* **451**:425–430. doi:10.1038/nature06553

Neumann G, Watanabe T, Ito H, Watanabe S, Goto H, Gao P, Hughes M, Perez DR, Donis R, Hoffmann E, Hobom G, Kawaoka Y. 1999. Generation of influenza A viruses entirely from cloned cDNAs. *Proc Natl Acad Sci U S A* **96**:9345–9350. doi:10.1073/pnas.96.16.9345

Nielsen SB, Otzen DE. 2019. Quartz Crystal Microbalances as Tools for Probing Protein–Membrane InteractionsMethods in Molecular Biology. Humana Press Inc. pp. 31–52. doi:10.1007/978-1-4939-9512-7_2

Nieto-Garai JA, Glass B, Bunn C, Giese M, Jennings G, Brankatschk B, Agarwal S, Börner K, Xabier Contreras F, Knölker HJ, Zankl C, Simons K, Schroeder C, Lorizate M, Kräusslich HG. 2018. Lipidomimetic compounds act as HIV-1 entry inhibitors by altering viral membrane structure. *Front Immunol* **9**. doi:10.3389/fimmu.2018.01983

Niko Y, Didier P, Mely Y, Konishi G, Klymchenko AS. 2016. Bright and photostable push-pull pyrene dye visualizes lipid order variation between plasma and intracellular membranes. **6**:18870. doi:10.1038/srep18870

Nikolaus J, Stöckl M, Langosch D, Volkmer R, Herrmann A. 2010. Direct visualization of large and protein-free hemifusion diaphragms. *Biophys J* **98**:1192–1199. doi:10.1016/j.bpj.2009.11.042

Nisole S, Stoye JP, Saïb A. 2005. TRIM family proteins: Retroviral restriction and antiviral defence. *Nat Rev Microbiol*. doi:10.1038/nrmicro1248

Nozaki Y, Lasič DD, Tanford C, Reynolds JA. 1982. Size analysis of phospholipid vesicle preparations. *Science (80-)*. doi:10.1126/science.7089571

Olson F, Hunt CA, Szoka FC, Vail WJ, Papahadjopoulos D. 1979. Preparation of liposomes of defined size distribution by extrusion through polycarbonate membranes. *BBA - Biomembr* **557**:9–23. doi:10.1016/0005-2736(79)90085-3

Op den Kamp JA. 1979. Lipid asymmetry in membranes. *Annu Rev Biochem*. doi:10.1146/annurev.bi.48.070179.000403

Oppenheim JJ, Biragyn A, Kwak LW, Yang D. 2003. Roles of antimicrobial peptides such as defensins in innate and adaptive immunityAnnals of the Rheumatic Diseases. BMJ Publishing Group. pp. 17–21. doi:10.1136/ard.62.suppl_2.ii17

Ozato K, Shin DM, Chang TH, Morse HC. 2008. TRIM family proteins and their emerging roles in innate immunity. *Nat Rev Immunol*. doi:10.1038/nri2413

Padilla-Parra S, Marin M, Kondo N, Melikyan GB. 2012. Synchronized retrovirus fusion in cells expressing alternative receptor isoforms releases the viral core into distinct sub-cellular compartments. *PLoS Pathog* **8**. doi:10.1371/journal.ppat.1002694

Pan R, Gorny MK, Zolla-Pazner S, Kong X-P. 2015. The V1V2 Region of HIV-1 gp120 Forms a Five-Stranded Beta Barrel. *J Virol* **89**:8003–8010. doi:10.1128/jvi.00754-15

Papahadjopoulos D, Watkins JC. 1967. Phospholipid model membranes. II. Permeability properties of hydrated liquid crystals. *BBA - Biomembr* **135**:639–652. doi:10.1016/0005-2736(67)90095-8

Passos V, Zillinger T, Casartelli N, Wachs AS, Xu S, Malassa A, Steppich K, Schilling H, Franz S, Todt D, Steinmann E, Sutter K, Dittmer U, Bohne J, Schwartz O, Barchet W, Goffinet C. 2019. Characterization of Endogenous SERINC5 Protein as anti-HIV-1 Factor. *J Virol* JVI.01221-19. doi:10.1128/JVI.01221-19

Perlmutter JD, Hagan MF. 2015. Mechanisms of virus assembly. *Annu Rev Phys Chem* **66**:217–239. doi:10.1146/annurev-physchem-040214-121637

Perreira JM, Chin CR, Feeley EM, Brass AL. 2013. IFITMs restrict the replication of multiple pathogenic viruses. *J Mol Biol*. doi:10.1016/j.jmb.2013.09.024

Pittman AE, Marsh BP, King GM. 2018. Conformations and Dynamic Transitions of a Melittin Derivative That Forms Macromolecule-Sized Pores in Lipid Bilayers.

Langmuir **34**:8393–8399. doi:10.1021/acs.langmuir.8b00804

Platt EJ, Bilska M, Kozak SL, Kabat D, Montefiori DC. 2009. Evidence that Ecotropic Murine Leukemia Virus Contamination in TZM-bl Cells Does Not Affect the Outcome of Neutralizing Antibody Assays with Human Immunodeficiency Virus Type 1. *J Virol*. doi:10.1128/jvi.00709-09

Plemper RK, Melikyan GB. 2013. Membrane fusionEncyclopedia of Biological Chemistry: Second Edition. Elsevier Inc. pp. 621–626. doi:10.1016/B978-0-12-378630-2.00639-3

Porto WF, Irazazabal L, Alves ESF, Ribeiro SM, Matos CO, Pires ÁS, Fensterseifer ICM, Miranda VJ, Haney EF, Humblot V, Torres MDT, Hancock REW, Liao LM, Ladram A, Lu TK, De La Fuente-Nunez C, Franco OL. 2018. In silico optimization of a guava antimicrobial peptide enables combinatorial exploration for peptide design. *Nat Commun* **9**:1–12. doi:10.1038/s41467-018-03746-3

Punjani A, Rubinstein JL, Fleet DJ, Brubaker MA. 2017. CryoSPARC: Algorithms for rapid unsupervised cryo-EM structure determination. *Nat Methods* **14**:290–296. doi:10.1038/nmeth.4169

Pye VE, Rosa A, Bertelli C, Struwe WB, Maslen SL, Corey R, Liko I, Hassall M, Mattiuzzo G, Ballandras-Colas A, Nans A, Takeuchi Y, Stansfeld PJ, Skehel JM, Robinson C V., Pizzato M, Cherepanov P. 2020. A bipartite structural organization defines the SERINC family of HIV-1 restriction factors. *Nat Struct Mol Biol* **27**:78–83. doi:10.1038/s41594-019-0357-0

Qiu X, Eke IE, Johnson SF, Ding C, Zheng Y-H. 2020. Proteasomal degradation of human SERINC4: a potent host anti-HIV-1 factor that is antagonized by Nef. *bioRxiv* 2020.12.07.414888. doi:10.1101/2020.12.07.414888

Racaniello VR, Baltimore D. 1981. Cloned poliovirus complementary DNA is infectious in mammalian cells. *Science (80-)* **214**:916–919. doi:10.1126/science.6272391

Ragland SA, Criss AK. 2019. Protocols to Interrogate the Interactions Between Neisseria gonorrhoeae and Primary Human NeutrophilsMethods in Molecular Biology. Humana Press Inc. pp. 319–345. doi:10.1007/978-1-4939-9496-0_19

Rahman K, Coomer CA, Majdoul S, Ding SY, Padilla-Parra S, Compton AA. 2020. Homology-guided identification of a conserved motif linking the antiviral functions of IFITM3 to its oligomeric state. *Elife* **9**. doi:10.7554/eLife.58537

Rand RP, Parsegian VA. 1989. Hydration forces between phospholipid bilayers. *BBA - Rev Biomembr* **988**:351–376. doi:10.1016/0304-4157(89)90010-5

Rantalainen K, Berndsen ZT, Antanasijevic A, Schiffner T, Zhang X, Lee WH, Torres JL, Zhang L, Irimia A, Copps J, Zhou KH, Kwon YD, Law WH, Schramm CA, Verardi R, Krebs SJ, Kwong PD, Doria-Rose NA, Wilson IA, Zwick MB, Yates JR, Schief WR, Ward AB. 2020. HIV-1 Envelope and MPER Antibody Structures in Lipid Assemblies. *Cell Rep* **31**. doi:10.1016/j.celrep.2020.107583

Rathinakumar R, Walkenhorst WF, Wimley WC. 2009. Broad-spectrum antimicrobial peptides by rational combinatorial design and high-throughput screening: The importance of interfacial activity. *J Am Chem Soc* **131**:7609–7617. doi:10.1021/ja8093247

Rausch JM, Marks JR, Rathinakumar R, Wimley WC. 2007. β-Sheet pore-forming peptides selected from a rational combinatorial library: Mechanism of pore formation in lipid vesicles and activity in biological membranes. *Biochemistry*

46:12124–12139. doi:10.1021/bi700978h
Rausch JM, Marks JR, Wimley WC. 2005. Rational combinatorial design of pore-forming β-sheet peptides. *Proc Natl Acad Sci U S A* **102**:10511–10515. doi:10.1073/pnas.0502013102
Rawle RJ, Villamil Giraldo AM, Boxer SG, Kasson PM. 2019. Detecting and Controlling Dye Effects in Single-Virus Fusion Experiments. *Biophys J* **117**:445–452. doi:10.1016/j.bpj.2019.06.022
Rey FA, Lok SM. 2018. Common Features of Enveloped Viruses and Implications for Immunogen Design for Next-Generation Vaccines. *Cell*. doi:10.1016/j.cell.2018.02.054
Richards MJ, Hsia CY, Singh RR, Haider H, Kumpf J, Kawate T, Daniel S. 2016. Membrane Protein Mobility and Orientation Preserved in Supported Bilayers Created Directly from Cell Plasma Membrane Blebs. *Langmuir* **32**. doi:10.1021/acs.langmuir.5b03415
Risselada HJ, Bubnis G, Grubmüller H. 2014. Expansion of the fusion stalk and its implication for biological membrane fusion. *Proc Natl Acad Sci U S A* **111**:11043–11048. doi:10.1073/pnas.1323221111
Ritchie TK, Grinkova Y V., Bayburt TH, Denisov IG, Zolnerciks JK, Atkins WM, Sligar SG. 2009. Chapter 11 Reconstitution of Membrane Proteins in Phospholipid Bilayer Nanodiscs. *Methods Enzymol*. doi:10.1016/S0076-6879(09)64011-8
Rosa A, Chande A, Ziglio S, De Sanctis V, Bertorelli R, Goh SL, McCauley SM, Nowosielska A, Antonarakis SE, Luban J, Santoni FA, Pizzato M. 2015. HIV-1 Nef promotes infection by excluding SERINC5 from virion incorporation. *Nature* **526**:212–7. doi:10.1038/nature15399
Ryu W-S. 2017. Virus Life CycleMolecular Virology of Human Pathogenic Viruses. Elsevier. pp. 31–45. doi:10.1016/b978-0-12-800838-6.00003-5
Sakuma R, Noser JA, Ohmine S, Ikeda Y. 2007. Rhesus monkey TRIM5α restricts HIV-1 production through rapid degradation of viral Gag polyproteins. *Nat Med* **13**:631–635. doi:10.1038/nm1562
Salimi H, Johnson J, Flores MG, Zhang MS, O'Malley Y, Houtman JC, Schlievert PM, Haim H. 2020. The lipid membrane of HIV-1 stabilizes the viral envelope glycoproteins and modulates their sensitivity to antibody neutralization. *J Biol Chem* **295**:348–362. doi:10.1074/jbc.RA119.009481
Sanganna Gari RR, Seelheim P, Marsh B, Kiessling V, Creutz CE, Tamm LK. 2018. Quaternary structure of the small amino acid transporter OprG from Pseudomonas aeruginosa. *J Biol Chem* **293**:17267–17277. doi:10.1074/jbc.RA118.004461
Sarabipour S, Chan RB, Zhou B, Di Paolo G, Hristova K. 2015. Analytical characterization of plasma membrane-derived vesicles produced via osmotic and chemical vesiculation. *Biochim Biophys Acta - Biomembr* **1848**:1591–1598. doi:10.1016/j.bbamem.2015.04.002
Sarzotti-Kelsoe M, Bailer RT, Turk E, Lin C, Bilska M, Greene KM, Gao H, Todd CA, Ozaki DA, Seaman MS, Mascola JR, Montefiori DC. 2014. Optimization and validation of the TZM-bl assay for standardized assessments of neutralizing antibodies against HIV-1. *J Immunol Methods* **409**:131–46. doi:10.1016/j.jim.2013.11.022
Schmid MF, Booth CR. 2008. Methods for aligning and for averaging 3D volumes with

missing data. *J Struct Biol* **161**:243–248. doi:10.1016/j.jsb.2007.09.018
Schmidt FI, Bleck CKE, Mercer J. 2012. Poxvirus host cell entry. *Curr Opin Virol*. doi:10.1016/j.coviro.2011.11.007
Schneider F, Waithe D, Clausen MP, Galiani S, Koller T, Ozhan G, Eggeling C, Sezgin E. 2017. Diffusion of lipids and GPI-anchored proteins in actin-free plasma membrane vesicles measured by STED-FCS. *Mol Biol Cell* **28**:1507–1518. doi:10.1091/mbc.e16-07-0536
Schuler MA, Denisov IG, Sligar SG. 2013. Nanodiscs as a new tool to examine lipid-protein interactions. *Methods Mol Biol* **974**:415–433. doi:10.1007/978-1-62703-275-9_18
Schulte B, Selyutina A, Opp S, Herschhorn A, Sodroski JG, Pizzato M, Diaz-Griffero F. 2018. Localization to detergent-resistant membranes and HIV-1 core entry inhibition correlate with HIV-1 restriction by SERINC5. *Virology* **515**:52–65. doi:10.1016/j.virol.2017.12.005
Schütte OM, Mey I, Enderlein J, Savi F, Geil B, Janshoff A, Steinem C. 2017. Size and mobility of lipid domains tuned by geometrical constraints. *Proc Natl Acad Sci U S A* **114**:E6064–E6071. doi:10.1073/pnas.1704199114
Schwarzer R, Levental I, Gramatica A, Scolari S, Buschmann V, Veit M, Herrmann A. 2014. The cholesterol-binding motif of the HIV-1 glycoprotein gp41 regulates lateral sorting and oligomerization. *Cell Microbiol* **16**:1565–1581. doi:10.1111/cmi.12314
Schwenen LLG, Hubrich R, Milovanovic D, Geil B, Yang J, Kros A, Jahn R, Steinem C. 2015. Resolving single membrane fusion events on planar pore-spanning membranes. *Sci Reports* **5**:srep12006. doi:10.1038/srep12006
Scott HL, Skinkle A, Kelley EG, Waxham MN, Levental I, Heberle FA. 2019. On the Mechanism of Bilayer Separation by Extrusion, or Why Your LUVs Are Not Really Unilamellar. *Biophys J* **117**:1381–1386. doi:10.1016/j.bpj.2019.09.006
Scott RE. 1976. Plasma membrane vesiculation: A new technique for isolation of plasma membranes. *Science (80-)* **194**:743–745. doi:10.1126/science.982044
Sengupta K, Raghunathan VA, Katsaras J. 2003. Structure of the ripple phase of phospholipid multibilayers. *Phys Rev E - Stat Physics, Plasmas, Fluids, Relat Interdiscip Top* **68**:12. doi:10.1103/PhysRevE.68.031710
Sengupta P, Seo AY, Pasolli HA, Song YE, Johnson MC, Lippincott-Schwartz J. 2019. A lipid-based partitioning mechanism for selective incorporation of proteins into membranes of HIV particles. *Nat Cell Biol* **21**:452–461. doi:10.1038/s41556-019-0300-y
Sergi P-P, Marin M, Gahlaut N, Suter R, Kondo N, Melikyan GB. 2013. Fusion of Mature HIV-1 Particles Leads to Complete Release of a Gag-GFP-Based Content Marker and Raises the Intraviral pH **8**:e71002. doi:10.1371/journal.pone.0071002
Sezgin E, Carugo D, Levental I, Stride E, Eggeling C. 2020. Creating supported plasma membrane bilayers using acoustic pressure. *Membranes (Basel)* **10**. doi:10.3390/membranes10020030
Sezgin E, Kaiser H-J, Baumgart T, Schwille P, Simons K, Levental I. 2012. Elucidating membrane structure and protein behavior using giant plasma membrane vesicles. *Nat Protoc* **7**:1042–1051. doi:10.1038/nprot.2012.059
Shagaghi N, Palombo EA, Clayton AHA, Bhave M. 2018. Antimicrobial peptides:

biochemical determinants of activity and biophysical techniques of elucidating their functionality. *World J Microbiol Biotechnol*. doi:10.1007/s11274-018-2444-5

Shapiro HM. 1994. Cell Membrane Potential Analysis. *Methods Cell Biol* **41**:121–133. doi:10.1016/S0091-679X(08)61713-6

Sharma S, Lewinski MK, Guatelli J. 2018. An N-Glycosylated Form of SERINC5 Is Specifically Incorporated into HIV-1 Virions. *J Virol* **92**. doi:10.1128/JVI.00753-18

Shenkarev ZO, Balandin S V., Trunov KI, Paramonov AS, Sukhanov S V., Barsukov LI, Arseniev AS, Ovchinnikova T V. 2011. Molecular mechanism of action of β-Hairpin antimicrobial peptide arenicin: Oligomeric structure in dodecylphosphocholine micelles and pore formation in planar lipid bilayers. *Biochemistry* **50**:6255–6265. doi:10.1021/bi200746t

Shi G, Kenney AD, Kudryashova E, Zani A, Zhang L, Lai KK, Hall-Stoodley L, Robinson RT, Kudryashov DS, Compton AA, Yount JS. 2020. Opposing activities of IFITM proteins in SARS-CoV-2 infection. *EMBO J*. doi:10.15252/embj.2020106501

Shi J, Xiong R, Zhou T, Su P, Zhang X, Qiu X, Li H, Li S, Yu C, Wang B, Ding C, Smithgall TE, Zheng Y-H. 2018. HIV-1 Nef Antagonizes SERINC5 Restriction by Downregulation of SERINC5 via the Endosome/Lysosome System. *J Virol* **92**. doi:10.1128/jvi.00196-18

Shillcock JC, Lipowsky R. 2005. Tension-induced fusion of bilayer membranes and vesicles. *Nat Mater* **4**:225–228. doi:10.1038/nmat1333

Shrivastava-Ranjan P, Flint M, Bergeron É, McElroy AK, Chatterjee P, Albariño CG, Nichol ST, Spiropoulou CF. 2018. Statins suppress Ebola virus infectivity by interfering with glycoprotein processing. *MBio* **9**. doi:10.1128/mBio.00660-18

Sibold J, Tewaag VE, Vagedes T, Mey I, Steinem C. 2020. Phase separation in pore-spanning membranes induced by differences in surface adhesion. *Phys Chem Chem Phys* **22**:9308–9315. doi:10.1039/d0cp00335b

Siegel DP. 1993. Energetics of intermediates in membrane fusion: comparison of stalk and inverted micellar intermediate mechanisms. *Biophys J* **65**:2124–2140. doi:10.1016/S0006-3495(93)81256-6

Simons K, Ikonen E. 1997. Functional rafts in cell membranes. **387**:569–572. doi:10.1038/42408

Singer SJ, Nicolson GL. 1972. The fluid mosaic model of the structure of cell membranes. *Science (80-)* **175**:720–731. doi:10.1126/science.175.4023.720

Singh AP, Nicholls P. 1985. Cyanine and safranine dyes as membrane potential probes in cytochrome c oxidase reconstituted proteoliposomes. *J Biochem Biophys Methods* **11**:95–108. doi:10.1016/0165-022X(85)90045-4

Skinkle A. 2019. Cell-derived plasma membrane vesicles are permeable to hydrophilic macromolecules. *Biophys J* **188**:P1292-1300. doi:10.1101/731364

Skorupka KA, Roganowicz MD, Christensen DE, Wan Y, Pornillos O, Ganser-Pornillos BK. 2019. Hierarchical assembly governs TRIM5α recognition of HIV-1 and retroviral capsids. *Sci Adv* **5**. doi:10.1126/sciadv.aaw3631

Smith SE, Weston S, Kellam P, Marsh M. 2014. IFITM proteins - Cellular inhibitors of viral entry. *Curr Opin Virol*. doi:10.1016/j.coviro.2013.11.004

Soloviov D, Cai YQ, Bolmatov D, Suvorov A, Zhernenkov K, Zav'yalov D, Bosak A, Uchiyama H, Zhernenkov M. 2020. Functional lipid pairs as building blocks of

phase-separated membranes. *Proc Natl Acad Sci U S A* **117**:4749–4757. doi:10.1073/pnas.1919264117

Sood C, Marin M, Chande A, Pizzato M, Melikyan GB. 2017. SERINC5 protein inhibits HIV-1 fusion pore formation by promoting functional inactivation of envelope glycoproteins. *J Biol Chem* **292**:6014–6026. doi:10.1074/jbc.M117.777714

Sood C, Marin M, Mason CS, Melikyan GB. 2016. Visualization of Content Release from Cell Surface-Attached Single HIV-1 Particles Carrying an Extra-Viral Fluorescent pH-Sensor. *PLoS One* **11**:e0148944. doi:10.1371/journal.pone.0148944

Sougrat R, Bartesaghi A, Lifson JD, Bennett AE, Bess JW, Zabransky DJ, Subramaniam S. 2007. Electron tomography of the contact between T cells and SIV/HIV-1: implications for viral entry. *PLoS Pathog* **3**:e63. doi:10.1371/journal.ppat.0030063

Spector AA, Yorek MA. 1985. Membrane lipid composition and cellular function. *J Lipid Res* **26**:1015–35. doi:10.1016/S0022-2275(20)34276-0

Speerstra S, Chistov AA, Proskurin G V., Aralov A V., Ulashchik EA, Streshnev PP, Shmanai V V., Korshun VA, Schang LM. 2018. Antivirals acting on viral envelopes via biophysical mechanisms of action. *Antiviral Res* **149**:164–173. doi:10.1016/j.antiviral.2017.11.018

Sreerama N, Woody RW. 1993. A Self-Consistent Method for the Analysis of Protein Secondary Structure from Circular Dichroism. *Anal Biochem* **209**:32–44. doi:10.1006/abio.1993.1079

St. Vincent MR, Colpitts CC, Ustinov A V., Muqadas M, Joyce MA, Barsby NL, Epand RF, Epand RM, Khramyshev SA, Valueva OA, Korshun VA, Tyrrell DLJ, Schang LM. 2010. Rigid amphipathic fusion inhibitors, small molecule antiviral compounds against enveloped viruses. *Proc Natl Acad Sci U S A* **107**:17339–17344. doi:10.1073/pnas.1010026107

Stamatatos L, Lim M, Cheng-Mayer C. 2000. Generation and structural analysis of soluble oligomeric gp140 envelope proteins derived from neutralization-resistant and neutralization-susceptible primary HIV type 1 isolates. *AIDS Res Hum Retroviruses*. doi:10.1089/08892220050058407

Stamatatos L, Wiskerchen M, Cheng-Mayer C. 1998. Effect of major deletions in the V1 and V2 loops of a macrophage-tropic HIV type 1 isolate on viral envelope structure, cell entry, and replication. *AIDS Res Hum Retroviruses*. doi:10.1089/aid.1998.14.1129

Stano A, Leaman DP, Kim AS, Zhang L, Autin L, Ingale J, Gift SK, Truong J, Wyatt RT, Olson AJ, Zwick MB. 2017. Dense array of spikes on HIV-1 virion particles. *J Virol* **91**:415–17. doi:10.1128/JVI.00415-17

Staropoli I, Dufloo J, Ducher A, Commere P-H, Sartori-Rupp A, Novault S, Bruel T, Lorin V, Mouquet H, Schwartz O, Casartelli N. 2019. Flow Cytometry Analysis of HIV-1 Env Conformations at the Surface of Infected Cells and Virions: Role of Nef, CD4, and SERINC5. *J Virol* **94**. doi:10.1128/jvi.01783-19

Staykova M, Holmes DP, Read C, Stone HA. 2011. Mechanics of surface area regulation in cells examined with confined lipid membranes. *Proc Natl Acad Sci U S A* **108**:9084–9088. doi:10.1073/pnas.1102358108

Steck TL, Ye J, Lange Y. 2002. Probing red cell membrane cholesterol movement with cyclodextrin. *Biophys J*. doi:10.1016/S0006-3495(02)73972-6

Steffen I, Simmons G. 2016. Pseudotyping Viral Vectors With Emerging Virus Envelope

Proteins. *Curr Gene Ther* **16**:47–55. doi:10.2174/1566523216666160119093948
Stein BS, Gowda SD, Lifson JD, Penhallow RC, Bensch KG, Engleman EG. 1987. pH-independent HIV entry into CD4-positive T cells via virus envelope fusion to the plasma membrane. *Cell* **49**:659–668. doi:10.1016/0092-8674(87)90542-3
Stein H, Spindler S, Bonakdar N, Wang C, Sandoghdar V. 2017. Production of isolated giant unilamellar vesicles under high salt concentrations. *Front Physiol* **8**. doi:10.3389/fphys.2017.00063
Steinkühler J, De Tillieux P, Knorr RL, Lipowsky R, Dimova R. 2018. Charged giant unilamellar vesicles prepared by electroformation exhibit nanotubes and transbilayer lipid asymmetry. *Sci Rep* **8**:1–9. doi:10.1038/s41598-018-30286-z
Steltenkamp S, Müller MM, Deserno M, Hennesthal C, Steinem C, Janshoff A. 2006. Mechanical properties of pore-spanning lipid bilayers probed by atomic force microscopy. *Biophys J* **91**:217–226. doi:10.1529/biophysj.106.081398
Straus MR, Tang T, Lai AL, Flegel A, Bidon M, Freed JH, Daniel S, Whittaker GR. 2020. Ca 2+ Ions Promote Fusion of Middle East Respiratory Syndrome Coronavirus with Host Cells and Increase Infectivity . *J Virol* **94**. doi:10.1128/jvi.00426-20
Stremlau M, Perron M, Lee M, Li Y, Song B, Javanbakht H, Diaz-Griffero F, Anderson DJ, Sundquist WI, Sodroski J. 2006. Specific recognition and accelerated uncoating of retroviral capsids by the TRIM5α restriction factor. *Proc Natl Acad Sci U S A* **103**:5514–5519. doi:10.1073/pnas.0509996103
Suddala KC, Lee CC, Meraner P, Marin M, Markosyan RM, Desai TM, Cohen FS, Brass AL, Melikyan GB. 2019. Interferon-induced transmembrane protein 3 blocks fusion of sensitive but not resistant viruses by partitioning into virus-carrying endosomes. *PLoS Pathog* **15**. doi:10.1371/journal.ppat.1007532
Sun X, Whittaker GR. 2003. Role for influenza virus envelope cholesterol in virus entry and infection. *J Virol* **77**:12543–12551.
Sundquist WI, Kräusslich HG. 2012. HIV-1 assembly, budding, and maturation. *Cold Spring Harb Perspect Med*. doi:10.1101/cshperspect.a006924
Suzuki J, Denning DP, Imanishi E, Horvitz HR, Nagata S. 2013. Xk-related protein 8 and CED-8 promote phosphatidylserine exposure in apoptotic cells. *Science (80-)* **341**:403–6. doi:10.1126/science.1236758
Sych T, Mély Y, Römer W. 2018. Lipid self-assembly and lectin-induced reorganization of the plasma membrane. *Philos Trans R Soc B Biol Sci*. doi:10.1098/rstb.2017.0117
Symons JL, Cho K-J, Chang JT, Du G, Waxham MN, Hancock JF, Levental I, Levental KR. 2020. Lipidomic atlas of mammalian cell membranes reveals hierarchical variation induced by culture conditions, subcellular membranes, and cell lineages. *Soft Matter*. doi:10.1039/d0sm00404a
Szoka F, Papahadjopoulos D. 1978. Procedure for preparation of liposomes with large internal aqueous space and high capture by reverse-phase evaporation. *Proc Natl Acad Sci U S A*. doi:10.1073/pnas.75.9.4194
Tada T, Zhang Y, Koyama T, Tobiume M, Tsunetsugu-Yokota Y, Yamaoka S, Fujita H, Tokunaga K. 2015. March8 inhibits HIV-1 infection by reducing virion incorporation of envelope glycoproteins. *Nat Med*. doi:10.1038/nm.3956
Takahashi D, Shukla SK, Prakash O, Zhang G. 2010. Structural determinants of host defense peptides for antimicrobial activity and target cell selectivity. *Biochimie*.

doi:10.1016/j.biochi.2010.02.023
Takeuchi Y, McClure MO, Pizzato M. 2008. Identification of gammaretroviruses constitutively released from cell lines used for human immunodeficiency virus research. *J Virol* **82**:12585–8. doi:10.1128/JVI.01726-08
Tamm LK. 2003. Hypothesis: Spring-loaded boomerang mechanism of influenza hemagglutinin-mediated membrane fusion. *Biochim Biophys Acta - Biomembr*. doi:10.1016/S0005-2736(03)00159-7
Tamm LK. 1993. TOTAL INTERNAL REFLECTANCE FLUORESCENCE MICROSCOPYOptical Microscopy. Elsevier. pp. 295–337. doi:10.1016/b978-0-08-057139-3.50015-6
Tamm LK. 1984. The substrate supported lipid bilayer-a new model membrane system. *Klin Wochenschr* **62**:502–503.
Tamm LK, Groves JT. 2009. Supported membranes in structural biology. *J Struct Biol*. doi:10.1016/j.jsb.2009.07.016
Tamm LK, McConnell HM. 1985. Supported phospholipid bilayers. *Biophys J* **47**:105–13. doi:10.1016/S0006-3495(85)83882-0
Tartour K, Appourchaux R, Gaillard J, Nguyen XN, Durand S, Turpin J, Beaumont E, Roch E, Berger G, Mahieux R, Brand D, Roingeard P, Cimarelli A. 2014. IFITM proteins are incorporated onto HIV-1 virion particles and negatively imprint their infectivity. *Retrovirology* **11**. doi:10.1186/s12977-014-0103-y
Tartour K, Nguyen XN, Appourchaux R, Assil S, Barateau V, Bloyet LM, Burlaud Gaillard J, Confort MP, Escudero-Perez B, Gruffat H, Hong SS, Moroso M, Reynard O, Reynard S, Decembre E, Ftaich N, Rossi A, Wu N, Arnaud F, Baize S, Dreux M, Gerlier D, Paranhos-Baccala G, Volchkov V, Roingeard P, Cimarelli A. 2017. Interference with the production of infectious viral particles and bimodal inhibition of replication are broadly conserved antiviral properties of IFITMs. *PLoS Pathog* **13**. doi:10.1371/journal.ppat.1006610
Tatulian SA, Tamm LK. 1996. Reversible pH-dependent conformational change of reconstituted influenza hemagglutinin. *J Mol Biol*. doi:10.1006/jmbi.1996.0402
Tavares FN, da Costa E V., Kew OM, da Silva EE. 2013. Complete genome sequence of the last representative genotype of wild indigenous poliovirus type 1, which circulated in Brazil. *Genome Announc* **1**. doi:10.1128/genomeA.00811-13
Teissier E, Penin F, Pécheur EI. 2011. Targeting cell entry of enveloped viruses as an antiviral strategy. *Molecules*. doi:10.3390/molecules16010221
Terrettaz S, Stora T, Duschl C, Vogel H. 1993. Protein Binding to Supported Lipid Membranes: Investigation of the Cholera Toxin-Ganglioside Interaction by Simultaneous Impedance Spectroscopy and Surface Plasmon Resonance. *Langmuir* **9**:1361–1369. doi:10.1021/la00029a033
The Lancet. 2009. Urgently needed: new antibiotics. *Lancet*. doi:10.1016/S0140-6736(09)62076-6
Thonghin N, Kargas V, Clews J, Ford RC. 2018. Cryo-electron microscopy of membrane proteins. *Methods*. doi:10.1016/j.ymeth.2018.04.018
Timilsina U, Umthong S, Lynch B, Stablewski A. 2020. Serinc5 potently restricts retrovirus infection in vivo. *MBio* **11**:1–18. doi:10.1128/mBio.00588-20
Tissot C, Mechti N. 1995. Molecular cloning of a new interferon-induced factor that represses human immunodeficiency virus type I long terminal repeat expression. *J*

Biol Chem **270**:14891–14898. doi:10.1074/jbc.270.25.14891
Toohey K, Wehrly K, Nishio J, Perryman S, Chesebro B. 1995. Human Immunodeficiency Virus Envelope V1 and V2 Regions Influence Replication Efficiency in Macrophages by Affecting Virus Spread. *Virology* **213**:70–79. doi:10.1006/viro.1995.1547
Torres MDT, Sothiselvam S, Lu TK, de la Fuente-Nunez C. 2019. Peptide Design Principles for Antimicrobial Applications. *J Mol Biol*. doi:10.1016/j.jmb.2018.12.015
Trautz B, Pierini V, Wombacher R, Stolp B, Chase AJ, Pizzato M, Fackler OT. 2016. The Antagonism of HIV-1 Nef to SERINC5 Particle Infectivity Restriction Involves the Counteraction of Virion-Associated Pools of the Restriction Factor. *J Virol* **90**. doi:10.1128/jvi.01246-16
Trautz B, Wiedemann H, Lüchtenborg C, Pierini V, Kranich J, Glass B, Kräusslich H-G, Brocker T, Pizzato M, Ruggieri A, Brügger B, Fackler OT. 2017. The host-cell restriction factor SERINC5 restricts HIV-1 infectivity without altering the lipid composition and organization of viral particles. *J Biol Chem* **292**:13702–13713. doi:10.1074/jbc.M117.797332
Tristram-Nagle S, Nagle JF. 2004. Lipid bilayers: Thermodynamics, structure, fluctuations, and interactions. *Chem Phys Lipids*. doi:10.1016/j.chemphyslip.2003.09.002
Turelli P, Mangeat B, Jost S, Vianin S, Trono D. 2004. Inhibition of Hepatitis B Virus Replication by APOBEC3G. *Science (80-)* **303**:1829. doi:10.1126/science.1092066
Turk M, Baumeister W. 2020. The promise and the challenges of cryo-electron tomography. *FEBS Lett* **594**:3243–3261. doi:10.1002/1873-3468.13948
Tyler AII, Law R V., Seddon JM. 2015. X-ray diffraction of lipid model membranes. *Methods Mol Biol* **1232**:199–225. doi:10.1007/978-1-4939-1752-5_16
Uchihashi T, Scheuring S. 2018. Applications of high-speed atomic force microscopy to real-time visualization of dynamic biomolecular processes. *Biochim Biophys Acta - Gen Subj*. doi:10.1016/j.bbagen.2017.07.010
Umashankar M, Sánchez-San Martín C, Liao M, Reilly B, Guo A, Taylor G, Kielian M. 2008. Differential Cholesterol Binding by Class II Fusion Proteins Determines Membrane Fusion Properties. *J Virol* **82**:9245–9253. doi:10.1128/jvi.00975-08
Usami Y, Wu Y, Göttlinger HG. 2015. SERINC3 and SERINC5 restrict HIV-1 infectivity and are counteracted by Nef. *Nature* **526**:218–23. doi:10.1038/nature15400
Uzgiris EE, Kornberg RD. 1983. Two-dimensional crystallization technique for imaging macromolecules, with application to antigen-antibody-complement complexes. *Nature* **301**:125–129. doi:10.1038/301125a0
Van Damme N, Goff D, Katsura C, Jorgenson RL, Mitchell R, Johnson MC, Stephens EB, Guatelli J. 2008. The Interferon-Induced Protein BST-2 Restricts HIV-1 Release and Is Downregulated from the Cell Surface by the Viral Vpu Protein. *Cell Host Microbe* **3**:245–252. doi:10.1016/j.chom.2008.03.001
Van Duijl-Richter MKS, Blijleven JS, van Oijen AM, Smit JM. 2015. Chikungunya virus fusion properties elucidated by single-particle and bulk approaches. *J Gen Virol* **96**. doi:10.1099/vir.0.000144
Van Meer G. 1989. Lipid traffic in animal cells. *Annu Rev Cell Biol*.

doi:10.1146/annurev.cb.05.110189.001335
Van Meer G, Voelker DR, Feigenson GW. 2008. Membrane lipids: Where they are and how they behave. *Nat Rev Mol Cell Biol*. doi:10.1038/nrm2330
Vartanian JP, Henry M, Marchio A, Suspène R, Aynaud MM, Guétard D, Cervantes-Gonzalez M, Battiston C, Mazzaferro V, Pineau P, Dejean A, Wain-Hobson S. 2010. Massive APOBEC3 editing of hepatitis B viral DNA in cirrhosis. *PLoS Pathog* **6**:1–9. doi:10.1371/journal.ppat.1000928
Vázquez RF, Ovalle-García E, Antillón A, Ortega-Blake I, Bakás LS, Muñoz-Garay C, Maté SM. 2021. Asymmetric bilayers mimicking membrane rafts prepared by lipid exchange: Nanoscale characterization using AFM-Force spectroscopy. *Biochim Biophys Acta - Biomembr* **1863**:183467. doi:10.1016/j.bbamem.2020.183467
Veatch SL, Keller SL. 2005. Seeing spots: Complex phase behavior in simple membranes. *Biochim Biophys Acta - Mol Cell Res*. doi:10.1016/j.bbamcr.2005.06.010
Veatch SL, Keller SL. 2003. Separation of Liquid Phases in Giant Vesicles of Ternary Mixtures of Phospholipids and Cholesterol. *Biophys J* **85**:3074–3083. doi:10.1016/S0006-3495(03)74726-2
Viard M, Parolini I, Sargiacomo M, Fecchi K, Ramoni C, Ablan S, Ruscetti FW, Wang JM, Blumenthal R. 2002. Role of Cholesterol in Human Immunodeficiency Virus Type 1 Envelope Protein-Mediated Fusion with Host Cells. *J Virol*. doi:10.1128/jvi.76.22.11584-11595.2002
Vigant F, Hollmann A, Lee J, Santos NC, Jung ME, Lee B. 2014. The Rigid Amphipathic Fusion Inhibitor dUY11 Acts through Photosensitization of Viruses. *J Virol* **88**:1849–1853. doi:10.1128/jvi.02907-13
Vigant F, Jung M, Lee B. 2010. Positive reinforcement for viruses. *Chem Biol*. doi:10.1016/j.chembiol.2010.10.002
Vigant F, Lee J, Hollmann A, Tanner LB, Akyol Ataman Z, Yun T, Shui G, Aguilar HC, Zhang D, Meriwether D, Roman-Sosa G, Robinson LR, Juelich TL, Buczkowski H, Chou S, Castanho MARB, Wolf MC, Smith JK, Banyard A, Kielian M, Reddy S, Wenk MR, Selke M, Santos NC, Freiberg AN, Jung ME, Lee B. 2013. A Mechanistic Paradigm for Broad-Spectrum Antivirals that Target Virus-Cell Fusion. *PLoS Pathog* **9**:e1003297. doi:10.1371/journal.ppat.1003297
Vigant F, Santos NC, Lee B. 2015. Broad-spectrum antivirals against viral fusion. *Nat Rev Microbiol*. doi:10.1038/nrmicro3475
Vogel SK, Greiss F, Khmelinskaia A, Schwille P. 2017. Control of lipid domain organization by a biomimetic contractile actomyosin cortex. *Elife* **6**:e24350. doi:10.7554/eLife.24350
Wagner ML, Tamm LK. 2001. Reconstituted syntaxin 1A/SNAP25 interacts with negatively charged lipids as measured by lateral diffusion in planar supported bilayers. *Biophys J* **81**:266–275. doi:10.1016/S0006-3495(01)75697-4
Wagner ML, Tamm LK. 2000. Tethered Polymer-Supported Planar Lipid Bilayers for Reconstitution of Integral Membrane Proteins: Silane-Polyethyleneglycol-Lipid as a Cushion and Covalent Linker. *Biophys J* **79**:1400–1414. doi:10.1016/S0006-3495(00)76392-2
Waheed AA, Ablan SD, Soheilian F, Nagashima K, Ono A, Schaffner CP, Freed EO. 2008. Inhibition of Human Immunodeficiency Virus Type 1 Assembly and Release

by the Cholesterol-Binding Compound Amphotericin B Methyl Ester: Evidence for Vpu Dependence. *J Virol*. doi:10.1128/jvi.00917-08

Walls AC, Park YJ, Tortorici MA, Wall A, McGuire AT, Veesler D. 2020. Structure, Function, and Antigenicity of the SARS-CoV-2 Spike Glycoprotein. *Cell* **181**:281-292.e6. doi:10.1016/j.cell.2020.02.058

Wan C, Kiessling V, Tamm LK. 2008. Coupling of cholesterol-rich lipid phases in asymmetric bilayers. *Biochemistry* **47**:2190–8. doi:10.1021/bi7021552

Wan W, Briggs JAG. 2016. Cryo-Electron Tomography and Subtomogram AveragingMethods in Enzymology. pp. 329–367. doi:10.1016/bs.mie.2016.04.014

Wang TY, Silvius JR. 2001. Cholesterol does not induce segregation of liquid-ordered domains in bilayers modeling the inner leaflet of the plasma membrane. *Biophys J* **81**:2762–2773. doi:10.1016/S0006-3495(01)75919-X

Ward AE, Kiessling V, Pornillos O, White JM, Ganser-Pornillos BK, Tamm LK. 2020. HIV-cell membrane fusion intermediates are restricted by Serincs as revealed by cryo electron and TIRF microscopy. *J Biol Chem* **295**:15183–15195.

Wehrly K, Chesebro B. 1997. p24 Antigen Capture Assay for Quantification of Human Immunodeficiency Virus Using Readily Available Inexpensive Reagents. *Methods* **12**:288–293. doi:10.1006/METH.1997.0481

Wei X, Decker JM, Liu H, Zhang Z, Arani RB, Kilby JM, Saag MS, Wu X, Shaw GM, Kappes JC. 2002. Emergence of Resistant Human Immunodeficiency Virus Type 1 in Patients Receiving Fusion Inhibitor (T-20) Monotherapy. *Antimicrob Agents Chemother* **46**:1896–1905. doi:10.1128/AAC.46.6.1896-1905.2002

Weidner JM, Jiang D, Pan X-B, Chang J, Block TM, Guo J-T. 2010. Interferon-Induced Cell Membrane Proteins, IFITM3 and Tetherin, Inhibit Vesicular Stomatitis Virus Infection via Distinct Mechanisms. *J Virol* **84**:12646–12657. doi:10.1128/jvi.01328-10

Wen Y, Dick RA, Feigenson GW, Vogt VM. 2016. Effects of Membrane Charge and Order on Membrane Binding of the Retroviral Structural Protein Gag. *J Virol* **90**:9518–32. doi:10.1128/JVI.01102-16

White J, Helenius A. 1980. pH-Dependent fusion between the Semliki Forest virus membrane and liposomes. *Proc Natl Acad Sci U S A* **77**:3273–3277. doi:10.1073/pnas.77.6.3273

White JM, Delos SE, Brecher M, Schornberg K. 2008. Structures and mechanisms of viral membrane fusion proteins: multiple variations on a common theme. *Crit Rev Biochem Mol Biol* **43**:189–219.

White JM, Whittaker GR. 2016. Fusion of Enveloped Viruses in Endosomes. *Traffic* **17**:593–614. doi:10.1111/tra.12389

Whitmore L, Wallace BA. 2008. Protein secondary structure analyses from circular dichroism spectroscopy: Methods and reference databases. *Biopolymers* **89**:392–400. doi:10.1002/bip.20853

WHO. 2015. Draft Global action plan on antimicrobial resistance WHA68.7. *World Heal Organ*.

Wolf MC, Freiberg AN, Zhang T, Akyol-Ataman Z, Grock A, Hong PW, Li J, Watson NF, Fang AQ, Aguilar HC, Porotto M, Honko AN, Damoiseaux R, Miller JP, Woodson SE, Chantasirivisal S, Fontanes V, Negrete OA, Krogstad P, Dasgupta A, Moscona A, Hensley LE, Whelan SP, Faull KF, Holbrook MR, Jung ME, Lee B.

2010. A broad-spectrum antiviral targeting entry of enveloped viruses. *Proc Natl Acad Sci U S A* **107**:3157–3162. doi:10.1073/pnas.0909587107

Wytrwal M, Bednar J, Nowakowska M, Wydro P, Kepczynski M. 2014. Interactions of serum with polyelectrolyte-stabilized liposomes: Cryo-TEM studies. *Colloids Surfaces B Biointerfaces* **120**:152–159. doi:10.1016/j.colsurfb.2014.02.040

Xu J, Ji C, Wang L, Cao Y, Dai Jianliang, Ye X, Zeng L, Dai Jianfeng, Wu Q, Xie Y, Mao Y. 2003. Cloning and expression of a novel human C5orf12 gene, a member of the TMS_TDE family. *Mol Biol Rep* **30**:47–52. doi:10.1023/A:1022250428015

Xue C, Lin TY, Chang D, Guo Z. 2017. Thioflavin T as an amyloid dye: fibril quantification, optimal concentration and effect on aggregation. *R Soc Open Sci* **4**:160696. doi:10.1098/rsos.160696

Yamaguchi M, Danev R, Nishiyama K, Sugawara K, Nagayama K. 2008. Zernike phase contrast electron microscopy of ice-embedded influenza A virus. *J Struct Biol* **162**:271–276. doi:10.1016/j.jsb.2008.01.009

Yang C, Zhao X, Sun D, Yang L, Chong C, Pan Y, Chi X, Gao Yanhang, Wang M, Shi X, Sun H, Lv J, Gao Yuanda, Zhong J, Niu J, Sun B. 2016. Interferon alpha (IFNα)-induced TRIM22 interrupts HCV replication by ubiquitinating NS5A. *Cell Mol Immunol* **13**:94–102. doi:10.1038/cmi.2014.131

Yang L, Huang HW. 2002. Observation of a membrane fusion intermediate structure. *Science (80-)* **297**:1877–1879. doi:10.1126/science.1074354

Yang S-T, Kiessling V, Simmons JA, White JM, Tamm LK. 2015. HIV gp41–mediated membrane fusion occurs at edges of cholesterol-rich lipid domains. *Nat Chem Biol* **11**:424–431. doi:10.1038/nchembio.1800

Yang S-T, Kiessling V, Tamm LK. 2016. Line tension at lipid phase boundaries as driving force for HIV fusion peptide-mediated fusion. *Nat Commun* **7**:11401. doi:10.1038/ncomms11401

Yang S-T, Kreutzberger AJB, Kiessling V, Ganser-Pornillos BK, White JM, Tamm LK. 2017. HIV virions sense plasma membrane heterogeneity for cell entry. *Sci Adv* **3**:e1700338. doi:10.1126/sciadv.1700338

Yang S-TT, Kreutzberger AJ, Lee J, Kiessling V, Tamm LK. 2016. The role of cholesterol in membrane fusion. *Chem Phys Lipids* **199**:136–143. doi:10.1016/j.chemphyslip.2016.05.003

Yeager M, Dryden KA, Ganser-Pornillos BK. 2013. Lipid monolayer and sparse matrix screening for growing two-dimensional crystals for electron crystallography: Methods and examplesMethods in Molecular Biology. Humana Press Inc. pp. 527–537. doi:10.1007/978-1-62703-176-9_28

Yeaman MR, Yount NY. 2003. Mechanisms of antimicrobial peptide action and resistance. *Pharmacol Rev*. doi:10.1124/pr.55.1.2

Yewdall AN, Mason AF, Van Hest JCM. 2018. The hallmarks of living systems: Towards creating artificial cells. *Interface Focus*. doi:10.1098/rsfs.2018.0023

Yoder N, Jalali-Yazdi F, Noreng S, Houser A, Baconguis I, Gouaux E. 2020. Light-coupled cryo-plunger for time-resolved cryo-EM. *J Struct Biol* **212**. doi:10.1016/j.jsb.2020.107624

Yu A, Skorupka KA, Pak AJ, Ganser-Pornillos BK, Pornillos O, Voth GA. 2020. TRIM5α self-assembly and compartmentalization of the HIV-1 viral capsid. *Nat Commun* **11**. doi:10.1038/s41467-020-15106-1

Zhang X, Shi J, Qiu X, Chai Q, Frabutt DA, Schwartz RC, Zheng Y-H. 2019. CD4 expression and Env conformation are critical for HIV-1 restriction by SERINC5. *J Virol* JVI.00544-19. doi:10.1128/JVI.00544-19

Zhang Xianfeng, Zhou T, Yang J, Lin Y, Shi J, Zhang Xihe, Frabutt DA, Zeng X, Li S, Venta PJ, Zheng Y-H. 2017. Identification of SERINC5-001 as the Predominant Spliced Isoform for HIV-1 Restriction. *J Virol* **91**:e00137-17. doi:10.1128/JVI.00137-17

Zhang Y, Lu J, Liu X. 2018. MARCH2 is upregulated in HIV-1 infection and inhibits HIV-1 production through envelope protein translocation or degradation. *Virology* **518**:293–300. doi:10.1016/j.virol.2018.02.003

Zheng SQ, Palovcak E, Armache J-P, Verba KA, Cheng Y, Agard DA. 2017. MotionCor2: anisotropic correction of beam-induced motion for improved cryo-electron microscopy. *Nat Methods* **14**:331–332. doi:10.1038/nmeth.4193

Zhu P, Chertova E, Bess J, Lifson JD, Arthur LO, Liu J, Taylor KA, Roux KH. 2003. Electron tomography analysis of envelope glycoprotein trimers on HIV and simian immunodeficiency virus virions. *Proc Natl Acad Sci U S A* **100**:15812–15817. doi:10.1073/pnas.2634931100

Zhu P, Liu J, Bess J, Chertova E, Lifson JD, Grisé H, Ofek GA, Taylor KA, Roux KH. 2006. Distribution and three-dimensional structure of AIDS virus envelope spikes. *Nature* **441**:847–852. doi:10.1038/nature04817

Ziblat R, Fargion I, Leiserowitz L, Addadi L. 2012. Spontaneous formation of two-dimensional and three-dimensional cholesterol crystals in single hydrated lipid bilayers. *Biophys J*. doi:10.1016/j.bpj.2012.05.025

Zimmerberg J, Akimov SA, Frolov V. 2006. Synaptotagmin: Fusogenic role for calcium sensor? *Nat Struct Mol Biol* **13**:301–303. doi:10.1038/nsmb0406-301

Zimmerberg J, Curran M, Cohen FS, Brodwick M. 1987. Simultaneous electrical and optical measurements show that membrane fusion precedes secretory granule swelling during exocytosis of beige mouse mast cells. *Proc Natl Acad Sci U S A* **84**:1585–1589. doi:10.1073/pnas.84.6.1585

Zutz A, Schölz C, Schneider S, Pierini V, Münchhoff M, Sutter K, Wittmann G, Dittmer U, Draenert R, Bogner JR, Fackler OT, Keppler OT. 2020. SERINC5 Is an Unconventional HIV Restriction Factor That Is Upregulated during Myeloid Cell Differentiation. *J Innate Immun* **12**:399–409. doi:10.1159/000504888